Investigations on Frequency Selective Reflectors towards Gain Enhancement of Wideband Planar Compact Antennas

THESIS

Submitted in partial fulfillment of the requirements
for the degree of

DOCTOR OF PHILOSOPHY

by

Ashish Kumar Verma
ID No. 2018PHXF0017P

Under the Supervision of

Prof. Rahul Singhal

BIRLA INSTITUTE OF TECHNOLOGY AND SCIENCE, PILANI
2023

BIRLA INSTITUTE OF TECHNOLOGY AND SCIENCE, PILANI

CERTIFICATE

This is to certify that the thesis titled **Investigations on Frequency Selective Reflectors towards Gain Enhancement of Wideband Planar Compact Antennas** submitted by **Ashish Kumar Verma** ID No **2018PHXF0017P** for award of Ph.D. of the Institute embodies original work done by him under my supervision.

Signature of the Supervisor: ____________________

Name in capital letters: PROF. RAHUL SINGHAL

Designation: Associate Professor
Department of Electrical and Electronics Engineering,
Birla Institute of Technology and Science, Pialni Campus,
Pilani, Rajasthan- 333 031

Date: ____________________

Dedicated to the almighty
and my family.

ACKNOWLEDGMENTS

I am delighted to express my profound respect and heartfelt appreciation to Prof. Rahul Singhal, my Ph.D. supervisor from the Department of Electrical & Electronics at BITS Pilani, Pilani Campus. His wisdom, vision, expertise, guidance, enthusiastic involvement, and unwavering encouragement have been invaluable during the planning and development of this research. I am sincerely grateful for his meticulous efforts in thoroughly reviewing and enhancing the manuscript, without which the completion of this work would not have been possible.

I would like to sincerely extend my gratitude to Prof. V. Ramgopal Rao, the Vice-Chancellor of BITS, Pilani, for providing me with the invaluable opportunity to pursue my doctoral studies at this esteemed institution. I also wish to convey my sincere thanks to Prof. Sudhirkumar Barai, the Director of BITS, Pilani, for his constant encouragement and support. Prof. Chandra Shekhar, an Emeritus Professor of the EEE Department, deserves my appreciation for his unwavering encouragement and assistance. Furthermore, I am immensely grateful to Prof. M. B. Srinivas, the Dean of the Academic-Graduate Studies & Research Division (AGSRD), and Prof. Shamik Chakraborty, the Associate Dean of the AGSRD, for their invaluable support throughout my doctoral program. I also acknowledge Prof. Kuldip Singh Sangwan, Senior Professor in Mechanical Engineering Department & Chief, Workshop Unit at BITS, Pilani for providing fabrication facility and rendering necessary technical assistance.

I am deeply indebted to my doctoral advisory committee (DAC) members, Prof. Navneet Gupta, Head of EEE department and Prof. Praveen Kumar AV, and DRC committee for their unwavering guidance and motivations during my Ph.D. journey.

I would also like to express my gratitude to the staff members of the EEE Department, namely Mr. Ravinder Kumar Yadav, Mr. Tulsi Ram Sharma, Mr. Ashok Saini, Mr. Manoj Kumar, Mr. Amitabh Jangir, Mr. Yogesh, Mr. Sanjay Bharbava, Mr. Ramavatar, and Mr. Surendra, for their invaluable assistance in the laboratory and other official tasks.

I cannot conclude this section without mentioning the support from faculty members Prof. V.K. Chaubey, Dr. Syed Mohammad Zafaruddin, Prof. Nitin Chaturvedi, Prof. Vinay Chamola and senior colleagues Dr. Abhishek Joshi and Dr. Ritish Kumar. I would also like to thanks to my fellow colleagues, Mr. Abheek Gupta, Mr. Pranay Bharadwaj, Mr. Premsai Regalla, Mr. Anukaran Khanna, Mr. Akhilesh Kumar Mishra, and Ms. Shambhavi Shukla. There are many other people whose names

do not appear here but whose love, support and contributions in various forms have motivated me and helped me to complete this work.

In addition, I would want to express my gratitude to both of my parents for always being an eternal source of inspiration for me. I would want to express my deepest appreciation to my sisters and my brother for their unconditional love, faith, patience, and support they have always shown me. I also would like to acknowledge my wife and son for their support, without which it would have been difficult to maintain patience while pursuing research.

Finally, I am indebted and grateful to the Almighty for helping me in this endeavor.

Ashish Kumar Verma

ABSTRACT

The Thesis explores and discusses the techniques to design frequency selective surfaces (FSSs) to demonstrate band reject and reflect responses from microwave (3-30 GHz) to terahertz (THz) frequency regime. The performance analysis of conventionally known polarization independent (PI) FSSs composed of array of symmetric unit elements with respect to incident electromagnetic (EM) waves such as arrays of square loop, complementary square loop (SL) and crossed dipole (CD) unit cell elements have been performed through simulations using a full wave solver available with a commercial software, Computer Simulation Technology Microwave Studio (CST-MWS). Preliminary investigations on the effect of electric properties of materials such as permittivity and conductivity of metals on transmission characteristics of FSSs have been carried out. The FSSs composed of diagonally asymmetric unit elements are then designed and analyzed. The unit cells with distinct aspect ratio (A/R) of periodicity along both horizontal and vertical directions are considered as asymmetric arrays. These asymmetric unit elements are based on rectangular loops, elliptical loops and rhombic loops respectively to demonstrate polarization dependent (PD) transmission characteristics. The PD FSSs are then evaluated and their wave propagation characteristics under oblique EM wave incidence are compared. The orthogonally oriented arrays of PD FSSs are then printed on opposite sides of the dielectric substrate to demonstrate wide stopband responses with similar transmission but dissimilar reflection characteristics. Similar transmission as well as reflection characteristics are obtained when both arrays of PD FSSs are patterned on one of the sides of the substrate.

To attain relatively large rejection bandwidth, two rhombic loops or a dual rhombic loop (DRL) based unit cells are then arranged in rectangular lattice with periodicity ratio of 1:2 along two orthogonal directions. These orthogonal arrays of DRLs are developed on opposite sides of dielectric substrate as a back-to-back (BTB) arrangement and later, both layers are patterned or merged on one of the sides of substrate. BTB DRL and MDRL exhibit similar attributes but with relatively large rejection band. Further, a detailed evaluation of the performance of C-band and ultra-wideband (UWB) single-layered bandstop frequency selective reflectors (FSRs) is carried out. These FSRs use a polarization dependent single rectangular loop pair (RLP) as their foundation. The RLP array is placed in a square and rectangular grid and simulated in order to investigate the signal rejection and reflection properties when transverse electric (TE) and transverse magnetic (TM) waves are incident on it. In addition, in

order to explore wave propagation and its influence on wave polarization, orthogonal RLP patterns are printed BTB on a laminate. When orthogonal FSS arrays are mearged on any one of the sides of the dielectric substrate as merged RLP, the reflection phase nonlinearities of the BTB RLP arrays are mitigated. In order to analyze the transmission properties, of these reflectors, equivalent circuit models (ECMs) of these reflectors are also studied. Experiments are then conducted after the development of both MRLP and MDRLP based FSSs to assess their potential to reject signals across wideband (WB) and ultra-wideband (UWB) spectrums. The array of M-RLP placed in a square grid displays rejection and reflection with PI behaviour, and is angularly stable (AS). In contrast, the array of merged RLP that is laid in a rectangular grid displays UWB rejection covering a band from 2.3 GHz to 11.5 GHz.

The effect of FSRs on compact antennas is investigated by integrating them with antennas. Planar slot antennas being bi-directional radiators are preferred for their performance assessments when united with FSRs. Three different types of reflectors are utilized in conjunction with a triangular slot antenna operating at 8.2 GHz. These reflector configurations include BTB DRL, MDRL reflector and the reflector formed by stacking two orthogonal PD arrays of DRLs as cascaded DRL (CDRL) respectively. Through simulations, the impedance band and radiation characteristics of the antenna are analyzed. The experiments are conducted after fabricating the antenna and antenna integrated with MDRL at an optimum distance. The triangular slot antenna exhibits an impedance band ranging from 7.79 GHz to 8.61 GHz (9.64% bandwidth), with a boresight gain of 3.88 dB at 8.2 GHz. Upon integration with the proposed MDRL FSS, the antenna offers an impedance band with a span of 7.96 to 8.6 GHz and a 4.5 dB enhancement of antenna gain by use of FSR with a linear reflection phase.

A UWB FSR, MDRLP is integrated with a Norman window-shaped UWB slot antenna. Various configurations of the UWB antenna and reflector with different spacing are analyzed, and an optimal configuration for experimental validation is then determined. The radiation pattern of the antenna is analyzed at different frequencies in the presence of the UWB FSR. When MDRLP is positioned as a reflector on the opposite side of the slot antenna, the UWB slot antenna exhibits a peak gain of 7.86 dB, resulting in a 3.6 dB improvement in gain in the zenith (θ=0°) direction. Furthermore, experimental validations are also conducted on a modified hexagonal slot antenna that is excited by a sectoral feed for the UWB frequency range.

Tessellated RL (TRL)based reflective surface with WB reject characteristics are proposed and designed. The hexagonal slot antenna is assembled with TRL reflector in different combinations of TRL FSSs, both on the slot side and the feed side, to assess their impact on antenna impedance and radiation characteristics. Experiments once carried out, resulting in a peak gain of 4.31 dB in the zenith and 4 dB in the nadir. The zenith note a gain enhancement of 2.4 dB when the TRL FSS is loaded on the feed side, while the nadir record a gain enhancement of 3.8 dB when the RL FSS is loaded on the slot side.

To further investigate the impact of AS and PI FSSs on antenna gain improvement applications, the study incorporates three distinct loop-type reflectors, i.e., SL, TRL, and MDRL. These FSSs are designed and integrated with a triangular slot antenna operating at 10 GHz. Under oblique incidences, RL and SL FSSs exhibit stopband responses in the X-band frequency range with PD and PI, respectively. The third FSS unit cell, constructed by arranging RLs in two orthogonal arrays over a dielectric substrate, demonstrates bandstop characteristics with PI under normal incidence. For analysis purposes, a straightforward microstrip line feed-excited triangular slot antenna operating at 10 GHz is designed. All three finite FSSs, comprising (5×5) unit cells, but with distinct substrate dimensions, are loaded onto the triangular slot antenna at an optimized separation.

The significance of AS and PI is examined by rotating the FSSs positioned beneath the antenna in two orthogonal directions and loading these reflectors onto the two orthogonal orientations of the antenna. Experimental validation is conducted for all three antenna prototypes. When loaded with RL, MDRL, and SL FSSs, the antenna achieves gain enhancements of 4.8 dB, 7 dB, and 4.8 dB, respectively, in the boresight direction. The effectiveness of reflector size is further demonstrated through simulations and experiments by loading the antenna with FSSs developed on substrates of equal size. The measurements indicate that the AS and PI FSS (SL) provides the highest gain enhancement of 8.1 dB, while the non-PI and AU FSSs (RL and MDRL) yield comparable gains of 7.25 dB and 7.17 dB, respectively. These results suggest that features such as AS and PI are not significantly relevant and can be compromised in gain enhancement applications.

Simulations are performed further to investigate the potential benefits of FSSs in the THz frequency range. Conventional metallo-dielectric FSSs designed for THz frequencies are analyzed to showcase their bandstop and bandpass characteristics. Moreover, the selective transmission properties of these FSSs offer potential advantages in reducing mutual coupling and cross talk between adjacent functional blocks in integrated circuits (ICs). In this context, two types of FSSs, planar and non-planar, are explored. The planar FSSs are based on metalo-dielectric finite arrays, while the non-planar FSSs employing finite arrays of cubic pillars. The metalo-dielectric FSSs utilize metallic square pixels and interconnected square pixels to provide high

isolation between neighboring functional blocks in THz ICs, thereby helping combat electromagnetic interference (EMI) and crosstalk. Additionally, the performance analysis of finite arrays of all-dielectric micro pillar-based FSSs is presented. These arrays consist of dielectric cubic pillars arranged in a straight line and organized in a square lattice. The FSSs are illuminated from both lateral and orthogonal directions by electromagnetic waves. The study compares the transmission properties of arrays containing COC micro pillars (AD-FSS), SiO_2-filled COC micro pillars (SD-FSS), and metal-coated COC micro pillars (MD-FSS). The results demonstrate that AD-FSS is a cost-effective and efficient technique for reducing mutual coupling in narrowband frequency ranges. On the other hand, MD-FSS exhibits a broader stopband and superior rejection capabilities. Therefore, both AD-FSS and MD-FSS solutions can effectively mitigate cross talk and interference in next-generation THz ICs. In summary, these proposed FSS solutions offer promising techniques to address interference and crosstalk issues in future THz ICs.

Contents

List of Figures

List of Tables

List of Acronyms/Abbreviations

5G	Fifth Generation
AD-FSS	All Dielectric FSS
AMC	Artificial Magnetic Conductor
AR	Axial Ratio
AS	Angularly Stable
AU	Angular Unstable
BP	Bandpass
BS	Bandstop
BTB DRL	Back-to-back Dual Rhombic Loop
BTB DRLP	Back-to-back Dual Rectangular Loop Pair
BTB ELIP	Back-to-back Elliptical Loop
BTB RECT	Back-to-back Rectangular Loop
BTB RL	Back-to-back Rhombic Loop
BTB RLP	Back-to-back Rectangular Loop Pair
BW	Bandwidth
CD	Crossed Dipole
CD-Tr	Translated Crossed Dipole
CM	Circuit Model
CP	Circularly Polarized
CSL	Complementary Square Loop
CST	Computer Simulation Technology
dB	Decibel unit
DR	Dielectric Resonator
EBG	Electromagnetic Bandgap
ECM	Equivalent Circuit Model
EM	Electromagnetic
EMI/EMC	Electromagnetic interference/ Electromagnetic compatibility

FBW	Fractional Bandwidth
FDTD	Finite Difference in Time Domain
FEM	Finite Element Method
FSS	Frequency Selective Surface
HDRL	Horizontal Dual Rhombic Loop
HDRLP	Horizontal Dual Rectangular Loop Pair
HELLIP	Horizontal Elliptical Loop
HIS	High Impedance Surface
HRECT	Horizontal Rectangular Loop
HRL	Horizontal Rhombic Loop
HRLP	Horizontal Rectangular Loop Pair
IoT	Internet of Things
LHCP	Left Hand Circularly Polarized
LP	Linearly Polarized
MD-FSS	Metallo-Dielectric FSS
MDRL	Merged Dual Rhombic Loop
MDRLP	Merged Dual Rectangular Loop Pair
MELLIP	Merged Elliptical Loop
MIMO	Multi-Input-Multi-Output
MRECT	Merged Rectangular Loop
MRL	Merged Rhombic Loop
MRLP	Merged Rectangular Loop Pair
MWS	Microwave Studio
PCM	Polarization Converting Metasurface
PD	Polarization Dependent
PI	Polarization Independent
PRS	Partially Reflecting Surface
PSS	Polarization Selective Surface
PTLM	Periodic Transmission Line Method

RCS	Radar Cross Section
RF	Radio Frequency
RHCP	Right Hand Circuarly Polarized
RL	Radio Frequency
SAR	Specific Absorption Rate
SD-FSS	Substrate Dielectric FSS
SL	Square Loop
SL-Tr	Translated Square Loop
SSL	Single Square Loop
TE	Transverse Electric
THz	Terahertz
TM	Transverse Magnetic
TRL	Tessellated Rhombic loop
TSL	Tilted Square Loop
VDRL	Vertical Dual Rhombic Loop
VDRLP	Vertical Dual Rectangular Loop Pair
VELLIP	Vertical Elliptical Loop
VNA	Vector Network Analyzer
VRECT	Vertical Rectangular Loop
VRL	Vertical Rhombic Loop
VRLP	Vertical Rectangular Loop Pair

List of Notations

S_{21}	Transmission coefficient
S_{11}	Reflection coefficient
λ_0	Free space wavelength
σ	Conductivity
$tan\delta$	Loss tangent
ε_r	Relative permittivity
f_r, f_z, f_{stop}	Transmission zero frequency
f_p, f_{pass}	Transmission pole frequency
f_l	Lower corner edge frequency
f_h	Upper corner edge frequency

Chapter 1

Frequency Selective Surfaces: Introduction

A brief overview of frequency selective surfaces (FSSs) and their applications in diverse wireless applications are outlined in this chapter. The crucial performance measures, analysis methods and characterization techniques of FSSs are described followed by literature review. The research motivations and objectives of the thesis are also highlighted.

1.1 Background

With rapid surge in demand of seamless wireless communication systems, new standards for both multiband and wideband frequency ranges in distinct frequency regimes such as microwave (3-30 GHz), millimeter wave (30-300 GHz) and even Terahertz (THz) $>$ 300GHz frequency are proposed. Although multiband communications enable devices to operate on multiple bands simultaneously or switch between bands to optimize performance, reduce interference, and enhance reliability, The demand for high data rate wireless communication systems has been growing rapidly in recent years, driven by the increasing need for faster and more reliable connectivity in various applications such as mobile devices, Internet of Things (IoT), autonomous vehicles, virtual reality and imaging applications. High data rate wireless communication systems allow users to transfer large amounts of data quickly and efficiently, enabling seamless access to multimedia content, real-time streaming, and other bandwidth intensive applications.

To facilitate the high data rate communications, the radio frequency (RF) circuits along with high gain and directional antennas operating over wide frequency band are intended to improve the carrier to noise ratio (CNR) for an improved radio link between communicating devices and systems [1]. In addition to the rising need for such wireless applications, the signals need to be segregated from one another and secured, in order to keep away electromagnetic interference (EMI). EMI issues are significant challenges in modern wireless communications especially at high frequency. EMI is the disturbance caused by electromagnetic radiation from electronic devices, while electromagnetic compatibility (EMC) refers to the potential of electronic devices to operate in a shared EM environment with interference avoidance. EMI/EMC issues can lead to degraded performance, loss of data, and even complete system failure. In wireless communication systems, EMI/EMC issues can be produced by various factors, such as electromagnetic radiation from other electronic devices, antenna coupling, and signal reflections.

To address EMI/EMC issues in modern wireless communication systems, various techniques and solutions are employed. The intrinsic properties of FSSs for manipulation of EM waves are subject matter of interest in this context. Generally, any FSS is an of array elements, arranged in a quasi-periodic or periodic grid, that allow, prevent, or absorb the incident EM waves of a particular frequency or band or even multiple frequency bands of distinct polarization states. This arrangement can be in either a two-dimensional or three-dimensional configuration. These elements arranged as an array are individually known as unit cells, elements or structures.

These purposefully engineered surfaces are particularly advantageous in reforming antenna characteristics such as reduction of radar cross section (RCS) [2], enhancement of antenna gain and directivity [3], [4], and in mutual coupling reduction in multi-input-multi-output (MIMO) antenna [5] etc. FSSs are also extensively investigated as passband radomes [6], high impedance surfaces (HISs) [7], artificial magnetic conductors (AMCs) [8], shielding surfaces, and reflectors towards enabling smart home applications.

AMCs are HISs that function identically to perfect magnetic conductors (PMCs) due to the periodic placement of metallic sections and shorting to ground with metallic vias. HISs reflect electromagnetic radiation incident on them with a reflection phase of zero degrees, as opposed to out of phase for perfect electric conductors [7]. AMC surfaces are beneficial for a wide range of applications, including directional printed antennas and cavity resonator antennas, among others. In addition, the translucent property of FSSs is utilized as partially reflective surfaces (PRS), which are typically placed on the top of an antenna as a superstrate to improve the radiation performance, or PRS is replaced with the ground plane of antenna to provide high directional radiation characteristics with partial reflection to reduce the antenna RCS.

FSS can be broadly categorized based on unit cell element, design of their structure and applications. Basic elements or the unit-cells of FSS can be classified in four groups as depicted in Figure 1.1 [9]. The unit cells such as straight elements, n-straight element joined together making a junction, anchor element, Jerusalem cross and square spiral fall under first group. Loop type unit cells are classified into second group, polygonal plates belong to third group while the fourth group consists of combination type unit cells.

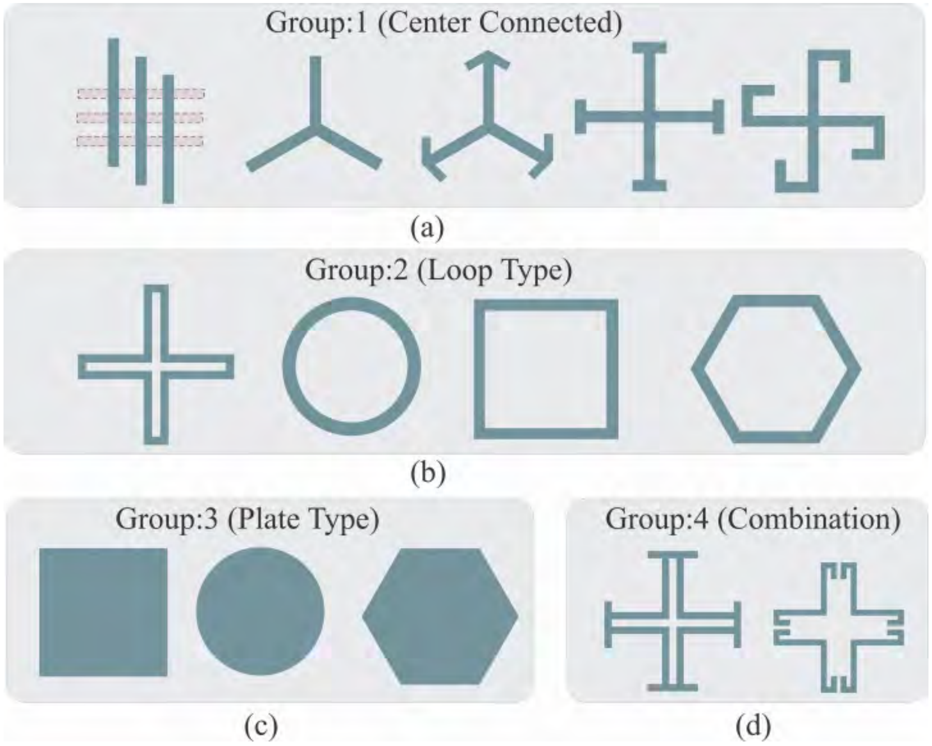

Figure 1.1: Types of unit cells [9]

These various types unit-cells constitute the FSS as 2-D or 3-D structures which can be arranged as single layer or multiple layer FSSs. These FSSs can be either free-standing i.e., metallic surface [10] or metal-dielectric surface or FSS can be made of dielectric materials only, i.e., all-dielectric FSS (ADFSS) [11]. Generally, multiple layer FSS structures [12] are employed to reshape their reflection or transmission or absorptive characteristics improve the performance of candidate like antennas and microwave circuits. Further on the basis of application FSS can be classified as passive FSS, active FSS, FSS absorber, conformal FSS [13] etc.

1.2 Characteristics and features of FSSs

FSSs have specific reflective, transmissive or absorptive characteristics for the electromagnetic waves incident either normally or obliquely on these surfaces as shown in Figure 1.2. Basically, the FSS structure behaves on the basis of element geometry. First type of FSS structure composed of metallic patches on substrate material which is a capacitive type FSS, exhibits lowpass filter characteristics. The second type of geometry is its complementary structure, i.e., grid of metals. Such FSS are referred as inductive FSS and exhibit highpass filter type characteristics. Further the bandpass filter and bandstop filter characteristics are also shown in the Figure 1.3 [14].

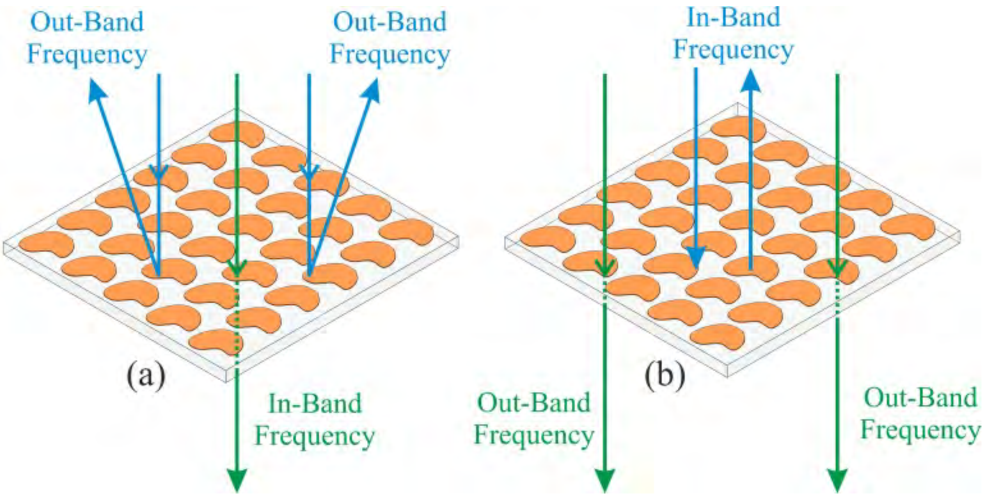

Figure 1.2: Functionality of (a) transmissive and (b) reflective FSS [15]

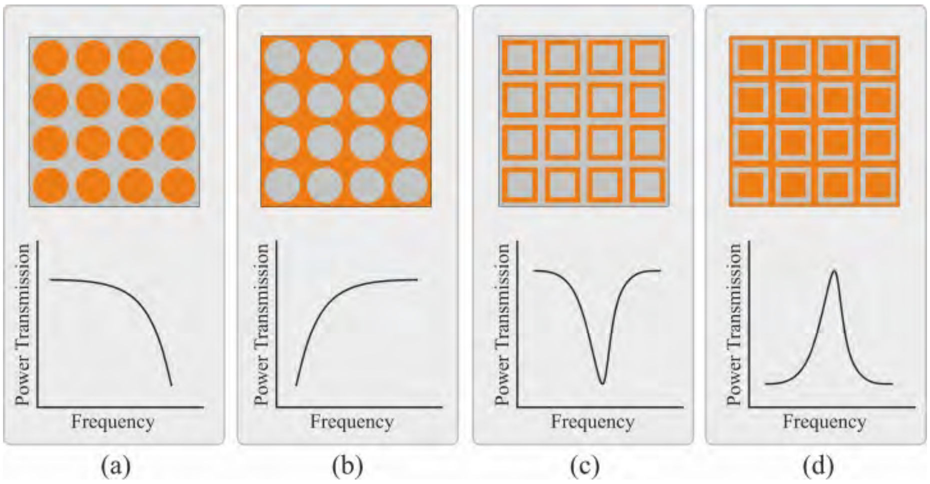

Figure 1.3: Characteristics of conventional FSSs [14]

1.2.1 EM incidence with TE/TM polarization

The categorization of FSSs based on transmission responses as discussed in Figure 1.3, may be further be extended when they are illuminated by EM waves with two distinct polarization states such as TE and TM incidence or EM wave incident at arbitrary polarization angle, ϕ. An FSS is considered as PI when it maintains its transmission response under EM waves irrespective of any polarization state. Moreover, an FSS is known as PD FSS if it exhibits distinct transmission responses under TE, TM or arbitrary polarized incident EM waves. It is well known that FSSs with grid of unit elements that possess four-fold structural symmetry, are generally PI FSSs. As the symmetry of FSS unit cells is disrupted, FSSs typically exhibit PD characteristics. Such FSSs have also been exploited as Polarization selective surfaces, Polarization rotators and polarization converters, etc. There are numerous wireless applications such as EM shield, radomes, absorbers, etc, that require PI FSSs.

1.2.2 FSSs under oblique incidences

The FSSs can also be categorized based on their transmission features dependent EM waves illuminating them obliquely. The FSSs are considered as angularly stable (AS) if they maintain their transmission characteristics under oblique EM incidences. Moreover, an FSS without AS feature, can not be PI.

1.2.3 Analysis methods of FSSs

FSSs can be analyzed by three ways such as lumped element model, periodic transmission line method (PTLM), and full wave numerical approaches. The lumped element method is the simplest way to analyze the FSS structure in terms of lumped parameters such as capacitance (C) and inductance (L) as an LC resonant circuit [7]. This method gives the band-gap feature of electromagnetic band gap (EBG) structures. Due to simplified approximation of L and C, this method is not very accurate. Alternatively, PTLM is helpful for the analysis of periodic structures using Floquet periodic conditions [16]. The surface wave mode, leaky wave modes, left- and right-hand regions and band gaps can be easily determined using this method. This method is limited to simple and general geometries. Due to rapid development of computational electromagnetics, various numerical methods such as Finite Element Method (FEM) or Finite Difference Time Domain (FDTD) techniques are applied for the analysis of FSSs. These analytical methods can be applied to arbitrary FSS configurations (single-layer FSSs, cascaded or multi-layered FSSs and conformal FSSs) [17].

1.2.4 Characterization of FSSs

For the characterization of FSS, the following performance parameters are considered such as reflection and transmission coefficients of FSS, and phase reflection characteristics. The measurement set up for the transmission/ reflection characteristics of FSS under test (FUT) is shown in Figure 1.4 and Figure 1.5 respectively.

Both the horn antennas are connected to vector network analyzer (VNA) through coaxial cables as shown in Figure 1.4 to measure the transmission coefficients of FSS.

To determine the phase reflection characteristics of any FSS the measurement setup is depicted in the Figure 1.5 which requires transmitting and receiving horn antennas placed adjacent to each other in an anechoic chamber facing the FUT.

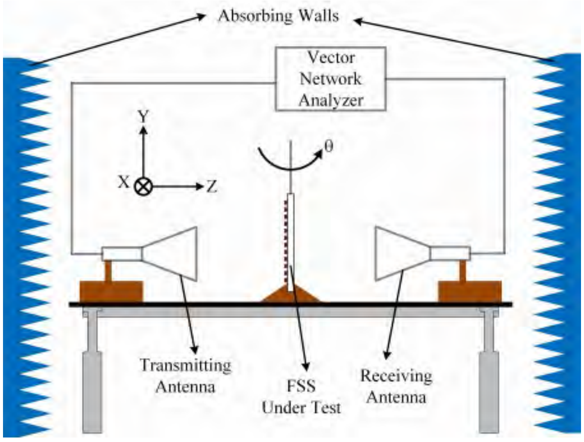

Figure 1.4: Measurement setup for Transmission of FSS

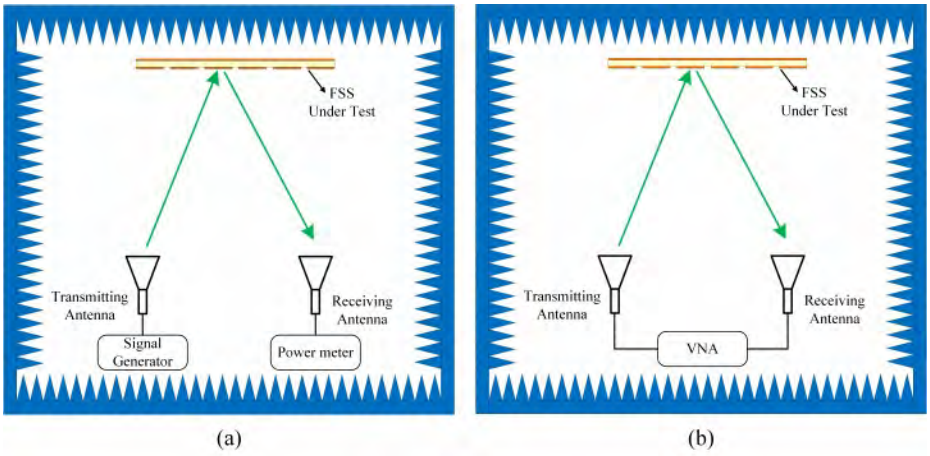

(a)

(b)

Figure 1.5: Measurement setup for Phase reflection characteristics

1.3 Appplications of FSSs

To accomplish antennas with improved radiation characteristics, FSSs are incorporated with the planar antennas either as superstrate or a HIS ground plane of antenna. The integration of FSS to the antenna improves the performance of antennas such as enhancement in impedance bandwidth(BW), gain, directivity, antenna efficiency and RCS reduction [18], [19] etc. The artificial surface may also be used for antenna miniaturization [20], [21].

Active FSSs are realized using solid state switches like PIN diodes [22], [23], [24] or Varactor diodes [25]. These FSS are used in EM shielding for numerous applications such as EMI reduction in medical instruments and making buildings protective from unwanted interfering signals in smart home applications [26]. Moreover, FSSs are also used as absorbers which find application in stealth technology as these absorbers reduce the RCS of fighter aircrafts [27]. By using FSS, mode suppression of antenna can also be achieved. Wearable FSS based antenna with improved performance and reduced specific absorption rate (SAR) are reported [28]. Resonant cavity antennas i.e., Fabry-Perot antennas [29], [30] exploit FSSs which reduces its profile also and make them highly directive.

FSSs have also found a potential application as microwave absorbers [31], polarization conversion surface [32] i.e., polarization rotators [33], polarizers [34] and polarization selective surfaces [35] respectively. Such FSSs are exploited to provide the degree of freedom to use antennas to get desired polarization., from linear to circular and vice-versa. Recently, FSSs have also been used to provide isolation between antennas placed on substrate to realize MIMO antenna [5], [36] and to generate electronically steerable beam antennas [37] which is suitable for modern wireless communication and fifth generation (5G) technologies.

1.4 Literature review

FSSs are being widely explored over the globe at industrial level towards innovative products as well as at academic level for knowledge expansion. In earlier days, FSS were used with parabolic reflectors. Munk filed the patent on periodic structures for scanning applications which was published in 1974. A significant work has been done for the modelling of FSSs such as equivalent circuit modelling [38], and transmission line modelling [16]. FSSs are being investigated for enhancing the performance of antennas A detailed analysis of elementary properties of single layered FSSs and cascaded FSSs were presented using various methodologies to predict their frequency response [39].

Band reject FSSs are explored and developed using distinct types of unit cells, such as crossed dipoles [40], Jerusalem cross unit cells [41], square loops [42], square loops [43], FSSs based on a combination of different types of unit cells [44], etc. It is now widely recognized that loop-type FSSs offer wider band widths than dipole-type FSSs [9]. FSSs with multiple loop-based unit cells or FSSs with multiple layers are also employed to attain a high roll-off factor and wider bands. Circuit modelling is used to analyse higher order FSSs for wider stopband using dual and triple layers of square loop array [43].

A compact, polarization independent wide stopband FSS for C and X band was demonstrated based modified square loop array patterned on both sides of FR-4 dielectric substrate [45]. FSSs made up of symmetric unit cells towards incident EM waves show polarization independence and characteristics for TE and TM incidences are similar [45]. Dissociation in characteristics for distinct polarization polarization for linearly polarized incident waves can be realized by deviating from the symmetry of unit cell elements of FSSs [35].

Joshi and Singhal obtained different bands of rejection separate stop bands for TE and TM normally incident waves upon a square loop AMC with unevenly wide vertical and horizontal gratings but with uniform inter-element spacing [46]. The reported AMC was integrated with direct fed planar hexagonal towards gain enhancement.

For wideband applications in X, Ku, and mm wave bands, novel FSS designs are suggested. Both sides of the RO4003 substrate have identical metallic FSS layers. The geometry parameters are optimized to maximize the bandstop at the stipulated in-band maximum transmission level of 10 dB. Two separate FSS unit cell designs use the same architecture but have different size to function in the lower and higher bands. The unit cell being symmetrical also ensures resonance stability for TE and TM polarizations and incidence angles [47].

Apart from explored conventional type FSSs, several techniques are also employed to devise FSSs with miniaturized unit elements. A novel miniaturized unit element based FSS with bandpass characteristics was demonstrated in which the dimension was much smaller than operating wavelength. The proposed FSS consisted of metallic patches on the top side while the wire mesh on the bottom side of substrate of thickness of 0.5 mm, relative permittivity, ε_r=3.3 and loss tangent tan δ=0.002. The periodicity of both metallic patch and wire mesh was same and too less than operating wavelength. The resonance was observed due to capacitive surface formed due to conductive array of patches and coupled inductive surface of wire mesh. Through easy fabrication techniques the FSS developed later, characterized for X band frequencies [48].

Another novel miniaturized unit-cell based bandpass FSS was proposed for stable performance in resonance for different angles of incidences and polarizations. The size of the miniaturized unit cell was even smaller than its resonance frequency. The FSS was designed to operate for the band of 2.4 GHz-2.484 GHz (IEEE 802.11b/g/n band) [49]. Moreover, active FSSs with reconfigurable or programmable transmission responses are also expected to offer reliable wireless communication links as reconfigurable intelligent surfaces or intelligent surfaces [50].

An active FSS switching from reflective to transparent state and vice-versa by electronic elements/devices was demonstrated. The frequency response of the FSS is almost stable when the wave polarization changed, or the angle of incidence changed up to ±45° from normal. The square loop aperture-based unit cell of FSS is connected to adjacent unit cells through PIN diodes. Experiments demonstrated that by switching PIN diodes from ON to OFF states, around 10 dB additional transmission loss could be introduced on an average at the resonance frequency, for both polarization [22].

A novel polarization insensitive active FSS with wide stopband response is reported by Ghosh et al. in [25]. The unit cell of FSS had periodic array of metallic circular loops printed on dielectric substrate. Each loop is connected with adjacent loop through varactor diodes using surface mount technique. The structure displayed a wide stopband characteristic which is tuned from 0.54 GHz to 2.50 GHz on varying the reverse-bias voltage across the varactor diode.

Novel dual polarized active FSSs with tunable bandstop characteristics are demonstrated. The two structures consisted of unit cells tunable circular loops and tunable split rings to provide tunability over wide and narrow frequency ranges respectively. Using a novel biasing technique for both FSSs, in which PIN diodes and resistors are mounted on highly conducting layers on both sides of thin and flexible substrate, the independent alteration of transmission response is obtained at vertical and horizontal polarizations. Further the shape of full rings and split rings are convoluted in order to achieve stable response with respect to angles of incidence [26].

An active HIS with potential of electromagnetic wave absorption is reported. The tunable HIS composed of conductive square patches shorted with ground plane through via connections. The adjacent patches are connected through varactor diodes which were biased using resistive grid made by using surface mount resistors. An equivalent circuit approach is used to predict the behavior of varactor diode resistance for normal EM wave incidence. It is observed that the lossy nature of varactor resistance caused significant absorption [51].

In addition, the integration of FSSs with compact antennas is consistently drawing the attention of researchers and scientists to offer numerous advantages wireless applications. A dual band coplanar waveguide (CPW)fed patch antenna integrated with EBG substrate is demonstrated to operate at 2.45 GHz and 5.2 GHz bands. A common fabric is used for the proposed textile antenna. The 3×3 array of EBG structure composed of square loop surrounded by its concentric square patch. It is shown that antenna with EBG substrate had less back radiation thus, reduced SAR more than 10 dB and improved the gain by 3 dB [28]. Using resonant cavity model, a low profile and high gain antenna is reported in which single layered AMC surface is used as ground plane and as PRS as superstrate. The AMC is optimized using full-wave analysis for desired center frequency and bandwidth. Ray optics is used to give physical insight of the antenna and it is observed that antenna profile is reduced to half in comparison to PEC-PMC based quarter wave length resonant cavity antenna while radiation characteristics are maintained [52].

A resonant cavity antenna with conductive ground plane as substrate and aperture type highly reflective FSS as superstrate for directivity improvement of microstrip antenna is reported. The resonance features were analyzed for the aperture type FSS consisting of an array of 12×12-unit cells. Its high reflective behavior enabled the significant improvement in antenna impedance band and directivity by 0.6 GHz and 8.95 dBi respectively [4]. A Fabry-Perot cavity (FPC) antenna is reported with high directional characteristics for Ku-band (12-18 GHz). The resonant cavity is composed of a ground plane and a single metallic grid. The resonance is excited by a patch antenna placed at the vicinity of the ground plane [53]. A novel C-band point-to-point FPC antenna with high gain of 14.2 dB at 4.8 GHz and gain variations $<$ 4dB over entire band from 4.0-5.4 GHz was presented in [54]. The wide-band aperture coupled antenna (ACMA) is loaded by multi-layer FSS as superstrates. The proposed antenna system has wideband width due to resonance overlapping or resonance merging concept. The effect of misalignment of FSS over ACMA is also studied and found that the misalignment caused boresight maxima shifted by 3° [54]. A wideband circularly polarized (CP) FPC antenna is reported by Fen quin et al. [55]. The two-layer PRS with positive reflection phase gradient is used to improve 3-dB gain and bandwidth from 8.8 GHz to 11.7 GHz with a peak gain of 14.7 dBi. The CP antenna have also shown the wide Axial Ratio BW (8.5-11.5 GHz) [55].

The gain improvement and RCS reduction of a circularly polarized (CP) microstrip antenna is achieved using a shared aperture MS. The reported Fabry-Parot cavity antenna consisted of a PRS and a polarization conversion surface. The polarization conversion surface provides a 180° phase difference to reduce wideband RCS in the direction of normal incidence. The FPC cavity composed of the PRS and the ground plane of the CP microstrip antenna for gain enhancement. An improvement of 1.15 dB in the gain of antenna is reported over frequency range of 9 GHz to 17 GHz. The wideband RCS reduction is also achieved with values of 10.9 dB and 10.68 dB for dual polarization in the direction of normal incidence [56].

A reflective polarization converting metasurface (PCM) based on HIS in the X-band is reported by Loncar et al. in which the metasurface converted linearly polarized (LP) incident EM wave into its orthogonal polarization up on reflection. The polarization conversion is accomplished by guiding and coupling EM waves between pairs of perpendicular slots in a ground plane placed at the edge of each unit cell. The three-layered unit cell consisted of patch layer (top), slot layer (middle) and microstrip layer (bottom). A polarization conversion ratio of 99.4 % and half power bandwidth of 22 % is observed for the proposed PCM [32].

Recently, a wideband CP-FPC antenna for 5G-MIMO applications has been demonstrated and analyzed employing equivalent circuit and ray optics. The antenna comprises of simple corner cut CP antenna with a diagonal slot and a PRS located half-wavelength apart. The reported antennas have a wide impedance bandwidth of 25 GHz to 33 GHz (27.6%) and almost constant gain with a peak value of 14.1 dBiC and 3-dB Axial Ratio (AR) bandwidth for operating frequency range from 26 GHz to 31.3 GHz. To achieve polarization diversity, the MIMO antenna is realized using the same antenna with high isolation between 2×2 radiating elements and reduced-envelope correlation coefficient, which is suitable for future fifth generation (5G) communications [57].

The antenna is a simple circular patch antenna loaded by a circular metasurface (MS) with the same diameter (0.67λ) which is placed directly over the patch antenna thus, making it compact and low profile with thickness of 3.048 mm. The MS consists of repeatedly positioned rectangular-loop unit cells in the vertical and horizontal dimensions. The antenna's frequency reconfigurability is accomplished by rotating the MS. Rotation of the MS altered the effective relative permittivity of the substrate, thereby altering the antenna's operating frequency. In the tuning range [58], the exhibited antenna had a tuning range of 4.76 to 5.51 GHz, a fractional tuning range of 14.6 %, radiation efficiency greater than 80 %, and a maximal gain of 5 dBi [58].

Recently, polarization and frequency reconfigurable antenna with dual layer MS is proposed. The antenna operates at around 4 GHz and 5 GHz. The polarization at 5 GHz is reconfigured to linear polarization, left hand circular polarization (LHCP) and right hand circular polarization (RHCP) by rotation of polarization reconfigurable MS while, the operating frequency around 4 GHz can be reconfigured from 4 GHz to 4.35 GHz (8.4 %) by rotation of frequency reconfigurable MS with polarization unaffected [59]. A rectangular planar UWB monopole radiator when integrated with UWB reflector composed of asymmetric structure with circular aperture, provides an enhancement of 4.5 dB in gain of antenna. [60]

Recently, the gain of dielectric resonator (DR) slot hybrid is also enhanced by 3.3 dB by integrating it with a both side printed ultrathin FSS. This FSS is composed of array in which bidirectional lumped resister loaded arrows are printed on top side and circular split rings are printed on bottom side of low loss RT duroid LZ substrate. The FSS exhibits 47.3 % wide stopband with linearity in reflection phase within the X-band. The linear and reflection phase for an FSS is desired to obtain improved antenna radiation performance through constructive interference between waves reflected by FSSs and directly radiated waves from antenna along the antenna boresight [61]. In [62], the study of AMC reflection characteristics and its influence on planar dipole antenna is presented in the X-band frequency range. The antenna gain is improved by controlling the reflection phase and the distance between antenna and reflector. In order to reduce the mutual coupling between multiple antenna systems, an isolation enhancement technique is reported using metasurface as superstrate over closely spaced H-plane microstrip patch antennas. The epsilon and mu near zero (μ,$\varepsilon \rightarrow 0$) metasurface exploited as superstrate enhances the isolation to 30 dB at the operating frequency. The near zero refractive index property of the reported metamaterial improves the directivity of the antennas. A significant improvement of efficiency and gain of the antenna by 3.4 dBi and 20% respectively is achieved by using the superstrate [5]. Recently, gain and isolation has been improved of two port MIMO antenna loaded by a novel metasurface as superstrate. The superstrate consists of hexagonal nested loop double negative metamaterial with 4×2 unit to provide isolation better than 24 dB over wireless local area network within frequency band of 5.68-6.05 GHz with improved gain of 7.98 dBi. The superstrate assisted in absorption of magnetic field component of magnetic field thus, reduced the mutual coupling between antenna elements [63].

In modern radio communication systems, a huge requirement for low cost, compact and planar antennas compatible with planar microwave circuits. Printed slot antennas offer such advantages with relatively large bandwidth, low cross polarization level than microstrip antennas. However, the slot antennas suffer from bi-directional radiation characteristics with low gain in boresight directions [64]. Antennas with high gain and directivity are necessary to enhance the system signal to noise ratio (SNR) towards a better connectivity between communicating parts within devices. Aside from absolute metal reflectors, FSS based reflectors are now accepted for demonstrating gain enhancement with directional radiation especially in boresight direction.

1.5 Gaps in existing research and motivation

- Single layered FSSs have been explored widely. However, the FSSs based on stacked layers or double side printed unit cells have not been explored much.
- FSSs based on single type of unit-cells have been found in the literature while the FSS based on complex/ merged unit cells are rarely explored.
- Gain enhancement for WB and UWB antenna over entire band is challenging and rarely reported.
- Although FSSs have been integrated with planar antennas for gain enhancement, there is an emphasis on peak gain enhancement rather than in boresight direction.

- FSSs in THz regime have not been explored much may be due to different development technologies.

The following objectives have been framed as motivated from the above gaps.

1.6 Objective and scope of the thesis

The objectives of the Thesis are as follows:

- To design and develop 2-dimensional (2-D) FSSs employing electromagnetic modelling through simulations and their characterization using measurements.
- To investigate techniques to improve the performance of compact planar reflective FSS structures for electromagnetic wave manipulation.
- To analyze the impact of characteristics of FSSs towards enhancing the performance of compact antennas, or to explore characteristics of compact antenna integrated with FSSs.
- To validate the designed antennas integrated with proposed FSSs through practical experiments and measurements.
- To explore FSS designs optimized to operate in THz regime.

The thesis primarily discusses techniques to design FSRs and their impact towards compact antenna applications. The 2-D reflecting surfaces discussed here are designed to operate within WB and UWB ranges. To design and develop WB and UWB reflectors, the loop type FSS unit structures are explored and modified. The techniques to transform PD FSSs to PI FSSs are explored and investigated. The advantage of the work discussed in the thesis is that low cost 2-D reflecting surfaces are designed and developed over affordable FR-4 laminate. Slot antennas typically being bi-directional radiators demonstrate moderate gains in both, the zenith and nadir. To demonstrate the gain enhancement, compact planar slot antennas are integrated with loop type unit structure based reflectors. Low profile reflectors can preferably be integrated with the compact antennas to ensure their deployment with portable devices for practical wirelss applications. The FSRs are designed to demonstrate almost stable PD and PI the features under oblique incidences up to 45°. The propagation features discussed during the course of this thesis primarily are $|S_{21}|$, $|S_{21}|$ and $\angle S_{11}$ respectively.

1.7 Thesis outline

This thesis is organized in seven chapters.

Chapter 1 introduces the significance of FSSs for modern wireless communications followed by literature review of FSSs and their applications.

Chapter 2 describes the simulation study of conventional FSSs based on SL and CSL type unit cells in distinct frequency regimes., S-band, Ku band, Ka Band, G Band, THz and IR frequencies respectively. Moreover, PD FSSs have been presented to demonstrate distinct transmission responses when subjected to TE or TM polarized EM waves for Microwave frequency range. Later, the techniques to transform the PD FSSs to PI FSSs have also been explored.

Chapter 3 emphasizes on dual rhombic loop based FSSs for extended bandstop characteristics in the X-band frequency range and two techniques explored in Chapter 2 have been exploited again to transform PD FSSs to PI FSSs under normal incidences are proposed. The ECMs, transmission responses of FSSs under obluque incidences, fabrication and experimental validation for both these FSSs are presented. The impact of loading of these FSSs with compact triangular slot antenna has also been investigated.

Chapter 4 describes the rectangular loop pair based FSS reflectors to demonstrate C-band and UWB band reject features respectively and their ECMs are also developed to validate EM simulations. The transmission responses of these FSS reflectors are also validated through experiments. Later, One reflector with UWB stopband has also been integrated with a UWB slot antenna to demonstrate antenna gain enhancement. Chapter 4 ends with integrating Tessellated Rhombic loop based PD wideband (4.6 GHz-14.4 GHz) reflector with a UWB hexagonal slot antenna for its gain enhancement.

Chapter 5 discusses the relevance of FSS features such as AS/ PI towards antenna gain enhancement by integrating distinct PD and PI FSS reflectors with compact triangular slot antenna.

Chapter 6 describes the preliminary work to show the scope of exploiting the inherent characteristics of bandstop-bandpass FSSs even at THz frequency ranges. The metallo-dielectic FSSs composed of pixelated FSS and interconnected metallic pixel to obtain tailorable transmission response to accomplish the requirement of cross talk reduction at THz frequencies in ICs. Additionally, three dimensional (3-D) FSS structures are explored for mutual coupling reduction and cross talk reduction between adject functional blocks of ICs.

Chapter 7 concludes the thesis with broad spectrum of application of FSSs.

Chapter 2

Conventional loop based FSSs in distinct EM bands

This chapter begins with preliminary performance analysis and comparision of square loop (SL) and crossed dipole (CD) FSS unit cells. The effect of translated FSS unit cells and lossy dielectric substrate on their propagation characteristics has also been investigated. Further, SL and complementary square loop (CSL) based FSS structures explored and compared to demonstrate bandstop and bandpass responses respectively for distinct frequency regions. The significance of ohmic and dielectric properties of the substrate are studied using EM simulations performed on CST MWS. This research is useful for acquiring quick comprehension of features of unit cells and potential material for substrates at different frequency ranges. The frequency band of EM spectrum with adequate levels of appropriate isolation while signal propagation is also discussed. Later, the performance analysis of FSS unit cells is presented under normal incidence when the structural symmetry is introduced through non-unity operation (A/R). These FSSs arrays are based on rectangular loop, elliptical loop and rhombic loop unit cells and EM simulations are are carried out using CST MWS. Their transmission characteristics under TE and TM incidences are compared. Finally, the technique to transform a PD FSS to PI FSS is also explored and TE/TM transmission responses under normal to oblique incidences have been presented.

2.1 Introduction

The FSS structures created by unit cells possessing four-fold symmetry [65] have been explored to demonstrate PI bandstop [66] as well as bandpass transmission responses [67]. Square loop [68], circular loop [69], [70], [71], crossed dipole [40], [72], Jerusalem cross [73], [74], type unit cells are a few of the commonly known PI FSSs. However, the FSSs tend lose their PI characteristics when unit cell structure is disrupted as observed in reference [75]. PD FSSs have also been explored to be utilized as polarization converters [76], polarization rotators [77] and polarization selective surfaces (PSSs) [78], [79] respectively.

This chapter discusses design and analysis of conventional FSSs based on SL and

CSL unit element followed by asymmetric unit cell such as rectangular loop, elliptical loop and rhombic loop based FSSs. The transmission responses of the FSSs are then reported and compared.

2.2 Square loop (SL) and crossed dipole (CD) unit cells

This section presents and compares two distinct types of bandstop FSSs based on an infinitely large array of translated CD and SL unit elements. The effects of translating the unit elements horizontally and vertically by half the periodicity are compared. Full-wave EM simulations reveal that the geometry of an FSS array whether a conventional or translated unit cell is unaffected by the translation of the unit cell, leading to almost identical transmission properties. Comparatively, the bandstop bandwidth of the SL-based FSS array is approximately 202.14% larger than that of the CD-based FSS array.

Techniques like transmission line modelling, although limited to simpler arrays, are sometimes used for the analysis of larger arrays when are not computationally intensive. But precision appears during a full wave numerical analysis on the cost of excess memory required for exhaustive computation. However, these FSS arrays are limited to applications of directivity [4] and, gain [46] enhancement of planar antennas when integrated with them.

In this section of this chapter, comparison of CD and SL based FSSs is presented. CD and SL unit cells posses a translational symmetry [80] which disappears when arrays of both unit cells are arranged periodically to constitute an FSS of infinite dimension. In an arrangement of FSS array, the unit cells appear to be translated by half of periodicity along the edges on the surface of the array. The propagation characteristics of arrays of both conventional as well as translated unit cells are investigated and the comparison is reported here. Also, the role of substrate losses to further improve the ability of signal rejection is explored and presented here.

The CD element is obtained by connecting both vertical and horizontal gratings in the centre, whereas the square loop is created by integrating perpendicular and parallel gratings at the extremities. The 1.5 mm thick substrate material used here is an inexpensive and readily available dielectric, FR-4 having, dielectric constant = 4.3, and loss tangent = 0.025. Metal trace width (w), crossed dipole arm (P), square loop arm (P), or length of vertical or horizontal grating (P), periodicity (d), and inter element spacing ($g = d - P$) are the design parameters for both FSS. Figure 2.1 (a) and (b) respectively show the geometries of CD and translated CD (CD-Tr) while their respective infinite arrays are depicted in Figure 2.1 (e) and (f). Similarly, the unit cell geometries of SL FSS and translated SL (SL-Tr) are illustrated in Figure 2.1 (c) and (d) respectively. The infinite arrays of SL as well SL-Tr FSSs are shown in Figure 2.1 (g) and (h) respectively. Table 2.1 summarizes the optimal values for design parameters.

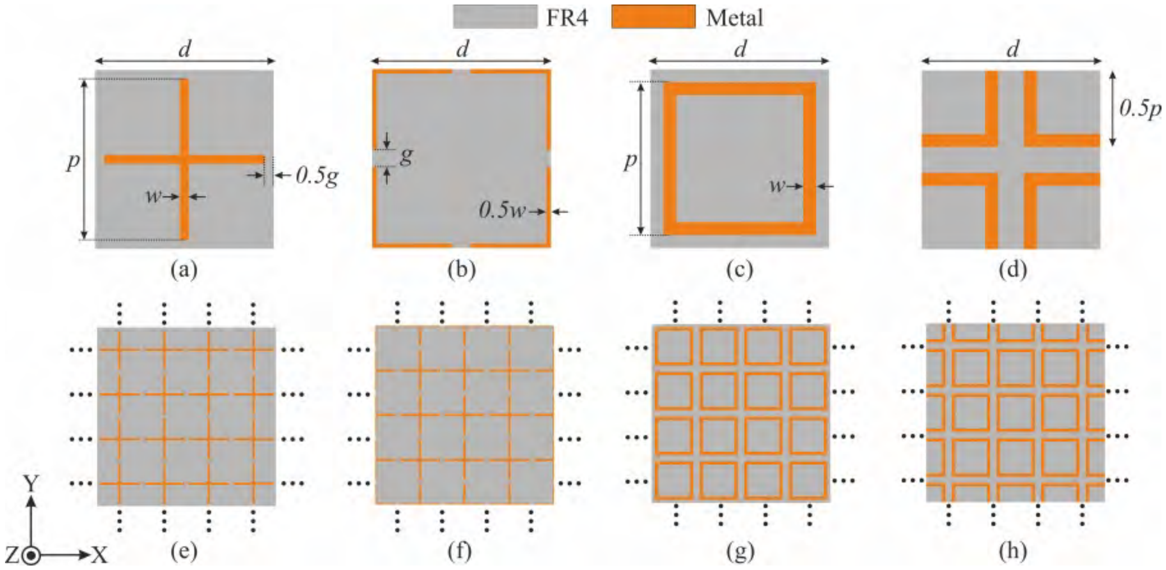

Figure 2.1: Conventional unit cells and translated unit cells (a) CD, (b) CD-Tr, (c) SL, (d) SL-Tr; Infinite arrays of (e) CD, (f) CD-Tr, (g) SL, (h) SL-Tr

Table 2.1: Features of FSS unit cells

Dimensions for (in mm)	w	P	d	g
Crossed dipole	0.5	9	10	1
Square Loop	1	5.9	6.9	1

2.2.1 Results for basic Loop and translated elements

As mentioned previously, the CD unit cell is formed as a result of integration of vertical and horizontal gratings at center whereas the SL array is created by joining horizontal and vertical gratings in the extremities. Full wave EM simulations are carried out with periodic boundary conditions to model the FSS unit cells mentioned above. The magnitudes of the transmission coefficients, $|S_{21}|$ and the reflection coefficients, $|S_{11}|$, for CD and CD-Tr unit elements are shown in Figure 2.2 (a). Also, the reflection and transmission phases of CD and CD-Tr unit elements are illustrated in Figure 2.2 (b). Similary, Figure 2.3 (a) demonstrates $|S_{21}|$ and $|S_{11}|$ for SL and SL-Tr FSS unit cellss while their respective reflection and transmission phases are shown in Figure 2.3 (b). The results for both basic unit cells and translated unit cells are found to be identical.

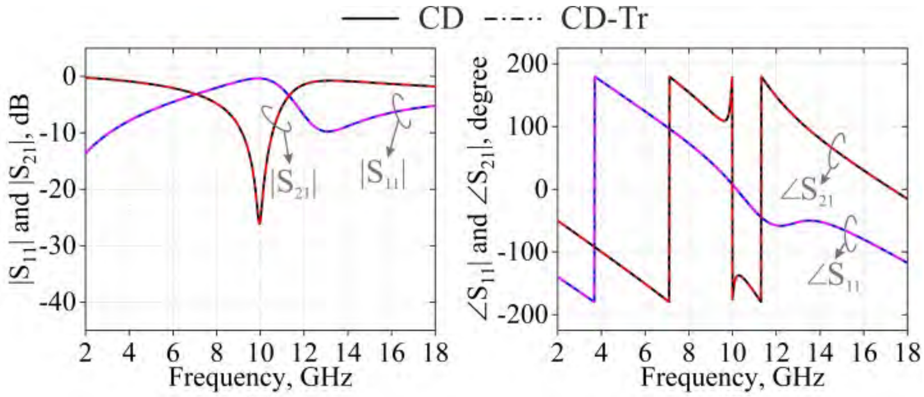

(a) (b)

Figure 2.2: Propagation characteristics (a) $|S_{21}|$ and $|S_{11}|$, (b) $\angle S_{21}$ and $\angle S_{11}$ for CD and CD-Tr FSS

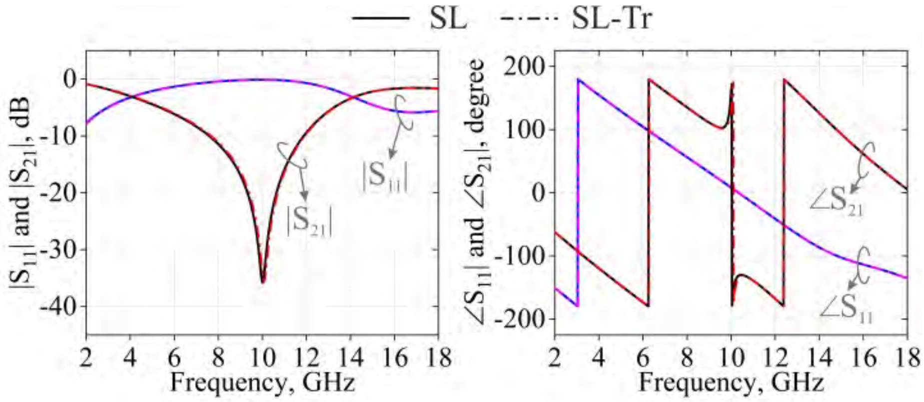

(a) (b)

Figure 2.3: Propagation characteristics (a) $|S_{21}|$ and $|S_{11}|$, (b) $\angle S_{21}$ and $\angle S_{11}$ for SL and SL-Tr FSS

The $|S_{21}|$ indicates that both CD and SL FSSs exhibit frequency band rejection with in-phase reflection around their resonant frequencies. At in-phase reflection frequency, the phase of reflection coefficient, $\angle S_{11}$ equals zero. The frequency range in which unit cell behaves as an AMC and has its operating band where $+90° > \angle S_{11} >$ -90°, according to [81]. Figures 2.2 and 2.3 reveal that the in-phase reflection appears at 10.17 and 10.34 GHz for CD and SL-FSS respectively. The CD and CD-Tr arrays display an operating band from 7.35 GHz to 16.54 GHz with a positive reflection phase gradient between 12.5 GHz and 13.5 GHz. The operating band for SL and SL-Tr FSS is between 6.57 and 14.18 GHz.

Figure 2.4 compares $|S_{21}|$ dB and $|S_{11}|$ dB of conventional CD and SL-FSS unit cells with their translated counterparts. The band reject capability of the SL FSSs is 2.83 GHz wider than that of the CD FSSs. SL FSSs can exhibit a high magnitude of EM wave rejection by 9.65 dB or more. Figure 2.4 demonstrates that dipole type FSSs are slightly feeble ($|S_{21}| \approx$-26 dB) to reject incident EM waves at the resonant frequency (9.95 GHz) on the FSS surfaces.

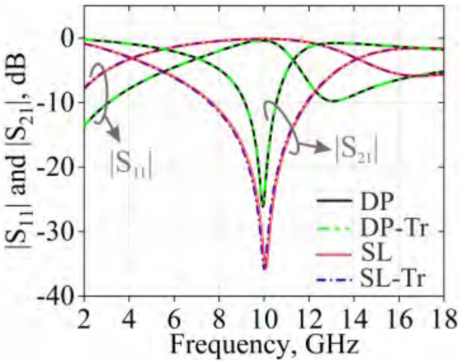

Figure 2.4: Transmission and reflection characteristics of CD and SL FSS unit cells

Figure 2.5 demonstrates the significant impact of the lossy substrate by demonstrating that the null frequency during transmission and the widths of the stopband are unaffected by the substrate type, while the $|S_{21}|$ is -26.1 dB for lossy CD and and -35.75 dB for lossy SL FSS, respectively. At the resonance frequency, the $|S_{21}|$ for the lossless CD and the SL FSS are -48 dB and -54.7 dB, respectively.

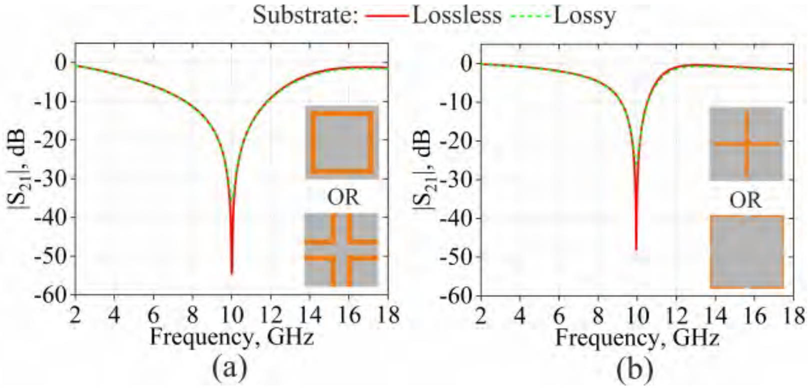

Figure 2.5: $|S_{21}|$ with and without substrate loss for (a) SL FSS, (b) CD FSS

In this study, SL and CD based FSS are compared. Using electromagnetic full-wave simulations with periodic boundary conditions, the conventional SL and CD FSS unit cells and their tranalated counterparts are analysed. Relatively SL-FSS has a wider bandwidth and signal isolation than CD FSSs. It has also been observed that substrates with low losses when used for FSSs exhibit better ability to reject incident EM radiation.

The following section further provides the simulation and analysis of FSSs based on SL and CSL in distinct EM bands to discuss their transmission characteristics.

2.3 Polarization independent loop based FSSs

FSSs are expected to be PI mostly when the unit cell structure holds a four fold symmetry and do not discriminate among different polarization states of incident EM waves. Several loop based FSSs e.g., square loops (SL), circular loops, hexagonal loops or octagonal loops those are structurally symmetric, show PI behaviour when analyzed. In the section ahead, SL and CSL based conventional FSS unit cells are analyzed.

2.3.1 Design of SL/CSL unit cells

The conventional structure of SL and CSL based unit cells are deployed in Figure 2.6. A SL metal layer is printed on substrate to form a SL unit cell while a square loop of similar shape and size is etched out in case of CSL unit cell. In both cases, features of square loops printed or etched remain same, i.e., thickness of the substrate (t), unit cell periodicity (p), loop width (w), and size of the square loop (d).

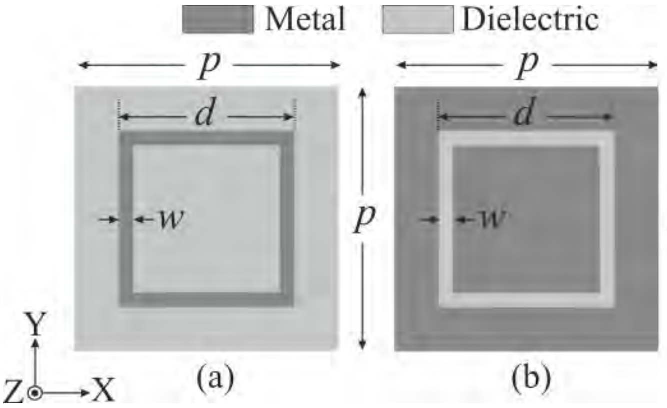

Figure 2.6: Conventional unit cells of (a) SL,and (b) CSL FSS

FSSs based on SL and CSL unit elements are intended to operate around the center frequency in six distinct frequency bands of EM spectrum and they are S-band (3 GHz); Ku band (15 GHz); Ka-band (33 GHz); G-band (200 GHz); THz (3 THz) and IR (300 THz). To accomodate all frequency bands during simulations, 'w' and inter element spacing, '$P-d$' are maintained at $0.2\lambda_0$ for both cases of SL and CSL unit structures.Through the knowledge of center frequency of each band of interest, the free space wavelength, λ_0 may be elaluated. All the geometrical features of unit structures of SL and CSL FSSs are summarized in Table 2.2.

To achieve adequate magnitude of signal transmission as well as isolation within a given frequency band, it is crucial to select the appropriate thickness of substrate dielectric material and metal layer. Figure 2.7 depicts the properties of the dielectric

Table 2.2: Distinct geometrical features of loop based FSSs in six different frequency bands

Parameters	EM bands					
	S-Band	Ku-Band	Ka-Band	G-Band	THz Frequency Range	IR Frequency Range
P	21.12 mm	4.138 mm	1.746 mm	0.307 mm	23.459 μm	0.144 μm
d	19.12 mm	3.738 mm	3.738 mm	0.277 mm	21.459 μm	0.124 μm
w	2 mm	0.4 mm	0.4 mm	0.03 mm	2 μm	0.02 μm
t	0.035 mm	0.035 mm	0.035 mm	0.001 mm	0.1 μm	0.01 um
Substrate thickness	0.8 mm	0.8 mm	0.2 mm	0.05 mm	0.8 μm	0.1 μm

materials employed for substrates and metal layers used for analysis in this study.

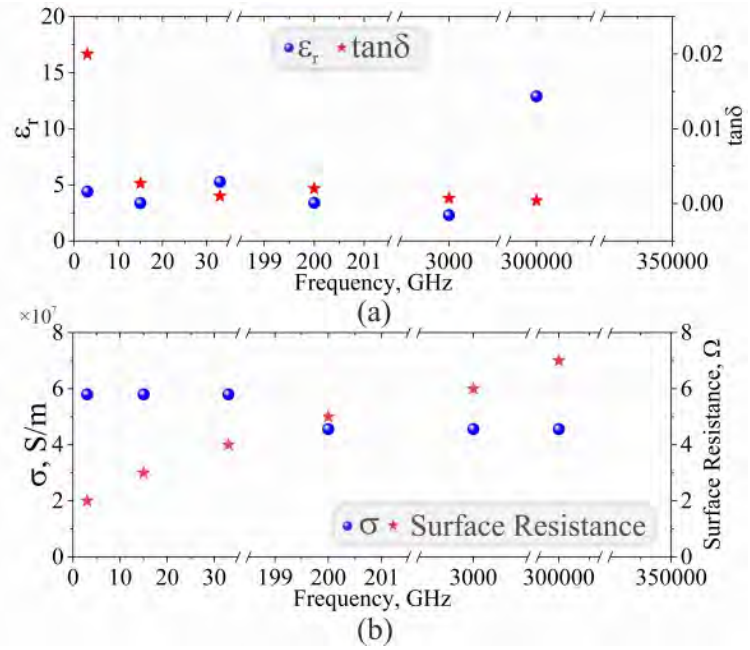

Figure 2.7: Properties of (a) dielectric materials (ε_r and tanδ) and (b) metal layers (δ and Ω) used at distinct frequency bands

Dielectric constant (ε_r) alongwith loss tangent (tanδ) are two important electrical characteristics of substrate materials used here. Substrate materials used here for FSSs are FR4 [31] for S-band, RO4003 [82], [83] for Ku-Band, glass [84] for Ka-band, kapton [85] for G-band and cyclic olefin copolymer (COC) [86] for THz while GaAs [87] for IR. For the FSSs operating within S-, Ku-, and Ka-band, metal layers are assured to be made of copper, whereas for FSSs to operate beyond 100 GHz in G-band or in THz, and infrared, the metal layers are assured to be developed by depositing gold. CST MWS simulations are used to determine discrete values of surface resistances of metal layers with given conductivity. Figure 2.7 (b) shows that the surface resistance over the metal layer rises as the frequency of interest rises.

2.3.2 Transmission and reflection responses

The loop and complementary loop based unit cells are enclosed within bounding boxes to simulate them in CST MWS at center frequency of suggested EM bands. Periodic boundary conditions, during simulations are applied along X- and Y- directions while along Z-directions, Floquet ports are applied to observe response of wave propagation through unit structures. The transmission responses of all six FSSs, including transmission coefficients $|S_{21}|$, reflection coefficients $|S_{11}|$, reflection phases $\angle S_{11}$, and transmission phases $\angle S_{21}$, are simulated and compared in Figure 2.8.

In addition, Table 2.3 also summarizes the responses of SL and CSL FSSs to incident EM waves designed for each of the six frequency values considered for analysis.

Table 2.3: Summary of SL and CSL responses in distinct EM bands

Frequency Range		S-band	Ku-Band	Ka-Band	G-Band	THz Frequency Range	IR-Frequency Range
Dimensions		$0.21\lambda_0 \times 0.21\lambda_0$	$0.21\lambda_0 \times 0.21\lambda_0$	$0.19\lambda_0 \times 0.19\lambda_0$	$0.20\lambda_0 \times 0.20\lambda_0$	$0.23\lambda_0 \times 0.23\lambda_0$	$0.14\lambda_0 \times 0.14\lambda_0$
Substrate		FR4	RO4003	Glass	Kapton	COC	GaAs
SL	f_z	3 GHz	15 GHz	32.99 GHz	200 GHz	3 THz	301.68 THz
	Isolation, dB	-40.29	-49.91	-52.97	-40.9	-31.49	-21.35
	10 dB Stopband	(2.4-3.7) GHz	(11.7-18.1) GHz	(24-41.8) GHz	(156.8-242.3) GHz	(2.4-3.6) THz	(243.7-442.6) THz
	FBW (%)	43.82	43.40	54.07	42.79	38.68	57.93
CSL	f_p	2.96 GHz	14.06 GHz	31.73 GHz	188.9 GHz	3.06 THz	327.7 THz
	Transmission, dB	-0.19	-0.1	-0.1	-0.25	-0.44	-4.51
	3 dB Passband	(2.2-3.9) GHz	(10.8-18.4) GHz	(25.6-39.3) GHz	(144.5-248.1) GHz	(2.2-4.2) THz	-
	FBW (%)	55.67	51.72	41.89	52.77	62.97	-

The frequencies at which minimum and maximum transmission is observed are defined as transmission zero, f_z and pole, f_p respectively. The transmission and rejection bandwidths in normalized curves are defined as the frequency range in which $|S_{21}| \geq$-3 dB and $|S_{21}| \leq$-10 dB implicating a passband and a stopband respectively.

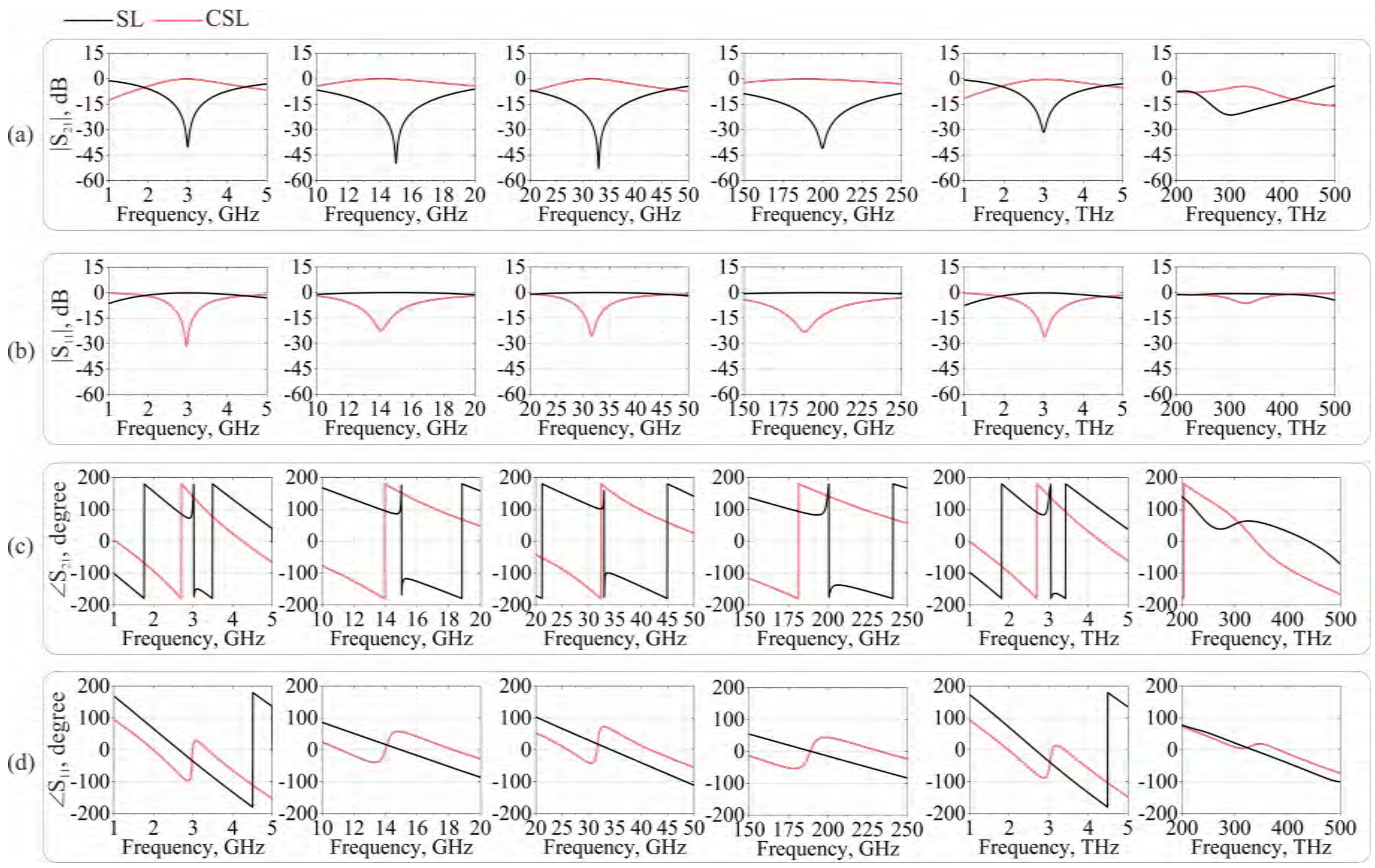

Figure 2.8: Responses of SL and CSL unit elements (a) $|S_{21}|$ (b) $|S_{11}|$, (c) $\angle S_{21}$ and (d) $\angle S_{11}$ at 3G, 15, 33 and 200 GHz, 3 THz and 300 THz respectively (from left to right)

The plots showing $|S_{21}|$ and $|S_{11}|$ versus frequency are displayed in Figure 2.8(a) and (b) suggesting that SL FSSs act as a bandreject filter for EM waves striking at f_z for both TE and TM polarization, whereas CSL FSSs allow the transmission of EM waves hitting at f_p. The pole frequency, f_p is observed at lower frequencies than f_z for all bands in frequency ranges, whereas f_p is observed at frequencies greater than f_z for bands in THz. In addition, it can be observed that the levels of signal rejection and transmission for both cases of SL and CSL element to degrade at THz and IR frequencies. The surface resistance as well as dielectric losses degrade the selective transmission by means of ohmic losses as a consequence of high absorption of EM waves at THz frequencies.

Moreover, the SL FSS exhibit non-linearities in transmission phase around f_z, whereas the CSL FSS exhibit a phase shift of 2π at f_p, as shown in Figure 2.8(c). In addition, response of SL unit cell show linearity in reflection phase throughout the stopband, while CSL unit element show non-linearity in reflection phase around f_p. At IR frequencies, these nonlinearities in transmission phase tend to diminish probably due to weak transmission.

2.3.3 Effect of material properties

In Figure 2.9, the effect of dielectric properties of substrate material on propagation characteristics of both types of FSSs in different frequency domains is illustrated when the ratio $(\varepsilon_r/\varepsilon_{r0})$ is varied. Figure 2.9 also displays the ε_{r0} at their respective frequencies.

As ε_r of the substrate material increases, frequencies f_z and f_p acquire lower values. In addition, the width of stopband for SL FSS decreases marginally as $\varepsilon_r/\varepsilon_{r0}$ increases, with an exception of SL at 33 GHz, where SL exhibits an increase in widths of rejection band. The increased bandwidth at 33 GHz is a result of reduced losses of the glass substrate employed for SL FSS at 33 GHz in comparison to the RO4003 at 15 GHz and Kapton substrates at 200 GHz respectively. Furthermore, the passband width of CSL FSS decreases as $\varepsilon_r/\varepsilon_{r0}$ increases for the substrate material increases. At IR frequency range, the transmission incident EM waves through CSL FSS is restricted due to the increased dielectric and metallic losses.

Figure 2.10 illustrates the transmission response due to lossy dielectric substrate for SL and CSL at distinct frequency regions. Changes in f_z, f_p, widths of passband-stopband and levels of transmission-rejection are displayed as a function of relative to the ratio of loss tangents, i.e., $(\tan\delta)/(\tan\delta)_0$. Figure 2.10 also displays the loss tangent, $(\tan\delta)_0$ at frequencies f_p and f_z.

It appears that f_z and f_p do not change significantly as substrate losses increase.

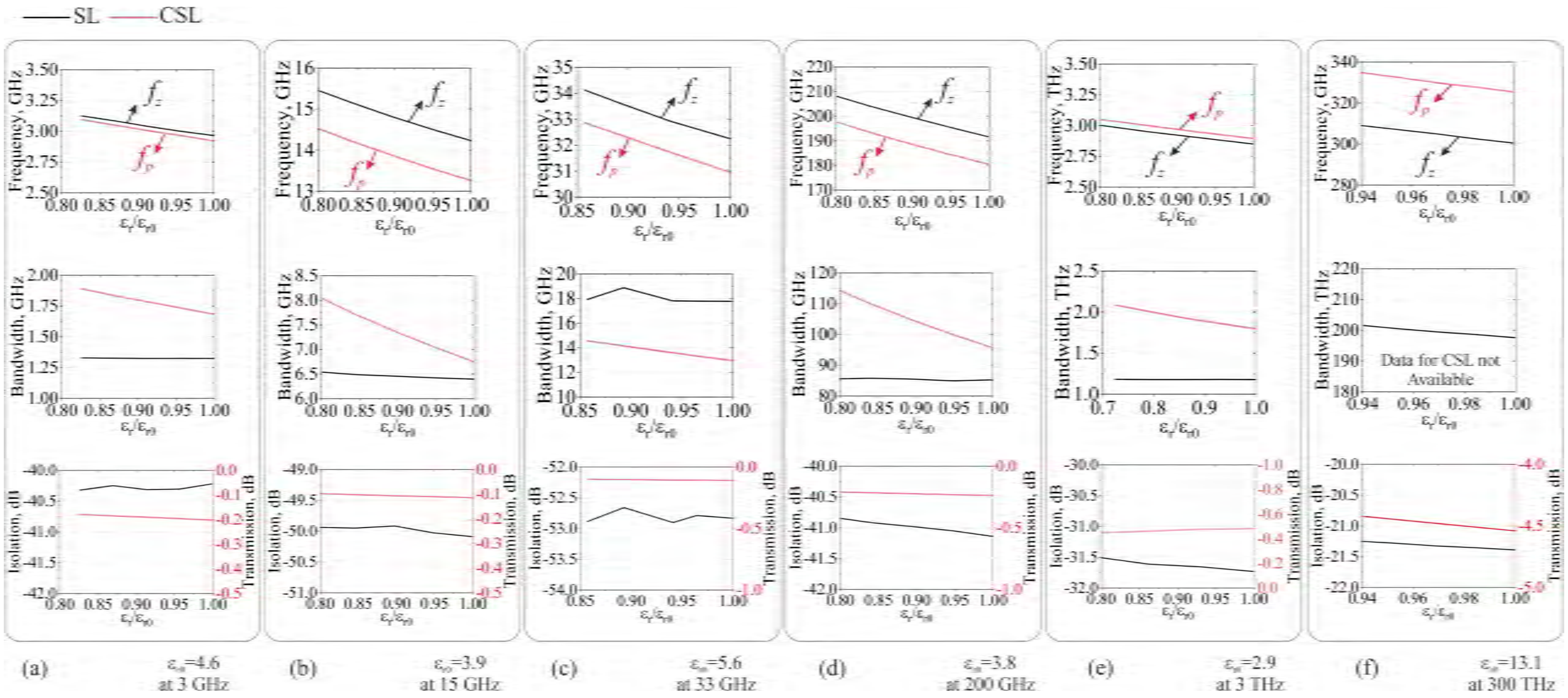

Figure 2.9: Effect of $\varepsilon_r/\varepsilon_{r0}$ on frequencies (top to bottom) for (a) S-Band, (b) Ku-Band, (c) Ka-Band, (d) G-Band, (e) THz and (f) IR (left to right)

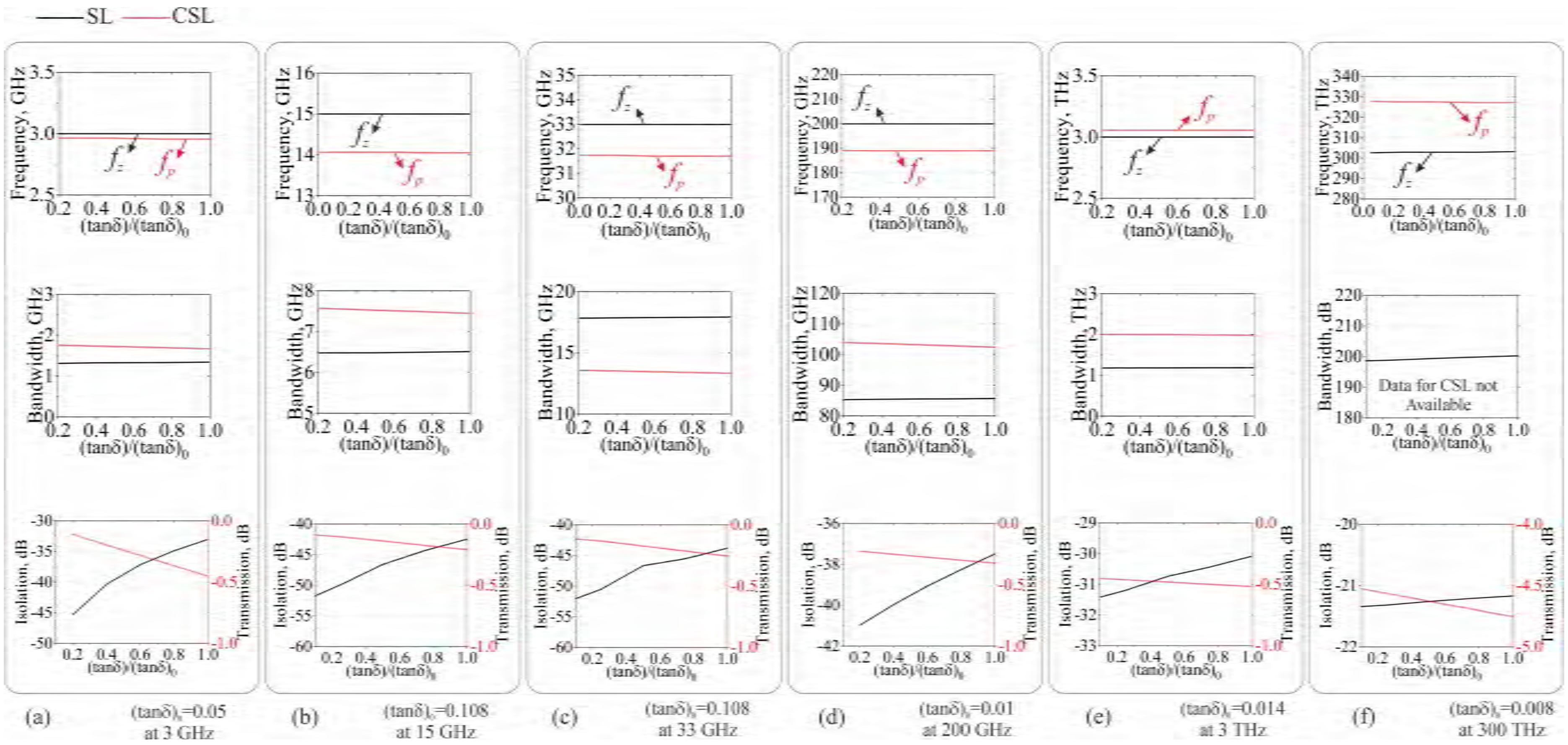

Figure 2.10: Effect of lossy dielectric substrate on frequencies, f_z and f_p); width of stop/pass band and levels of rejection/transmission (top to bottom) for (a) S-Band, (b) Ku-Band, (c) Ka-Band, (d) G-Band, (e) THz and (f) IR (left ro right)

With higher substrate losses, the width of the stopband for SL FSS decreases very marginally, whereas the width of the passband for CSL FSS expands. Figure 2.10 does not depict the bandwidth of CSL FSS, identical to Figure 2.9. The losses of the dielectric substrate have a significant impact on the transmission and isolation of signals in the mm-wave and THz bands. It has been observed that maximum of signal rejection capability of SL FSS improves as dielectric substrate losses diminish. Similarly, the maximum of signal transmission of CSL FSS degrades as dielectric material losses increase. In order to accomplish maximum signal reject or transmission through an FSS, it is necessary that FSS is developed over substrate with lower losses.

Furthermore, the metal conductivity also has significant impact on signal transmission and rejection, particularly at THz frequencies. Despite the fact that signal transmission or rejection improves when the value of conductivity increases, surface resistance leads to ohmic losses and thus, degrade signal rejection and transmission. The frequencies f_z, f_p and widths of stop as well as passband are unaffected by changes in the surface resistance and metal conductivity.

The section addressed the performance analysis of conventional SL and CSL for the microwave, mm waves to IR frequency ranges. The transmission responses of both FSSs are analysed and investigated for six distinct frequency regimes of EM spectrum. To determine the appropriate materials for substrate and metal layer to develop FSSs, the effect of ε_r, tanδ, metal conductivity and surface resistance are studied. The operating frequency, width of stopband and passband, and levels of transmission/ rejection are investigated for change in material properties of the substrate and conductivity of metallic layer employed for FSSs' development. Further,PD and PI FSSs are explored

2.4 Techniques to transform PD to PI surfaces

The inherent characteristics of FSSs to control or manipulate the incident EM waves make them useful as reflectors, EM shields for smart buildings [88], radomes [89], [90] , absorbers [91], [92], artificial magnetic conductors [93], electromagnetic band gap structures. Aside from such applications, FSSs have also been integrated with compact antennas for reduction of RCS, improvement in gain and directivity [94], [95]. The FSS structures created by unit cells with four-fold symmetry [65] have been explored to demonstrate polarization independent (PI) bandstop [66] as well as bandpass transmission responses [67]. Square loop [68], circular loop [69], [96], [71], crossed dipole [40], [72], Jerusalem cross [73], [74] type unit cells are a few of the commonly known PI FSSs. However, the FSSs tend lose their PI characteristics when unit cell structure is disrupted as observed in reference [75]. PD FSSs have also been explored to be utilized as polarization converters [76], polarization rotators [77] and PSSs [78], [79] respectively.

In this section, three distinct loop type FSSs are first designed to demonstrate PD stopband characteristics and then the orthogonal arrays these PD FSSs' layers are developed on opposite sides of the substrate to demonstrate similar transmission coefficients under orthogonally polarized EM waves incidences demonstrating non-linearity in reflection phase. Later, these of PD FSSs are fabricated on one of the sides of the substrate to get merged type FSSs. Merged type FSSs also exhibit similar transmission as well as reflection coefficients under normal incidence. The transmission responses of these FSSs are also evaluated under oblique EM wave incidences through simulations and compared.

2.4.1 PD unit cell design

Figure 2.11 displays the geometry of FSS unit cells patterned over 1.57 mm thick FR-4 substrate. Vertically oriented rectangular loop (VRECT), elliptical loop (VELIP) and rhombic loop (VRL) based unit cells are revealed in Figure 2.11 (a), (b) and (c) respectively. Rotating VRECT, VELIP and VRL unit cells by 90° in XY plane, horizontally oriented HRECT, HELIP and HRL are formed as shown in Figure 2.11 (d), (e) and (f) respectively. The unit cells are designed such that to keep substrate dimensions and their aspect ratio (A/R) of all unit cell geometries. (l_{y1}:l_{x1}) equal.

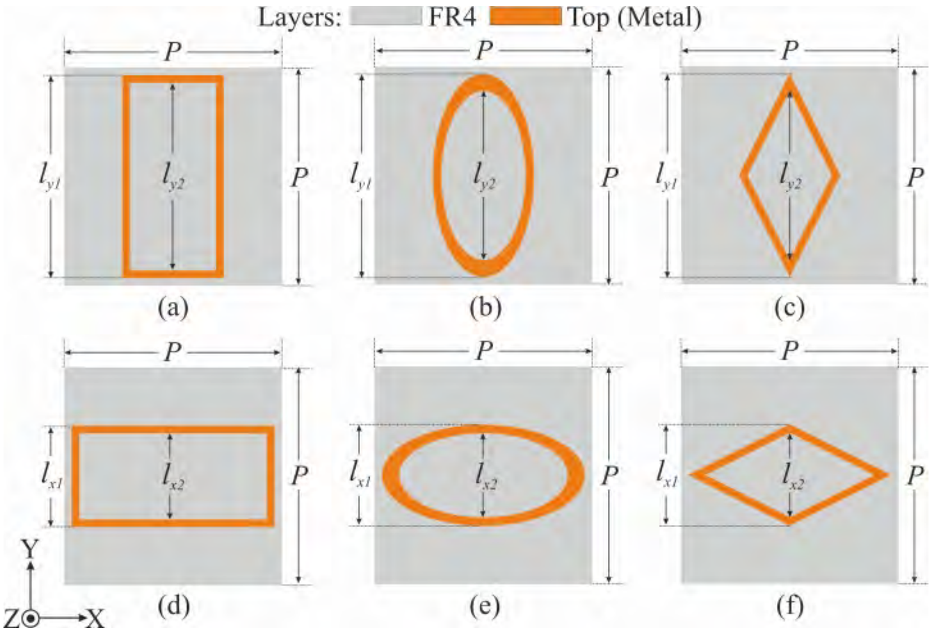

Figure 2.11: Unit Cell Geometries (a) VRECT, (b) VELIP, (c) VRL, (d) HRECT, (e) HELIP, and (f) HRL FSSs respectively

Table 2.4: Geometrical parameters of FSSs

FSS Parameters	Rectangular Loop Values (mm)	Elliptical Loop Values (mm)	Rhombic Loop Values (mm)
P	14.42	14.42	14.42
l_{x1}	6.71	6.71	6.71
l_{x2}	5.71	5.59	5.59
l_{y1}	13.42	13.42	13.42
l_{y2}	12.42	11.18	11.18

Table 2.4 summarizes the geometrical parameters of the unit cells.

All three unit cells for PD FSS are simulated using CST Microwave studio in both directions, i.e., horizontal and vertical using Floquet ports in Z-directions. The periodic boundary conditions are applied along the edges of subatrate in X- or Y-directions. The values of transmission coefficients, $|S_{21}|$ along with magnitude and phase of reflection coefficient, $|S_{11}|$ with respect to frequency (2 to 14 GHz) are displayed in Figure 2.12. The values are evaluated under normally incidentTE and TM waves.

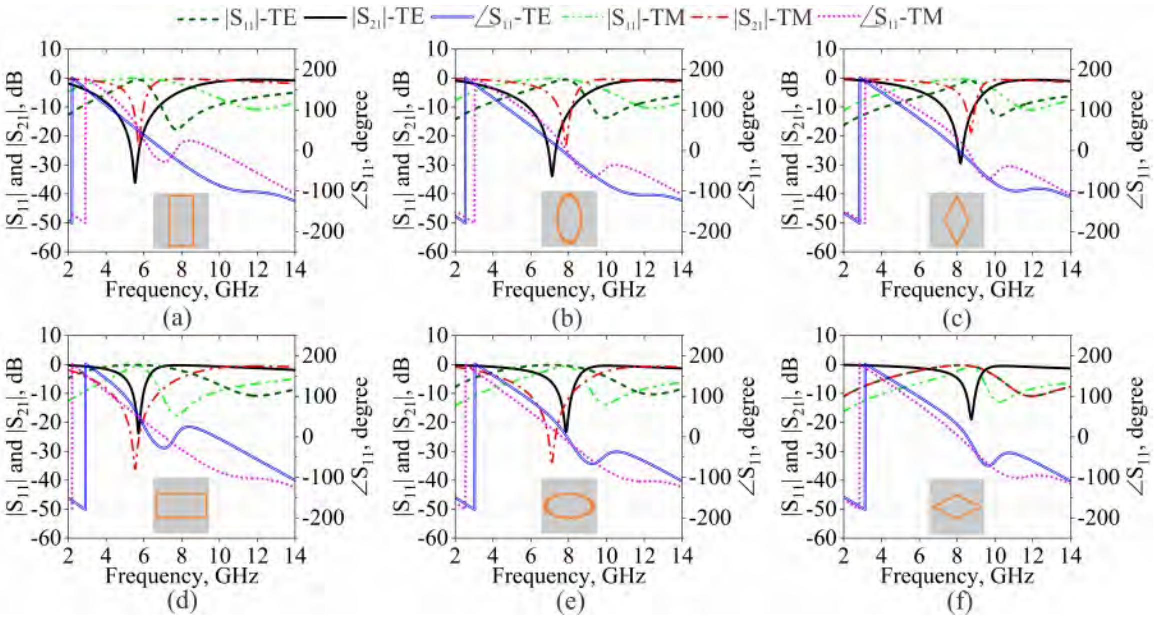

Figure 2.12: Transmission and reflection responses of (a) VRECT, (b) VELIP, (c) VRL, (d) HRECT, (e) HELIP, and (f) HRL FSSs under normal incidence

The $|S_{11}|$, $|S_{21}|$ and reflection phase of VRECT, VELIP and VRL FSSs are depicted in Figure 2.12 (a), (b) and (c) respectively while for HRECT, HELIP and HRL FSSs, these responses are shown in Figure 2.12 (d), (e) and (f) respectively.

It is observed that VRECT, VELIP and VRL FSSs demonstrate distinct trans-

Table 2.5: Transmission responses of PD FSSs

Unit Cell	TE			TM		
	f_r(GHz)	10dB Stopband (GHz)	FBW (%)	f_r(GHz)	10dB Stopband (GHz)	FBW(%)
VRECT	5.52	4.26-6.74	45.09	5.75	5.39-5.99	10.54
VELIP	7.13	5.85-8.20	34.45	7.86	7.44-8.16	9.23
VRL	8.18	7.25-8.89	20.32	8.73	8.44-8.96	5.97
HRECT	5.75	5.39-5.99	10.54	5.52	4.26-6.74	45.09
HELIP	7.86	7.44-8.16	9.23	7.13	5.85-8.20	34.45
HRL	8.73	8.44-8.96	5.97	8.18	7.25-8.89	20.32

mission responses on illumination by normally incident TE and TM waves. Also, the transmission null frequencies, 'f_r' for VRECT, VELIP and VRL FSSs appear at relatively lower values for normal TE incidences when compared with values under normally incident TM waves. Similarly, orthogonally oriented HRECT, HELIP and HRL FSSs also demonstrate distinct transmission responses under normally incident TM waves, but the transmission responses are interchanged for TE and TM incidences. Since, the electrical length of elliptical loop is apparently more than that of rhombic loop array and smaller than that of rectangular loop array. Thus, rectangular loop based FSSs exhibit f_r relatively at a lower frequency range when compared to elliptical loop based FSSs while rhombic loop based FSSs exhibit stopband frequencies relatively at a higher band than observed for elliptical loop based FSSs.

Moreover, VRECT, VELIP and VRL FSSs demonstrate linear reflection phase for TE waves over their respective stopbands while HRECT, HELIP and HRL FSSs exhibit linear phase in reflection response under normal TM incidences. Also, VRECT, VELIP and VRL FSSs exhibit non-linearity in reflection phase with TM incidences while HRECT, HELIP and HRL FSS illustrate non-linearities in reflection phase under TE incidence. Table 2.5 displays summary of the transmission responses of PD FSSs including based on the frequencies, f_r, widths of 10 dB stopbands, and the fractional bandwidths (FBW).

From comparison it is found that rectangular loop based FSSs exhibit wider stopband when compared with elliptical and rhombic loop-based PD FSSs. Moreover, rectangular loop based FSS operates at lower frequency range in C-band while elliptical loop based FSS operates at higher frequencies in C-band and rhombic loop based FSS operates almost in X-band.

Another configuration of closely rhombic loop-based PD FSS is explored here, i.e., the tessellated rhombic loop (TRL) FSS. The structural features are displayed along the geometry in Figure 2.13. Figure 2.13 (a) illustrate the structure of large array of TRL FSS while the top and side views of corresponding unit structure is depicted

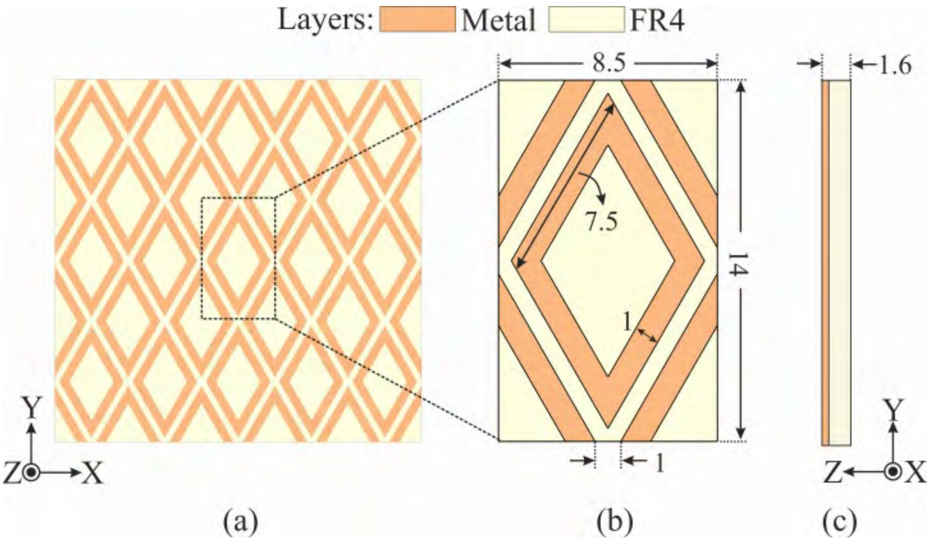

Figure 2.13: Geometry of (a) TRL FSS and its unit cell structure (all dimensions are in 'mm') (b) Top view, (c) side view

in Figure 2.13 (b) and (c) respectively. Similar to PD arrays, the TRL based FSS is also patterned over FR-4 substrate. Simulations are performed by employing similar boundary conditions and excitation as described earlier, the propagation characteristics of TRL based FSS are obtained under normal incidences. The $|S_{21}|$ dB, $|S_{11}|$ dB and $\angle S_{11}$ under normal TE and TM incidences are depicted in Figure 2.14.

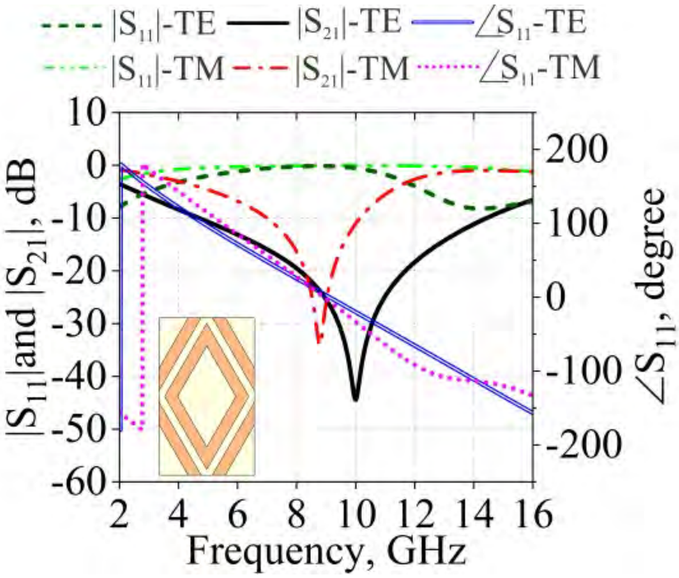

Figure 2.14: Transmission and reflection responses of TRL FSS under normal incidence

Interestingly, TRL based FSS also behave distinctly when exposed to normally impinging TE and TM waves thereby demonstrating dissimilar responses of $|S_{21}|$ dB, $|S_{11}|$ dB and $\angle S_{11}$ degree. Moreover, the densely packed arrangement of rhombic loops in TRL FSS offers wider bandstop (103% under TE mode and 37 % under TM mode) featues when compared to rhombic loop based FSS. The detailed assessment of TRL FSS with its efficacy for compact antenna applications are further explored and discussed in chapter 4 and 5 respectively.

2.4.2 PI unit cell design

Later, both orthogonally oriented unit cell structures of RECT, ELIP and RL FSSs are transformed to single unit cell of BTB arrangement, i.e., BTB RECT, BTB ELIP and BTB RL FSSs where orthogonal layers are etched on both sides of FR-4 dielectric as revealed in Figure 2.15 (a), (b) and (c) respectively.

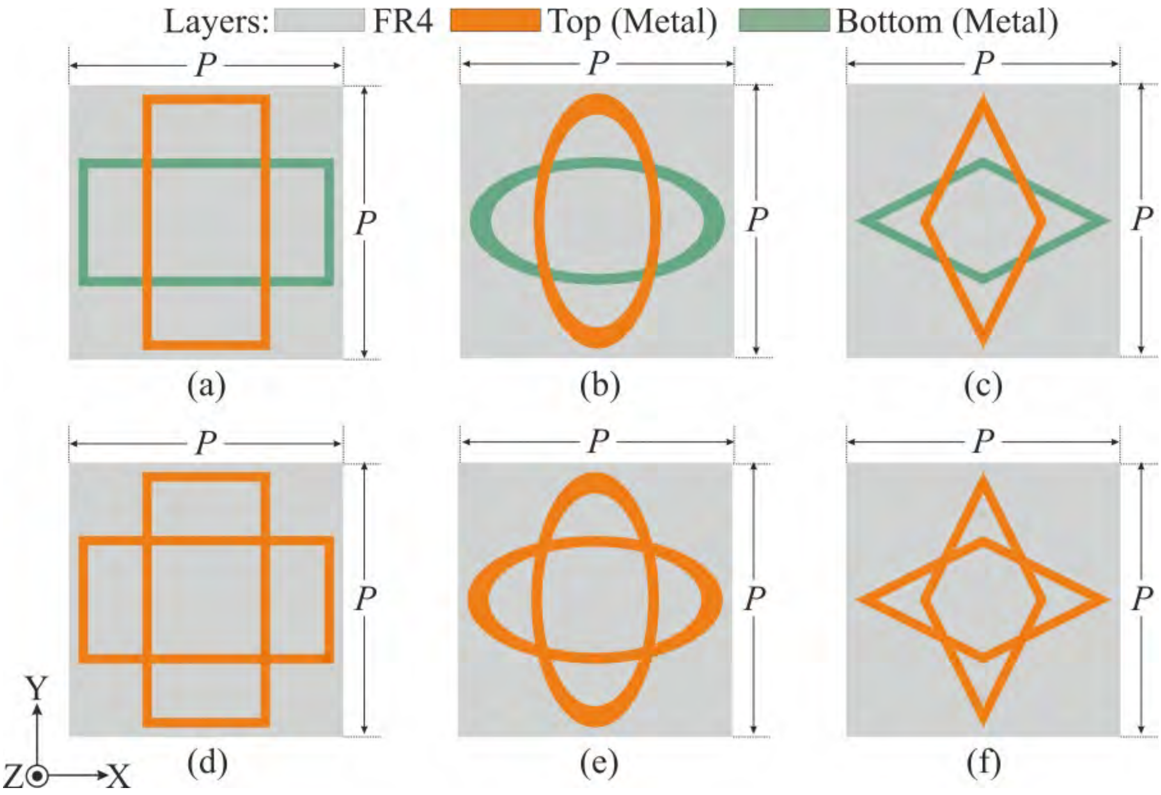

Figure 2.15: Unit Cell Geometries (a) BTB RECT, (b) BTB ELIP, (c) BTB RL, (d) MRECT, (e) MELIP, and (f) MRL FSSs respectively

The $|S_{21}|$, $|S_{11}|$ and reflection phase plots of these FSS unit cells under normal incidence are displayed in Figure 2.16 (a), (b) and (c) respectively. It is observed that BTB RECT, BTB ELIP and BTB RL FSSs demonstrate one narrow stopband with weak signal rejection and one wide stopband with prominent signal rejection capability owing to two orthogonal layers of BTB type configuration.

It is interesting to note that BTB type FSSs demonstrate similar $|S_{21}|$ response for normal TE and TM incidences. However, the $|S_{11}|$ responses remain distinct under TE and TM modes respectively.

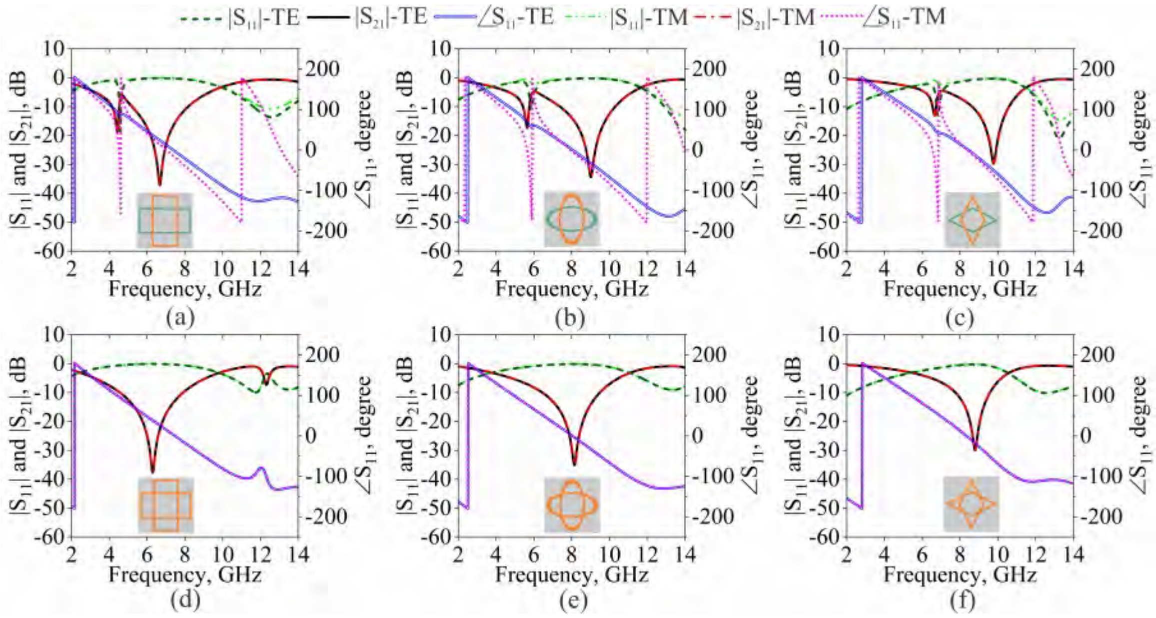

Figure 2.16: Transmission and reflection responses of (a) BTB RECT, (b) BTB ELIP, (c) BTB RL, (d) MRECT, (e) MELIP, and (f) MRL FSSs under normal incidence

Later, both orthogonal unit cell patterns are developed on one of the sides of substrate to obtain a merged rectangular loop (MRECT), merged elliptical loop (MELIP) and merged rhombic loop (MRL) FSSs as shown in Figure 2.15 (e), (f) and (g) respectively. The transmission responses $|S_{21}|$ and $|S_{11}|$ and reflection phase for MRECT, MELIP and MRL FSSs under normally incident TE and TM waves are shown in Figure 2.16(d), (e) and (f) respectively.

It is evident that MRECT, MELIP and MRL FSSs demonstrate similar transmission as well as reflection characteristics under TE and TM incidences. Table 2.6 summarizes the transmission characteristics of all BTB type and merged type FSSs.

It is evident that merged type FSSs offer wider stopbands when compared to BTB type FSSs. Moreover, similar to PD FSSs, BTB RECT demonstrates wider stopband when compared to BTB ELIP and BTB RL FSSs while MRECT FSSs provide the widest stopband (53.85%) among all the BTB and merged type FSSs.

The propagation characteristics of BTB and merged type FSSs under oblique incidences are evaluated where the incidence angle 'θ' has a value between 0° to 45° in step of of 5° using CST MWS. However, the responses of FSSs under oblique incidences are illustrated in steps of of 15° to ensure the clarity within the figures.

Table 2.6: Rejection frequency and span of BTB and Merged Type FSSs

Unit Cell	TE			TM		
	f_r(GHz)	10dB Stopband (GHz)	FBW (%)	f_r(GHz)	10dB Stopband (GHz)	FBW(%)
BTB RECT	4.42 & 6.66	(4.12-4.51) & (5.19-8.15)	9.03, 44.38	4.42 & 6.66	(4.12-4.51) & (5.19-8.15)	9.03, 44.38
BTB ELIP	5.63 & 9.04	(5.04-5.77) & (7.37-10.29)	13.50, 33.06	5.63 & 9.04	(5.04-5.77) & (7.37-10.29)	13.50, 33.06
BTB RL	6.64 & 9.79	(6.53-6.72) & (8.65-10.60)	2.86, 20.26	6.64 & 9.79	(6.53-6.72) & (8.65-10.60)	2.86, 20.26
MRECT	6.29	4.56-7.92	53.85	6.29	4.56-7.92	53.85
MELIP	8.15	6.43-9.47	38.24	8.15	6.43-9.47	38.24
MRL	8.80	7.75-9.59	21.22	8.80	7.75-9.59	21.22

2.4.3 Oblique incidence response of PD FSSs

The scattering parameters $|S_{21}|$ and $|S_{21}|$ responses of VRECT FSS under oblique incident TM and TE waves are shown in Figure 2.17 (a) and (c) respectively while Figure 2.17 (b) and (d) demonstrate $|S_{21}|$ and $|S_{11}|$ when HRECT FSS is illuminated

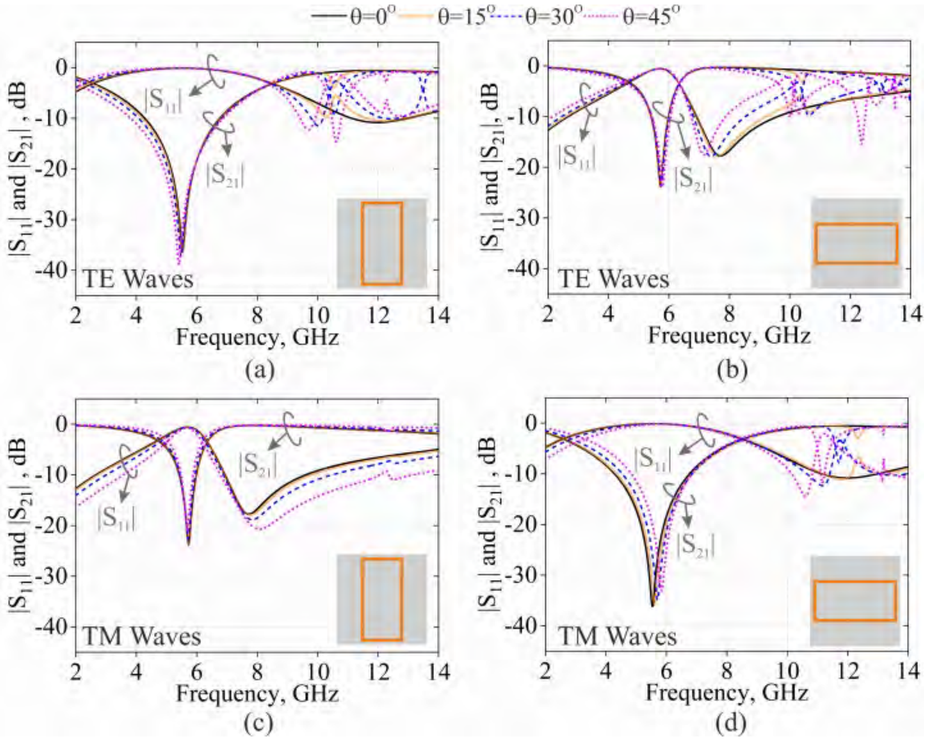

Figure 2.17: Transmission and reflection responses of (a) VRECT, (b) HRECT FSSs under oblique TE wave incidences; (c) VRECT and (d) HRECT under oblique TM wave incidences respectively

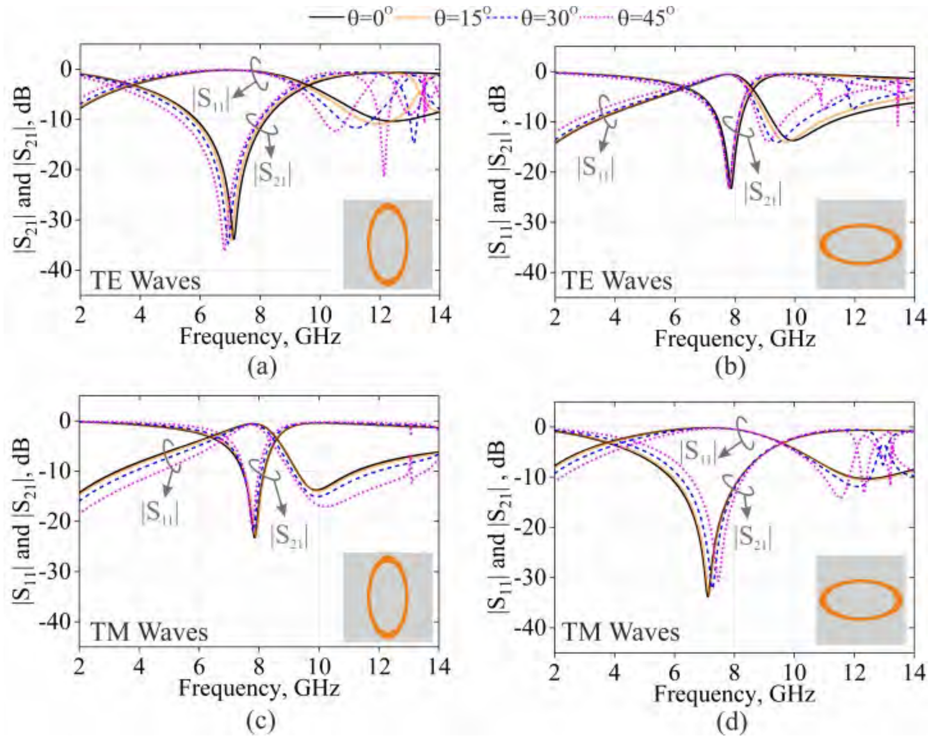

Figure 2.18: Transmission and reflection responses of (a) VELIP, (b) HELIP FSSs under oblique TE wave incidences; (c) VELIP and (d) HELIP under oblique TM wave incidences respectively

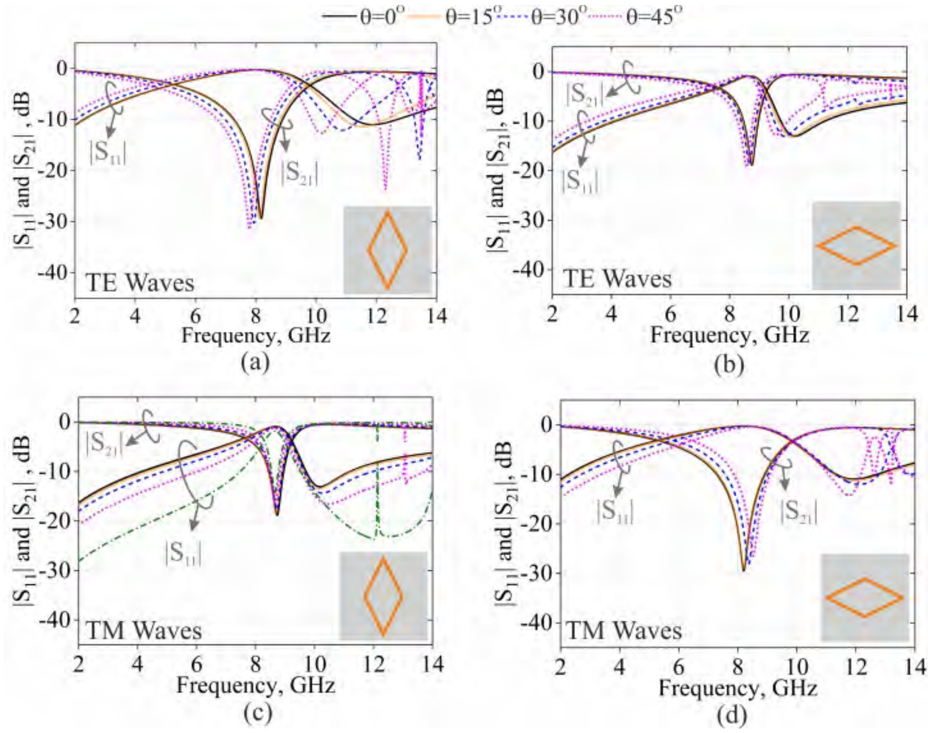

Figure 2.19: Transmission and reflection responses of (a) VRL, (b) HRL FSSs under oblique TE wave incidences; (c) VRL and (d) HRL under oblique TM wave incidences respectively

by obliquely incident TM and TE waves respectively. Both VRECT and HRECT FSSs maintain their characteristics under oblique incidence. Figure 2.18 (a) and (c) depict $|S_{21}|$ and $|S_{11}|$ responses of VELIP FSS when illuminated by obliquely incident TE and TM waves, whereas Figure 2.18 (b) and (d) depict $|S_{21}|$ and $|S_{11}|$ responses of HELIP FSS when oblique TM and TE incidences are used for illumination, respectively. Similar to VRECT and HRECT FSSs, both VELIP and HELIP FSSs also demonstrate stable transmission response under oblique TE and TM incidences.

Similarly, Figure 2.19 (a) and (c) show VRL FSS's variations of $|S_{21}|$ and $|S_{11}|$ with frequencies under obliquely incident TE and TM waves while Figure 2.19 (b) and (d) show HRL FSS's responses.

It is found that all PD FSSs exhibit stable transmission characteristics when angle of incidence of impinging EM waves increases. However, from close observation, it is found that rectangular loop based FSS offer excellent AS response when compared to elliptical and rhombic loop-based PD FSSs owing to their relatively more edge to edge coupling between adjacent unit cells.

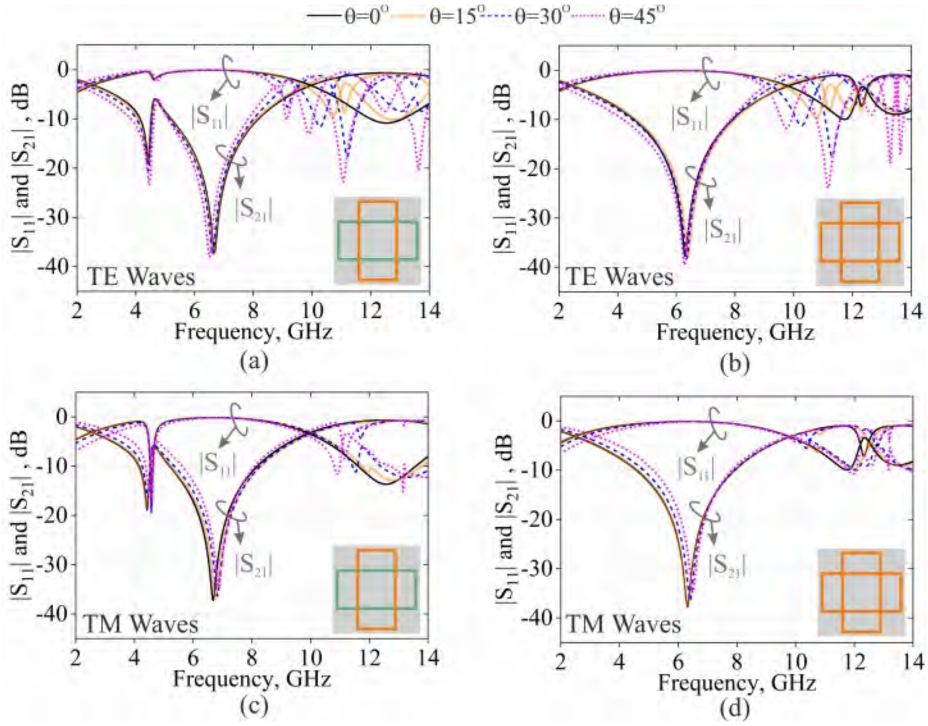

Figure 2.20: Transmission and reflection responses of (a) BTB RECT, (b) MRECT FSSs under oblique TE wave incidences; (c) BTB RECT and (d) MRECT under oblique TM wave incidences respectively

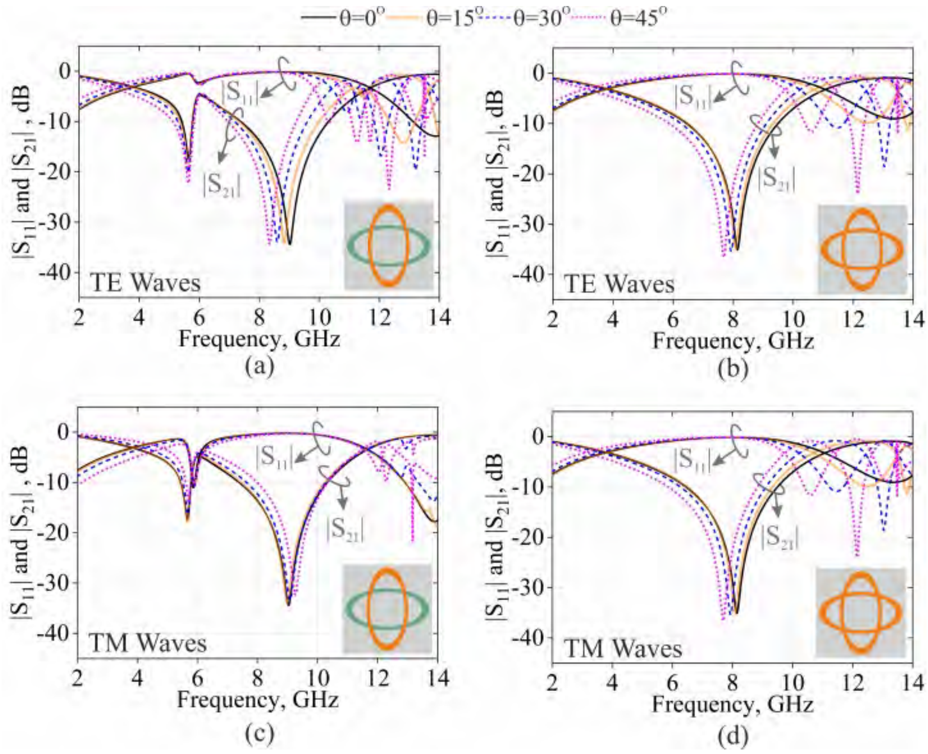

Figure 2.21: Transmission and reflection responses of (a) BTB ELIP, (b) MELIP FSSs under oblique TE wave incidences; (c) BTB ELIP and (d) MELIP under oblique TM wave incidences respectively

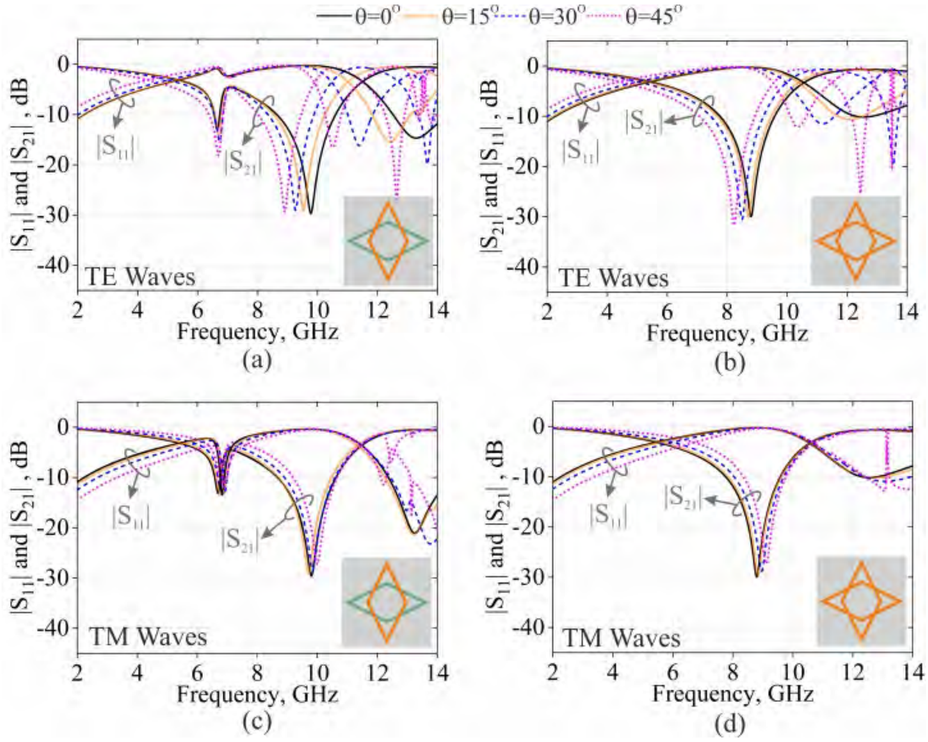

Figure 2.22: Transmission and reflection responses of (a) BTB RL, (b) MRL FSSs under oblique TE wave incidences; (c) BTB RL and (d) MRL under oblique TM wave incidences respectively

2.4.4 Oblique incidence response of PI FSSs

The transmission responses of BTB RECT FSSs under TE and TM oblique incidences are shown in Figure 2.20 (a) and (c) whereas the transmission responses of MRECT FSS under similar conditions are displayed in Figure 2.20 (b) and (d) respectively. Similarly, Figure 2.21 (a) and (c) show the transmission responses of BTB ELIP FSSs under TE and TM oblique incidences, while Figure 2.21 (b) and (d) depict the transmission responses of MELIP FSS. Further, Figure 2.22 (a) and (c) exhibit BTB RL FSS transmission responses under TE and TM oblique incidences, whereas Figure 2.22 (b) and (d) show responses for MRL FSS.

BTB RECT FSSs demonstrate stable transmission response under oblique incidence over its stopband. However, at higher frequencies beyond 8 GHz, under TE incidence, the stability in $|S_{21}|$ and $|S_{11}|$ tend to degrade as angle of incidence 'θ' increases. MRECT FSS, also provides excellent AS transmission response when illuminated by obliquely incident both TE and TM waves.

From Figure 2.21 (a) it is observed that BTB ELIP FSSs shows slight deviation in stopband frequency or angle of incidence of TE waves increases while it maintains its transmission response under oblique TM incidence as observed from Figure 2.21 (c). Similarly, it is evident from Fig 2.22 (a) that stability in transmission response of BTB RL FSS is slightly inferior to BTB ELIP and BTB RECT FSSs respectively. However, it also shows stable transmission response under oblique TM incidences.

Despite the fact that MRECT FSS provides more stable transmission responses

Table 2.7: Comparison of AS/PI bandwidths of FSSs (in GHz)

Unit cell configuration/ Loop Shape	Incidence angle, θ°	Vertical	Horizontal	BTB	Merged
Rectangular	0	0.6	0.6	2.96	3.36
	15	0.57	0.57	2.91	3.29
	30	0.52	0.6	2.68	3.1
	45	0.42	0.61	2.22	2.67
Elliptical	0	0.72	0.72	2.92	3.04
	15	0.61	0.7	2.56	2.7
	30	0.56	0.69	2.01	2.27
	45	0.46	0.73	1.26	1.65
Rhombic	0	0.45	0.45	1.95	1.84
	15	0.4	0.49	1.57	1.69
	30	0.16	0.5	0.98	1.18
	45	0.01	0.51	0.26	0.57

under obliquely incident TE and TM waves than MELIP and MRL FSS, all the three types of merged FSS possess the ability to maintain their transmission responses reasonably under oblique incidences.

Table 2.7 summarizes the effective BWs of PD (Vertical and Horizontal-type) FSSs and PI (BTB and Merged type) FSS over which PD FSSs preserve AS and PI FSSs preserve their AS/PI responses respectively. The effective BW is the width of stopband These BWs for FSSs for all PD type of configurations are calculated as difference between maximum of lower corner edge frequency and minimum of upper corner edge frequency of transmission coefficients $|S_{21}| \leq$-10dB for distinct θ between 0° to 45°. Similarly, the BWs of AS/PI responses for PI FSSs are obtained for their respective wider stopbands. Thus, the overall stopbands provided by PD and PI FSSs are regarded as the minimum frequency band from all transmission responses at normal and oblique incidences where $|S_{21}| \leq$-10dB.

2.4.5 Conclusion

This chapter starts with comparison of the performance of SL and CD FSS unit cells by evaluating the impact of translated FSS unit cells and a lossy dielectric substrate on their transmission and reflection properties. Additionally, SL and CSL based FSS structures are designed to demonstrate bandstop and bandpass responses for distinct frequency regions. The characteristics of their transmission and reflection are then compared. Using CST MWS EM simulations, the significance of dielectric constant of substrate, dielectric and ohmic losses is explored. Later, the performance analysis of PD FSS unit cells based on rectangular loop, elliptical loop and rhombic loops under normal and oblique incidence is presented. Their transmission characteristics under TE and TM incidences are compared. The technique for transforming a PD FSS into a PI FSS is also described.

The preliminary analysis of conventional loops suggests that translation in unit cell geometry by half of periodicity along vertical and horizontal directions for infinitely large FSS arrays do not bring major change in transmission response. In addition, FSS transmission response deteriorate at higher frequency range around THz and IR and low-loss materials are required to avoid the degradation of signal levels at THz and IR. It is also evident that PD FSSs in horizontal configurations demonstrate wider BW with AS response when compared to FSSs in vertical configurations. Similarly, PI FSSs in merged configurations provide wider stopbands when compared with BTB type FSSs.

Chapter 3

Dual-rhombic loop based X-band reflectors

Techniques explored in chapter 2 are being confined here through dual rhombic loop (DRL) based FSSs. DRL based unit elements, have been designed and developed to offer wide stopband for X-band frequencies. DRL based two orhogonally oriented PD FSSs are designed to provide propagation characteristics under TE and TM polarized incidences respectively. Both vertically, and horizontally oriented FSSs are first developed BTB on opposite sides of substrate and then later, in other cases printed on one of the sides of substrate to explore PI behaviour. DRL based FSSs are then integrated with a triangular slot antenna to investigate the effect of FSSs reflectors towards antenna gain enhancement in boresight direction.

In this chapter, a directional X-band triangular slot antenna is developed and a technique to enhance boresight gain using FSR is proposed. The effect of reflection phase of RLs based bandstop FSSs on boresight gain and operating band of slot antenna is studied through simulations. The antenna is backed by three FSSs separately to study their effect on triangular slot antenna. FSSs with non-linear reflection phase exhibit lower average antenna gain when compared with reflectors having linear reflection phase.

3.1 Introduction

Bandwidth and the capability of FSS to reject incident EM waves are two critical performance factors for a stopband FSS or surface based stopband filters. According to [9], FSSs those are square or circular loops are the most prevalent for larger bandwidths. The bandstop capability of FSS is directly proportional to the array's loss factor, which need to be kept to a minimum. In order to gain a rapid understanding, square loop FSSs have been analysed by employing straightforward circuit modelling, which was restricted to just considering EM waves with normal incidence [97].According to Parker1981's [69] research, circular loop based FSSs analyzed earlier, exhibited wide stopband properties. Later on, an updated circuit model for FSSs was provided that additionally accounted for oblique incidences reference [98], [38]. According to reference [99], FSS based on SL have been extensively incorporated with tiny antennas both as superstrates and as reflectors in order to accomplish better levels of antenna band width and directivity. In addition, multifunctional FSS that incorporate active components on square loop or ring unit cells have been described for the purpose of altering the properties of the FSS from transmission to reflection [22]. This allows the FSS to be switchable. These FSSs are not sensitive to the polarisation of the EM waves that are incident on them, and their transmission response is the same regardless of the polarisation state of the EM waves that are incident on them. The FSSs comprised of unit cells with asymmetric aspect ratio compared to arriving EM waves. These FSSs show PD behaviour when subjected to EM incidences with different polarisation states [35]. Several additional aspects of the FSS have been investigated, one of which is the use of unit cell's asymmetric structure. A select handful of these include polarisation conversion [100], polarisation rotation [101], and FSS as a polarisation selective surface [35]. Separate stopbands are seen for TE and TM polarized incidences in a square loop FSS that was composed of gratings that were horizontal and vertical and differed in breadth from one another. The AMC, which was made up of these unit cells, was incorporated with a prop feed hexagonal ultra-wideband antenna in order to improve its gain [46]. In this chapter, two orthogonally orinented PD FSSs based on rhombic loops are developed using simulations and EM modelling, following which, the results of those designs are analysed.

3.2 Dual-rhombic loop (DRL) FSS

Figure 3.1 illustrates the design flow of the unit cell structures. The unit structure involves two rhombic loops, kept adjacent to each other, once to make vertical double rhombic loop (VDRL) and then as horizontal double rhombic loop (HDRL) as displayed in the Figure 3.1. The VDRL are oriented in such a way to keep the periodicity ratio in, Y-direction and X-direction, equal to 1:2. The rotation of VDRL by 90° yields HDRL FSS. Both the horizontal and vertical unit elements based on rhombic loops are developed on the affordable a FR-4 laminate and arrayed in a grid of square grid. As shown in Figure 3.1, in one case, VDRL and HDRL unit cells are developed over on opposite surfaces of the substrate to obtain BTB DRL while in another case, they are subsequently merged on the one of the sides of FR-4 laminate to get MDRL.

The full wave simulations are performed as per the frequency domain solver that is included with CST MWS. These simulations are carried out by applying boundary conditions along the X- and Y-axes, respectively, and activating them. Figures 3.2 (a) and (b) show, as expected from a PD FSS response of wave propagation through

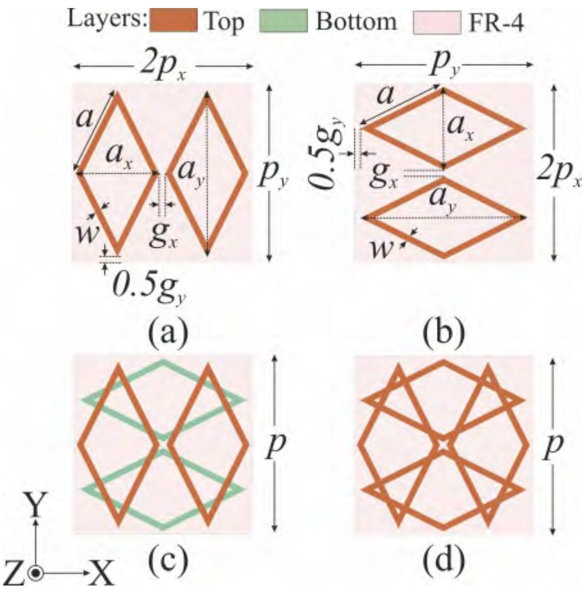

Figure 3.1: (a) VDRL, (b) HDRL, (c) BTB DRL, (d) MDRL unit cells (a=7.5, P=14.42, P_x =7.21, P_y=14.42, w=0.5, a_x=6.71, a_y=13.42, g_x=0.5, g_y=0.25, All values are in mm)

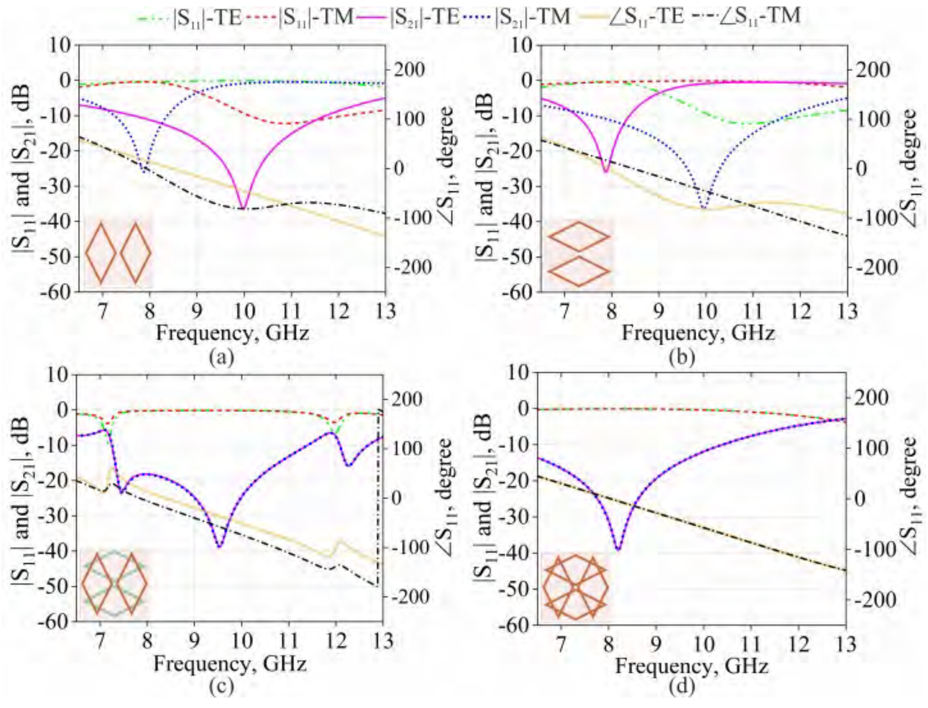

Figure 3.2: EM simulation responses of DRL unit cells (a) Vertical, (b) Horizontal, (c) BTB, and (d) Merged respectively

VDRL and HDRL unit cells after simulations respectively. VDRL FSS provides distinct responses for TM and TE incidences. For the VDRL, the null frequencies differ from TM and TE incidences due to difference in lengths of both the diagonals of rhombus. Linear reflection phase is observed in TE polarized incident waves while non-linearity in reflection phase is seen in TM polarization. TM response to VDRL

Table 3.1: Transmission responses of DRL FSSs

Unit Cell	TE				TM			
	f_r(GHz)	f_l (GHz)	f_h (GHz)	BW (GHz)	f_r (GHz)	f_l (GHz)	f_h (GHz)	BW (GHz)
VDRL	9.96	7.61	11.72	4.11	7.89	7.24	8.37	1.13
HDRL	7.89	7.24	8.37	1.13	9.96	7.61	11.72	4.11
BTB-DRL	7.46 & 9.52	7.25	11.4	4.15	7.46 & 9.52	7.25	11.4	4.15
MDRL	8.20	5.6	10.4	4.8	8.20	5.6	10.4	4.8

covers the whole X-band but TE do not. For HDRL, responses of VDRL get swapped and responses to TE incidence cover the whole X-band.

Applying techniques introduced in chapter 2, both the VDRL and HDRL are printed in BTB configuration utilizing opposite surfaces of FR-4 laminate. Figure 3.2 (c) shows that both-sides-printed FSS, i.e., BTB DRL demonstrates slight non-linearity in reflection phase inspite of exhibiting X-band rejection with PI to normally incident EM waves. As displayed in Figure 3.2 (c), the reflections are degraded or the return loss from the surface is lowered if there is any non-linearity lying inside the reflection band. Bringing the VDRL and HDRL together on any one side of the dielectric laminate results in the MDRL FSS, as shown in Figure 3.1, which minimizes phase non-linearities in the reflection observed with BTB DRL. Moreover, MDRL is an AMC as it demonstrates in-phase reflection at 8 GHz. Table 3.1 summarizes the results of the transmission characteristics of VDRL, HDRL, BTB DRL, and MDRL FSSs for comparison.

In Table 3.1, 'f_r' is the band reject frequency and BW is the difference of higher corner frequency, 'f_h' and lower corner frequency, 'f_l' where the transmission loss is more than 10 dB. Also, BTBDRL unit cell shows similar wider stopband features with 44.50% fractional BW for both TE and TM incidences while MDRL FSS exhibits a wider stopband around 8.20 GHz.

3.2.1 Parametric analysis of DRL FSSs

To gain additional insight into how loop line width (w), periodicity (p), and unit cell aspect ratio (A/R) of rhombic loop unit cell influence the transmission response of X-band FSSs, a parametric analysis of the BTB DRL and MDRL FSS is carried out.

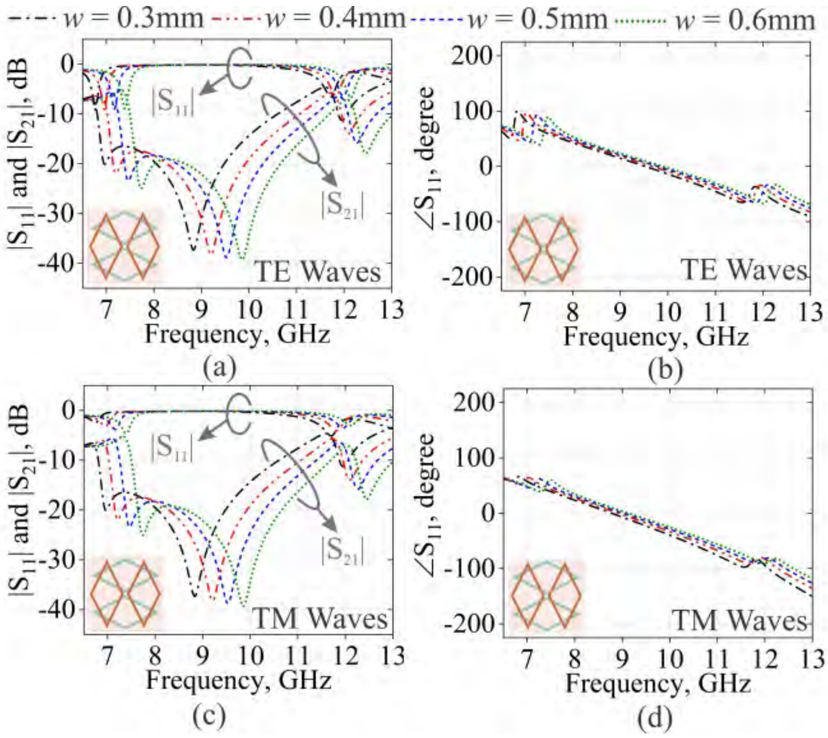

Figure 3.3: Loop line width variation on BTB DRL FSS (a) $|S_{21}|$ and $|S_{11}|$ (b) Reflection phase (TE), (c) $|S_{21}|$ and $|S_{11}|$ (d) Reflection phase (TM)

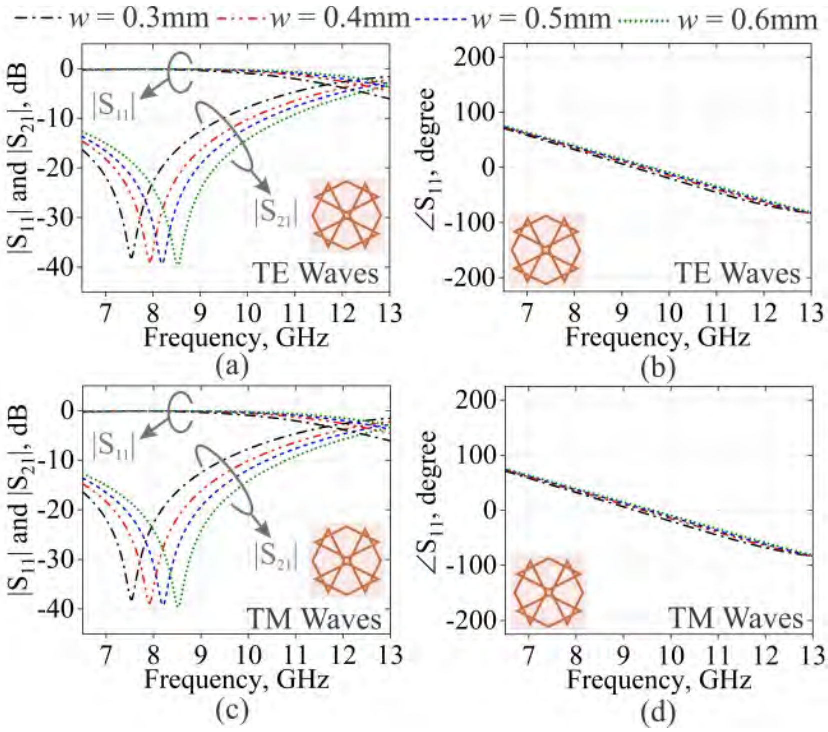

Figure 3.4: Loop line width variations on MDRL FSS: (a) $|S_{21}|$ and $|S_{11}|$ (b) Reflection phase (TE), (c) $|S_{21}|$ and $|S_{11}|$ (d) Reflection phase(TM)

3.2.1.1 Effect of loop width

To understand the influence of loop line width of DRL, the line width is changed from 0.3 mm to 0.6 mm in steps of 0.1 mm. Figure 3.3 demonstrates the simulated response of BTB DRL for loop width variation. As the width increases, the simulations indicate that f_r move to higher values. In addition, the 10 dB bandwidth of stopband increases marginally with change in loop line width. With increasing loop line width, the non-linearity of the reflection phase shifts marginally towards higher frequencies. Figure 3.4 demonstrates transmission response of MDRL FSS. Due to the the effect of loop line width variations. Simulations show that as loop line width broadens, f_r move to higher values again similar to case of BTB DRL. Although the reflection phase for MDRL remains linear regardless of loop line width expansion.

3.2.1.2 Effect of unit cell periodicity

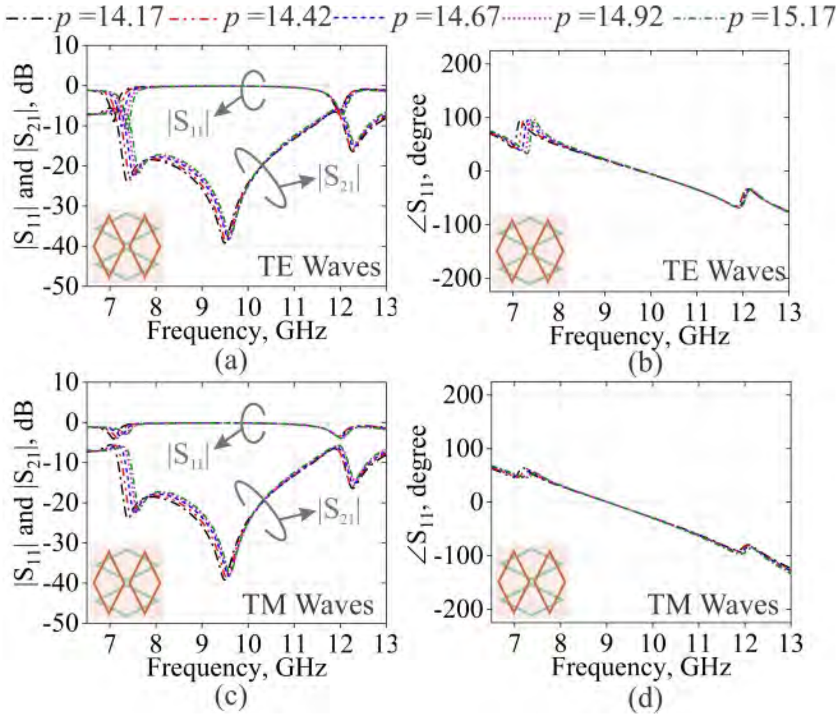

Figure 3.5: Periodicity variations on BTB DRL FSS: (a) $|S_{21}|$ and $|S_{11}|$ (b) Reflection phase (TE), (c) $|S_{21}|$ and $|S_{11}|$ (d) Reflection phase (TM)

Figures 3.5 and 3.6 demonstrate, the impact of periodicity on the transmission properties of BTB DRL and MDRL FSSs respectively. The periodicity varies between 14.17 and 15.17 mm at intervals of 0.25 mm, moving from 14.17 to 15.17 mm. When the periodicity of the BTB DRL FSS grows, illustrated in Figure 3.5, there is a little drift towards higher frequencies in the stopband frequencies. The non-linearities seen in reflection phase move slightly to higher values with increase in BTB DRL FSS periodicity. The stopband frequency of the MDRL FSS is not susceptible to periodicity as the BTB DRL FSS is, and it tend to move a little to lower frequency as the periodicity of unit elements increases. As can be seen in Figure 3.6, the linearity is preserved in the MDRL reflection phase when periodicity of unit structures increases.

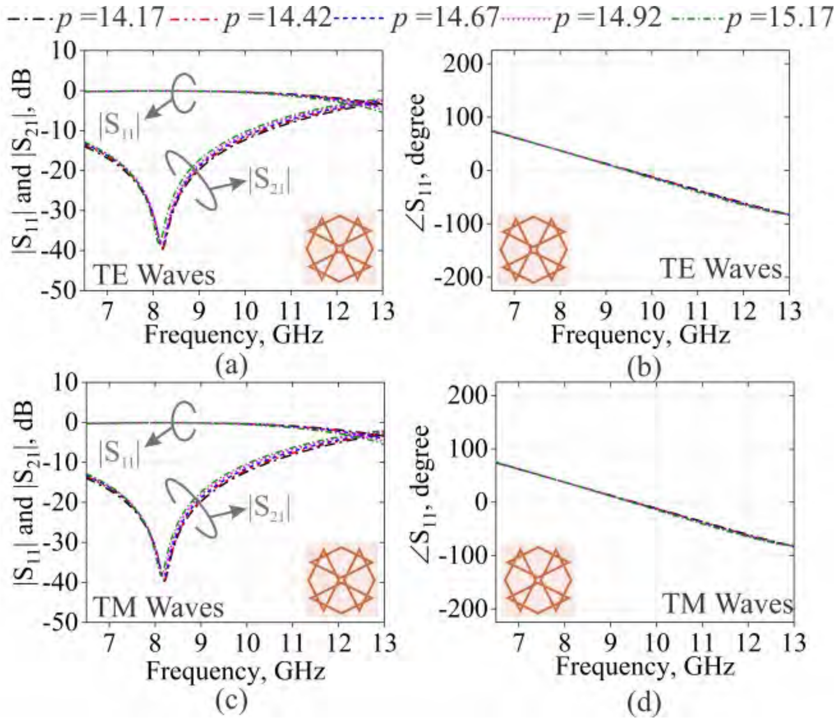

Figure 3.6: Periodicity variation on MDRL FSS: (a) $|S_{21}|$ and $|S_{11}|$ (b) Reflection phase (TE), (c) $|S_{21}|$ and $|S_{11}|$ (d) Reflection phase (TM)

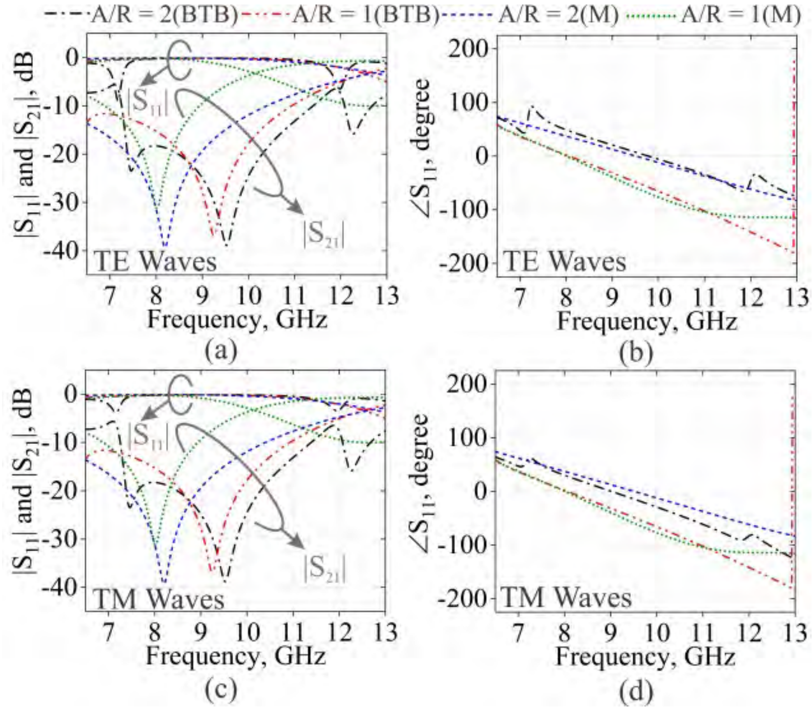

Figure 3.7: Aspect Ratio (A/R) variation on BTB DRL and MDRL unit cells: (a) $|S_{21}|$ and $|S_{11}|$ (b) Reflection phase (TE), (c) $|S_{21}|$ and $|S_{11}|$ (d) Reflection phase (TM)

3.2.1.3 Effect of periodicity aspect ratio (A/R)

Magnitude of $|S_{21}|$ and $|S_{11}|$ with phase of $\angle S_{11}$ of FSS based on PI (BTB DRL and MDRL) unit structures are shown together in Figure 3.7 to understand the impact of aspect ratio (A/R) of unit cells. Here, A/R eventually represents the ratio of periodicity decided in the vertical (Y) and horizontal (X) directions. When value A/R is reduced from 2 to 1, the unit structure changes its shape to tilted square loop (TSL). Consequently, the BTB DRL unit cell gets transformed to BTB TSL unit cell, and the MDRL unit cell appears to become a MTSL unit cell.

The simulations suggest that BTB TSL FSS, has a broader stopband when A/R=1 than A/R=2. But BTB DRL FSS provide better signal rejection compared to BTB TSL. In addition, both FSSs irrespective of their A/R values, exhibit nonlinear phase reflection properties. In contrast, MDRL with A/R=2, exhibits stopband and reflection phase linearity across the entire X-band as well as a superior rejection magnitude than MDRL with A/R=1.

3.2.1.4 DRL FSSs under oblique incidences

Both FSSs, i.e., BTB DRL and MDRL are explored further under inclined TM and TE incidences at incident angles, varying in range of $0° \leq \theta \leq 45°$. Figure 3.8 and Figure 3.9 each illustrate the magnitudes of $|S_{21}|$, $|S_{11}|$, and the reflection phase diagrams for an increment of 15° in ‘θ’ to ensure clarity in response chart for the both types of FSSs.

With increase in θ, the signal blocking efficacy of BTB DRL begins to deteriorate

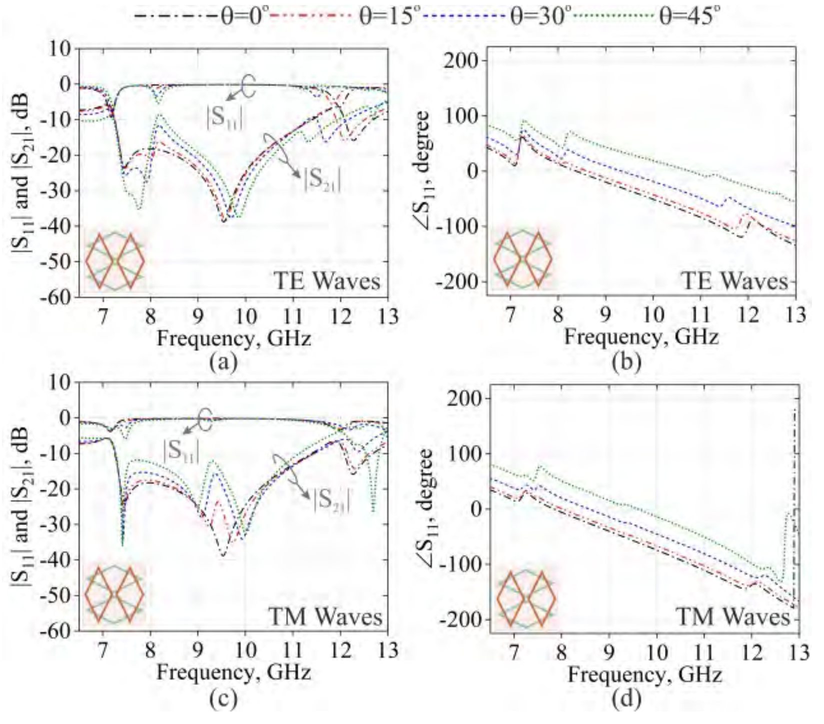

Figure 3.8: Transmission and reflection response of BTBDRL FSS under obliquely incident waves

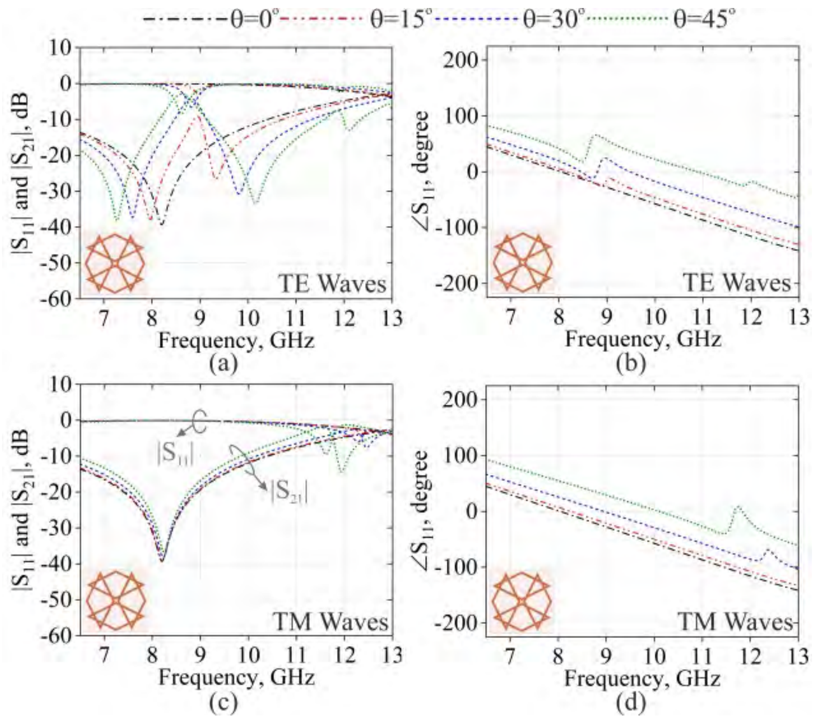

Figure 3.9: Transmission and reflection response of MDRL FSS under obliquely incident waves

at both lower and higher null around 8 and 9.5 GHz for both TE and TM incidences, respectively. The transmission coefficient '$|S_{21}|$', stays below 10 dB till θ=30° for TE and till θ=45° for TM incident EM waves. BTB DRL FSS offers a steady transmission response of up to 30° for TE and up to 45° for TM incidences. At the expense of signal rejection capability, the lossy behaviour of dielectric material may enhance the angular stability of BTB DRL FSS beyond 30° for TE waves. Moreover, the non-linearities still exist in the phase of reflection from BTB DRL FSS for TE and TM oblique incidences. Generally, MDRL FSS demonstrates a steady response only for oblique TM waves up to 45°.

Thus, BTB DRL FSS being angular stable till 45° appears to be a PI surface with almost X-band rejection capability while MDRL exhibits linearity in reflection phase with X-band rejection at normal incidence. With change in θ, MDRL response in TE deviates from that of TM, hence, PI is lost with AS.

3.2.2 ECM of DRL FSSs

The ECM of proposed DRL based FSS is suggested and discussed here. The ECM of BTB DRL and MDRL FSS is shown in Figure 3.10 (a) and (b) respectively. Layer #1 as indicated for first block of components represents ECM for VDRL while Layer #2 represents ECM for HDRL FSS. The way in which Layer #1 and Layer #2 are

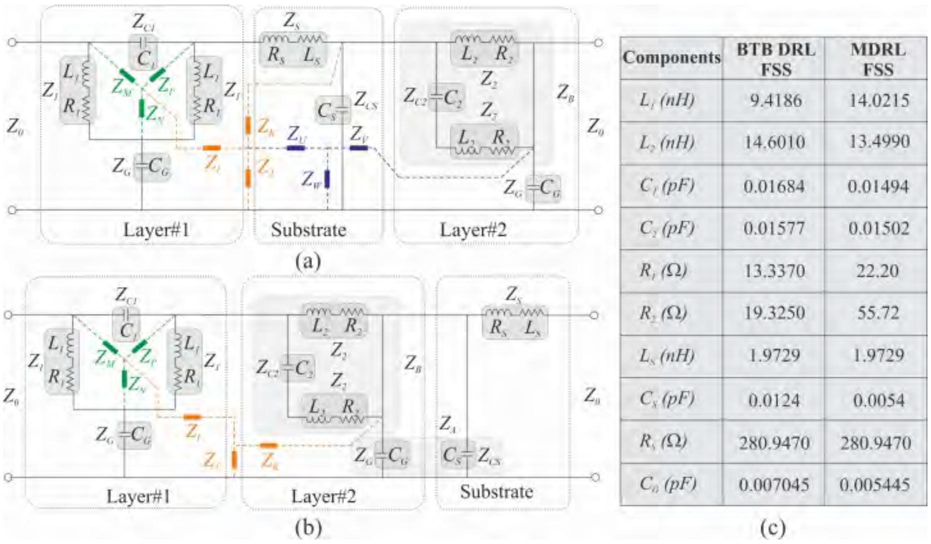

Components	BTB DRL FSS	MDRL FSS
L_1 (nH)	9.4186	14.0215
L_2 (nH)	14.6010	13.4990
C_1 (pF)	0.01684	0.01494
C_2 (pF)	0.01577	0.01502
R_1 (Ω)	13.3370	22.20
R_2 (Ω)	19.3250	55.72
L_S (nH)	1.9729	1.9729
C_S (pF)	0.0124	0.0054
R_S (Ω)	280.9470	280.9470
C_G (pF)	0.007045	0.005445

Figure 3.10: ECM for proposed FSSs under normal incidence:(a) BTB DRL, (b) MDRL and (c) ECM of component values

cascaded in ECM is chosen in similar fashion to the way BTB DRL and MDRL unit structures are physically developed. In ECM of BTB DRL, the substrate is loaded with Layer #1 and Layer #2 on both sides while in MDRL, the substrate is loaded at either side of Layer #1 or Layer #2. Circuit model in Layer #1 comprises of pair of inductors and resistors (L_1, R_1) indicating the presence of a pair of rhombic loop, separated by capacitor (C_1) corresponding to gap between DRLs. Additional capacitance (C_G) represents the capacitance developed due to unit cell array.

The substrate layer is modelled according to [102] with resistance (R_S) and inductor (L_S') in series to account for dielectric losses offered by substrate. Layer#2 comprises of two inductors (L_2) and two resistors (R_2) connected to a capacitor (C_2) on similar lines, but with a different topology than layer #1 alongwith capacitor (C_G). The optimized values of all lumped components used in ECM to achieve similar propagation characteristics of FSS as observed during simulations are summarised in 3.10(c).

The impedances Z_M, Z_N, Z_M,Z_I, Z_J, Z_K, Z_U, Z_V and Z_W in ECM for BTB DRL are marked in Figure 3.10 (a) while the impedances Z_M, Z_N, Z_P, Z_I, Z_J and Z_K for MDRL are marked in Figure 3.10(b). Impedances and their expressions are derived by simplifying the circuit using delta-to-star conversion. Thus, both the circuits are transformed to star-networks. The Z- and S-parameters are then derived using the expressions outlined in the reference [103]. Expressions for Z- and S- parameters are summarized in Table 3.2 where Z_1= R_1+X_{L1}, Z_2= R_2+X_{L2}, Z_S=R_S+X_{LS}, Z_{CS}=$\frac{1}{X_{CS}}$ and Z_G=$\frac{1}{X_{CG}}$ respectively.

Transmission reponses as evaluated from ECM analysis of BTB DRL and MDRL

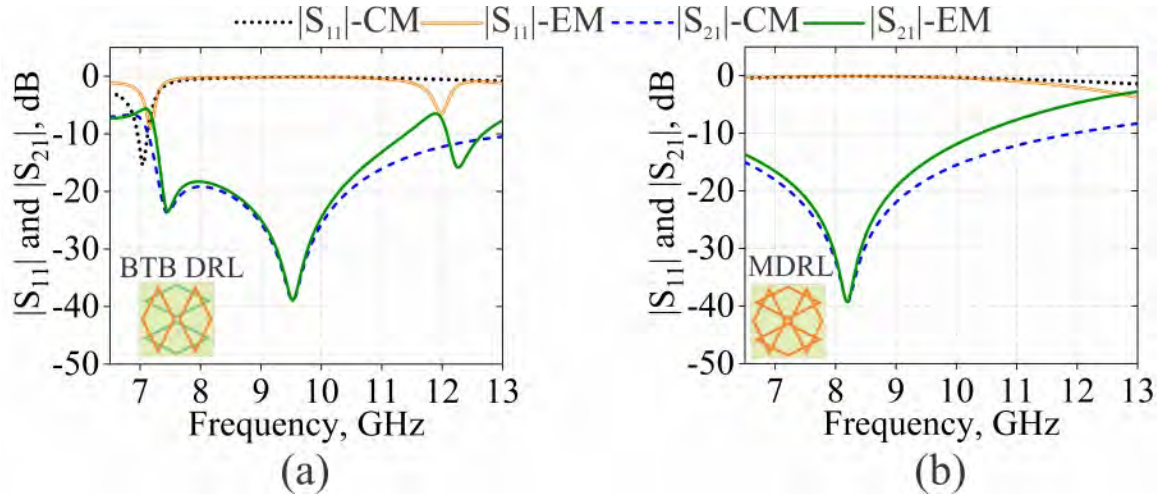

(a) (b)

Figure 3.11: Transmission and reflection responses of (a) BTB DRL FSS, and (b) MDRL FSSs obtained through EM and CM simulations respectively

are compared with responses observed during full wave simulations done on CST microwave studio. Comparisons as shown in Figure 3.11 (a) and (b), suggest that response of ECM is consistent with response of EM simulations of FSSs.

Table 3.2: Z- and S- parameters expressions used in ECM for BTB DRL and MDRL FSSs

Parameter	BTB DRL FSS	MDRL FSS
S_{11}	$\frac{(Z_{11}-Z_o)(Z_{22}+Z_o)-Z_{12}Z_{21}}{\Delta Z}$	
S_{21}	$\frac{2Z_{21}Z_o}{\Delta Z}$	
ΔZ	$(Z_{11}+Z_o)(Z_{22}+Z_o)-Z_{12}Z_{21}$	
Z_{11}	$Z_M+Z_IZ_U+Z_W$	$Z_M+Z_IZ_J$
$Z_{12}=Z_{21}$	Z_W	Z_J
Z_{22}	Z_V+Z_W	$Z_K+Z_S+Z_I$
Z_I	$\frac{(Z_N+Z_{C1})(Z_P+Z_S)}{Z_N+Z_P+Z_G+Z_S+Z_{CS}}$	$\frac{(Z_N+Z_G)(Z_P+Z_B)}{Z_N+Z_P+Z_G+Z_A+Z_B}$
Z_J	$\frac{(Z_N+Z_{C1})(Z_{CS})}{Z_N+Z_P+Z_G+Z_S+Z_{CS}}$	$\frac{(Z_N+Z_G)(Z_A)}{Z_N+Z_P+Z_G+Z_A+Z_B}$
Z_K	$\frac{(Z_P+Z_S)(Z_{CS})}{Z_N+Z_P+Z_G+Z_S+Z_{CS}}$	$\frac{(Z_P+Z_B)(Z_A)}{Z_N+Z_P+Z_G+Z_A+Z_B}$
Z_U	$\frac{(Z_T+Z_B)Z_S}{Z_T+Z_B+Z_S+Z_G}$	–
Z_V	$\frac{(Z_T+Z_B)Z_{C1}}{Z_T+Z_B+Z_S+Z_G}$	–
Z_W	$\frac{Z_{C1}Z_G}{Z_T+Z_B+Z_S+Z_G}$	–
Z_A	–	$\frac{Z_GZ_{CS}}{Z_G+Z_{CS}}$
Z_B	$\frac{Z_2(Z_2+Z_{C2})}{2Z_2+Z_{C2}}$	
$Z_M=Z_P$	$\frac{Z_1Z_{C1}}{2Z_1+Z_{C1}}$	
Z_N	$\frac{Z_1^2}{2Z_1+Z_{C1}}$	

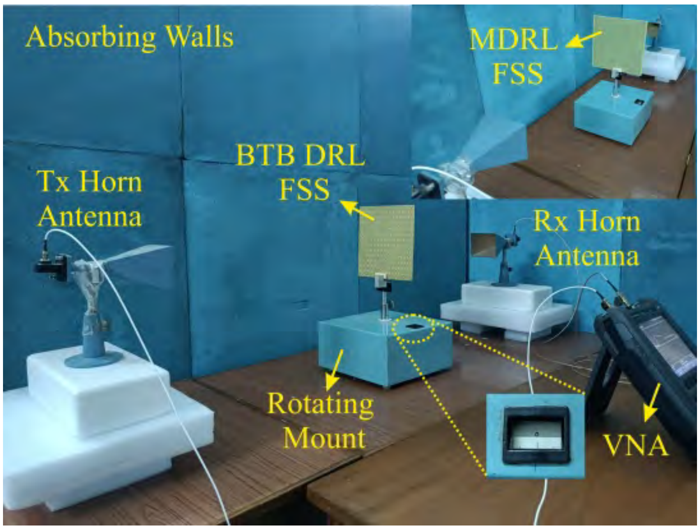

Figure 3.12: Measurement Setup for BTB DRL FSS and MDRL FSS (inset)

3.3 Fabrication of DRL FSSs and their experimental validation

The rhombic loop based FSSs have been developed using conventional printed circuit board (PCB) methodologies, and measurements have been performed by locating the FUT between a setup of two horn (WR-90) antennas radiating in X-band, as illustrated in Figure 3.12. Both horn antennas are positioned at fraunhofer far-field distance between them. The FUT is positioned on a mount with rotatory mechanism, and experiments are conducted.

The transmission response is measured through connecting VNA calibrated to record measurements using coaxial cables to horn antennas radiating in X-band. To record the transmission response, the FSS under test is then installed on a rotating mount in the X-Y plane between two horn antennas. As suggested in the reference [25], the FSS transmission response has been measured after well caliberating the VNA used to record measurements. Consequently, both the BTB DRL and MDRL FSSs for inclined as well as normal TE and TM incidences are measured.

FSSs are rotated along the Y-axis (vertical axis) from 0° to 45° after being installed on a rotating mount in X-Y plane. The magnitude of transmission coefficients (TE mode) captured and recorded for angular step of 5° along Y-axis. Rest of the methodology follows the procedure employed during measurements at normal incidence. Further, FSSs are rotated in X-Y plane by 90° which means measurements for TM incidences can be procured. Again FSS is rotated from 0° to 45° in Y-axis but the pattern appears to be orthogonal to previous measurements. Thus, effectively it is rotated in X-plane relative to the first step of measurements. For the purpose of picture clarity, measurements displayed for BTB DRL and MDRL are 15° apart instead of 5° as applied during real measurements.

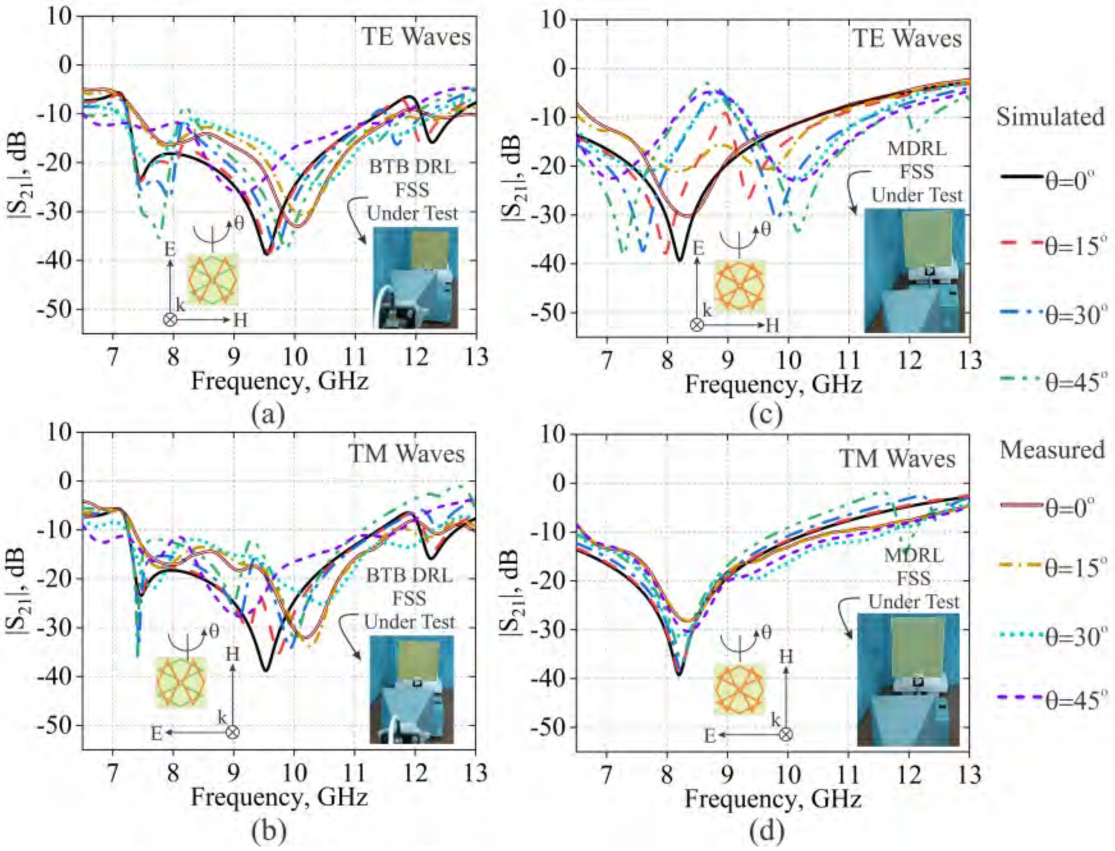

Figure 3.13: Simulated and measured $|S_{21}|$ dB of BTB DRL and MDRL FSSs, under oblique and normal incidences for TE (a,c), for TM (b,d)

3.3.1 Measurement results and comparison

Measured and simulated responses of BTB and MDRL FSSs under both oblique and normal incidences are shown in Figure 3.13 for the purpose of comparison. Here 'θ' is represented as the angle between the wave vector 'k' and normal. Standard horn antennas, radiating in X-band (WR-90) have lower and higher cut-off frequencies used in the measurements of DRL FSSs. As a consequence, the effective length of the loop for incident polarized wave appears to be increased due to merged structure of MDRL FSS, thus, the lower edge frequency moves towards lower values. As a consequence, the reduced BWs are recorded in TE and TM measurements of MDRL FSS. Thus, the lower edge frequency moves towards lower values.

Although the transmission loss appears to be different for TE and TM incidences within the operating band of BTB DRL FSS, the incident waves are rejected likewise. The BTB DRL FSS, thus, effectively functions as a PI FSS surface. On the other

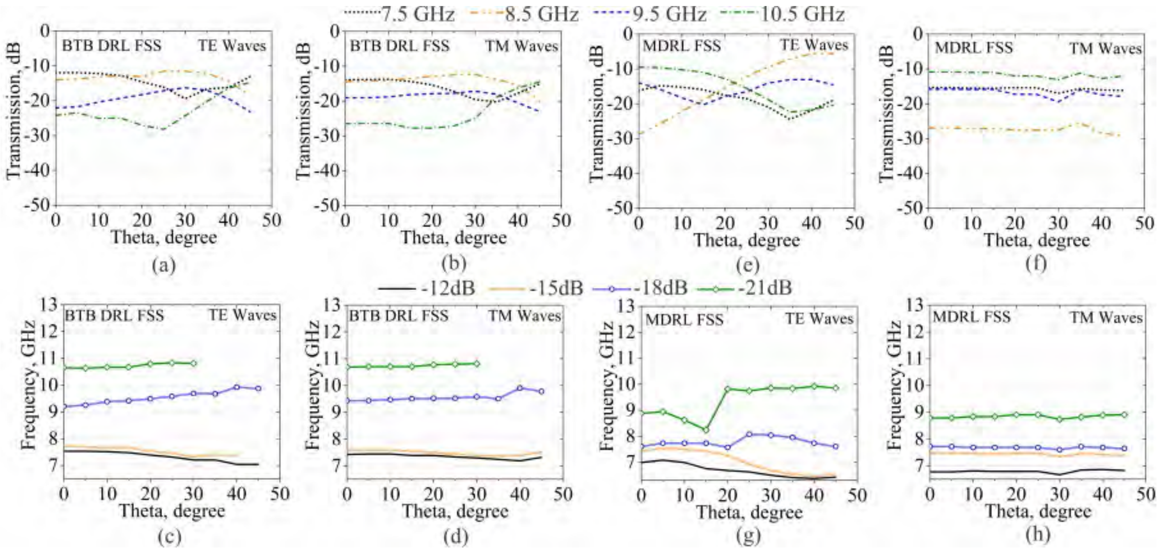

Figure 3.14: Variation $|S_{21}|$ dB with 'θ' at four frequencies from rejection band of BTB DRL FSSs (a) TE (b) TM oblique incidences; of MDRL FSS (e) TE (f) TM oblique incidences. Frequency 'f_r' shift at distinct transmittance values (dB) for BTB DRL FSS (c) TE (d) TM oblique incidences; for MDRL FSS (g) TE (h) TM oblique incidences

hand, MDRL FSS can reduce the non-linearity in reflection phase of BTB DRL at the expense of PI behaviour. MDRL do not exhibits PI response especially for oblique TE incidences. The differences observed among simulated and measured $|S_{21}|$ values under oblique and normal incidences is likely due to difference in properties of practical materials and development practices.

The behaviour of both FSSs towards wave propagation when TE/TM incidences are oblique is expounded further. Figures 3.14 (a) and (b) depict the change in TE/TM mode transmission coefficients of BTB DRL FSS under oblique incidences at four frequencies (7.5, 8.5, 9.5 and 10.5 GHz) located within its stopband. Figures 3.14 (c) and (d) display the frequency variations for TE and TM mode over inclined EM incidences at constant values of transmission coefficients at -12, -15, -18, and -21 dB. The magnitude of the transmission coefficient is observed to stay under -10 dB at 7.5, 8.5, 9.5, and 10.5 GHz for oblique TE and TM incident waves upto 45°. In addition, the the change in frequency in TE and TM mode with respect to incidence angles is less than 1 GHz. Maximum frequency deviation (TE mode) of 725 MHz is observed at -18 dB signal attenuation. Here, the feature of polarization-independence observed for BTB DRL FSS is determined by its wide stopband, which stay below -10 dB under TE and TM oblique incidences. The potential of BTB DRL FSS to filter incident EM energy is unaffected by change in the incidence angle of EM waves. Evidently, the fabricated BTB DRL FSS shows a capability of EM wave rejection by minimum 11 dB to a maximum of 34.8 dB, over the stopband of 4.3 GHz within a

Table 3.3: Proposed DRL based FSSs compared with reported X-band FSSs

Ref.	Substrate	Unit cell dimensions (mm^3)	FSS Type	-10dB Stop-band (GHz)	Reflection Phase	PI	AS	Application
[104]	FR4	7.6× 7.6 ×1.6	Single layer, Double sided	8.4-12.4, 12.4-15.8	Not Available	No	Yes (60°)	Bandstop filter
[105]	Arlon DI 880	7.7× 7.7 ×0.76	Dual layer, Single sided	7.94-11.53	Non-Linear	Yes	Yes (60°)	X-band applications
[106]	FR4	7.5× 7.5 ×5.2	Triple Layer	8-12.5	Not Available	Yes	Yes (45°)	X-band application
[61]	RT Duroid 5880 LZ	14.5× 14.5 ×0.254	Single layer, Double sided	8.15-13.2	Linear	Yes	Yes (40°)	Antenna gain enhancement
[62]	FR4	7.25× 7.25 ×2.4	Single layer and Grounded	Not Available	Linear	Not Available	Not Available	Antenna gain enhancement
Prop. FSS BTB DRL	FR4	14.42× 14.42 ×1.57	Single layer, Double sided	7.38-11.7	Non-Linear	Yes	Yes (45°)	WB AS reflector
Prop. FSS MDRL	FR4	14.42× 14.42 ×1.57	Single layer, Single sided	6.71-10.43	Linear	No	No	WB FSR

range of 7.38 GHz to 11.7 GHz.

Similarly, Figure 3.14 (e-h) demonstrates the variation in transmission coefficients and frequencies for inclined TE and TM waves for MDRL FSS. MDRL FSS is observed to lose its stability when exposed to TE waves incident at an angle. However, it retains the bandstop behaviour for incident TE and TM waves up to an angle of 10°.

The proposed rhombic loop based FSSs are compared to other X-band FSSs reported in recent published work in Table 3.3. The comparison suggests that polarization-independent BTB DRL FSS offers wideband rejection, and that its rejection capability is unaffected by the incidence angle of incident EM waves, making it angularly stable. While polarisation dependent MDRL has a linear reflection phase within a slightly narrower rejection band than BTB DRL FSS, its rejection band is slightly narrower. In addition to being inexpensive and simple to develop, the merit of the proposed FSSs lies in fact that only an array of RLs is employed to get a wider stopband with PI in the BTB DRL FSS while reflection phase linearity in the MDRL FSS.

The following section presents the enhancement of boresight gain enhancement of a microstrip fed X-band antenna with triangular slot by integrating DRL based FSSs as described earlier in this chapter. The triangular slot antenna is backed by both BTB DRL and MDRL FSSs in two different assemblies. Also, the slot antenna is back by a cascaded DRL (CDRL) based FSS reflector formed when two single side printed orthogonal layers of dual rhombic loops (DRLs) are stacked together.

3.4 DRL FSS integrated with triangular X-band slot antenna

The boresight gain of a microstrip fed triangular slot antenna operating in X-band frequency range is enhanced using FSSs and the technique is presented in this section. The triangular slot antenna when backed by three distinct configurations of DRL based FSSs exhibit better antenna performance as studied through simulations. Two single side printed orthogonal layers of arrays of RLs kept in pair are stacked together to form the reflective surface. Antenna backed by CDRL layers exhibit wide stopbands but with high reflection phase non-linearities even for normally incident orthogonally polarized EM waves. The reflection phase non-linearities are suppressed when both layers are printed on opposite sides of the dielectric substrate. The non-linearities are completely eliminated when both the layers are merged and printed on one of the sides of the dielectric substrate to get MDRL based FSS. For measurements, the triangular slot antenna and MDRL FSSs are developed and integrated to perform experiments. The triangular slot antenna prototype exhibits an impedance bandwidth of 650 MHz from 7.96-8.61 GHz and a maximum gain of 8.5 dB in antenna boresight including 4.5 dB enhancement due to frequency selective reflectors. Finally, the measurement results observed during experiments are found to be in almost agreement to results observed during simulation studies and also, are compared to be on a par with other antennas recently reported in published work.

3.4.1 Triangular slot antenna (8.2 GHz) design

The antenna with triangular slot is designed on an affordable substrate (FR-4) as shown in Figure 3.15. An equilateral triangular slot is etched from 30×30 mm^2 ground plane supported by a substrate with thickness of 1.57 mm. The slot is excited by a center fed 50 Ω microstrip line developed on opposite side of slot on the substrate. The design features of equilateral triangle slot antenna are mentioned in Table 3.4.

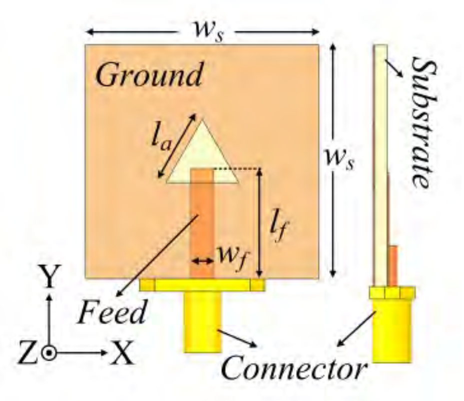

Figure 3.15: Geometry of triangular slot antenna

Table 3.4: Features of equilateral triangular slot antenna

Parameter	w_s	l_a	w_f	l_f
Value(mm)	30	11.9	3	13.7

The triangular slot antenna is designed for ITU 8.2 GHz frequency band [107], [108]. The dimension of equilateral triangular slot is chosen as per the closed form expressions suggested for triangular slot antenna [109] but with modification in the effective length to make the slot equilateral. The resonance frequency of triangular is tailored when the length of triangular slot is varied. The effect of side 'l_a' on resonant frequency of triangular slot antenna is presented in Figure 3.16 (a). It can be observed that the resonance frequency drifts towards lower frequency as the length 'l_a' of triangular slot is increased and vice-versa. Therefore, the side of triangular slot antenna is chosen 11.9 mm for the desired frequency of operation. The reflection coefficient curve of designed antenna is shown in Figure 3.16. The antenna impedance band ranges from 7.81 GHz to 8.61 GHz which covers the ITU 8.2 GHz frequency band [110], [107]. The boresight gain at resonant frequency is 2.73 dB while the peak boresight gain is 2.85 dB observed at 8.4 GHz. Figure 3.16 (b) shows boresight gain, reflection coefficient (in dB) and the surface current density (SCD) for the slot antenna with microstrip feed at 8.2 GHz on the antenna in inset. It is observed that the SCD is high at the lower edges of triangular slot and at microstrip feed which suggests the radiation from the slot.

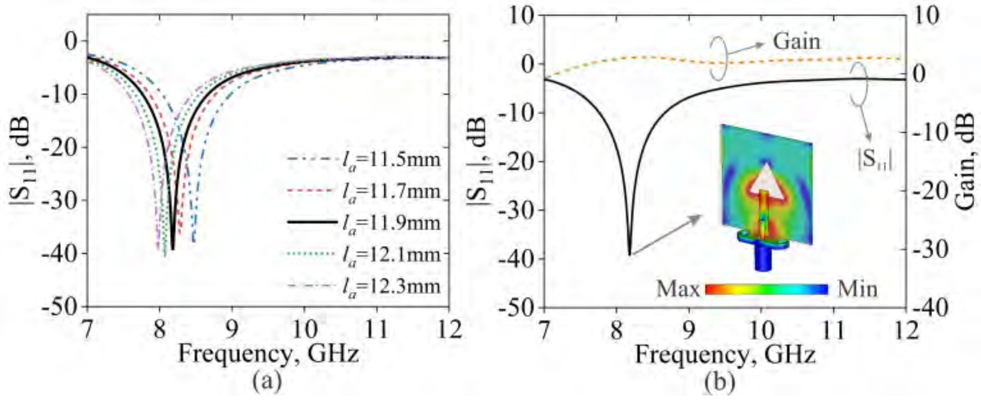

Figure 3.16: Reflection coefficient, boresight gain and surface current distribution on triangular slot antenna

3.4.2 DRL based X-band reflectors

An arbitrary frequency selective reflector (FSR) composed of m×n unit elements and a planar antenna with aperture dimensions $W_a \times L_a$ are depicted in Figure 3.17 (a) and (b) respectively. Thus, the following condition must be fulfilled in order to obtain antenna gain enhancement:

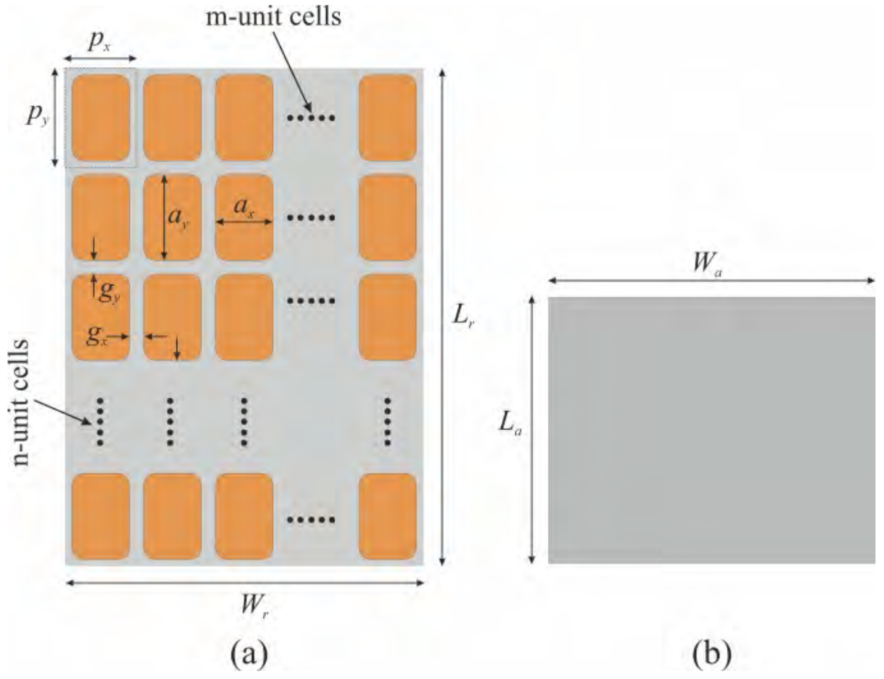

Figure 3.17: Illustration of (a) an arbitrary FSS reflector with m×n unit cells, (b) a planar source antenna

$$m.P_x \geq W_a \tag{3.4.1}$$

and

$$n.P_y \geq L_a \tag{3.4.2}$$

Where $P_x = a_x + g_x$ and $P_y = a_y + g_y$.

To study the impact of reflecting FSSs on the triangular slot antenna, three distinct configurations of FSSs reflectors are used. The unit cells of DRL based FSS as earlier shown in Figure 3.1 are repeatedly shown in Figure 3.18 to highlight features of RLs.. The proposed FSSs are composed of orthogonally oriented two metallic layers of RLs kept in pair on FR4 substrate as shown with dimensions (in mm) in Figure 3.18(a) and (b). These arrays are stacked together to form CDRL FSS as shown in Figure 3.18(c). Rest two configurations of FSS reflectors as discussed in earlier sections, i.e., BTB DRL and MDRL have also been shown in Figure 3.18 (d) and (e) respectively.

These RL based unit elements are simulated employing full wave EM solver available with CST MWS after applying boundary conditions periodically along edges of the substrate and Floquet ports for excitation along Z-direction. The magnitudes of transmission coefficients (in dB), and reflection coefficients (in dB) along with reflection phase diagrams of proposed FSSs are revealed in Figure 3.19.

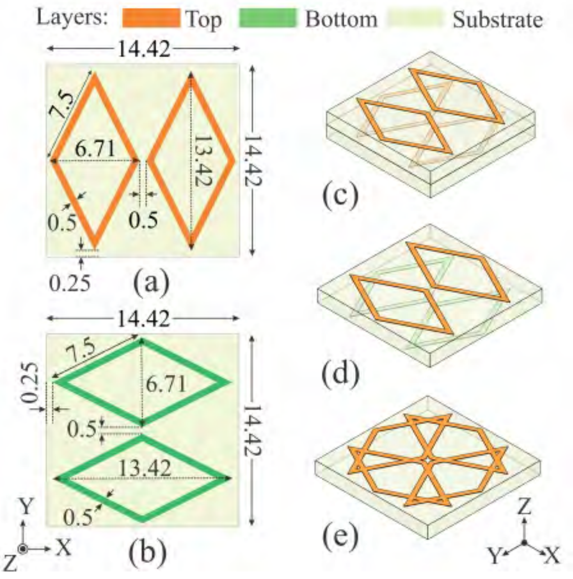

Figure 3.18: RL unit cells (a) VDRL, (b) HDRL, (c) CDRL, (d) BTB DRL and (e) MDRL (all dimensions are in mm.)

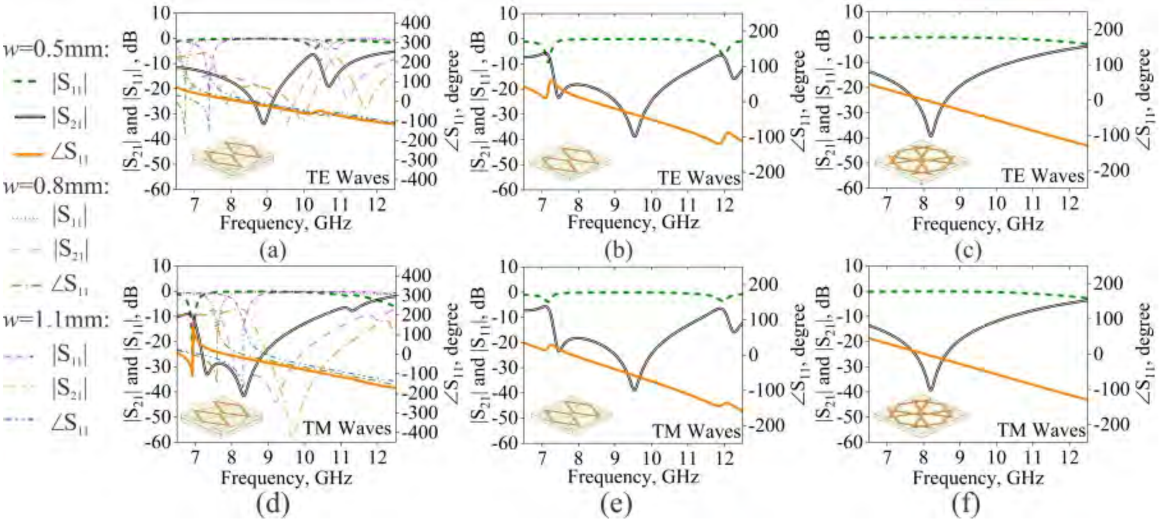

Figure 3.19: Simulated propagation characteristics of FSS unit cells under TE incidence for : (a) CDRL FSS, (b) BTB DRL FSS ,(c) MDRL FSS, and under TM incidence for : (d) CDRL FSS, (e) BTB DRL FSS and (f) MDRL FSS

From comparison of simulation responses , it can be observed that CDRL FSS exhibits dissimilar propagation characteristics for TE and TM incidences while BTB DRL and MDRL FSS exhibits similar behaviour for TE and TM incidences. Comparing the reflection phases of these FSSs, it is found that the non-linearities in reflection phases of CDRL are very high while the non-linearities are moderately suppressed in BTB DRL FSS. These non-linearities in reflection phases appear due to dielectric substrate available between layer #1 and layer #2. Linear reflection phase is observed on printing both layer #1 and #2 on one of the sides substrate. Mostly, non-linearities reflection phase is observed at lower edge frequencies. To study the effect of non-linear phase response, the width 'w' of RL is varied and the value of 'w' which provided non-linear response within operating band of slot antenna is chosen during simulation. Therefore, reflection phase responses are displayed in Figure 3.19 for distinct values of 'w'.The stopbands and reflection phases of DRL based FSSs for normally incident TE and TM waves striking normally are summarized for comparison in Table 3.5.

Table 3.5: Transmission characteristics derived from simulations of proposed DRL based FSSs under normal incidence

Unit Cell	Stopband(TE), GHz	Stopband(TM), GHz	Reflection Phase for TE and TM incidence
CDRL	5.7-9.9 &10.4-11.3	6.9-10.5	Distinct and highly non-linear
BTB DRL	7.25-11.4	7.25-11.4	Distinct and moderately non-linear
MDRL	5.6-10.4	5.6-10.4	Similar and linear

Although CDRL and MDRL bandwidths are larger than shown here as they are limited to 6.6 GHz at lower edge due to WR-90 horn antennas employed for the practical measurements.

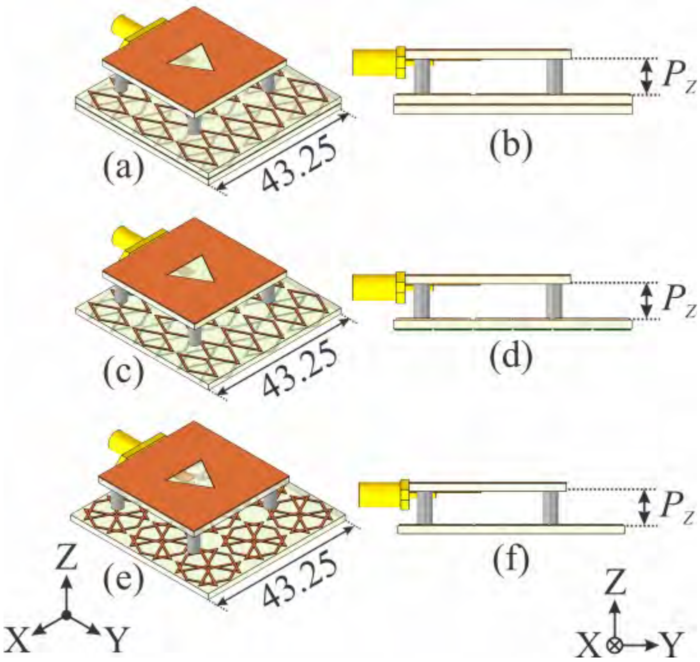

Figure 3.20: Isometric and side views of triangular slot antenna backed by (a) and (b) CDRL FSS, (c) and (d) BTB DRL, and (e) and (f) MDRL FSS respectively

3.4.3 Triangular slot antenna backed by FSRs

The slot antenna is further, integrated with 3×3 array of CDRL, BTB DRL and MDRL FSSs separately to study the impact of these FSSs on the triangular slot antenna. These FSSs are placed behind the triangular slot antenna at a height 'P_Z' as shown in Figure 3.20.

The initial separation, P_Z between antenna and TRL FSS is determined using following expressions as suggested in the references [111], [112], [113], [114]. However, the expression needs to be modified owing to the presence of dielectric material of the antenna and the reflecting surface.

$$P_{Zeff} = \frac{\lambda_0}{4\pi}\left(\phi_{FSS} + \phi_{GND}\right) - N\frac{\lambda_0}{2}, \qquad N = 0, \pm1, \pm2, \pm3, \cdots \tag{3.4.3}$$

where

$$P_{Zeff} = P_Z\sqrt{\varepsilon_e - Sin^2\theta} \tag{3.4.4}$$

Here, ϕ_{FSS} is the reflection phase demonstrated by FSS which it found to be 0° at 8 GHz and $\phi_{GND} = \pi$ for slot antenna. The effective relative permittivity, ε_e is approximated by averaging the relative permittivity of air and that of dielectric substrate, ε_r. Under normal incidence, $\theta = 0°$ and setting N=0 for the fundamental mode, For FR4, the height between antenna and FSS becomes $P_{Zeff} \approx \dfrac{\lambda_0}{4\sqrt{\varepsilon_r}} \approx \dfrac{\lambda_0}{6.4}$.

Further, the parametric analysis of separation between antenna and the FSSs is performed using CST MWS while placing these FSSs at distinct heights of $\lambda_0/8$, $\lambda_0/6$, $\lambda_0/4$ and $\lambda_0/2$ from triangular slot antenna where free space wavelength,'λ_0' is calculated at 8.2 GHz. The reflection coefficients and gains in boresight are obtained through simulations and compared in Figure 3.21.

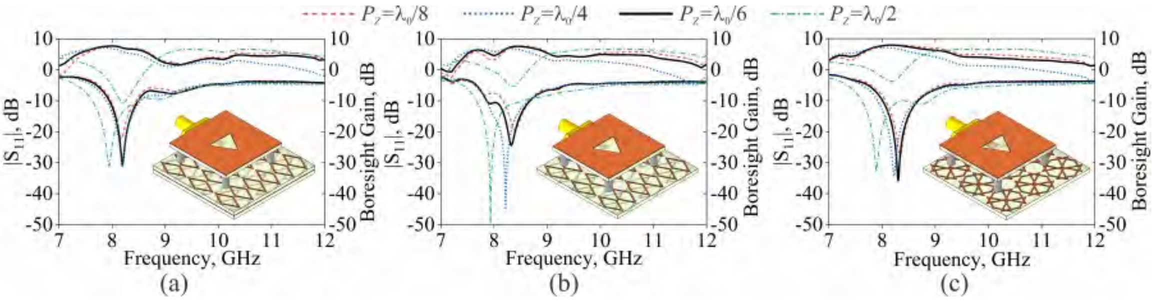

Figure 3.21: Comparison of reflection coefficients and gain in boresight direction of triangular slot antenna when backed by (a) CDRL, (b) BTB DRL, and (c) MDRL FSSs, at distinct heights

The antenna resonance frequency shifts towards lower frequencies when CDRL, BTB DRL and MDRL FSSs are placed at height of $\lambda_0/2$. Also, gain in boresight is suppressed. It is also observed that the gain enhancement is minimum when backed by CDRL and maximum when backed by MDRL FSSs.

For distinct heights of $\lambda_0/8$, $\lambda_0/6$ and $\lambda_0/4$, the slot antenna's impedance bandwidth remains almost same for all the configurations. Since, there is minimum drift in antenna resonance frequency and a better impedance matching is observed when height of FSSs is $\lambda_0/6$ from slot antenna. Therefore, $\lambda_0/6$ is chosen to be an optimum height which comes out to be is 6 mm at 8.2 GHz. The comparison of reflection coefficients and gains of slot antenna integrated with DRL based FSSs at an optimum height of 6mm are compared as depicted in Figure 3.22 and also summarized in Table 3.6.

Impedance matching improves when triangular slot antenna is united with by MDRL FSS. CDRL FSS suppresses the gain of the antenna at boresight especially at lower and upper edge frequencies of impedance band of the antenna. BTB DRL FSS also suppresses the antenna boresight gain in antenna impedance band. During preliminary simulations, non-linear reflections at lower frequency range are observed

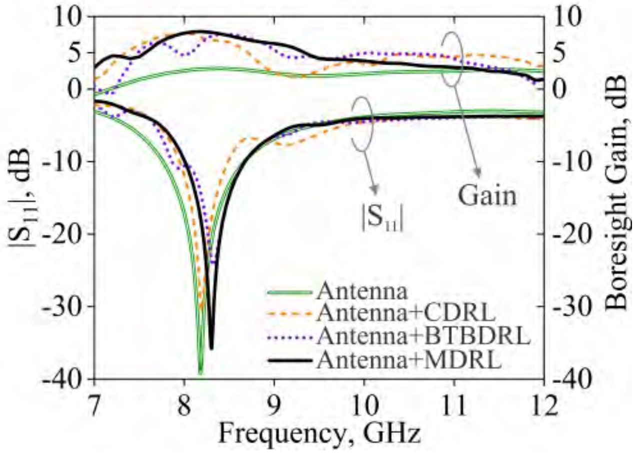

Figure 3.22: $|S_{11}|$ and boresight gains of triangular slot antenna compared with antenna backed by CDRL. BTB DRL and MDRL FSS

Table 3.6: Performance of antenna backed by FSS reflectors

Antenna Type	f_r(GHz)	S_{11} (dB)	-10dB Impedance Band (GHz)	Max.boresight Gain (dB)	Avg. boresight gain (dB)
Antena	8.2	-35.19	7.81-8.61	2.85	2.46
Antenna+CDRL	8.19	-30.7	7.94-8.48	7.96	6.6
Antenna+ BTB DRL	8.32	-24.25	7.85-8.67	7.59	6.46
Antenna +MDRL	8.3	-35.82	8.0-8.67	7.91	7.12

in reflection phase of CDRL FSS outside the antenna impedance band.

Further, the effect of aperture size of antenna is investigated. Since, the geometry of aperture is an equilateral triangle, therefore, aperture size depends on the edge length of triangular slot antenna. A performance comparison of effect of edge of triangular slot antenna loaded by MDRL as a reflector is depicted in Figure 3.23 and also summarized in Table 3.7.

Table 3.7: Comparison of slot antenna with distinct aperture size loaded by MDRL FSS

$l_a(mm)$	$f_r(GHz)$	Peak Boresight Gain(dB)
11.5	8.48	7.72
11.7	8.39	7.81
11.9	8.30	7.91
12.1	8.21	7.98
12.3	8.12	8.06

It is found that, as the edge of triangular slot increase, the antenna resonance frequency drifts towards lower values while peak gain in boresight direction increases. This confirms that MDRL FSS produces gain enhancement over wide frequency range.

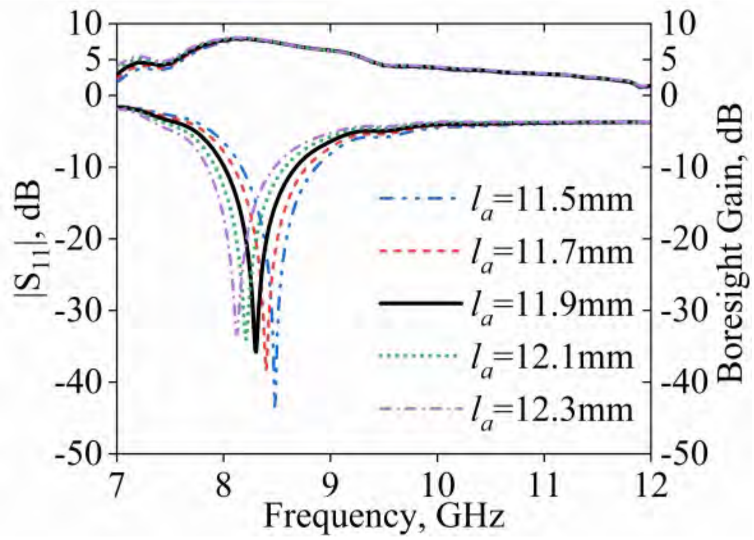

Figure 3.23: Effect of aperture size on $|S_{11}|$ dB and boresight gain of triangular slot antenna united with MDRL reflector

To observe the effect of non-linear phase response on antenna gain, the reflection phase characteristic is shifted to higher frequency by increasing the loop line width inwards as mentioned in section 3.2.1.1 while keeping inter RL spacing constant. The CDRL FSS with RL width of 1.1 mm exhibits the non-linear reflection phase around the resonance frequency of triangular slot antenna. The modified CDRL FSS is again integrated with triangular slot antenna to observe variations in antenna gain due to reflection phase non-linearity.

From Figure 3.24, it is observed that CDRL FSS with thicker loop width of 1.1 mm deteriorates the antenna performance as the gain in boresight direction is suppressed and impedance matching also becomes poor. The reflection coefficient, $|S_{11}|$ decreases due to CDRL (w=1.1mm) when observed at antenna feed. Boresight gain between 7-8 GHz deteriorates which again indicates poor impedance matching. Reflection from FSS should not be transferred to feed instead it should increase the gain after constructive interference. So, the reflection coefficient , '$|S_{11}|$ dB' of antenna should not change.

Figure 3.25 illustrates the surface current distribution on triangular slot antenna and on the surface of CDRL, BTB DRL and MDRL FSS at different resonance frequencies as observed after integration of antenna and FSS. The SCDs suggests that CDRL FSS is not uniformly illuminated by EM waves radiated from slot antenna. Also, the intensity of current density is not very high on its surface. A similar scenario with non-uniform SCD on BTB DRL is also observed. MDRL FSS, on the other hand is illuminated uniformly as the SCD intensity over slot antenna and MDRL FSS follows uniform current distribution on their respective surfaces. Thus, MDRL ap-

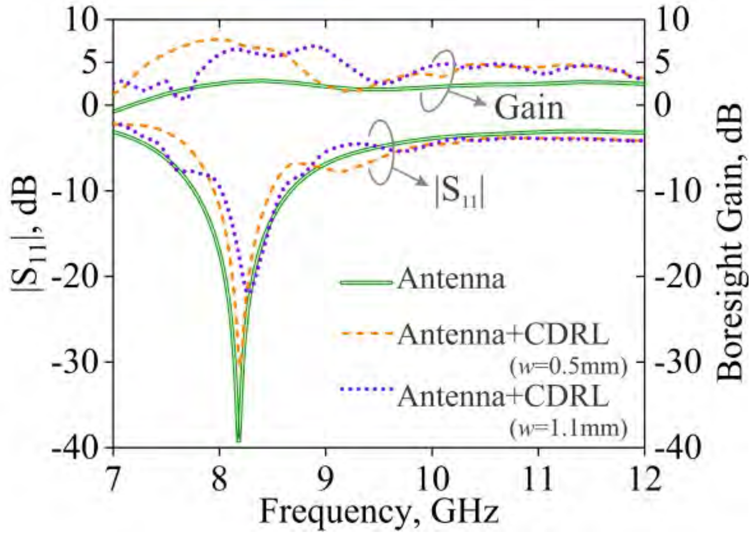

Figure 3.24: Effect of non-linear reflection phase of CDRL on slot antenna reflection coefficient and gain

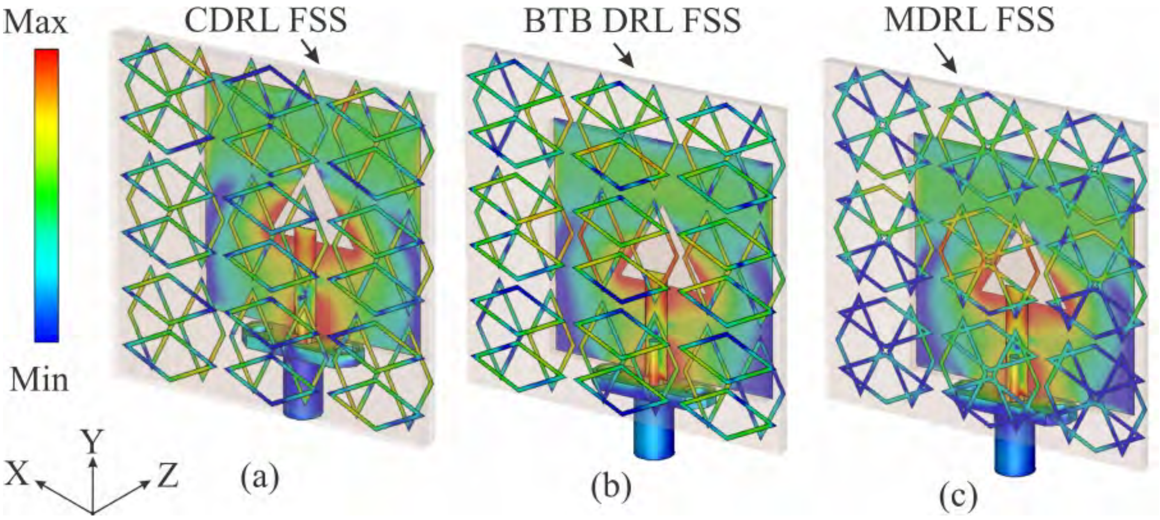

Figure 3.25: Simulated surface current distribution on triangular slot antenna backed by (a) CDRL FSS at 8.2 GHz, (b) BTB DRL FSS at 8.32 GHz and (c) MDRL FSS at 8.3 GHz

pears as a superior reflector compared to CDRL and BTB DRL FSSs.

After simulation studies, it is concluded that MDRL FSS backed slot antenna appeared to be optimum structure providing better performance. Thus, antenna and FSS are developed for validation of FSS backed slot antenna as discussed in the section ahead.

3.4.4 Integrated antenna fabrication and measurements

The triangular slot antenna and 3×3 array of MDRL FSS are fabricated using conventional PCB technology for experimental validation. The triangular slot and MDRL reflector are assembled together with four plastic spacers by maintaining the required separation of 6 mm between antenna and FSS as maintained in [62]. The fabricated antenna and MDRL FSS are integrated together as a single unit are presented in Figure 3.26.

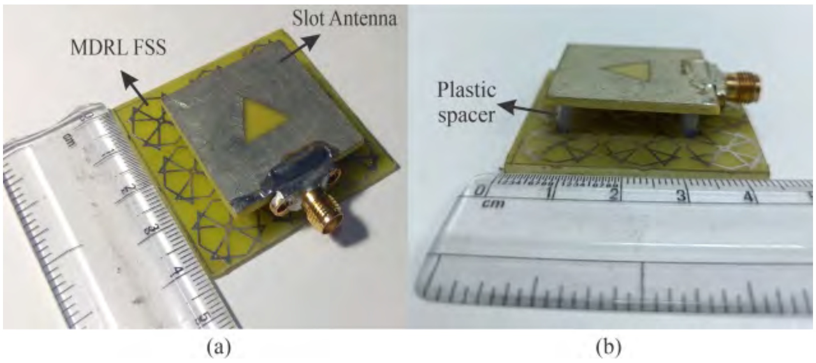

Figure 3.26: Fabricated MDRL backed triangular slot antenna prototype (a) 3D view #1, (b) 3D view #2

The S-parameter of the antenna is measured by calibrated vector network analyzer (VNA) (Keysight N9928A). The measured and simulated reflection coefficients and gain in boresight direction of triangular slot antenna are compared and depicted in Figure 3.27. Inset in Figure 3.27 show the enhancement of 4.5 dB achieved in antenna gain when MDRL array is employed beneath the slot antenna as a reflector.

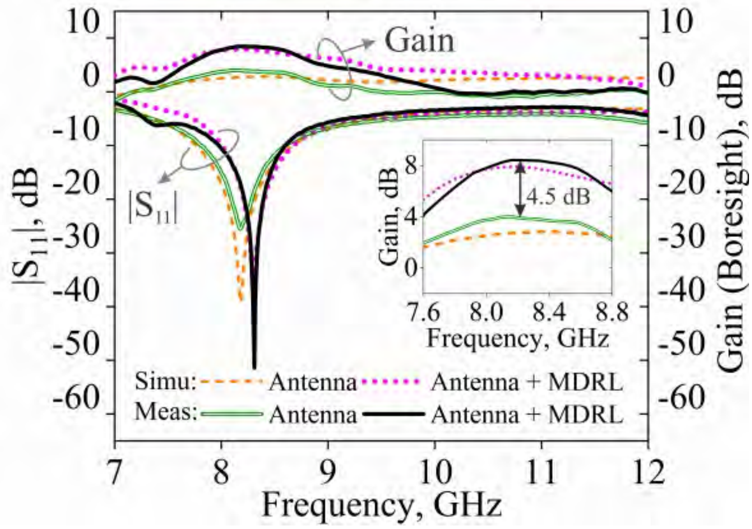

Figure 3.27: Comparison between measured and simulated $|S_{11}|$ dB and boresight gain of antenna alone and integrated with MDRL FSS

The measured impedance band (S_{11} ≤-10 dB) of antenna is 9.64% from 7.79 GHz to 8.61 GHz and the simulated impedance band is 9.74% from 7.81 GHz to 8.61 GHz. Also, the measured impedance band for slot antenna with MDRL FSS is 7.84% from 7.96 GHz to 8.6 GHz while the simulated band is 10% from 8.00 GHz to 8.67 GHz.

The plot in Figure 3.27 shows that triangular slot antenna exhibits an in-band gain of 3.65 dB on an average while the average in band gain for antenna integrated with MDRL FSS rises to 8.15 dB. Thus, a 4.5 dB gain enhancement is achieved in antenna boresight.

The antenna gain along with the radiation pattern are measured using standard horn antenna method. In this method, a standard X-band horn antenna is fed through RF generator and the triangular slot antenna is matched with the power meter. Both the horn antenna and triangular antenna are housed in an anechoic chamber. The triangular antenna is rotated at an angular step of 10° and the readings of power meter are recorded. The values for normalized radiation pattern of the antenna are thus obtained using Friss equation. Similarly, the radiation pattern of antenna integrated with FSS was plotted. The normalized radiation pattern in two principal (XZ and YZ) planes are plotted for both the cases i.e., for the slot antenna and antenna united with MDRL FSS in Figure 3.28.

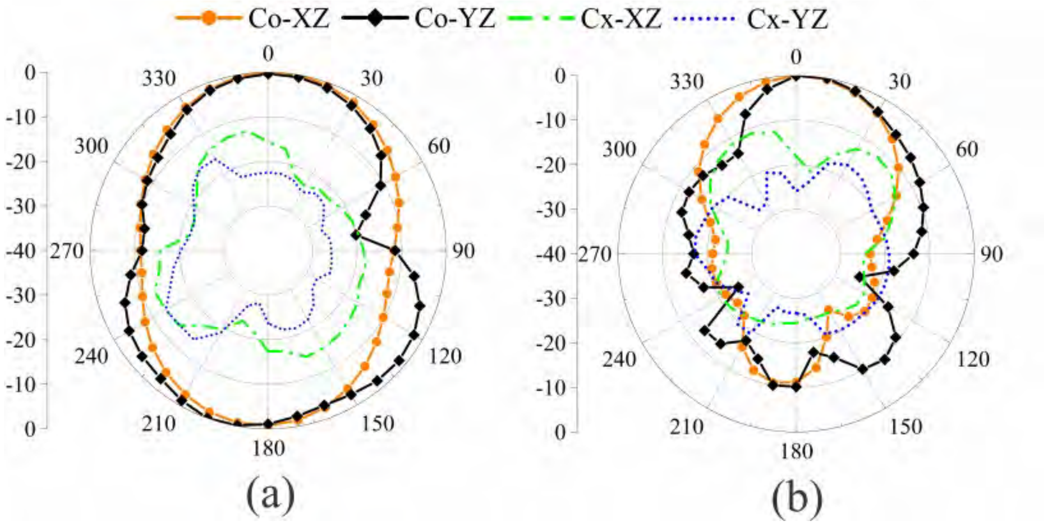

Figure 3.28: Radiation pattern measurements of (a) triangular slot antenna, and (b) triangular slot antenna backed by MDRL FSS

The triangular slot antenna radiates bidirectionally with 12.79 dB of peak cross-polar level where peak cross polar level is the difference of co-polar gain in boresight direction and peak cross-polar gain. The MDRL FSS reflects the power radiated by the slot antenna. Therefore, back lobe in 180° is suppressed by 10.43 dB in XZ - Plane and 9.06 dB in YZ plane. The side lobes appeared after suppression of back radiation. Figure 3.28 (a) and (b) when compared concludes that the reflector has suppressed the side lobes by ~10 dB, if any. From the plotted radiation pattern and their comparison, it can be concluded that the antenna when integrated with MDRL FSS becomes directional.

The proposed slot antenna is compared with antennas with existing literature is highlighted based on techniques employed to improve the gain of antennas in Table 3.8.

Table 3.8: Comparison of almost identical antennas reported in existing literature

Ref.	Antenna Dimension (mm^3)	-10dB Impedance Band (in GHz)	Max. Gain (Boresight)	Gain Enhancement	Gain Enhancement Technique
[115]	60×60×11	5.08-5.51	10.6	Not Mentioned	FPC+EBG
[18]	67.2×67.2×15.8	9.42-11.35	12	4.9	Superstrate
[116]	60×60×16.1	9.1-10.9	11.4	6.6	Superstrate
[117]	32×26×11.2	8-12	7.8	2.5	FSS Reflector
[118]	23.3×11.8×3	5.01-7.35	6.85	4.09	AMC Reflector
[61]	58×58×9.05	7.5-13	7.8	3.3	FSS Reflector
[This Work]	42.25×42.25×9.07	7.96-8.61	8.5	4.5	FSS Reflector

From the comparison, it is found that the antenna gain enhancement observed in the experiment is comparable to other techniques employed in the reported literature. A tradeoff between the dimensions of the integrated structure, band of operation and achieved antenna gain is required and a need for compromise do not disappear Here, the antenna is backed by an economical reflector utilizing a simpler technique to obtain linear reflection phase and thus, antenna gain enhancement.

3.5 Conclusion

RL based FSSs with wide stopbands are fabricated and experimentally validated in this work. FSSs are developed using two layers of PD orthogonally oriented pair of RLs. BTB DRL FSS with wide bandstop is developed by printing two orthogonal layers BTB on opposite sides of dielectric substrate. The non-linearity in reflection phase can be compensated by merging both orthogonal pairs on the one of the sides of substrate. Measurements reflect that BTB DRL exhibits a stopband of 4.3 GHz with one transmission null at 7.9 GHz and other at 10 GHz while MDRL FSS realized after merging both orthogonal layers on one side provides wide stopband of 3.7 GHz centered at 8.3 GHz with a much better rejection ability. The experiment results are in a good agreement to observations in simulations in transmission response. Later, a directional triangular slot antenna employing X-band reflecting surface towards enhanced boresight gain is developed and experimentally validated. Two orthogonal layers composed of arrays of RLs kept in pair are stacked together first forming CDRL FSS and then printed on opposite planes of FR-4 laminate as in BTB DRL FSS.

The non-linearities of any sort in reflection phase is eliminated when both layers are printed on one of the sides of FR-4 substrate as in MDRL FSS. MDRL FSS demonstrate a linear reflection phase when compared with other proposed frequency selective reflectors. For experiments, the proposed MDRL FSS is further integrated with triangular slot antenna. The triangular slot antenna demonstrates an impedance band of 7.79 GHz - 8.61 GHz (9.64%) and a boresight gain of 3.88 dB at 8.2 GHz. After the antenna is integrated with the proposed MDRL FSS, it exhibits an impedance band ranging from 7.96 GHz to 8.6 GHz with 8.38 dB boresight gain at 8.31 GHz. An enhancement of 4.5 dB is achieved in boresight gain using frequency selective reflector with linear reflection phase.

Chapter 4

Rectangular loop based wideband frequency selective reflectors

---

The technique of transforming PD to PI FSS unit structures have been exploited to demonstrate DRL based FSS reflectors in X-band frequency range in chapter 3. It has also been deduced that rectangular loop based FSSs offer stable and superior propagation characteristics relatively at lower frequencies when compared with elliptical and rhombic loop based FSS structures. Therefore, this chapter describes the design and performance assessment of rectangular loop pair (RLP) based FSS wideband reflector (MRLP) and UWB reflector (MDRLP) respectively for under EM incidence by employing similar techniques to transform PD FSS structures to PI structures. The ECM of both reflectors have also been developed. Although UWB reflector offers rejection of normally incident EM waves over UWB frequency range, it exhibits non-AS and non-PI behaviour under oblique EM incidence. The efficacy of UWB reflector towards compact antenna applications, a Norman window slot antenna is then united with the UWB reflector. Moreover, tessellated rhombic loop based PD reflector is also introduced in this chapter. The detailed assessment of TSL based reflector is described in chapter 5. The TSL based WB reflector is also integrated with a hexagonal UWB slot antenna. The hexagonal slot antenna is created by slight modifications to Norman window slot and rest of antenna features remain intact. Integrating hexagonal slot antenna with TSL reflector also provide antenna gain enhancement in boresight direction.

4.1 Introduction

SL FSSs have been extensively utilized in integration with low-profile antennas, serving as reflecting surfaces and superstrates, to achieve improved directivity and impedance BW [99]. Recently, researchers have also focused on design of UWB FSS reflectors, which are highly relevant for wireless applications as mentioned earlier. A research study introduced a UWB stopband FSS with convoluted elements [119]. However, this particular FSS exhibited weak rejection of EM incidence around 8 GHz under both TE and TM modes. Additionally, another study presented a UWB FSS that combined SL and cross unit elements [120]. The utilization of UWB reflectors holds promise in improving the performance of compact UWB antennas. For instance, an SL FSS, comprising vertical and horizontal gratings with different widths, demonstrated distinct transmission responses under TE and TM incidences [46]. This FSS, being an AMC, when applied beneath the direct fed hexagonal UWB antenna, enhanced the antenna's gain [46]. Similarly, another UWB FSS, consisting of three vertical strips made of metal interconnected by a pair rectangles, has been employed to boost the UWB antenna gain [121]. To ensure optimal performance as a reflector, an FSS should maintain its band reject properties even under oblique incidences, with PI and linearity in reflection phase being desirable traits.

4.2 Rectangular loop pair (RLP) FSS unit cell design

RLP based FSS unit cell structures are displayed in Figure 4.1. The unit elements are patterned on 1.57 mm thick FR4 substrate. Earlier in chapter 2, the rectangular loops PD and PI arrays have been discussed. The RLP based unit structures are further modified by inserting an inner rectangular loop concentrically with the outer rectangular loop. When such unit elements are oriented in a square lattice, they create vertical rectangular loop pair (VRL) as shown in Figure 4.1 (a). On rotating VRLP by 90°, the orthogonal PD array, i.e., horizontal rectangular loop pair (HRLP)

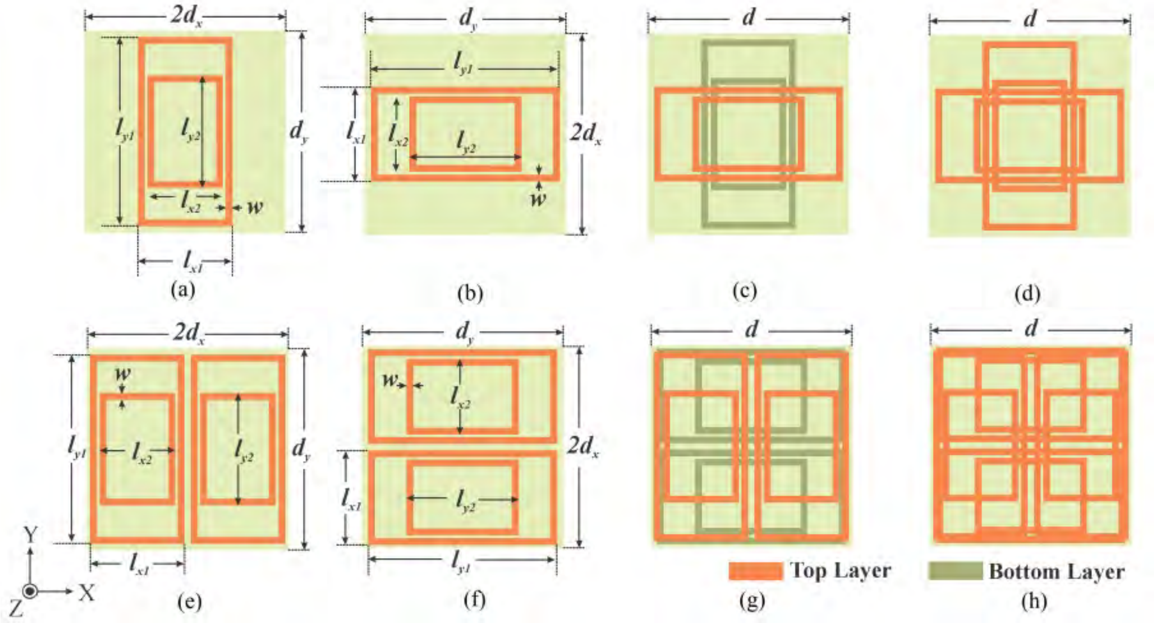

Figure 4.1: Unit elements of RLP FSS (a) VRLP, (b) HRLP, (c) BTB RLP, (d) MRLP (e) VDRLP, (f) HDRLP, (g) BTB DRLP and (h) MDRLP

Table 4.1: Design parameters of RLP FSS

Parameter	Value (mm)	Parameter	Value (mm)
d_x	7.83	l_{y1}	14.67
d_y	15.67	l_{y2}	8.72
l_{x1}	7.33	w	0.5
l_{x2}	5.86	d	15.67

is constituted as appear in Figure 4.1 (b). Printing these orthogonal arrays once on opposite sides and then on one side of the substrate, results BTB RLP and MRLP unit structures as illustrated in Figure 4.1 (c) and (d). The dimensional features of these FSS unit structures are provided in Table 4.1.

Incorporating boundary conditions and Floquet ports as descried in earlier chapters, the exhaustive simulations are performed using full wave EM solver available with CST MWS. The propagation features of VRLP unit structure are displayed in Figure 4.2 (a). VRLP FSS demonstrates the dual band characteristics with dissimilar $|S_{21}|$, $|S_{11}|$ and $\angle S_{11}$ when exposed to normally incident orthogonally polarized EM waves. The dual band phenomena appears due to two concentric rectangular loops. Thus, VRLP is PD by nature which demonstrates two transmission null frequencies f_{z1} and f_{z2} alongwith one transmission pole frequency f_p located in between them.

A dual-stopband phenomena is observed owing to pair of two rectangular loops present in the VRLP unit cell.

The lower resonance frequency, f_{z1} of RLP based PD FSS for impinging EM wave of specific polarized state is dependent on the larger dimension of the exterior rectangular loop which is approximately $\lambda_{0/4}$, where λ_0 is the free space wavelength at f_{z1}. Therefore, $\lambda_{0/4}$ can serve as the preliminary dimension prior to numerically optimized performance. In addition, important geometric parameters for FSSs, such as structural profile, width of loop, and periodicity can be altered to obtain a suitable frequency operation [9], [122], [15], [123].

The frequencies, f_{z1} and f_{z2} are the nulls of the stopbands in Figure 4.2 (a), where $f_{z2} > f_{z1}$ and f_p is the centre frequency of the passband. As shown in Figure 4.2 (a), frequencies f_{l1} and f_{l2} represent the lower cut-off or corner frequencies of transmission coefficients plot where $|S_{21}|$ =-10dB. As mentioned, f_p lies in between f_{z1} and f_{z2} when VRLP is exposed to normal TE incidence but difference in Both f_{z1} and f_{z2} expends for normal TM mode hitting on VRLP. Moreover, the phase of reflection of VRLP FSS under normal incidence (TE) exhibits linearity while these linearities in reflection phase are restricted to the pass band around its transmission band when VRLP is illuminated by normally incident TM waves. In addition, the distinct $|S_{11}|$ curves for normal TE and TM incidences corresponds to non-uniform reflections of EM waves from the VRLP FSS as observed from Figure 4.2(a).

Rotating VRLP unit element by 90° transform it to a PD HRLP unit element, as displayed in Figure 4.1 (b), as a result, swapping TE and TM responses as demonstrated for VRLP FSS to obtain TM and TE response of HRLP FSS respectively, as also reported in reference [35].

The propagation characteristics of BTB RLP FSS are displayed in Figure 4.2 (b). BTB RLP predominantly exhibits dual band reject feature with similar $|S_{21}|$ response under TE and TM incidence. Such dual band reject feature with similar $|S_{21}|$ is probably due to superposition of transmission responses of both orthogonal RLP layers. However, the $|S_{11}|$ stay dissimilar with respect to frequency which suggests the non-uniformity in reflection of incident EM energy from the surface of BTB RLP FSS. Also, the reflection phase, $\angle S_{11}$ indicates the non-linearity noticeable around frequency f_p under both normal TE and TM incidence. Table 4.2 displays the detailed propagation characteristics of VRLP, HRLP, and BTB RLP FSSs.

To customize performance parameters such as stopband frequency, BW of stopband and level of signal rejection for such PD arrays, the periodicity of unit elements along the axis parallel to their larger dimension becomes prominent. As RLP unit elements are brought closer to each other, the coupling between adjacent edges increases. Consequently, an expansion in BW of stopband under normal TE and TM

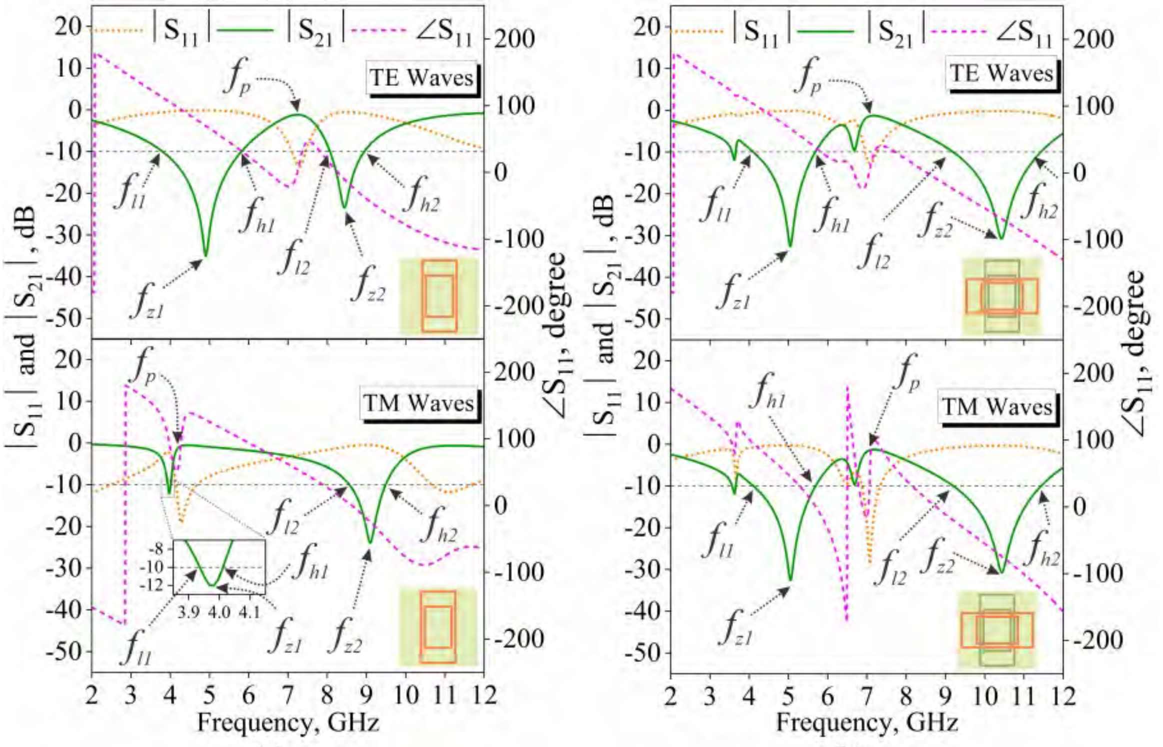

(a) (b)

Figure 4.2: Transmission and reflection response of VRLP and BTBRLP FSSs

Table 4.2: Simulated propagation characteristics of VRLP, HRLP and BTB RLP FSSs

<table>
<tr><td colspan="10">TE waves (Normal incidence)</td></tr>
<tr><td>Unit Cell</td><td>f_{z1}(GHz)</td><td>f_{l1}(GHz)</td><td>f_{h1}(GHz)</td><td>BW (GHz)</td><td>f_p(GHz)</td><td>f_{z2}(GHz)</td><td>f_{l2}(GHz)</td><td>f_{h2}(GHz)</td><td>BW (GHz)</td></tr>
<tr><td>VRLP</td><td>4.90</td><td>3.80</td><td>5.82</td><td>2.02</td><td>7.25</td><td>8.43</td><td>8.06</td><td>8.94</td><td>0.88</td></tr>
<tr><td>HRLP</td><td>3.98</td><td>3.93</td><td>4.01</td><td>0.08</td><td>4.40</td><td>9.10</td><td>8.56</td><td>9.94</td><td>1.38</td></tr>
<tr><td>BTB RLP</td><td>5.04</td><td>4.07</td><td>5.76</td><td>1.69</td><td>7.16</td><td>10.43</td><td>9.19</td><td>11.44</td><td>2.25</td></tr>
<tr><td colspan="10">TM waves (Normal incidence)</td></tr>
<tr><td>VRLP</td><td>3.98</td><td>3.93</td><td>4.01</td><td>0.08</td><td>4.40</td><td>9.10</td><td>8.56</td><td>9.49</td><td>1.38</td></tr>
<tr><td>HRLP</td><td>4.90</td><td>3.80</td><td>5.82</td><td>2.02</td><td>7.25</td><td>8.43</td><td>8.06</td><td>8.94</td><td>0.88</td></tr>
<tr><td>BTB RLP</td><td>5.04</td><td>4.07</td><td>5.76</td><td>1.69</td><td>7.16</td><td>10.43</td><td>9.19</td><td>11.44</td><td>2.25</td></tr>
</table>

incidences is observed.

Further, two unit cells of VRLP FSS are subsequently paired together by keeping them 0.5 mm apart to create vertical dual rectangular loop pair (VDRLP) unit structure. Thus, VDRLP comprises an array of RLPs that are arranged in a rectangular lattice. HDRLP is then formed by rotating VDRLP by 90° in its plane. Similar to BTB RLP, the FSS unit structure of BTB DRLP is evolved by printing both orthogonal DRLPs on opposite sides of the substrate. Figures 4.1(e), 4.1(f), and 4.1(g) depict the unit element geometries for each of the three FSSs. The gap between adjacent RLPs in DRLP array is maintained in such a way that the feature of the substrate for both RLP FSSs and DRLP FSSs stay unchanged. In other words, the periodicity of VDRLP, if defined in a ratio along Y-axis to that along X-axis comes out to be 2:1 while the periodicity of HDRLP can be better defined as the reciprocal of the ratio, i.e., 1:2.

As depicted in Figure 4.3 (a), VDRLP also exhibits dual stopband behaviour with dissimilar $|S_{21}|$, $|S_{11}|$ and $\angle S_{11}$ when exposed to normally incident TM and TE waves. From propagation characteristics, it is anticipated that f_{z1} and f_{z2} appear due to exterior and interior rectangular loops respectively. For VDRLP array, the vertical edges of loops being greater than the horizontal edges, thus, the transmission zero and pole frequencies for TE mode are greater than those for TM mode. Moreover, f_{z1} for TE incidence and f_p for TM mode are very near to one another at 4.93 GHz and 4.44 GHz, respectively. Likewise, f_{z2} for TM incidence is nearly equivalent to f_p for TE incidence. Similarly to VRLP FSS, the $|S_{11}|$ on VDRLP FSS for TE and TM modes, as shown in Figure 4.3 (a), do not overlap at the centre and corner edge frequencies. This disparity between $|S_{11}|$ for TE and TM modes indicates non-uniform reflections.

The presence of pole frequency is due to two distant zero frequencies appearing due to presence of a pair of loops in the unit element of VDRLP. The gap between horizontal gratings and vertical gratings of a RLP is different which leads to different

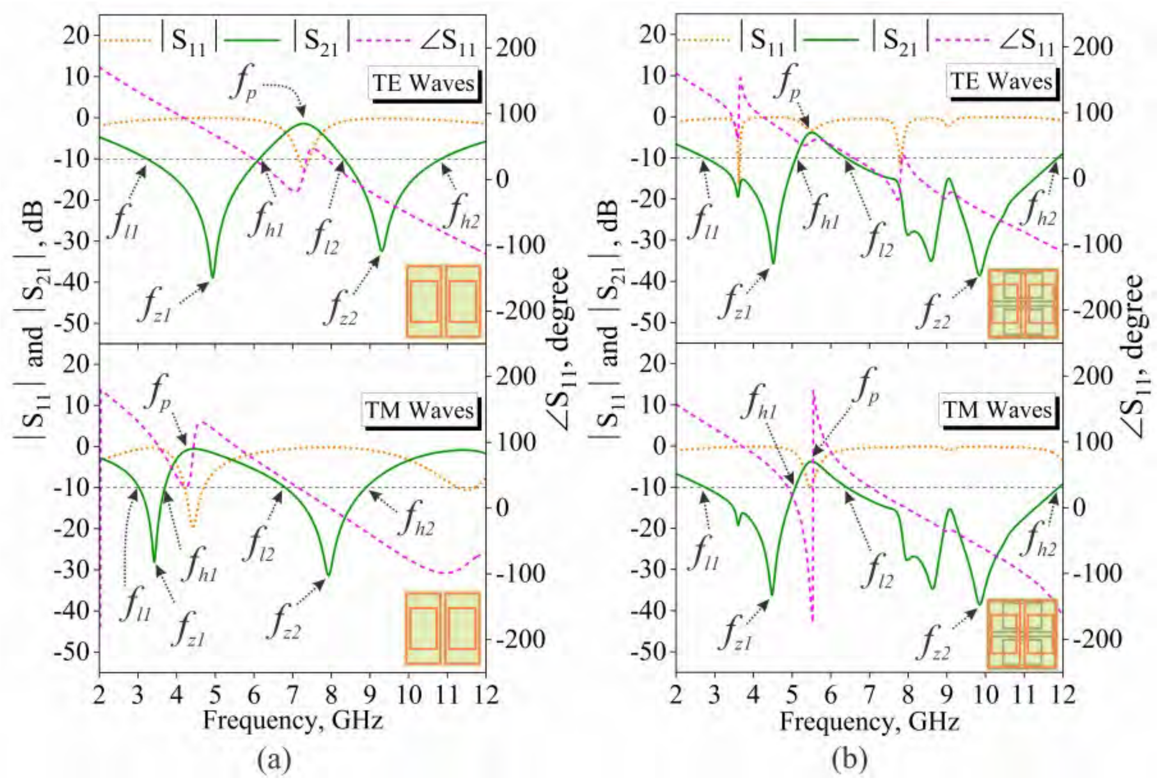

Figure 4.3: Propagation characteristics of VDRLP and BTB DRLP FSSs

TE and TM behaviour. All frequencies f_{z1}, f_{z2} and f_p have lower values in TM mode than that of TE mode although horizontal edges of RLP are smaller than the vertical edges. The difference of gap at horizontal edges of RLP is larger than at vertical edges which is why f_{z1}, f_{z2} and f_p appear at lower values in TM mode for VDRLP unit cell.

On rotating 90°, VDRLP unit structure turns into HDRLP FSS arrays with identical but swapped transmission zero and pole frequencies with VDRLP propagation characteristics under normal TM and TE incidences. Similar to single RLP arrays, both VDRLP and HDRLP are also PD by nature. Although the PD arrays of VDRLP or HDRLP can further be modified and optimized to function as a PSS. The emphasis of current discussion is devoted to produce WB and UWB reflecting surfaces with linear reflection phase. Figure 4.1 (g) follows the simple technique as discussed earlier in chapter 2 and 3, to achieve wide stopband with overlapping $|S_{21}|$ for TE and TM mode. By putting both DRLP based orthogonal arrays on opposite sides of the dielectric substrate to form a BTB DRL FSS unit structure, prescribed propagation characteristics are attained as displayed in Figure 4.3 (b).

Similar to BTB RLP array, BTB DRLP also exhibits multiband characteristics but with wider BWs due to multiple stopbands when compared with BTB RLP array. The transmission respose of BTB DRLP appears as a probable consequence

Table 4.3: Simulated propagation characteristics of VDRLP , HDRLP and BTB DRLP FSSs

TE									
Unit Cell	f_{z1} (GHz)	f_{l1} (GHz)	f_{h1} (GHz)	BW(GHz)	f_p (GHz)	f_{z2} (GHz)	f_{l2} (GHz)	f_{h2} (GHz)	BW(GHz)
VDRLP	4.93	3.22	6.13	2.91	7.28	9.30	8.32	10.85	2.53
HDRLP	3.39	3.10	3.65	0.55	4.44	7.88	6.70	8.91	2.21
BTB DRLP	4.48	2.74	5.09	2.35	5.51	9.85	6.38	11.92	5.54
TM									
VDRLP	3.39	3.10	3.65	0.55	4.44	7.88	6.70	8.91	2.21
HDRLP	4.93	3.22	6.13	2.91	7.28	9.30	8.32	10.85	2.53
BTB DRLP	4.48	2.74	5.09	2.35	5.51	9.85	6.38	11.92	5.54

of superposition of transmission responses as demonstrated by VDRLP and HDRLP arrays under normal incidences of EM waves with particular polarization (TE/TM) state. A small deviation in frequencies (f_{z1} and f_{z2}) is due to perturbation caused by commercially available dielectric material of substrate. Moreover, the dissimilarities in $|S_{21}|$ and $\angle S_{11}$ under normal TM/TE incidences, are predominantly caused by non-homogeneity in the dielectric substrate. Also, the non-linearities in phase of reflection from BTB DRL FSS persist similarly to BTB RLP FSS. The comparison of DRLP FSS transmission properties is presented in Table 4.3.

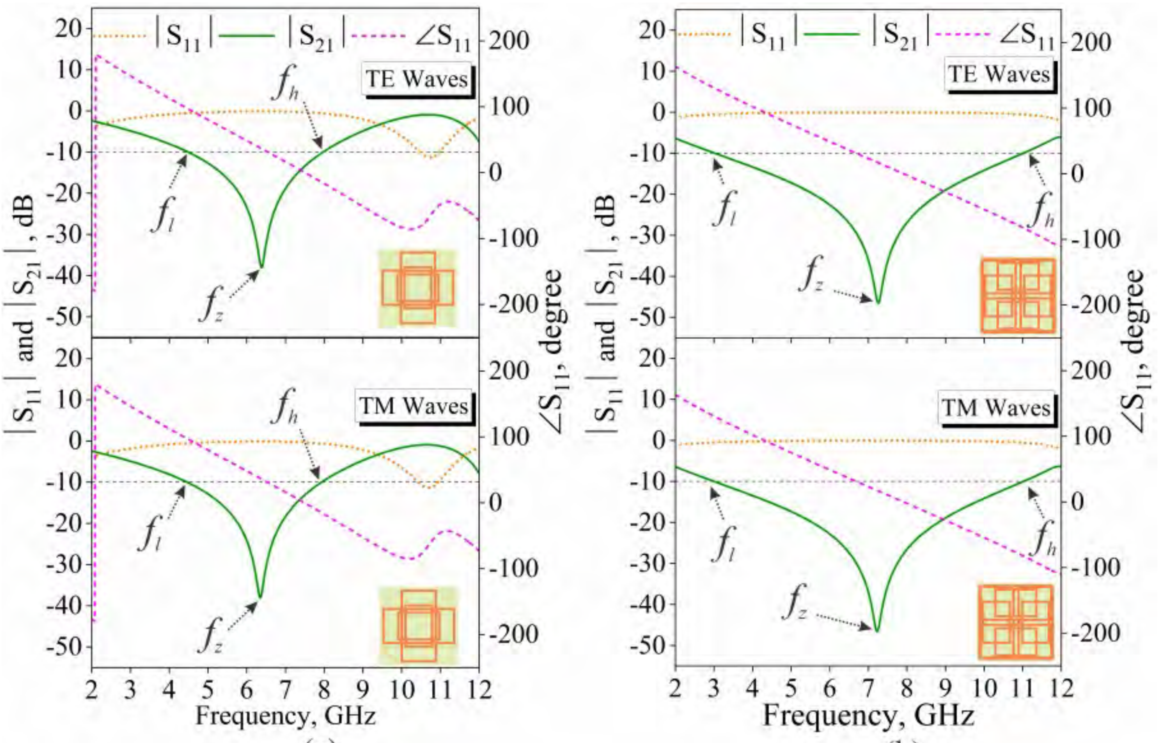

(a) (b)

Figure 4.4: Propagation characteristics of MRLP and MDRLP FSSs

The linearity in phase of reflection indicates a uniform reflection of incident EM

Table 4.4: Simulated propagation characteristics of MRLP FSS and MDRLP FSS

Unit Cell	TE				TM			
	f_z(GHz)	f_l(GHz)	f_h(GHz)	BW(GHz)	f_z(GHz)	f_l(GHz)	f_h(GHz)	BW(GHz)
MRLP	6.38	4.46	7.97	3.51	6.38	4.46	7.97	3.51
MDRLP	7.26	2.99	11.03	8.04	7.26	2.99	11.06	8.04

energy from any reflecting surface. Both orthogonal RLP patterns are therefore developed on one of the sides of dielectric laminate to yield the MRLP unit structure. Similarly, MDRLP is formed by merging both VDRLP and HDRLP FSSs over dielectric substrate. Both unit element geometries of MRLP and MDRLP reflectors are illustrated in Figures 4.1 (d) and 4.1 (h) respectively.

Both the MRLP and MDRLP FSS transmission properties are depicted in Figure 4.4 (a) and (b), respectively. Both FSSs have a broader stopband with a single transmission zero frequency (f_z) under normal incidence and are PI because of their axial symmetry. Table 4.4 summarizes transmission characteristics of MDRLP and MRLP FSS arrays. It is found that the BW provided by MDRLP FSS is 4.53 GHz greater than that of MRLP FSS. Additionally, the reflection phase of both FSSs is linear over the entire stopband. The following section describes the equivalent circuit modelling (ECM) for both RLP and DRLP based reflector arrays.

4.3 ECM for RLP and DRLP based reflectors

Under normal incidences, the metal layer can be modeled by incorporating a series connection of two inductances (L_{A1} and L_{A2}) along with two resistors (R_{A1} and R_{A2}) respectively. The capacitances C_{A1} and C_{A1} represent the gaps between two rectangular loops. The capacitances, C_{A1} and C_{A2} are connected respectively in parallel and in series with inductors L_{A1} and L_{A2}. Also, the capacitance 'C_{A3}' is incorporated to account for the reflections of EM incident energy as demonstrated in Figure 4.5.

Table 4.5: Circuit model components values for VRLP, HRLP, VDRLP and HDRLP FSSs

Components	VRLP	HRLP	VDRLP	HDRLP
L_{A1} (nH)	3.557	5.027	2.328	5.274
L_{A2} (nH)	2.568	6.468	1.938	4.876
C_{A1} (pF)	0.11494	0.03798	0.17289	0.14893
C_{A2} (pF)	0.13794	0.2049	0.14394	0.22089
C_{A3} (pF)	0.09596	0.03	0.13496	0.006
R_{A1} (Ω)	3.5388	16.5045	1.8094	5.7081
R_{A2} (Ω)	1.4396	2.1093	2.489	0.9097
L_S (nH)	5.6044	5.6044	9.001	9.001
C_S (pF)	0.02096	0.02096	0.09982	0.09982
R_S (Ω)	4.0099	4.0099	4.0099	4.0099

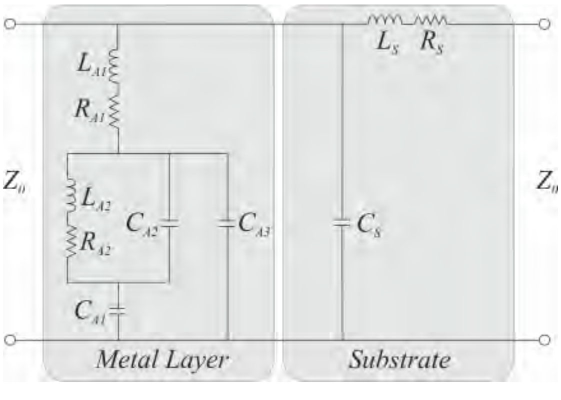

Figure 4.5: Circuit model for VRLP, HRLP, VDRLP and HDRLP FSSs

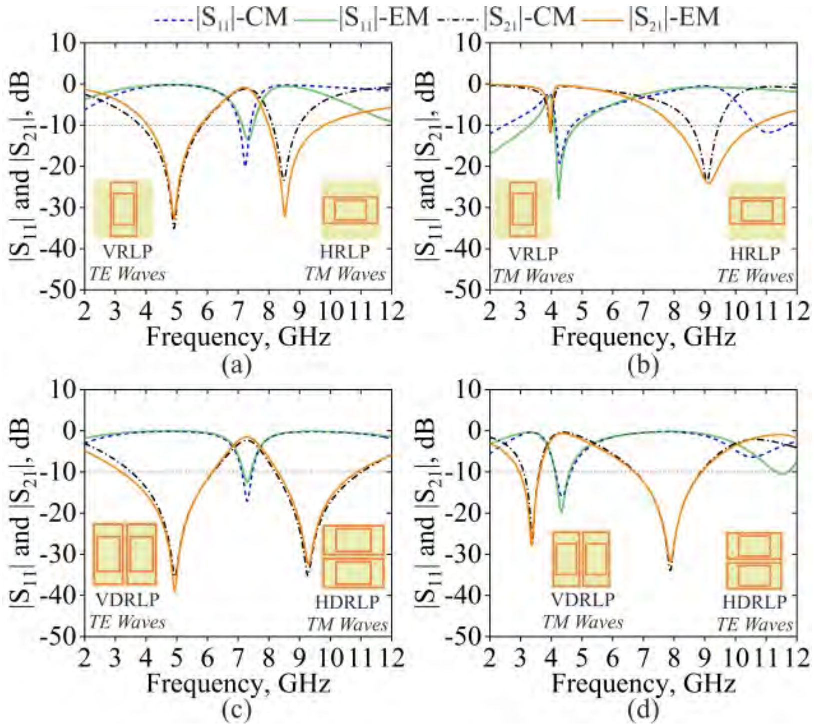

Figure 4.6: Transmission and reflection responses of PD FSSs compared after EM and CM simulations (Unit cells and EM polarization mode marked in inset

The components L_S and C_S respectively account for the dielectric substrate as also suggested in reference [102]. In addition, the losses in the dielectric material of the substrate are represented by R_S, connected to L_S in series as depicted in Figure 4.5. Here, the respective values of inductances and capacitances are predicted through the expressions as available in references [124], [125]. The values of respective components of the circuit models representing RLP and DRLP based PD arrays are mentioned in Table 4.5. The bases of variation in values of L_S and C_S for RLP and DRLP based PD arrays are pattern on metal layers and coupling between adjacent RLPs. Figure 4.6 demonstrates the comparison of the propagation characteristics, i.e., $|S_{21}|$ and $|S_{11}|$ for RLP and DRLP based PD arrays that are obtained through CM a with those obtained through full wave EM simulations.

Further, CM for both BTB RLP and DRLP arrays are illustrated in Figure 4.7 (a) where the equivalent models representing metallic and dielectric layers are connected as layer #1 (metal)-Substrate-layer #2 (metal) as displayed in Figure 4.7 (a). Similarly, both MRLP and MDRLP FSS arrays can equivalently be modeled as layer #1 (metal)-layer #2 (metal)-Substrate as illustrated in Figure 4.7(b). Table 4.6 provides the respective optimal circuit component values for BTB RLP and DRLP based arrays and MRLP and MDRLP arrays. The deviations in the values of L_S, C_S and R_S for MRLP and MDRLP arrays noticed here are due to merged metallic patterns, coupling between adjacent RLPs and dielectric losses of the substrate.

Table 4.6: Component values for BTBRLP, MRLP, BTBDRLP and MDRLP FSSs

Components	BTBRLP	MRLP	BTBDRLP	MDRLP
L_{A1} (nH)	2.067	1.958	6.776	2.539
L_{A2} (nH)	3.543	1.882	3.354	1.024
C_{A1} (pF)	0.13294	0.14094	0.04899	0.05099
C_{A2} (pF)	0.083	0.045	0.09196	0.10595
C_{A3} (pF)	0.09599	0.04096	0.12195	0.12795
R_{A1} (Ω)	4.7985	0.3099	2.4092	2.1093
R_{A2} (Ω)	6.3079	3.9889	5.7081	3.9082
L_{B1} (nH)	13.234	13.74	2.289	5.12
L_{B2} (nH)	3.612	3.682	5.075	13.234
C_{B1} (pF)	0.010194	0.001	0.16092	0.01997
C_{B2} (pF)	0.2119	0.1519	0.22089	0.27985
C_{B3} (pF)	0.004	0.011	0.06897	0.07493
R_{B1} (Ω)	24.9017	22.8024	3.3089	3.009
R_{B2} (Ω)	6.3079	9.6068	3.3089	15.9047
L_S (nH)	2.008	3.3268	5.6044	9.001
C_S (pF)	0.12575	0.05292	0.12575	0.07684
R_S (Ω)	4.0099	285.6029	4.0099	308.0023

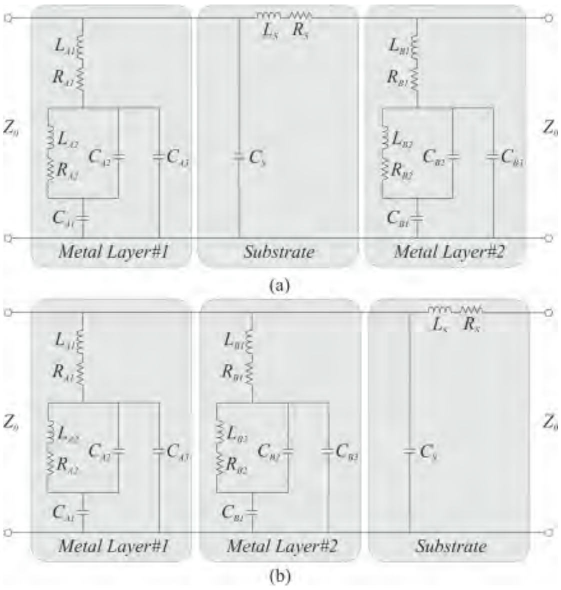

Figure 4.7: Circuit models for (a) BTB Type FSS, (b) Merged type FSSs

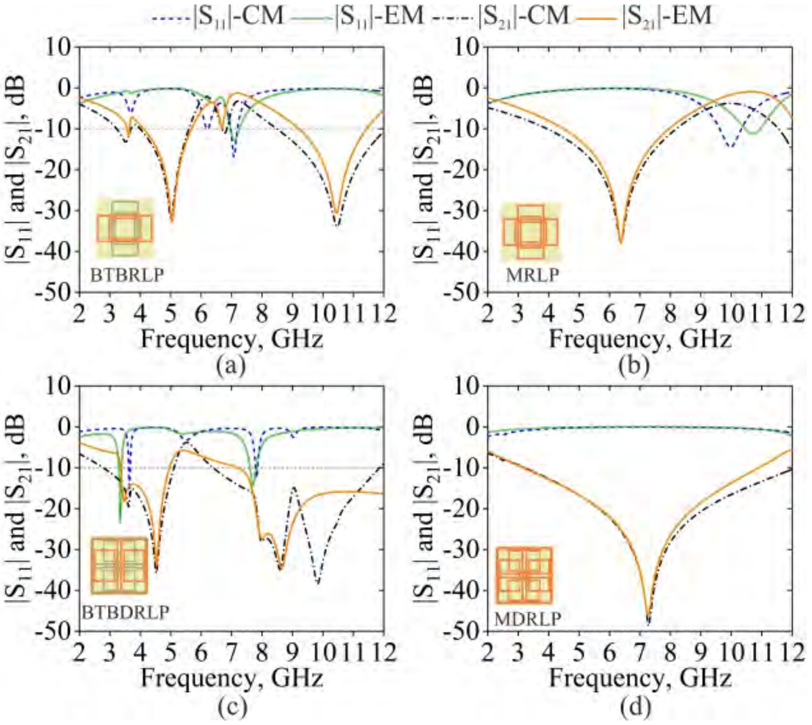

Figure 4.8: Transmission and reflection responses of BTB and merged FSSs compared after EM and CM simulations (Unit cells displayed in inset

The CMs of FSSs comparatively thus, fairly follow the EM simulations up to a decent extent. In the section ahead, the performance of single side printed RLP and DRLP based reflectors, i.e., MRLP and MDRLP, are further examined through experiments.

4.4 RLP FSS development and measurements

RLP FSS development involves the conventional technique of PCB fabrication to create a 13×13 array of MRLP and MDRLP FSSs on an FR-4 substrate for practical validation. Figure 4.9 illustrates the placement of these FSSs on a rotatory mount positioned in the middle of two standard UWB horn antennas, which are placed facing opposite to each other but set apart by a Fraunhoffer-farfield distance along the Z-axis. To establish connections, coaxial cables are used to link the two ports of a VNA to both the transmitting and receiving horn antennas. Initially, the UWB horn antennas are aligned for TE mode, and the S-parameters are captured following the methodology described in chapter 3. Similarly, to determine the S-parameters of FUTs for TM mode, both types of FSSs are rotated by 90° along the Z-axis during measurements.

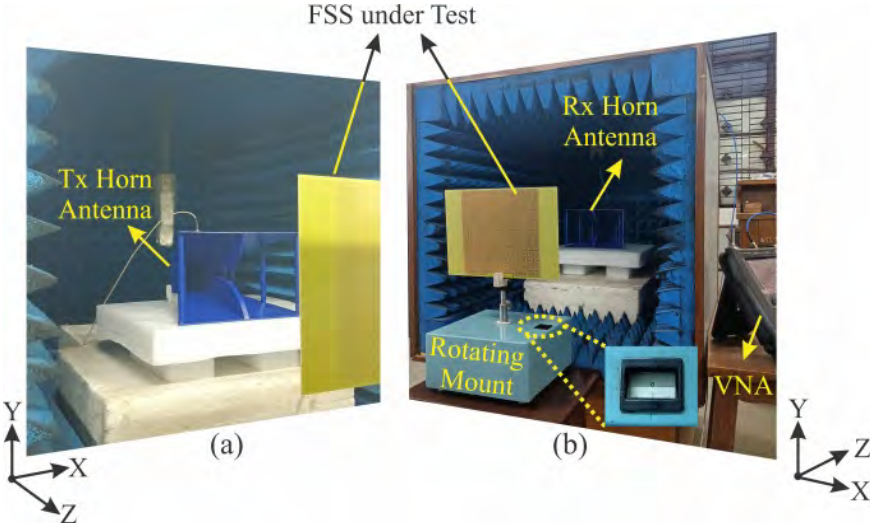

Figure 4.9: Measurement setup

Under normal incidence, the $|S_{21}|$ responses for both MRLP and MDRLP reflectors obtained through experiments are compared with those observed during simulations and presented in Figure 4.10 and Table 4.7 respectively.

Table 4.7: Simulated and experimentally measured responses of MRLP FSS and MDRLP FSS

Unit Cell	For TE Incidence				For TM Incidence			
	f_z(GHz)	f_l(GHz)	f_h(GHz)	BW(GHz)	f_z(GHz)	f_l(GHz)	f_h(GHz)	BW(GHz)
MRLP(Simulated)	6.38	4.46	7.97	3.51	6.38	4.46	7.97	3.51
MRLP(Measured)	6.37	4.5	8.4	3.9	6.3	4.0	7.98	3.98
MDRLP(Simulated)	7.26	2.99	11.03	8.04	7.26	2.99	11.03	8.04
MDRLP(Measured)	7.20	2.33	11.54	9.21	7.26	2.54	11.57	9.03

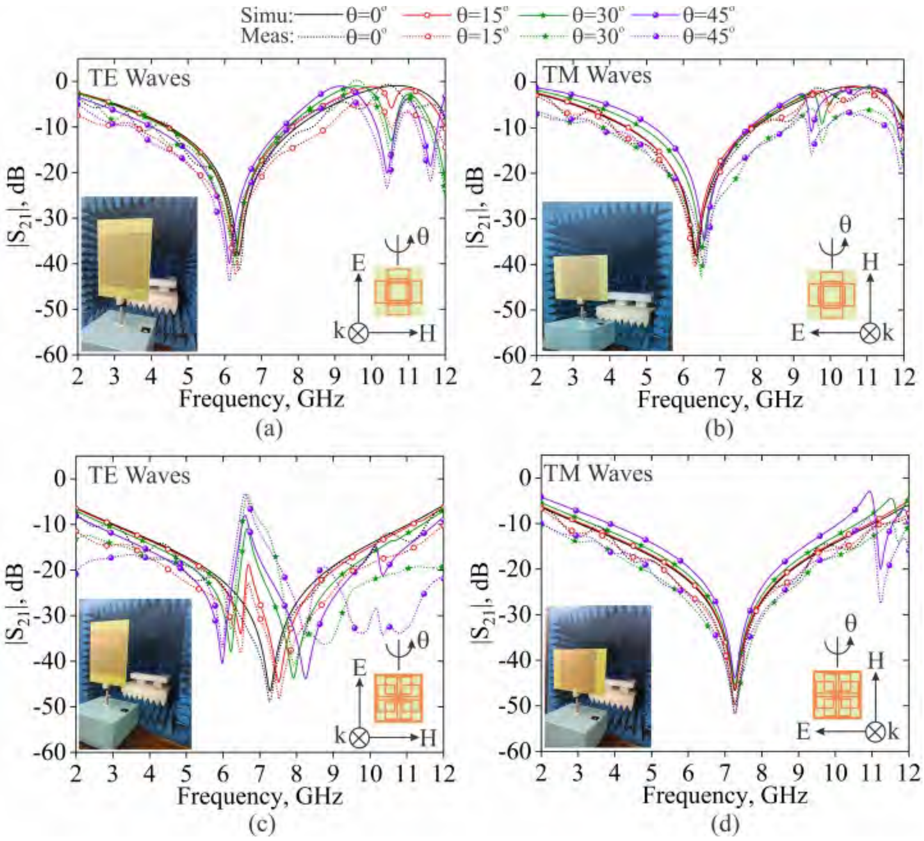

Figure 4.10: Simulated and measured ($|S_{21}|$) dB under normal and oblique incidences: (a) MRLP (TE), (b) MRLP (TM), (c) MDRLP (TE) and (d) MDRLP (TM)

The MDRLP FSS prototype offers a stopband that covers more than a UWB from 2.3 GHz to 11.6 GHz when TM and TE waves strike at normal. Thus, MDRLP exhibits 5 GHz wider stopband compared to that of MRLP FSS. Later, experiments to record transmission characteristics of these FSSs under oblique incidences from normal to 45° with angular step of 15° are presented. Figure 4.10 compares the experimental and simulated values of $|S_{21}|$ under oblique incidences for MRLP and MDRLP FSSs.

The MRLP FSS exhibits broad rejection across the C-band frequency range and appears to be a PI FSS. It is suitable for both antenna applications and shielding purposes. Contrarily, MDRLP FSSs demonstrate rejection in the UWB band when incident at a normal angle, along with linear phase reflection characteristics, although they lack the benefits of PI. Furthermore, MDRLP arrays are united with UWB slot antenna for the purpose of gain enhancement, as described in subsequent sections. Table 4.8 provides a comparison of both the FSSs with current literature.

Based on the comparison, MRLP and MDRLP are cost-effective reflectors suitable for UWB and wideband applications, exhibiting linearity in their reflection phase. The PI nature of MRLP FSS makes it appropriate for wideband shielding applications.

Table 4.8: Merged RLP based FSSs compared with alike FSSs reported in literature

Ref.	Dimensions (mm^3)	FSS Type	-10dB Stopband (GHz)	Fractional Band width (FBW), %	Max. Attenuation (dB)	Reflection Phase	Polarization Independance	Angular stability	Application
[126]	17 × 17 × 11.7	Double layer, double sided	4-12	100	64.5	Linear	Not mentioned	Not mentioned	Reflector for antenna
[127]	12 × 12 × 32	Double layer, double sided	6.5-14	73.17	58.3	Non-linear	Yes	45°:TE, TM	EM shielding
[128]	11 × 11 × 1.6	Single layer, single sided	2.6-11.1	124.08	49	Linear	Not mentioned	Not mentioned	Reflector for antenna
[129]	9 × 9 × 0.8	Single layer, single sided	4.85-17.23	112.137	48	Not mentioned	Yes	30°:TE, TM	EM shielding
[120]	16 × 16 × 1.5	Single layer, single sided	2.16-10	128.947	54	Linear	Yes	45°:TE	Reflector for antenna
[119]	10 × 10 × 1.6	Single layer, double sided	3.1-13.3	124.39	40.4	Not mentioned	Yes	45°:TE, TM	EM shielding
Prop. MRLP	15.67 × 15.67 × 1.57	Single layer, single sided	4.5-8.4	60.465	41.5	Linear	Yes	45°:TE, TM	EM shielding
Prop. MDRLP	15.67 × 15.67 × 1.57	Single layer, single sided	2.3-11.5	133.33	50	Linear	No	45°:TM	Reflector for antenna

Based on the comparison, MRLP and MDRLP are cost-effective reflectors suitable for UWB and wideband applications, exhibiting linear reflection phase characteristics. The MRLP FSS, with its PI nature, is well-suited for wideband shielding purposes. On the other hand, the MDRLP FSS has the capability to reflect EM waves over UWB frequency range. Additionally, both FSSs are expected to serve as reflectors when united with compact antennas thereby enhancing their gain along bore sight direction.

This work offers the advantage of utilizing the array of simple double rectangular loop in various configurations to serve as a dual stopband PD FSS, a linear phase WB and UWB reflector. These functionalities are achieved by adjusting the periodicity and orientation of the array, printing the PD arrays on opposite sides of a dielectric substrate, and combining them on one of the sides of the substrate, respectively.

4.5 RLP based FSR integrated with UWB Norman window slot antenna

A slot antenna with a Norman window shape radiating is proposed within UWB here. It is excited by a sectoral feed and exhibits sustained bidirectional radiation across the entire UWB. To further enhance its performance, the slot antenna is modified by integrating a UWB MDRLP reflector . The impact of the MDRLP reflector on the antenna's S-parameters and radiation patterns is investigated by employing the reflector first beneath the slot and then beneath the feed plane. The reflection coefficient, $|S_{11}|$ and gain in antenna boresight (θ=0°) are analyzed after ensuring appropriate separation between the antenna and FSS. The antenna is then fabricated, and experiments are conducted.

4.5.1 Evolution of UWB slot antenna

The geometry of Norman window slot antenna with its physical features is depicted in Figure 4.11. The schematic of the slot antenna is constructed using a1.57 mm thick copper cladded FR-4 laminate. A norman window shaped slot is created into the ground plane, and this slot is then excited by a sectoral feed. The shape of the slot is selected upon in order to achieve a wideband operation [130], [131], which is further modified by including a rectangular notch slot at the center of the base of Norman window shape in order to anticipate a broader frequency band.

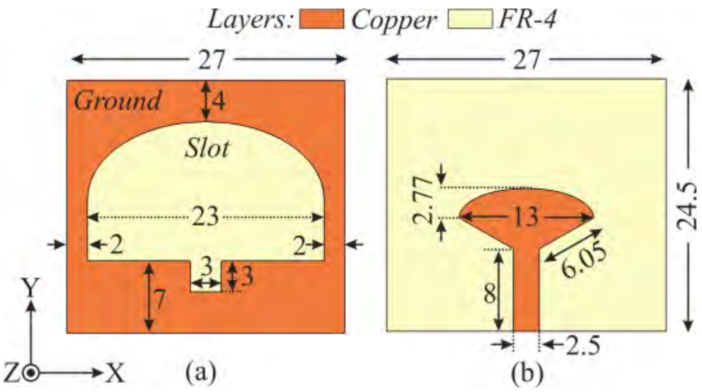

Figure 4.11: Features of Norman window slot antenna (a) Top View, (b) Bottom View (all dimensions are in mm

Table 4.9 describes the stages of evolution of the slot antenna design. The antenna design has evolved from a wide rectangular slot antenna with a microstrip line feed to the slot antenna shown in the Figure 4.11. Antenna at stage #1 resembles the one described in reference [132], but it is more compact and operates in two distinct frequency bands: 6.16 to 7.13 GHz and 9.54 to 11.54 GHz. The rectangular slot

Table 4.9: Evolution of proposed UWB slot antenna

Step	Description	Antenna Geometry (Top view: Left, Bottom View: Right)	Results
#1	Design of wide rectangular slot antenna fed by microstrip line	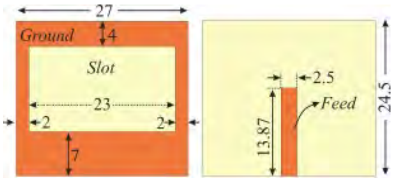	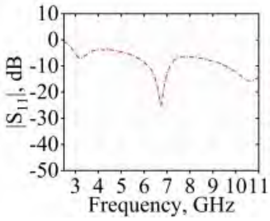
#2	Transforming the rectangular slot into a Norman window slot	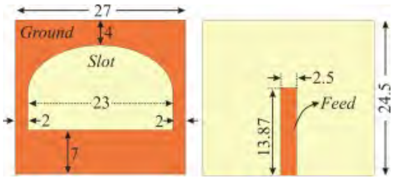	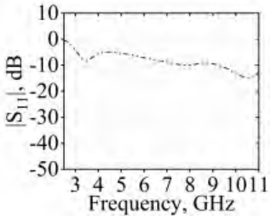
#3	Loading the microstrip line feed with a rectangular shaped tuning stub	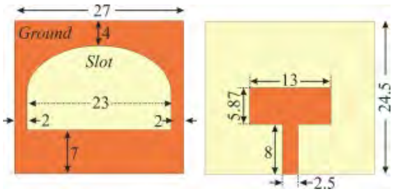	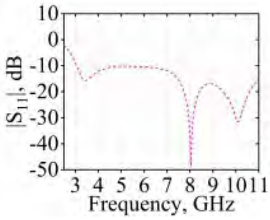
#4	Transforming rectangular tuning stub into sectoral feed	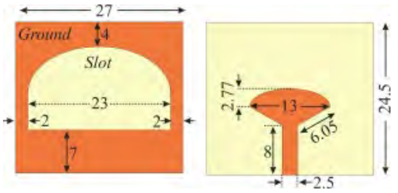	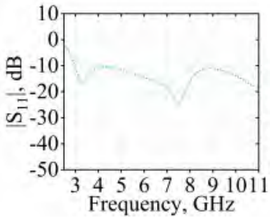
#5	Introducing a square slot in Norman window slot	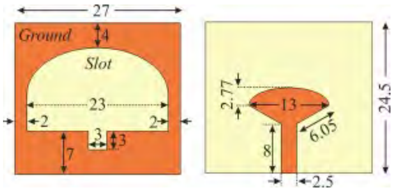	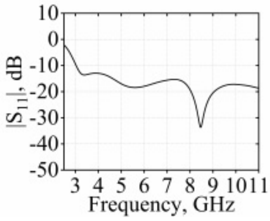

is subsequently transformed into a Norman window slot, which displays progressive changes in antenna impedance across a wider frequency range. In order to further improve impedance matching, a rectangular stub is added to the microstrip feed while maintaining the same feed length, as suggested by reference [133]. Later, a sectoral feed replaces the rectangular stub to optimize matching of impedance across the entire UWB spectrum. An additional square notch slot is added opposite the microstrip line input to modify the Norman window slot, which enhances impedance matching throughout the entire UWB spectrum.

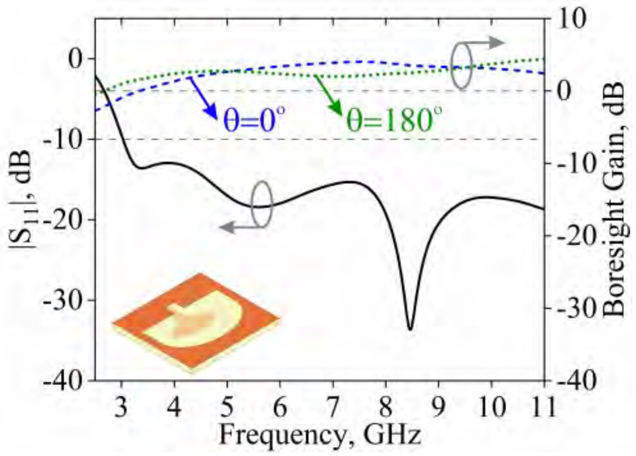

Figure 4.12: Simulated $|S_{11}|$ and antenna gain along zenith and nadir

The simulations suggest that the antenna operates in UWB spectrum. As a bidirectional radiator, the antenna radiates along the Z-axis in both zenith (at θ=0°) and nadir (at θ=180°). Figure 4.12 depicts the antenna gain in both the zenith and nadir directions. The antenna provides an average gain of 2.86 dB at θ=0° and 2.57 dB at θ=0° when evaluated over the whole UWB spectrum. A peak gain of 4 dB along the zenith and 4.18 dB along the nadir is noticed at 7.5 GHz and 10.6 GHz, respectively. Figure 4.13 depicts the antenna radiation pattern obtained through simulations at respective frequencies of 3.1, 4.5, 6, 7.5, 9, and 10.6 GHz where major and back lobe can be seen in the principal X-Z and Y-Z planes. The slot antenna demonstrates a stable bidirectional radiation pattern. By integrating the Norman window slot antenna with a UWB reflector, a directional radiation pattern can be expected.

4.5.2 Design of frequency selective reflector

The unit cell design of MDRLP UWB reflector has already been explored earlier sections in this chapter. The propagation characteristics of MDRLP FSS are again summarized in Figure 4.14

Based on previous sections in chapter 4, it has been established that the proposed MDRLP FSS displays UWB stopband. Additionally, the MDRLP demonstrates a linear reflection phase throughout the entire stopband. The linear nature of the reflection

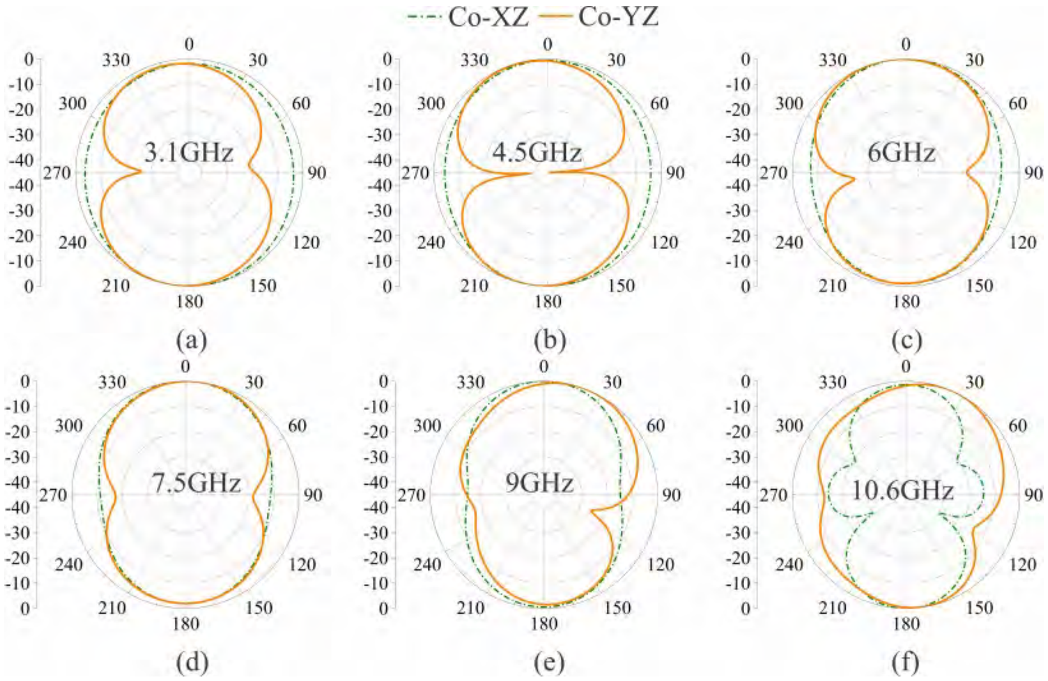

Figure 4.13: Radiation patterns (simulated) of Norman window slot antenna at different frequencies (in GHz) (a) 3.1, (b) 4.5, (c) 6, (d) 7.5, (e) 9, and (f) 10.6

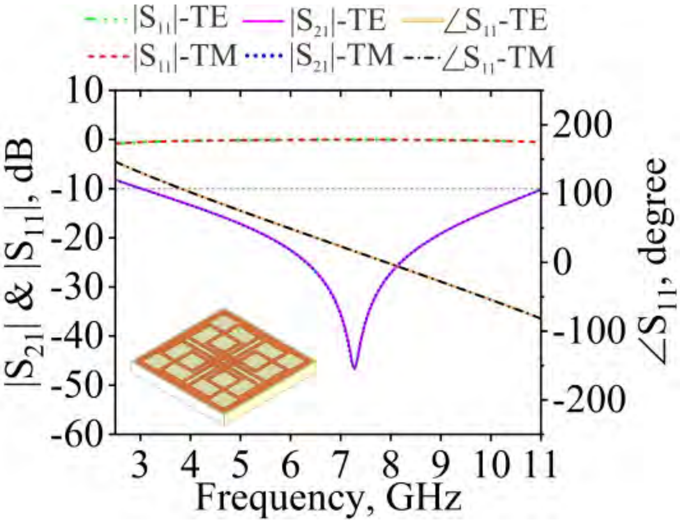

Figure 4.14: Simulated transmission response of proposed MDRLP FSS (MDRLP unit cell in inset)

phase show promise towards enhancing the gain of compact antennas by integrating with MDRLP FSSs. Apart from enhancement of antenna gain, the MDRLP reflector is also anticipated to enhance the directivity of the proposed antenna in the zenith direction.

4.5.3 Slot antenna integrated with MDRLP reflector

Four different configurations are used to integrate MDRLP FSS with the slot antenna in order to examine the influence of UWB reflector on the performance of the slot antenna. These configurations are shown in Figure 4.15.

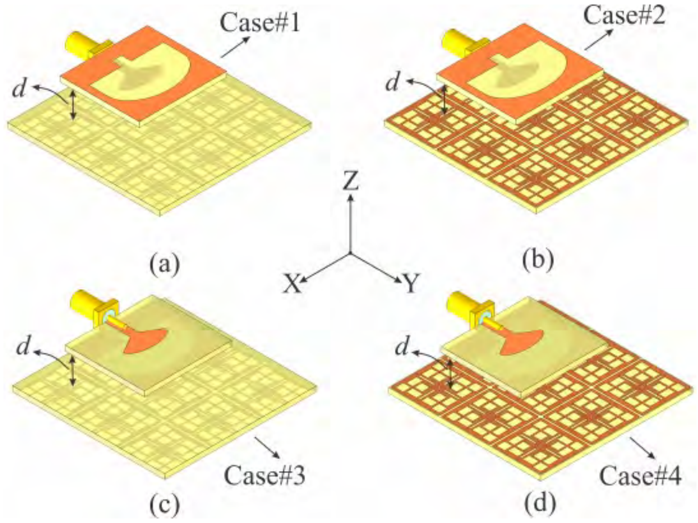

Figure 4.15: Different configurations integrated MDRLP and slot antenna (a) case#1, (b) case#2, case#3 and (d) case#4

Figure 4.15 (a) depicts case#1 when MDRLP FSS is augmented on the plane of antenna feed such that the metal pattern of MDRLP reflector remains on the bottom while the dielectric layer of the reflector faces the antenna feed. Case #2 is depicted in Figure 4.15(b) in which antenna orientation remains unchanged as in case #1 while reflector surface is flipped by 180°, i.e., the metal layer of reflector faces the antenna feed while dielectric layer is kept at the bottom. Figure 4.15 (c) illustrated case #3 in which the reflector orientation is kept similar to case #1 while the antenna is flipped by 180°, i.e., the antenna feed is kept at the top and the Norman window is kept at the bottom. Similarly, case#4 is obtained by flipping the reflector of case#3 and keeping orientation of slot antenna intact, as shown in Figure 4.15 (d).

As depicted in Figure 4.15, the spacing between the antenna and FSS is kept constant and denoted by'*d*'. Employing simulations using CST Microwave studio, parametric analysis of separation, '*d*' between MDRLP reflector and slot antenna is carried out. Figure 4.16 depicts the $|S_{11}|$ and gain in boresight direction for all orientations of antenna united with MDRLP reflector at distinct separation '*d*' between them. Here, '*d*' is altered from 7 mm to 12 mm at an increment step of 1 mm.

The parametric analysis of antenna united with MDRLP reflector suggests that the impedance matching deteriorates as '*d*' increases. Moreover, the antenna gain in boresight direction tends to decrease particularly in high frequency range while it

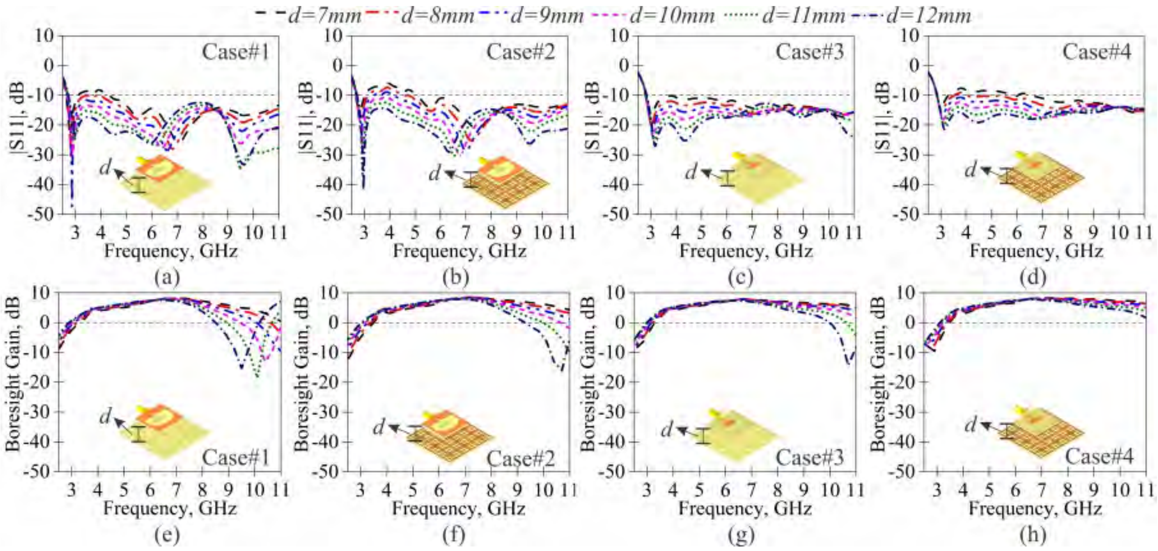

Figure 4.16: $|S_{11}|$ dB and antenna gain in boresight of antenna integrated with MDRLP FSS for (a,e) case#1, (b,f) case#2, (c,g) case#3, and (d,h) case#4

slightly increases at lower frequencies when '*d*' is increased. To maintain impedance band along with positive antenna gain in boresight direction across whole UWB range, an optimal separation between antenna and FSS needs to be maintained for all four cases. For each case #1 to case #4, this optimal separation is then determined. Table 4.10 provides the optimum separation of each case.

Table 4.10: Optimum separation and integrated antenna performance

Case	Optimum separation (d) in mm	Is UWB Impedance Band retained?	Is UWB Gain band retained?	Peak boresight gain (dB)	Gain enhancement, dB
Case#1	9	Yes	Yes	8.02	4.02
Case#2	10	Yes	Yes	8.17	4.17
Case#3	10	Yes	Yes	7.70	3.52
Case#4	11	Yes	Yes	7.89	3.71

The analysis suggests that case #2 provides the largest boresight gain and maximum gain improvement, although it comes with a comparatively high antenna profile due to large separation. Given that the selection criterion is based on achieving the highest gain along boresight, case #2 is chosen for further production and testing. According to Table 4.10, the antenna profile of case #2 exceeds that of case #1, case #3, and case #4, but it remains relatively compact compared to previous studies found in earlier publications.

Figure 4.17 illustrates the comparison between the $|S_{11}|$ of the slot antenna and an antenna united with MDRLP FSS, as well as the gains achieved in both boresight and backsight directions using CST MWS.

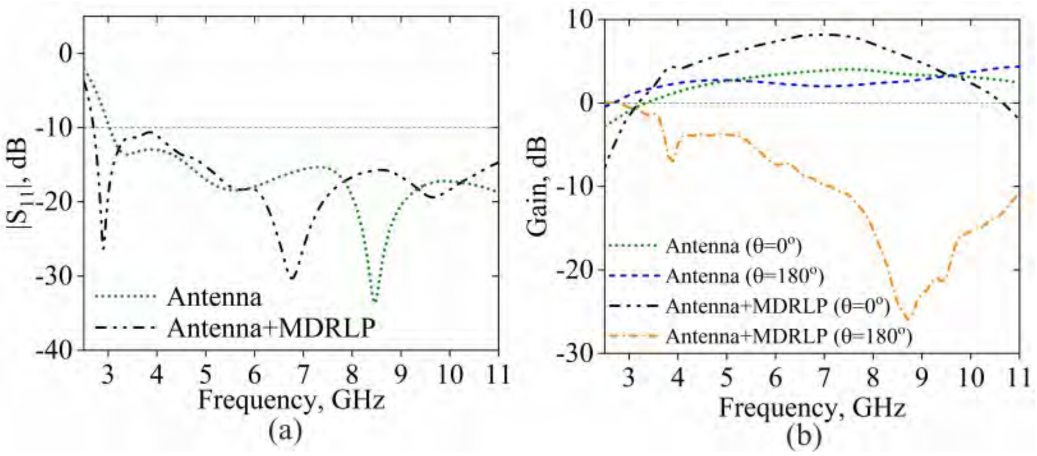

Figure 4.17: Simulated results of antenna compared with antenna configuration of case #2 (a) $|S_{11}|$ dB, (b) antenna gain in θ=0° and θ=180°

4.5.4 Fabrication of case #2 configuration and measurements

The Norman window slot antenna and FSS both are fabricated using conventional printed circuit technology on FR-4 substrates. On one side of the copper cladded FR-4, a slot is ethced, while on the opposite side, the feed is patterned. Figure 4.18 (a) and (b) depict, correspondingly, a photograph of a prototype antenna that has been fabricated. In addition, a three-by-three array of MDRLP FSS is manufactured and assembled with the slot antenna, as described in configuration of Case#2. Utilizing an expanded polyethylene (EPE) foam spacer, a gap of 10 mm is maintained in between the antenna and FSS prototypes. Figure 4.18 (c) is a photograph of an antenna that has been integrated with MDRLP FSS.

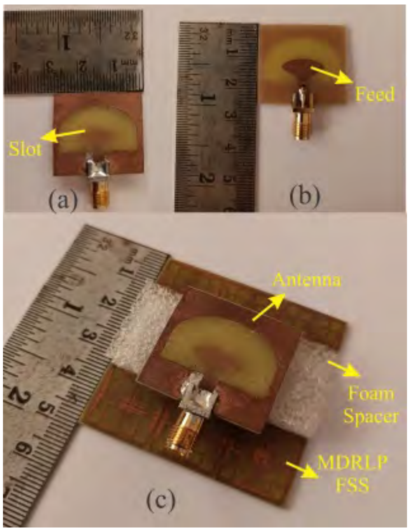

Figure 4.18: Fabricated prototypes of slot antenna (a) Top view, (b) Bottom view and (c) 3-D view of slot antenna integrated with FSS

4.5.5 Slot antenna measurements

The slot antenna's reflection coefficient, $|S_{11}|$, is measured by employing a pre-calibrated VNA. Additionally, the antenna's boresight gain is measured using the conventional horn antenna method. In Figure 4.19, a comparison is presented between $|S_{11}|$ and gain in boresight direction of developed antenna through experiments and the corresponding values obtained through simulations.

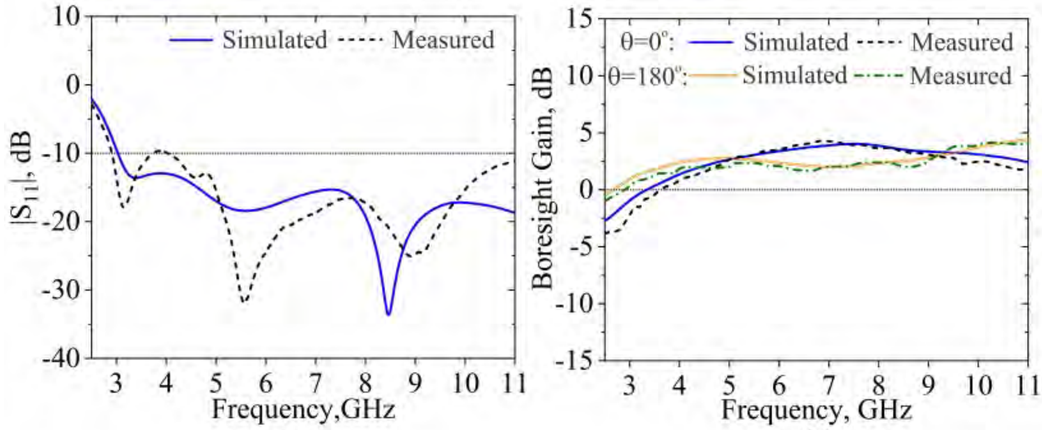

(a) (b)

Figure 4.19: Comparison of measured and simulated reflection coefficient and boresight gain of antenna

Through measurements of $|S_{11}|$, it has been demonstrated that antenna retains the UWB impedance characteristics. However, modest variations in measured values are observed as a result of practical tolerances. Furthermore, the antenna gain measured along both the directions (θ=0° and θ=180°) exhibits a reasonably close agreement with the simulated values.

To get radiation patterns, measurements of the developed antenna prototypes are performed in an anechoic environment. As a reference antenna, a standard transmitting horn antenna is utilised. The horn antenna is connected via coaxial cable to a signal generator, while a power meter is connected to the experimental antenna. The test antenna undergoes rotation in both principal planes from 0° to 360° with 10° increments, and the values of power received are measured. Figure 4.20 represents a plot of the normalized radiation patterns of the antenna at six distinct frequencies within UWB, i.e.,3.1, 4.5, 6 , 7.5, 9, and 10.6 GHz respectively.

The radiation patterns establish that the designed antenna radiates bidirectionally with a steady radiation characteristics except at 10.6 GHz, where it looks distinct from the slot owing to the appearance of nulls.

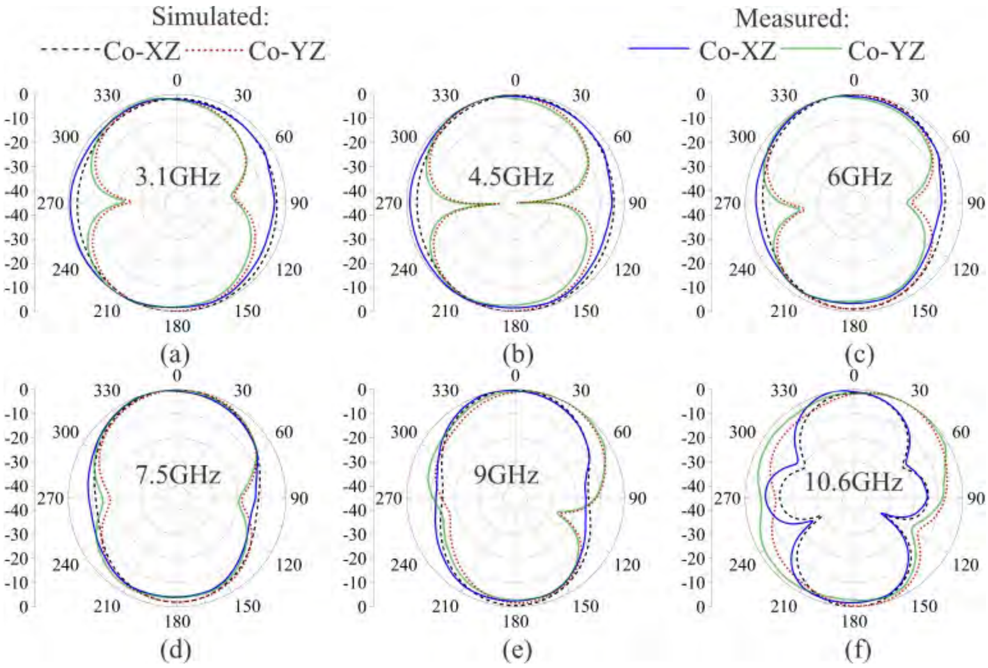

Figure 4.20: Normalized radiation pattern of antenna prototype at six distinct frequencies (in GHz) (a) 3.1, (b) 4.5, (c) 6, (d) 7.5, (e) 9 and (f) 10.6 GHz respectively

4.5.6 Measurements of antenna integrated with MDRLP FSS

Figure 4.21 depicts $|S_{11}|$ and gain at boresight of an antenna integrated with the MDRLP FSS.

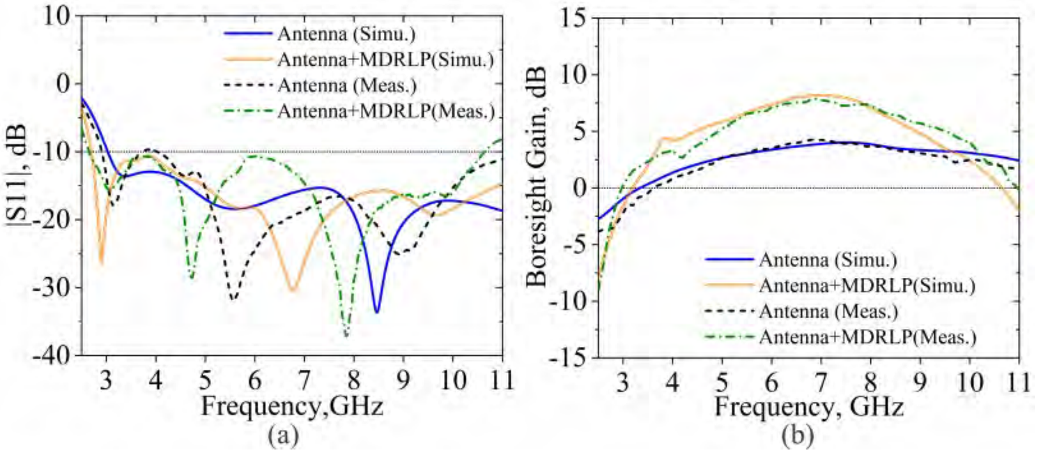

Figure 4.21: Simulated and measured (a) $|S_{11}|$ dB and (b) gain at boresight of antenna alone and antenna integrated with loaded with MDRLP FSS (Case#2)

The experiments show that on integration of antenna with MDRLP FSS, it maintains the impedance band which covers UWB, but with small changes due to practical defects. The antenna gain measured in both the zenith and nadir is pretty close to what the simulations show. Figure 4.22 shows the measured normalized radiation patterns of an antenna combined with FSS in both principal (X-Z and Y-Z) planes.

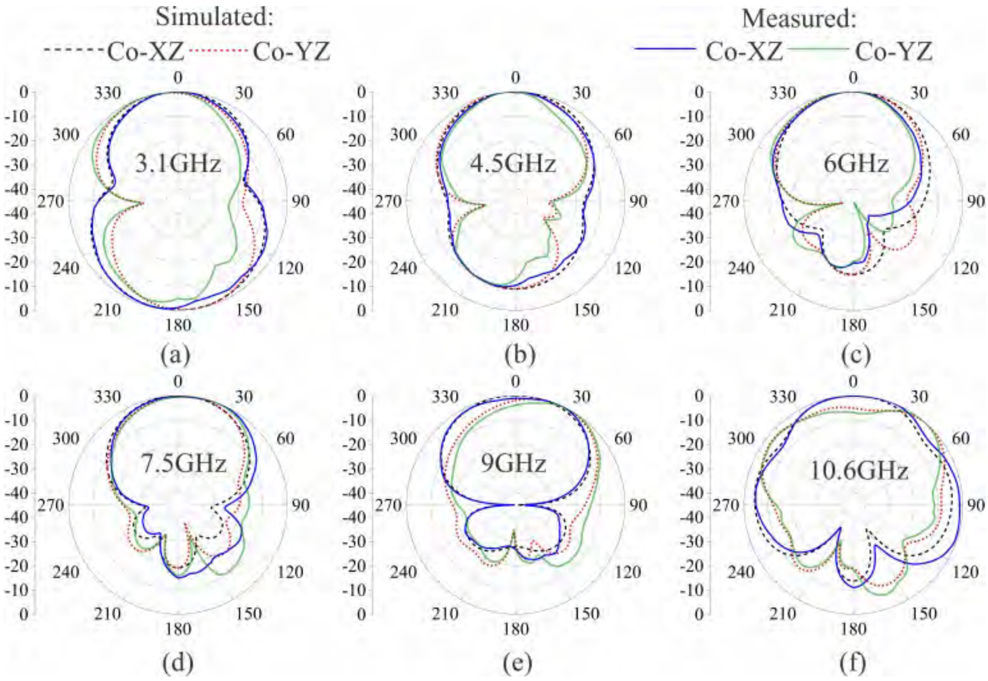

Figure 4.22: Normalized radiation pattern of antenna prototype (case#2) at six distinct frequencies (in GHz) (a) 3.1, (b) 4.5, (c) 6, (d) 7.5, (e) 9, and (f) 10.6 GHz

Based on the radiation pattern evaluated, it can be inferred that the antenna radiates bidirectionally at 3.1 GHz but predominantly emits radiation in a specific direction only above 4.5 GHz. The backward radiation (towards the ground) at 4.5 GHz is significantly reduced by approximately 8 dB as a result of poor reflections from FSS at frequencies near to lower cutoff.

In Table 4.11, the Norman window slot antenna united with MDRLP reflector is compared with several antennas that have been previously reported. The comparison in Table 4.11 is based on various factors such as antenna dimensions, maximum gain, magnitude of gain enhancement, and the number of reflecting surfaces integrated with the antennas. Except the antenna reported in reference [60], which operates in frequency band of 4.7-14.9 GHz, rest of all the antennas listed in Table 4.11 operate in UWB. The comparison establishes that the antenna integrated with a reflector is an appropriate solution to keep structure compact while offering similar gain enhancement. Although references [134], [121], [135], and [136] show slightly more improvement in gain than the antenna design proposed here, they achieve this by incorporating two reflecting surfaces. In addition, the largest volume is occupied by antenna proposed in reference antenna in reference [60], thus, exhibits the highest gain enhancement across the whole UWB. Furthermore, the antenna proposed here with an MDRLP reflector offers several advantages, including its compact profile, easier development, and nearly consistent enhancement of antenna gain throughout the band covered by the antenna.

Table 4.11: UWB slot antenna integrated with FSS compared with alike structures reported in literature

Ref. (Year)	Antenna Dimension(mm^3)	Substrate	Peak Gain (dB)	Gain Enhancement (dB)	Number of reflecting surface
[134], 2017	44×44×28	FR4	8.7	4.2	2
[121], 2017	85×85×18	FR4	8.9	4	2
[135], 2018	44×44×33.5	FR4	8.5	4.5	2
[136], 2019	82.5×82.5×22	RO4350B	9	3.7	2
[60], 2019	108×108×12.2	FR4	8.7	4.5	1
[137], 2022	45.64×34.23×29.4	FR4	7.9	3.5	2
[138], 2022	45×30×28.4	FR4	6.7	3.6	1
This Work	47×47×13.2	FR4	7.86	3.6	1

Further, a hexagonal UWB slot antenna with minor modifications to the Norman window slot antenna as discussed in earlier sections is designed and loaded with tessellated rhombic loop based PD reflector.

4.6 TRL based FSR integrated with UWB hexagonal slot antenna

A simple technique for gain enhancement of irregular hexagonal shaped UWB slot antenna by inclusion of closely packed or tessellated rhombic loop (TRL) based FSS is presented in the following sections. The hexagonal slot bidirectional radiator is designed to obtain stable radiation pattern over entire UWB (3.1-10.6 GHz). Also, as expected, UWB antenna exhibits non-uniform gain in the zenith (θ=0°) and the nadir (θ=180°). The slot antenna is further loaded with TRL FSS at both slot and feed side separately to study distinct configurations of antenna integrated with FSS and evaluate the impact of the configurations of FSS on antenna performance. Later, an antenna and antenna loaded with TRL FSS prototype are compared for experimental validations. Measurements show that the slot antenna radiates over the complete UWB and provides gain of 4.31 dB in the zenith while 4 dB gain in nadir. An enhancement in antenna gain of 2.44 dB in zenith and 3.8 dB in nadir directions are achieved when the slot antenna is integrated with TRL FSS along feed side and slot side separately. The measured results confirm the simulated results well.

In the following sections, details of UWB slot antenna designed, fabricated, and tested here, are presented and discussed. This slot antenna is then loaded with TRL based wide stopband FSS to analyze the performance of slot antenna. The FSS is first placed over the slot facing the TRL pattern and later with its flipped version. Later, both FSS orientations are applied over the feed side of the slot antenna as it radiates bidirectionally.

4.6.1 Design of irregular hexagonal slot antenna

The proposed irregular hexagonal slot antenna is displayed in Figure 4.23. The antenna is built on a FR-4 substrate with a thickness of 1.57 mm, ε_r of 4.4, and a tanδ of 0.025. A rectangular slot modified to a hexagonal slot by truncating two vertices of rectangle, is etched from the rectangular ground plane on one side of the FR-4 layer. On its opposite side, there is a microstrip line based sectoral feed. The sectoral feed couples with the slot electromagnetically and radiates the energy. The irregular hexagonal slot is modified by removing metallic square of dimension 3×3 mm^2 on the opposite side of sectoral feed to achieve a wider bandwidth with good impedance matching. Also, the microstrip feed is modified to sectoral feed by loading the microstrip line by radial stub to enable better antenna gain in boresight direction.

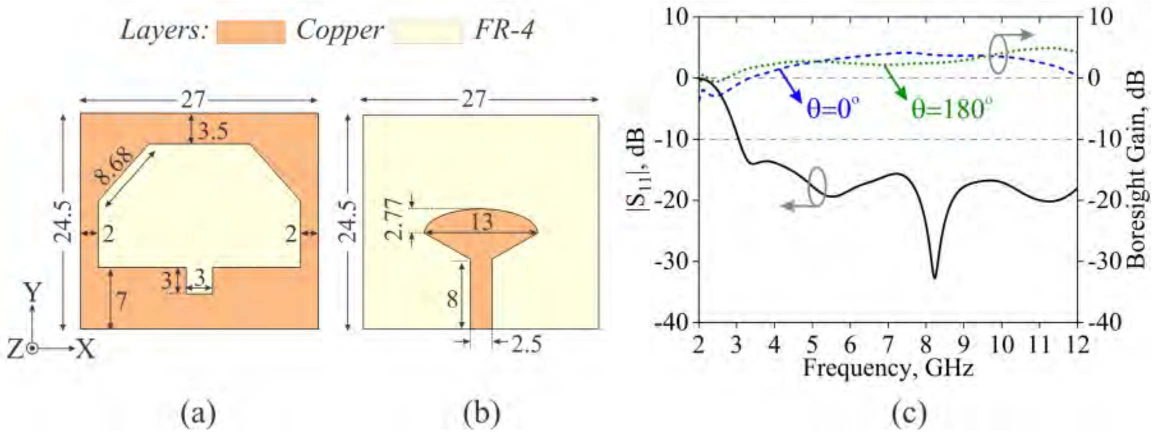

Figure 4.23: Schematic of the hexagonal slot antenna (a)Front View (b) Back View (all dimensions are in mm) (c) Simulated $|S_{11}|$ dB and antenna gain in zenith and nadir

The slot antenna radiates in both directions, i.e. zenith and nadir but with different antenna gain. The $|S_{11}|$ dB of antenna and gain in both boresight and backsight are presented in Figure 4.23(c). The antenna offers a complete UWB spectrum (3.1-10.6 GHz) with maximum boresight gain of 4.13 dB. The average in-band gain delivered by the irregular hexagonal slot antenna is 2.96 dB in zenith while in nadir, the average in-band gain is 2.69 dB. The maximum gain in backsight (θ=180°) achieved is 4.66 dB.

4.6.2 RL FSS unit cell

The top and side views of rhombic loop based FSS unit cell are illustrated in Figure 4.24 (a) and (b) respectively. The FSS is composed of closely packed TRLs printed over FR-4 substrate. The features of unit cell are displayed along the geometry.

The TRL unit element is analyzed using simulations based on frequency domain solver as provided with CST MWS simulation software. Unit cell boundaries are defined along edges of substrate for unit cell simulations, and Floquet ports are employed for excitation in the Z direction. FSS transmission characteristics are shown in Figure 4.24 (c). For Y-polarized incident EM waves, the TRL FSS appears as bandstop FSS that demonstrates a transmission null at 10 GHz and a 9.81 GHz wide stopband with a span of 4.66 to 14.47 GHz.

4.6.3 Antenna loaded with TRL FSS

Since,the slot antenna radiates in both the directions, the zenith and nadir, the TRL FSS is loaded with the slot in either direction separately parallel to plane of slot

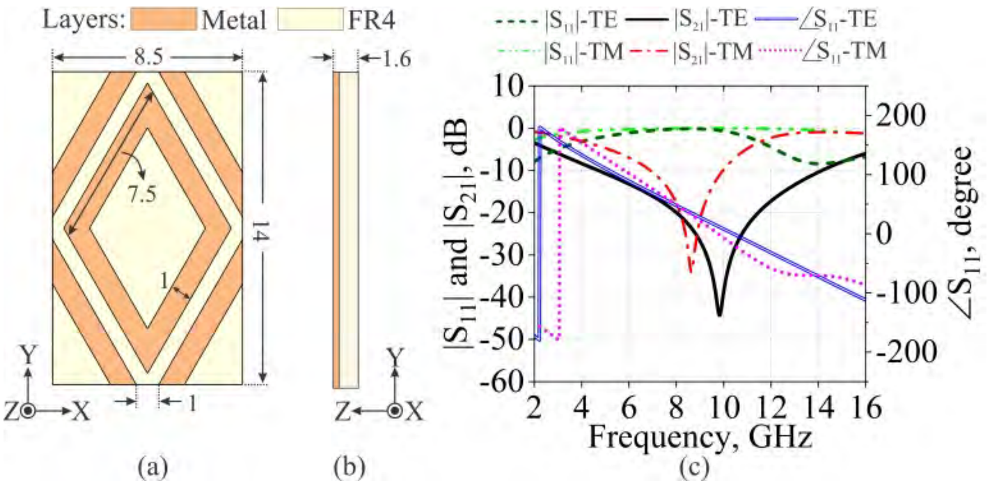

(a) (b) (c)

Figure 4.24: TRL unit cell (a) Front View, (b) Side view (all dimensions are in mm), (c) Transmission and reflection responses of TRL FSS

antenna. To evaluate the impact of TRL FSSs on slot antenna, the TRL FSS in four distinct configurations at a height '*d*' is loaded with slot antenna very similar to cases discussed in section 4.5.3. In case#1, the RL FSS is combined with slot antenna at feed side by keeping metal layer of FSS at the top while the TRL FSS is flipped in case#2. Similarly, TRL FSS is backed by slot antenna at slot side keeping metal trace of FSS at the top in Case #3 while, in case#4, the TRL is flipped with respect to Y axis keeping antenna orientation unchanged. The height '*d*' in all four configurations is changed from 7 mm to 12 mm in steps of 1 mm. The parametric analysis of FSSs placed at distinct heights is done using CST MWS. Figure 4.25 and 4.26 show $|S_{11}|$ dB and gain of the antenna when integrated with FSSs for all four cases respectively.

From the simulations of antenna and FSS by varying separation '*d*', it is found that the impedance matching improves as '*d*' increases but boresight gain starts falling at high frequencies. The optimum distance, '*d*' between antenna and FSSs is decided based on maximum boresight gain obtained, and the values are summarized in Table 4.12.

The antenna performance also depends on inclusion of dielectric layers of antenna and reflecting surfaces. However, the distinct configurations of antenna and TRL FSS do not exhibit a significant change owing to more air space than dielectric substrate.

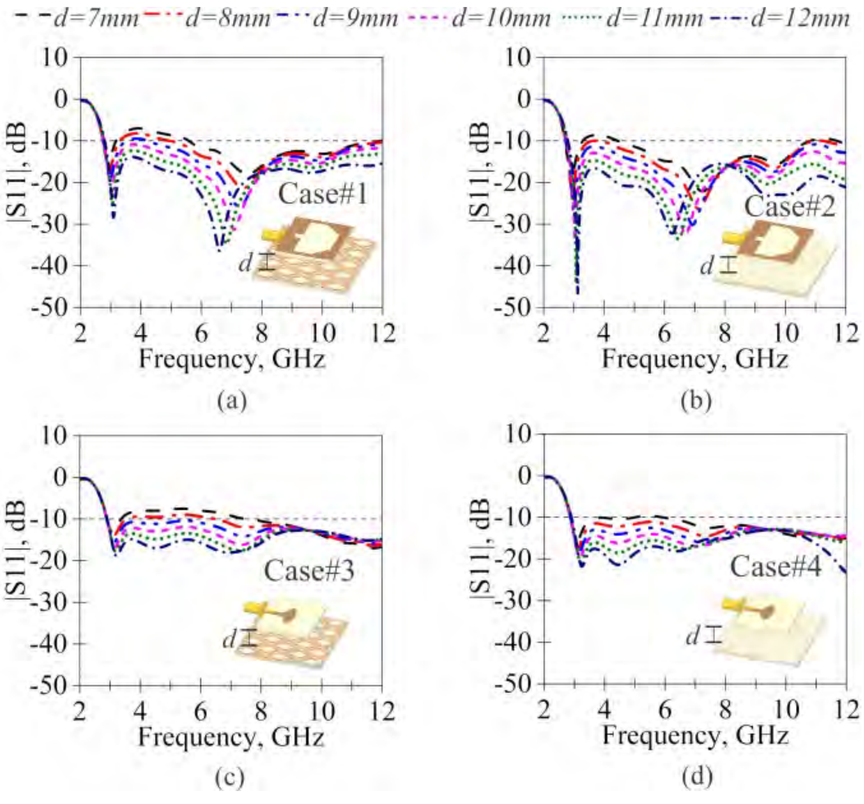

Figure 4.25: Effect of separation between antenna and FSS on reflection coefficients of antenna for (a) case#1 (b) case #2, (c) case#3 and (d), case#4

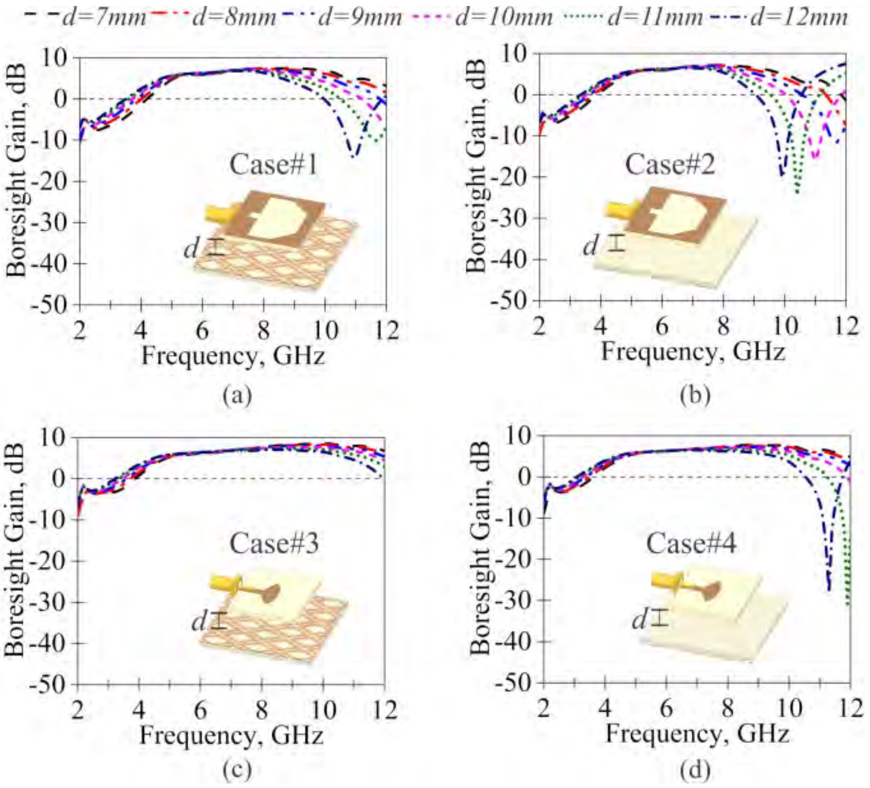

Figure 4.26: Effect of separation, '*d*' on gain of antenna respectively when FSSs are loaded at feed side for (a) case#1 (b) case #2, (c) case#3 and (d), case#4

Table 4.12: Antenna performance compared for all cases at optimum '*d*'

Case	Optimum separation '*d*' in mm	Is UWB Impedance Band (IB) retained?	Is UWB Gain band retained?	Avg. boresight Gain (dB)	Peak boresight gain (dB)	Gain enhancement relative to slot antenna, dB (Avg/Peak)
Case#1	10	Yes	Yes	4.74	7.16	1.78/3.03
Case#2	9	Yes	Yes	4.40	6.96	1.44/2.83
Case#3	9	Yes	Yes	5.87	7.99	3.18/3.33
Case#4	8	Yes	Yes	5.72	7.51	3.03/2.85

From Table 4.12, it is evident that the optimum separation between antenna and FSS is reduced by 1 mm in case#2 when compared with case#1 which is due to the dielectric substrate of flipped FSS. However, based on maximum gain in boresight direction, case#1 is preferred over case#2. Similarly, the gain enhancement in nadir is also achieved when FSS is loaded with slot antenna at slot side and a similar trend of optimum distance between the slot antenna and TRL FSS is also observed in case#3 and case#4.

From the comparison, case #3 is observed to be superior as the maximum average boresight gain of 5.87 dB is observed in this combination. However, the slot antenna integrated with TRL FSS as in case#1 and case#3 are developed and the experimental measurements are presented and compared in the following section.

4.6.4 Experimental measurements and results

The hexagonal slot antenna and TRL FSS are developed using standard PCB fabrication methodologies and the required separation,'*d*' between FSS and antenna is maintained by foam spacer. The photograph of fabricated prototypes and the measurement set up for the developed antennas are depicted in Figure 4.27 and 4.28 respectively.

(a) (b) (c) (d)

Figure 4.27: Photographs of developed prototypes (a) TRL FSS, (b) Top view of slot antenna, (c) Rear view of slot antenna, and (d) 3D view of slot antenna integrated with TRL FSS

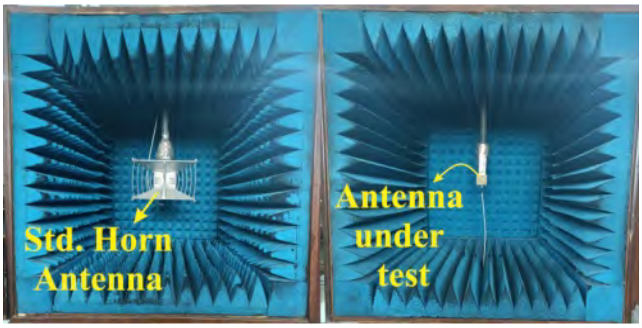

Figure 4.28: Measurement setup in compact anechoic chamber standard UWB horn (Left) and antenna under test (Right)

The $|S_{11}|$ dB of antenna alone and the antenna loaded with by TRL FSS (case#1 and case#3) are recorded by pre-calibrated Keysight's field fox N9925A VNA. The $|S_{11}|$ dB and antenna gain are presented in contrast in Figure 4.29.

The irregular hexagonal slot antenna and both case#1 and case#3 of slot antenna loaded with TRL FSSs cover UWB frequency range. The slot antenna exhibits an average gain of 2.96 dB (simulated), 2.56 dB (measured) gain in the zenith while 2.69 dB gain (simulated), 2.68 dB (measured) in the nadir. Here, the average gain is determined by taking average value of gain from 3.1 GHz to 10.6 GHz with an interval of 0.1 GHz. Moreover, the antenna demonstrates a maximum 4.13 dB gain (simulated), 4.31 dB gain (measured) in the zenith while 4.66 dB gain (simulated), 4 dB gain(measured) gain in the nadir. The peak gain in zentith direction is enhanced

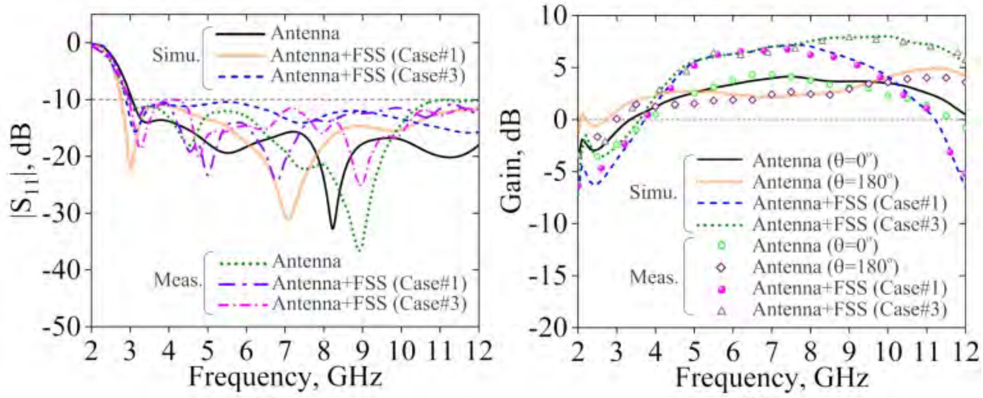

(a) (b)

Figure 4.29: Comparison of measurements with simulated (a) reflection coefficients, and (b) Gain of antennas

to 7.16 dB (simulated), 6.75 dB (measurement) when FSS is loaded to slot antenna at feed side as in case#1 while the average gain is enhanced to 4.75 dB gain (simulated), 4.49 dB (measured) for the same case#1.

Later, the slot antenna is assembled with TRL FSS as in case#3. It exhibits average gain of 5.87 dB (simulation), 7.82 dB (measured) in the zenith while the peak in nadir direction gain is enhanced to 7.99 dB (simulations) and 7.83 dB (measurements).

The normalized radiation patterns of the slot antenna alone and the antenna loaded with TRL FSS are achieved using standard horn antenna method. Both the antenna under test and the UWB standard horn are housed in an anechoic chamber for radiation pattern measurements, as shown in Figure 4.28. The horn antenna is connected to a signal generator and the slot antenna to be tested is coupled to power meter through power sensor. The antenna is then rotated in angular steps of 10° and the measured power is registered. The measured radiation patterns after normalization are plotted in both principal planes (X-Z and Y-Z planes) at 3.1, 4.5, 6, 7.5, 9, and 10.6 GHz. Simulated and experimentally measured patterns of slot antenna are displayed and compared in Figure 4.30.

The slot antenna, as expected, radiates bi-directionally and maintains the radiation pattern even at higher frequencies. Experimentally obtained radiation patterns exhibit decent similarity with the radiation patterns recorded at the time of simulations. Similarly, the measured radiation patterns of slot antenna integrated with TRL FSS for case#1 and case#3 are also displayed at same frequencies in Figure 4.31 and 4.32 respectively for comparison.

From Figure 4.31, it can be observed that the slot antenna loaded with TRL FSS in case#1 radiates bi-directionally at 3.1 GHz and then it appears that the directional behaviour of the antenna dominates at higher frequencies (from 6 GHz onwards).

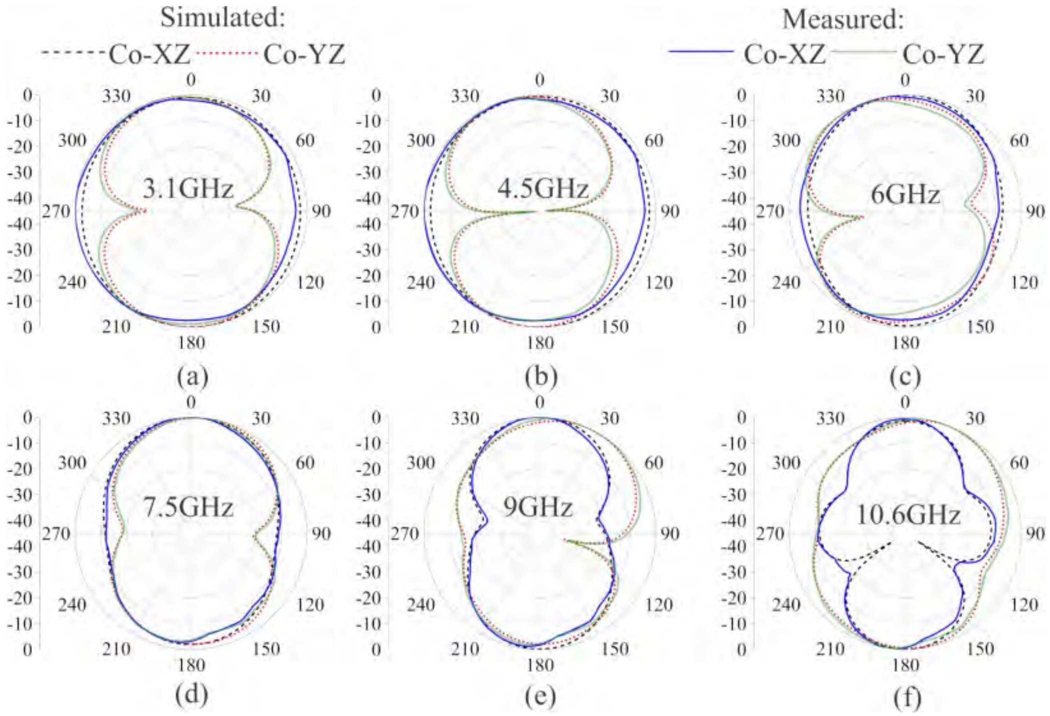

Figure 4.30: Radiation pattern measurements of proposed bi-directional slot antenna

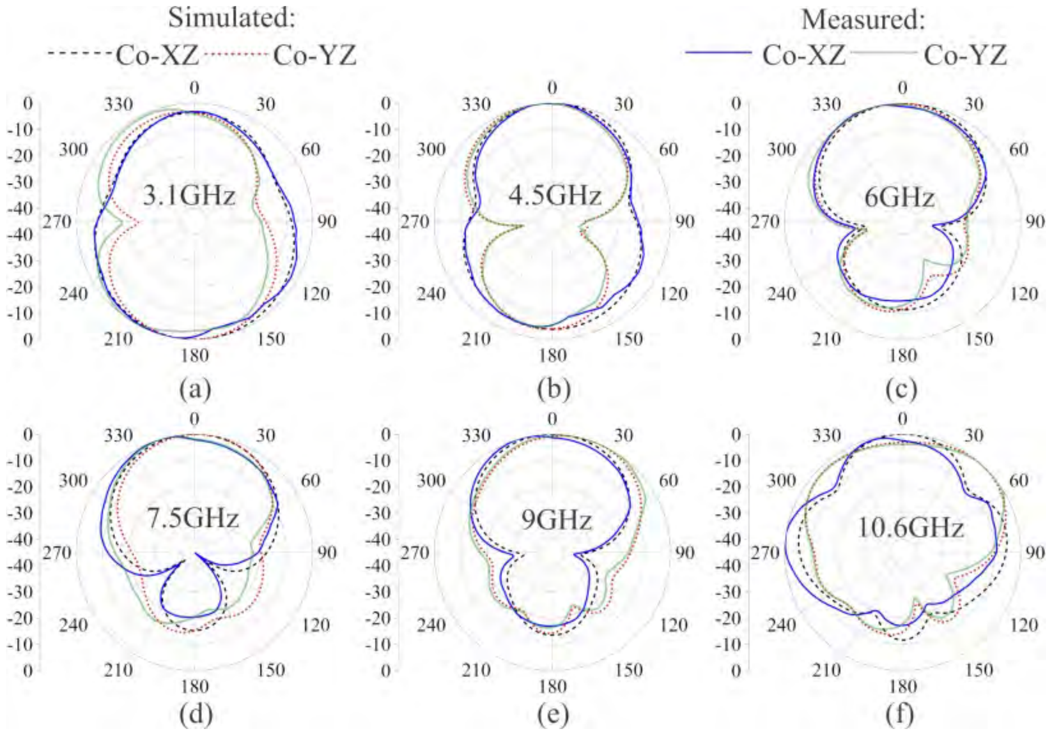

Figure 4.31: Radiation pattern measurements of slot antenna backed by TRL FSS (case#1)

Although the antenna lobe in nadir is suppressed by ∼ 5 dB even at 4.5 GHz, the pattern is not much directional. The directional behaviour of antenna in its partial impedance band also verifies the reflective nature of TRL FSS.

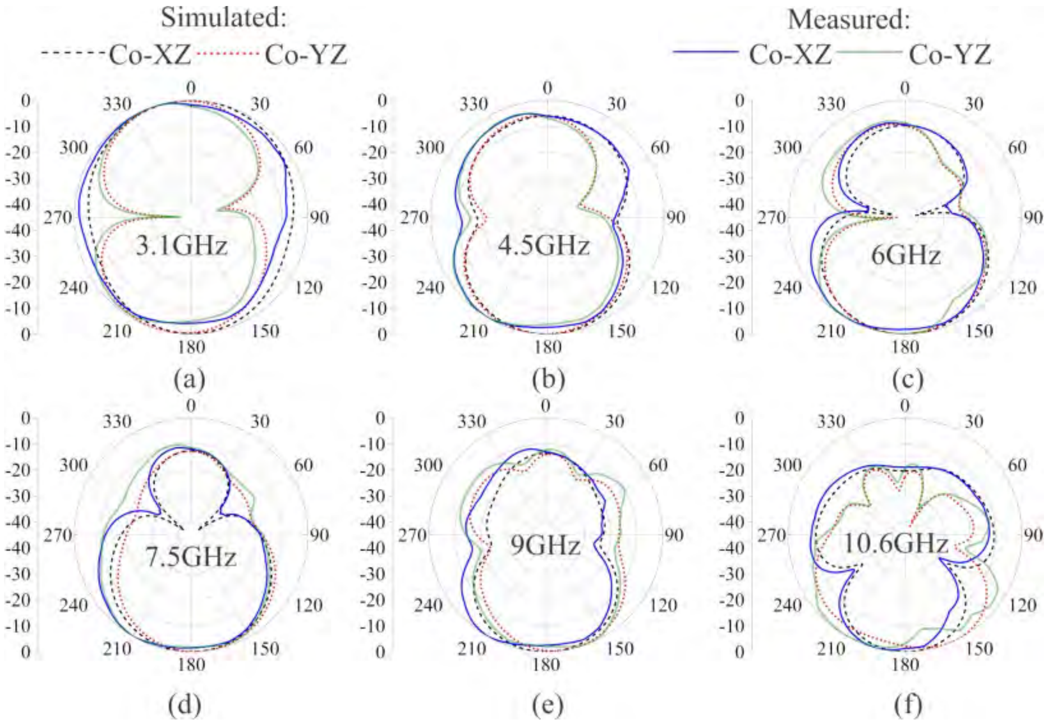

Figure 4.32: Radiation pattern of slot antenna backed by TRL FSS (case#3)

From the radiation patterns shown in Figure 4.32, again it can be observed that directional radiation pattern is demonstrated by the antenna, but in the opposite direction(nadir) when compared to antenna in case#1. Also for antenna in case#3, the directional behavior dominates at higher frequencies (from 6 GHz onwards). Even though the main beam in the zenith is attenuated by ∼10 dB at 4.5 GHz, the radiation pattern is not very directional. Thus, the antenna radiation pattern in zenith or nadir can be controlled by placing the TRL FSS in either side of the radiating slot.

Table 4.13: Comparison of reflector backed antenna with provided in reported literature

Ref.	Antenna dimension (mm^3)	Substrate	Peak boresight gain of antenna (dB)	Peak boresight Gain of Antenna integrated with FSSs (dB)	Gain enhancement (dB)	Number of Reflecting Surfaces
[136]	82.5×82.5×22	RO4350B	5.3	9	3.7	2
[135]	44×44×33.5	FR4	4	8.5	4.5	2
[134]	44×44×28	FR4	4.5	8.7	4.2	2
[60]	108×108×12.2	FR4	4.2	8.7	4.5	1
[121]	85×85×18	FR4	4.9	8.9	4	2
This Work (Case#1)	40×40×13.14	FR4	4.31	6.75	2.4	1
This Work (Case#3)	40×40×12.14	FR4	4	7.8	3.8	1

The proposed integrated TRL backed antenna is further compared with few of earlier reported antennas in published literature based on antenna size, maximum boresight gain and gain enhancement and the comparison is summarized in Table 4.13. From Table 4.13, it is evident that the integrated antenna occupies the lowest profile at the cost of moderate gain enhancement in comparison to others.

4.6.5 Conclusion

This chapter provides a comprehensive analysis of the effectiveness of single-layered FSS reflectors (MRLP and MDRLP) for wideband and UWB applications, respectively. These FSSs are derived from the designs of PD RLPs. The square and rectangular arrays of RLP are designed and simulated in order to explore their signal rejection and reflection properties for incident TE and TM waves. Additionally, orthogonal patterns are developed on opposite sides of FR-4 laminate to investigate transmission and reflection characteristics of BTB RLP unit structures. By merging orthogonal FSS arrays to get MRLP structure on one of the sides of FR-4 laminate, it is possible to reduce the reflection phase non-linearities of BTB RLP FSS. In order to analyze the transmission characteristics critically of RLP FSSs, ECMs are also provided. After the development of two FSSs, one with WB and the other with UWB rejection capabilities, experiments are conducted. All proposed FSSs' measured transmission responses are comparable to their simulated counterparts. In addition, an MDRLP-UWB FSS reflector of finite dimension is integrated with Norman window-shaped UWB slot antenna. The impact of loading MDRLP FSS reflector with the slot antenna is investigated in distinct configurations with varying antenna and reflector spacing. The optimal configuration for experimental validations is devised to analyze radiation characteristics through measurements. When incorporated with the UWB FSS, the slot antenna exhibits better directivity due to back lobe suppression. When FSS reflector is employed beneath the antenna slot, a peak gain of 7.86 dB, with an improvement of 3.6 dB in the zenith is demonstrated by the antenna.

TRL based FSS for bandstop characteristics are also proposed and designed. A modified hexagonal slot UWB antenna excited by a sectoral feed is then loaded by TRL FSS from slot and feed side, and the impact of employing FSSs beneath the antenna is assessed. The prototypes of slot antenna as well as the antenna combined with TRL FSS loaded at slot and feed side are developed and experiments are performed. The developed antenna exhibits a maximum gain of 4.31 dB in zenith and 4 dB in nadir direction. The antenna gain is enhanced in zenith by 2.4 dB when RL FSS is loaded at feed side while the gain is enhanced in nadir direction by 3.8 dB when the RL FSS is loaded at slot side.

Chapter 5

Relevance of AS/ PI of FSR towards antenna gain

The gain enhancement of Norman window and irregular hexagon shaped UWB slot antennas by integrating them with UWB (MDRLP) and wideband RL reflectors respectively is described in chapter 4. These reflectors have been loaded with the slot antennas in distinct configurations. Here, in this chapter, investigations on impact of FSS reflector characteristics preliminarly AS and PI on antenna gain is discussed. For the purpose, the significance of AS and PI towards antenna gain improvement using AS/AU, PD/PI FSRs is studied through both simulations and experiments. Three distinct FSRs based on RL, SL and MDRL are designed analysed again to demonstrate PD/ PI bandstop characteristics under normal and oblique incidences. These FSSs are employed beneath a triangular slot antenna which is excited by a microstrip line feed to radiate at at 10 GHz.

5.1 Introduction

This section emphasizes on the relevance of AS and PI towards antenna gain enhancement application through FSRs is investigated through simulations followed by experiments. Three distinct FSRs based on RL, SL and MDRL are designed and developed to analyze PD and independent bandstop characteristics under normal and oblique incidences. The finite arrays of these FSSs composed of same number of unit cells (5×5) are loaded at back of a backed by a triangular slot antenna operating at 10 GHz is excited by regular microstrip line feed. The, three distinct FSSs which demonstrate either PD or PI along with AU or AS are integrated with a triangular slot antenna to study their impact on impedance and radiation characteristics of the antenna. The relevance of AS and PI is then investigated by rotating the FSSs kept behind the antenna with respect to two orthogonal directions and by loading the orthogonally oriented antenna with the FSSs respectively. Later, FSRs of similar substrate size are printed and similar experiments are repeated. Surprisingly, AU and PD reflectors provide gain enhancement almost close to that provided by AS and PI reflectors. Stringent characteristics of FSSs i.e., AS and PI can be compromised for

FSRs in antenna gain enhancement techniques.

For certain wireless applications such as EM shielding applications [12], [25], radomes [6], FSS based absorbers [139], etc., it is required that FSS must be PI even under oblique incidences. However, for antenna applications of FSS as mentioned earlier, it is still essential to study and compare the impact of PI or AS FSS towards antenna performance. The triangular slot antenna in two orthogonal orientations is loaded with all the three FSSs one by one at distinct separations to investigate the impact of these FSSs on the slot antenna.

5.2 Distinct FSS unit cells design

The geometries of three metallo-dielectric FSS unit cells that are formed by patterning the metallic arrays over FR-4 substrate are illustrated in Figure 5.1. The FSS unit cells composed of closely packed rhombic loops (RLs) and SLs are shown here in Figure 5.1(a) and (c) respectively. The FSS unit cell shown in Figure 5.1(b) is based on two orthogonally oriented arrays of dual RLs (DRLs) arranged in rectangular grid with an A/R=1:2 along X- and Y- directions. Two such orthogonal layers of DRL arrays are then merged and printed over dielectric substrate to form MDRL FSS. The dimensions of all FSSs unit cells are in mm and displayed in the Figure 5.1.

The coefficients, $|S_{21}|$ and $|S_{11}|$ in dB under normally incident EM waves (θ=0°) of all the three FSSs are obtained employing full-wave EM simulations carried out on CST MWS software. Figure 5.2 depicts the transmission characteristics of RL, MDRL and SL FSSs respectively. It is observed that RL FSS being asymmetric towards incident EM waves, demonstrates unlike transmission and reflection characteristics when illuminated by TE and TM normal incidences. Both MDRL FSS and SL-FSS, exhibit similar transmission response to both TE and TM incident waves. Also, the wave propagation behaviour of RL, MDRL and SL FSSs when incidences are oblique, are obtained through EM simulations where the incidence angle, θ is extended from

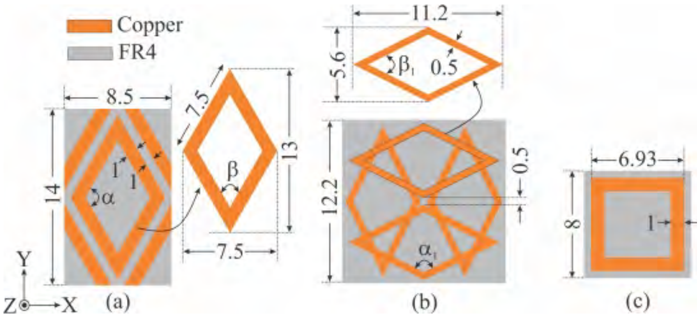

Figure 5.1: Unit cell designs (a) RL-FSS, (b) MDRL FSS, and (c) SL FSS (α=120°, β=60°, α_1=116.56°, β_1=63.43°, all dimensions are in mm)

0° to 30° with an increment of 15°. The $|S_{11}|$ and $|S_{21}|$ in dB for oblique TE and TM incidences for RL FSS are displayed in Figure 5.2 (a) and (d) respectively.

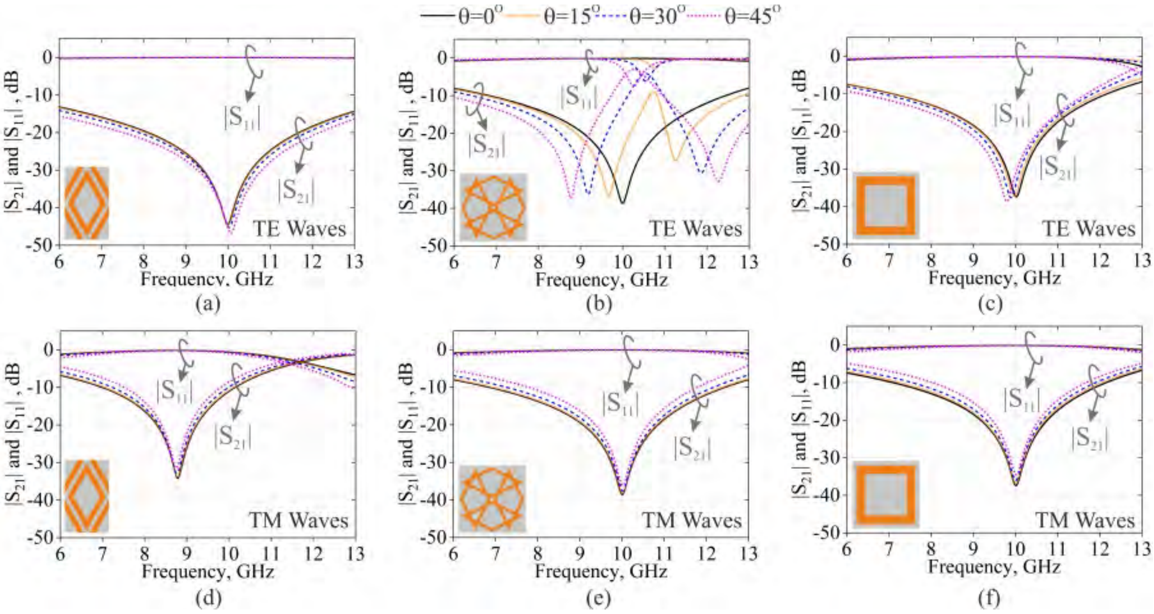

Figure 5.2: Transmission responses of (a) RL-FSS, (b) MDRL FSS, and (c) SL-FSS under TE incidence; transmission responses of (d) RL-FSS, (e) MDRL FSS, and (f) SL-FSS under TM incidences

RL FSS demonstrates distinct but stable $|S_{21}|$ and $|S_{11}|$ responses under oblique incidences. Similarly, Figure 5.2 (b) and (e) shows the variations in $|S_{11}|$ and $|S_{21}|$ with frequency under oblique TE and TM incidences for MDRL FSS while Figure 5.2 (c) and (f) shows the variations in $|S_{11}|$ and $|S_{21}|$ with frequency under oblique TE and TM incidences for SL FSS. MDRL FSS demonstrates stable transmission response under TM incidence only while SL FSS exhibits stable transmission response for incident but inclined TE and TM waves. Thus, RL FSS behaves as AS-PD FSS while MDRL FSS behaves as AU FSS. SL FSS on the other hand demonstrates as PI and it also maintains the transmission response even under oblique incidences. The comparison of RL, MDRL and SL FSSs based on their propagation characteristics under oblique and normal incidences is also summarized in Table 5.1.

Table 5.1: Transmission response of RL, MDRL and SL FSSs

Unit Cell	$f_z(GHz)$	10 dB Stopband	BW (GHz)	AS	PI
RL FSS	TE:10; TM:8.78	TE:4.68-14.44 ; TM: 6.99-10.15	TE: 9.75 ; TM: 3.16	Yes	No
MDRL FSS	TE/TM: 10	TE/ TM: 6.82-12.44	TE/ TM: 5.62	No	No
SL FSS	TE/TM: 10	TE/ TM: 7.08-12.17	TE/ TM: 5.08	Yes	Yes

The significance of features like AS and PI of any FSS towards gain enhancement of compact antennas is further investigated by loading proposed FSSs to a slot antenna redesigned to radiate at 10 GHz and discussed in the sections ahead.

5.3 Triangular slot antenna (10 GHz) design

The geometry of a triangular slot antenna used for further analysis is depicted in Figure 5.3 (a). The triangular slot antenna is designed on FR4 based laminate. An equilateral triangular slot is etched from one side of the copper clad while, a simple microstrip line is patterned on the opposite side of the laminate. The triangular slot antenna is optimized to radiate at a frequency of 10 GHz. The geometrical features of the equilateral triangular slot are chosen through closed form expressions suggested for triangular slot antennas in reference [109], but with a minor change in the effective length to make the slot equilateral. The features of the redigned triangular slot antenna are summarized in Table 5.2

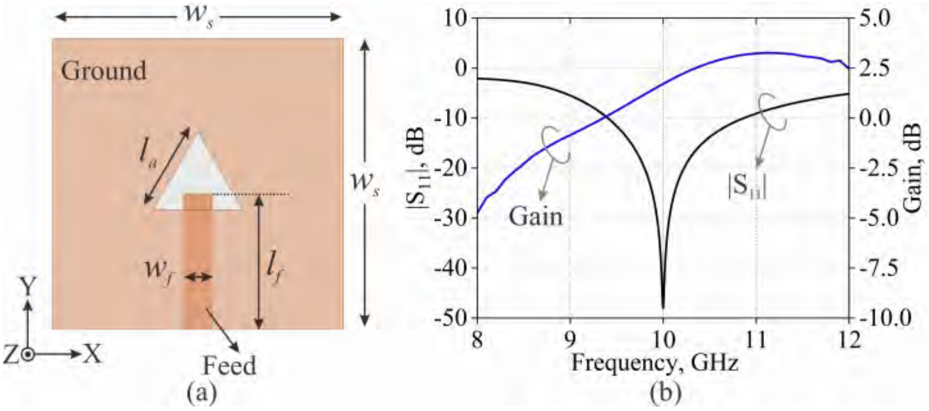

Figure 5.3: (a)Antenna geometry (b) $|S_{11}|$ and antenna gain (in boresight direction)

Table 5.2: Features of equilateral triangular slot antenna (10 GHz)

Parameter	w_s	l_a	w_f	l_f
Value(mm)	30	9.7	3	13.1

The antenna is designed and simulated using CST MWS. The reflection coefficient and the slot antenna gain in boresight direction is obtained and shown in Figure 5.3 (b). The antenna operates at 10 GHz and provides 1.46 GHz wide (14.5 %) 10 dB impedance band. The antenna demonstrates 0 dB gain at lower corner edge frequency, f_l which tends to increase up to a peak value of 3.18 dB at 10.9 GHz within its impedance band. Thus, the gain of triangular slot antenna in boresight direction is superior in the higher frequency region of antenna impedance band. Moreover, the antenna demonstrates an average of 1.91 dB gain over the antenna impedance band in the boresight direction.

Moreover, the triangular slot antenna is a linearly polarized antenna since the E-field vectors are parallel to antenna microstrip feed and aligned to Y-axis as also suggested in reference [140]. Since the antenna parameters as suggested in reference [109] are used with minor changes to develop an equilateral slot, the antenna is not further optimized for a better performance than shown in Figure 5.3 as a low gain antenna appears to be more appropriate to deduce the impact of loading FSSs.

Since the gain augmentation of compact planar antennas have earlier been reported by integrating them with AS/ PI FSSs typically [141], [138], [60], It generates the inquisitiveness to explore further their relevance towards antenna gain enhancement. Therefore,the antenna performance while integrating it with FSRs based on RLs (AS-PD), MDRL (AU-PD) and SL (AS-PI) respectively have been assessed in the following sections.

5.4 Antenna integrated with distinct FSSs

The triangular slot antenna is then backed by 5×5 arrays of RL, MDRL and SL FSS as displayed in Figure 5.4 (a),(b) and (c) respectively. All the FSSs are kept at a distance, '*d*' beneath the slot antenna. Here the dimensions of RL, MDRL and SL FSSs are are different, i.e., 42.5×42 mm^2, 61×61 mm^2 and 40×40 mm^2 respectively to accommodate an array of 5×5 unit cells. Since the size of MDRL unit cell is large, the size of MDRL FSS is greater than RL and SL FSSs. The orthogonally oriented antenna (ϕ=90°) is also loaded with RL, MDRL and SL FSSs as illustrated in Figure

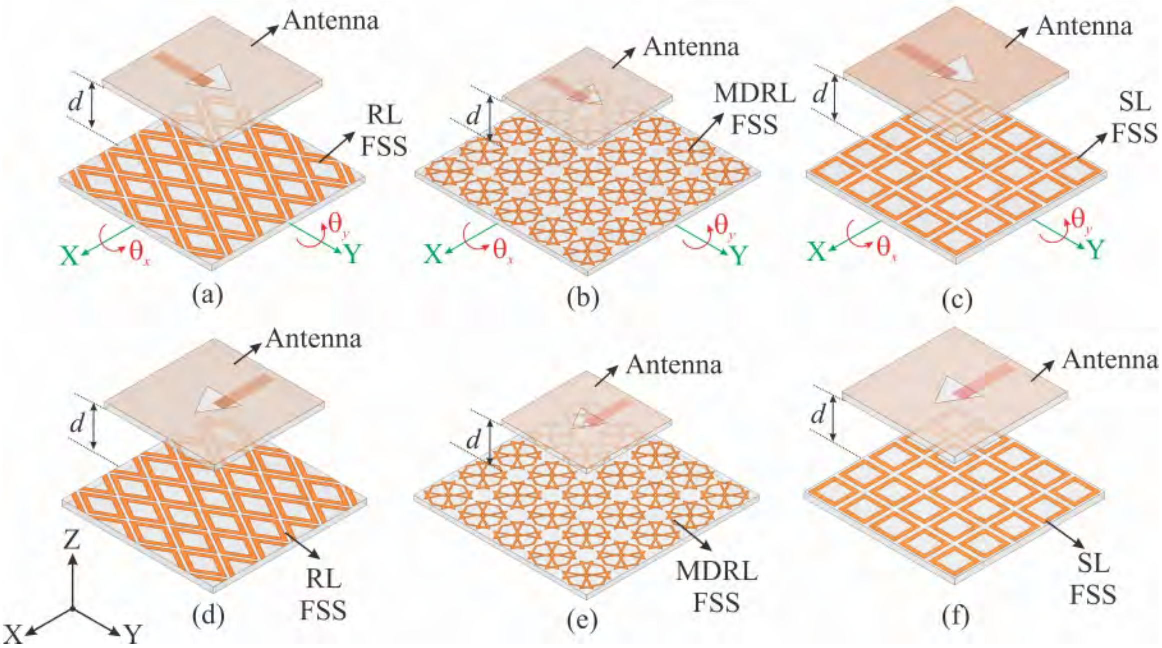

Figure 5.4: Antenna (ϕ=0°) loaded with (a) RL FSS, (b) MDRL FSS, and (c) SL FSS; orthogonally oriented antenna (ϕ=90°) is loaded with (d) RL FSS, (e) MDRL FSS, and (f) SL FSS

5.4 (d), (e) and (f) respectively. Here, 'ϕ' is the rotation angle of the antenna with respect to Z-axis when placed in X-Y plane. The two orientations of antenna, i.e., ϕ=0° and ϕ=90°, when integrated with these FSSs have been considered to investigate the significance of PD or PI FSSs on antenna performance.

The antenna demonstrates a superior behaviour in terms of boresight gain and impedance matching when antenna and FSS separation becomes $3\lambda_0/4$ which comes out to be 22.5 mm here, where, λ_0 is free space wavelength at the operating frequency of the slot antenna. Further, the separation between antenna and FSSs is fine tuned for small variations around the optimum separation of $3\lambda_0/4$. and the distance, 'd' is varied from 21 mm to 23.5 mm in step of 0.5 mm. It is found that there is a negligible change in antenna operating frequency and its impedance band when antenna and FSSs separation increases from 21mm to 23.5 mm. Since the small variations in separation between antenna and FSSs are not significant much, the optimum separation between them is considered at 21.5 mm. The comparison of antenna $|S_{11}|$ and boresight gain at optimum separation is depicted in Figure 5.5.

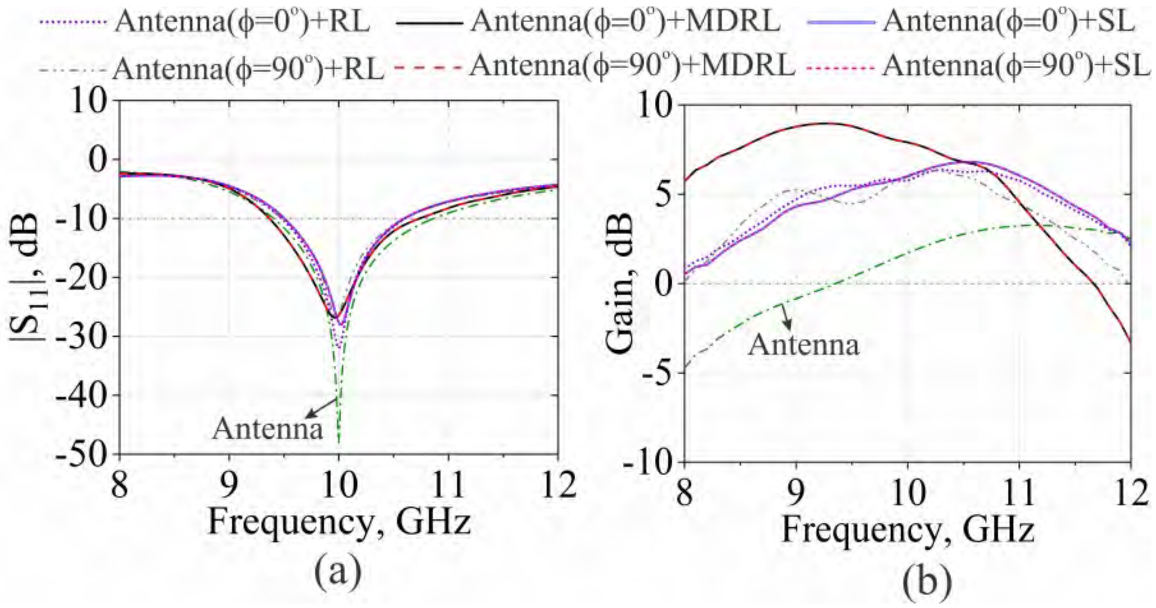

Figure 5.5: Comparison of (a) $|S_{11}|$ dB, and (b) gain at boresight of antenna alone and antenna integrated with RL, MDRL and SL FSSs for two antenna orientations (ϕ=0° and 90°) respectively

From the comparison, it is found that antenna operating frequency and its impedance band remains almost same when the antenna (orientation: ϕ=0°) is loaded with RL, SL and MDRL FSSs. RL and SL FSSs offer a peak gain enhancement of 3.10 dB and 3.54 dB respectively when assembled with the slot antenna while a 5.70 dB gain enhancement is observed when MDRL FSS is combined with the slot antenna. Thus, 5×5 MDRL FSS offers around 2 dB additional gain enhancement when compared to the 5×5 RL and SL FSSs. It appears that MDRL is superior to RL and SL FSS which may be due to its larger unit cell size of and thus the substrate size.

Further, the antenna orientation is changed to ϕ=0° from ϕ=90° by rotating the slot antenna by 90° with respect to Z-axis in XY plane for cross polarization state as also illustrated in Figure 5.4 (d), (e) and (f) respectively. The comparison of reflection coefficient, $|S_{11}|$ dB and antenna gain in boresight (orientation: ϕ=90°) loaded with RL, MDRL and SL FSSs is also depicted in Figure 5.5.

Unlike AS-PI SL FSS, MDRL FSS is an AU FSS but the antenna reflection coefficient as well as gain in boresight direction remain unchanged when orientation of the slot antenna is changed to orthogonal polarization state. Also, there is negligible change in $|S_{11}|$ dB and antenna gain of antenna loaded with RL FSS owing to its PD transmission response. 5×5 PI and PD reflectors both give similar response while 5×5 MDRL is giving high gain due to larger substrate size or larger unit cell size.

Therefore, the substrate size of RL and SL FSS is then made equal to the substrate size of MDRL FSS, i.e., 61×61 mm^2. Thus, RL and SL FSSs arrays with equal substrate dimension of 61×61 mm^2 but now with 7×7 of unit cells are further loaded at the same optimal separation of 21.5 mm and $|S_{11}|$ dB and gain at integrated antenna boresight are compared in Figure 5.6.

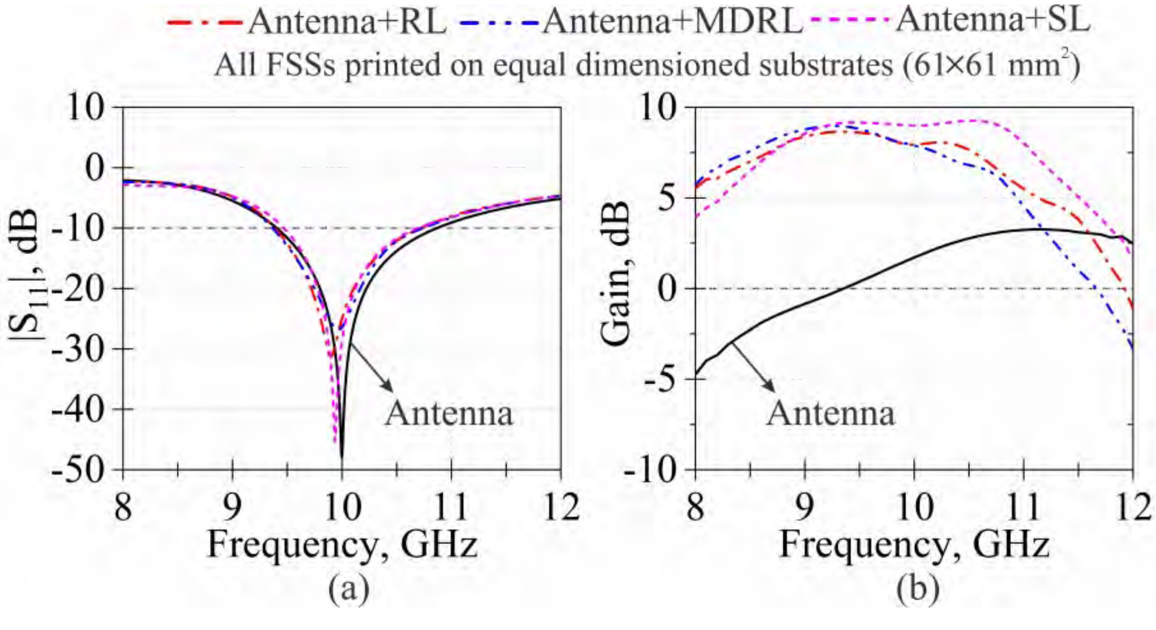

Figure 5.6: $|S_{11}|$ dB, and (b) antenna gain in boresight for slot antenna alone and antenna integrated with RL, MDRL and SL FSSs with equal sized (61×61 mm^2) substrates.

From the comparison, it is found that operating frequency and impedance band for all three FSS when loaded with slot antenna, is maintained. Although, the impedance matching of antenna slightly deteriorates when it is loaded with MDRL FSS and RL

FSSs while the matching improves when loaded with SL FSS. Also, almost similar gain enhancement of antenna is achieved when loaded with these FSSs. Although, SL FSS offers better gain enhancement, it is not marginally large when compared to those obtained by loading RL and MDRL FSSs with the slot antenna.

5.5 Relevance of AS and PI FSSs integrated with antenna

Moreover, to evaluate the significance of AS of these FSSs towards antenna performance enhancement, the FSSs are rotated at angles θ_y and θ_x with respect to Y- and X- directions respectively when the FSSs are kept behind the antenna. The antenna size and separation between antenna and FSSs put an upper bound on the angles, θ_y and θ_x. The maximum angle of rotation θ_m of FSSs with respect to X- or Y-axes while keeping them beneath the antenna is illustrated in Figure 5.7.

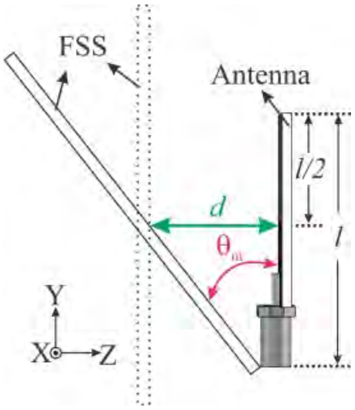

Figure 5.7: Maximum range of 'θ_m' when FSSs are rotated along the Y-axis

If the thickness of the FSS and antenna substrates are not considered, the maximum angle of rotation 'θ_m' may be determined from using equation 5.5.1

$$\theta_m = \tan^{-1}\left(\frac{d}{\sqrt{d^2 + \left(\frac{l}{2}\right)^2}}\right) \tag{5.5.1}$$

The relevance of AS of the FSSs towards gain enhancement of planar antennas is then analyzed through EM simulations. The FSRs are then rotated by angle θ_y and θ_x as shown earlier in Figure 5.4 (a), (b) and (c) respectively. Since, the antenna and FSSs separation is 21.5 mm ($\sim 0.75\lambda_0$), there is an upper bound on FSS rotation angle, θ_m with respect to antenna as computed using equation 5.5.1. Since, the length 'l=39.5mm' (including the length of connector), and d=21.5mm. The angle θ_m becomes 36° which further reduces to 34° if the thickness of antenna and FSS substrate (1.6mm) with thickness of connector are considered. Therefore, the FSRs are rotated, θ_y and θ_x from -30° to 30° alongwith X- and Y- axis respectively.

Figure 5.8 (a) displays the variations in impedance characteristics of antenna integrated with 5×5 unit cell arrays of FSSs against the FSSs rotation with respect to Y-axis. These impedance characteristics are antenna operating frequencies, 'f_r', lower and upper corner frequencies of antenna impedance band, i.e, f_l and f_h respectively.

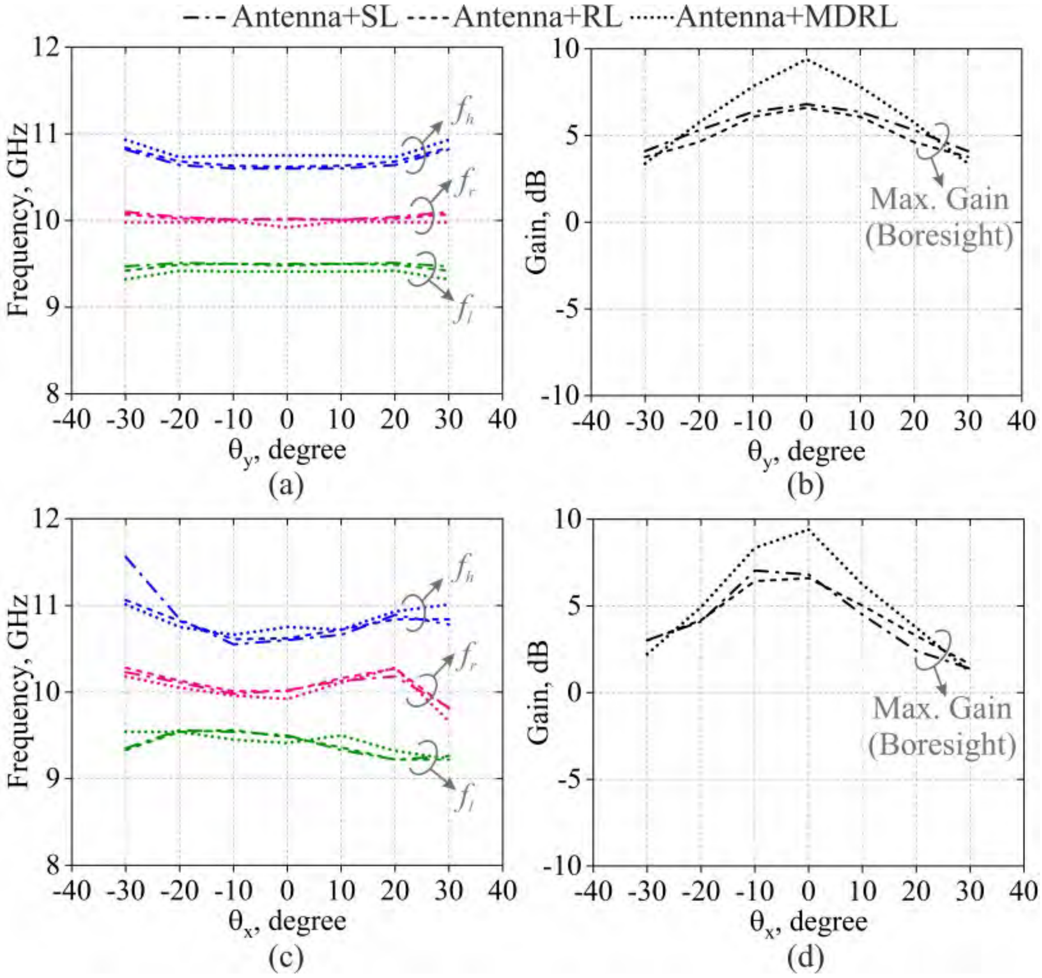

Figure 5.8: Variations in (a) f_r, f_l and f_h, (b) gain in boresight direction of antenna integrated with 5×5 unit cell FSSs arrays against FSSs' rotation angle θ_y; Variations in (c) f_r, f_l and f_h, (d) gain in boresight direction of antenna integrated with 5×5 unit cell FSS array against FSSs' rotation angle θ_x

It is observed that the antenna impedance characteristics do not deviate significantly when FSSs are rotated with respect to Y-axis. The variations in maximum antenna gain in boresight direction while on rotating these FSSs along Y-axis is depicted in Figure 5.8 (b). It is found that antenna gain in boresight direction tends to decay with FSSs rotation behind the antenna. Also, MDRL produces maximum gain at 0° but decays to same level as AS-PD RL FSS and AS-PI SL FSSs when θ_y= ±30°. Decay in gain is shown in case of AS FSS.

These FSSs are then rotated with respect to X-axis and the variations in impedance characteristics as well as maximum boresight gain of antenna integrated with these FSSs against θ_x are depicted in Figure 5.8 (c) and (d) respectively. A slight deviation in f_r, f_l and f_h is observed on the rotation of these FSSs kept behind the antenna. Also, the maximum gain in boresight direction of antenna integrated with FSSs reduces with increased angle of FSSs' rotation. Significantly, MDRL being non-PI and AU FSS provides a comparable performance to RL and SL even if the extra 2 dB gain is ignored due to large unit cell or substrate size.

Figure 5.9 (a) shows antenna impedance variations with rotation of equal substrate (61×61 mm^2) sized FSSs with respect to Y-axis while antenna gain variations are illustrated in Figure 5.9 (b). Similar to arrays of 5×5 unit cells, the 61×61 mm^2 substrate sized FSS rotation also does not affect antenna impedance characteristics while the gain in zenith tends to decrease. On the rotation of equal substrate sized

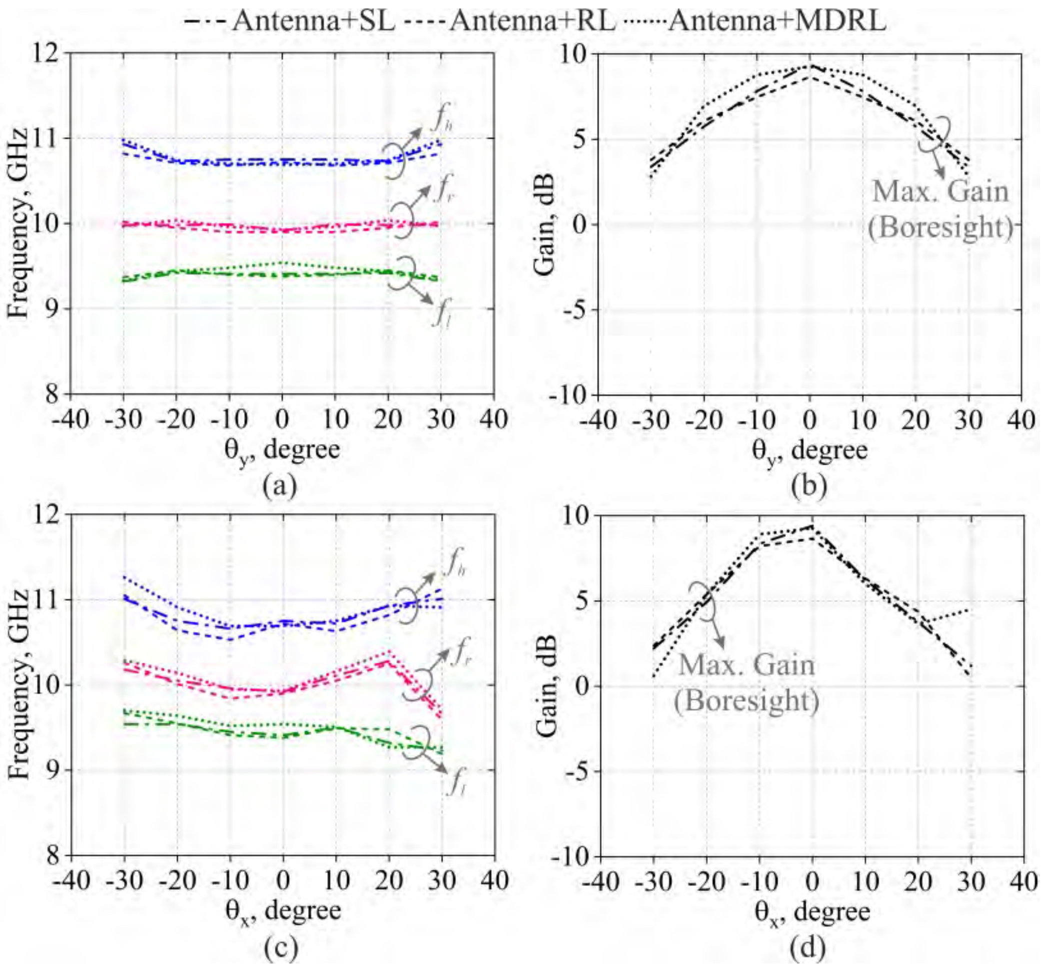

Figure 5.9: Variations in (a) f_r, f_l and f_h, (b) gain in boresight direction of antenna integrated with equal substrate sized FSSs against FSSs' rotation angle θ_y; Variations in (c) f_r, f_l and f_h, (d) gain in boresight direction of antenna integrated with equal substrate sized FSS against FSS' rotation angle θ_x

FSSs kept beneath the antenna with respect to X-axis, a little deviation in f_r, f_l, and f_h is observed as depicted in Figure 5.9 (c). Also, the maximum gain of antennas integrated with 61×61 mm^2 substrate sized FSSs decreases with increasing rotation angle as displayed in Figure 5.9.

Since, the antenna geometry being symmetric about Y-axis, the impedance characteristics and gain in boresight direction exhibit similar variations when FSSs are rotated in either direction with respect to Y-axis which is not followed when FSSs are rotated with respect to X-axis because of asymmetricity of antenna structure with respect to X axis. Thus, gain variation against θ_y is uniformly distributed over $-30° < \theta_y < +30°$ while the variation in gain against θ_x is slightly skewed towards θ_x=-10° instead of 0° due to asymmetricity.

5.6 Fabrication and measurements

The triangular slot (10 GHz) antenna and all the three 5×5 arrays of RL, MDRL and SL FSSs are fabricated employing standard PCB methodologies. The antenna is then backed by these FSSs at optimum separation maintained by EPE foam spacer. The images of antenna prototypes developed for experiments are displayed in Figure 5.10.

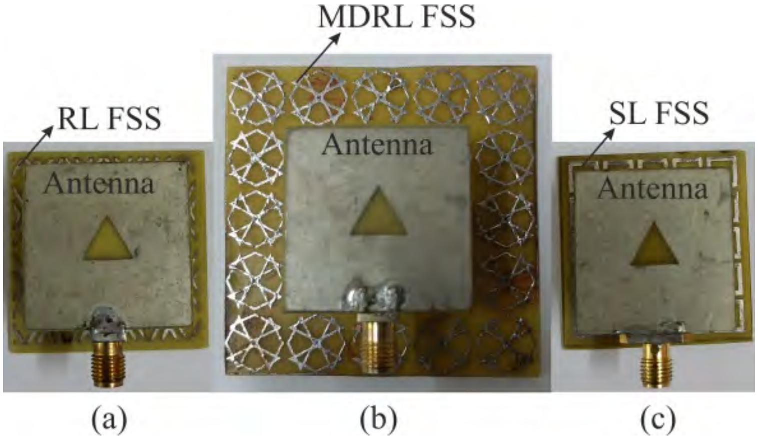

Figure 5.10: Fabricated antenna prototypes loaded with (a) RL FSS, (b) MDRL FSS, and (c) SL FSS respectively

The reflection coefficients, '$|S_{11}|$ dB' of slot antenna and all the antenna prototypes loaded with RL, MDRL and SL FSSs are measured using Keysight N9928A vector network analyzer (VNA). Similarly, antenna boresight gain of all antenna prototypes are evaluated using standard horn antenna where each antenna integrated with FSRs under test and the horn antenna antennas are housed in an anechoic chamber at far-field distance. Figure 5.11 shows the experimentally measured results along with simulated results all together for comparison.

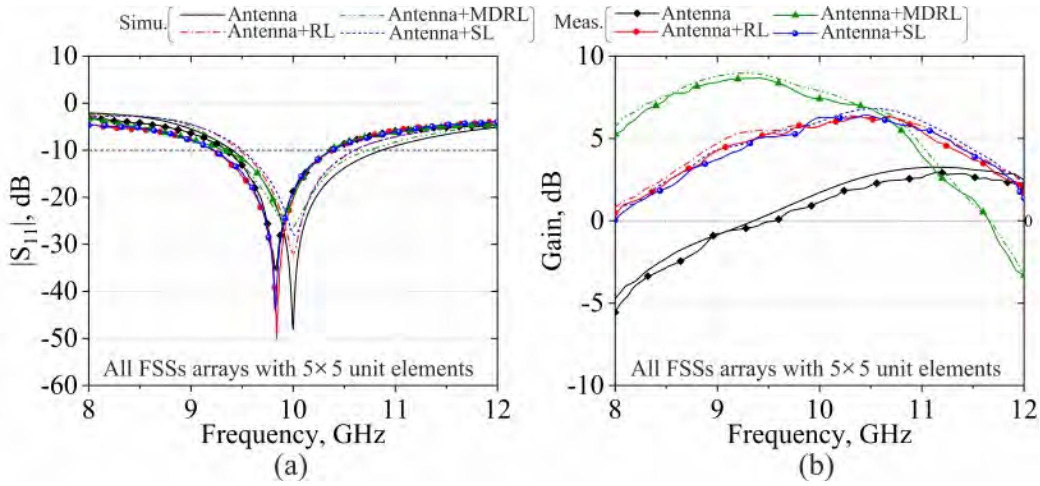

Figure 5.11: Simulated and experimentally measured (a) $|S_{11}|$ dB, and (b) Boresight gain of slot antenna alone, and slot antenna integrated with RL, MDRL and SL FSS respectively

From measurements of $|S_{11}|$ dB of the antennas, it is evident that there is a small but 0.17 GHz drift in operating frequency of antenna when compared to obtained from the simulation due to fabrication errors and practical tolerances. The slot antenna offers 10.45% wide impedance band in the frequency range of 9.34-10.37 GHz and peak boresight gain of 2.97 dB. Similarly, the drift in operating frequencies of antenna integrated with FSSs is due to fabrication errors, practical and substrate (FR-4) material properties of antenna as well as FSSs. The average gain enhancement of 4.87 dB, 4.85 dB and 7.17 dB is obtained when the developed antenna is back by 5×5 arrays of RL, SL and MDRL FSSs respectively. Further, all three FSSs arrays with equal substrate dimension of 61×61 mm^2 are also developed and loaded with the antenna at the same optimal separation, i.e., 21.5 mm. The developed prototypes antennas backed by FSSs are displayed in Figure 5.12.

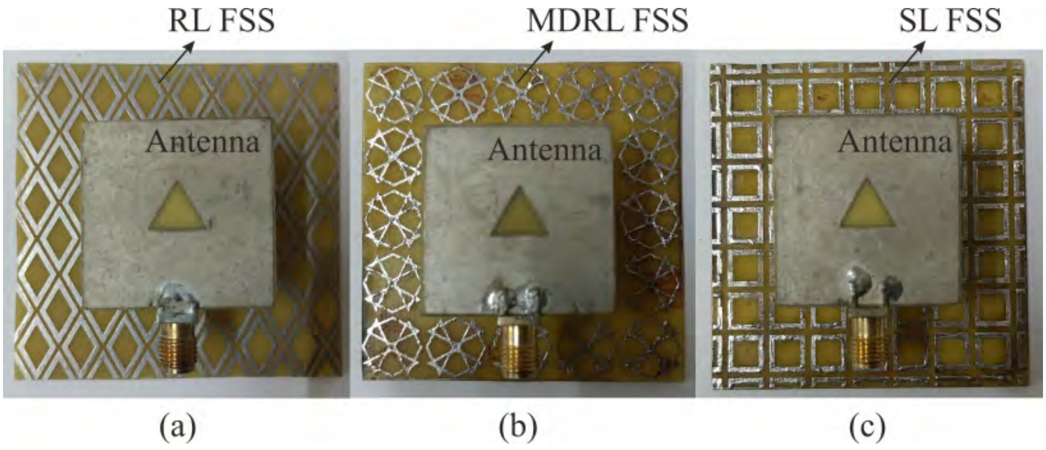

Figure 5.12: Fabricated antenna prototypes loaded with (a) RL FSS, (b) MDRL FSS, and (c) SL FSS, printed on equal dimensioned substrates

The $|S_{11}|$ dB and boresight gain of the three antenna configurations are then obtained through simulations and measured through experiments. A comparison between simulated as well as measured $|S_{11}|$ with boresight gain of antenna backed by all three FSSs reflectors of same dimensions are presented in Figure 5.13.

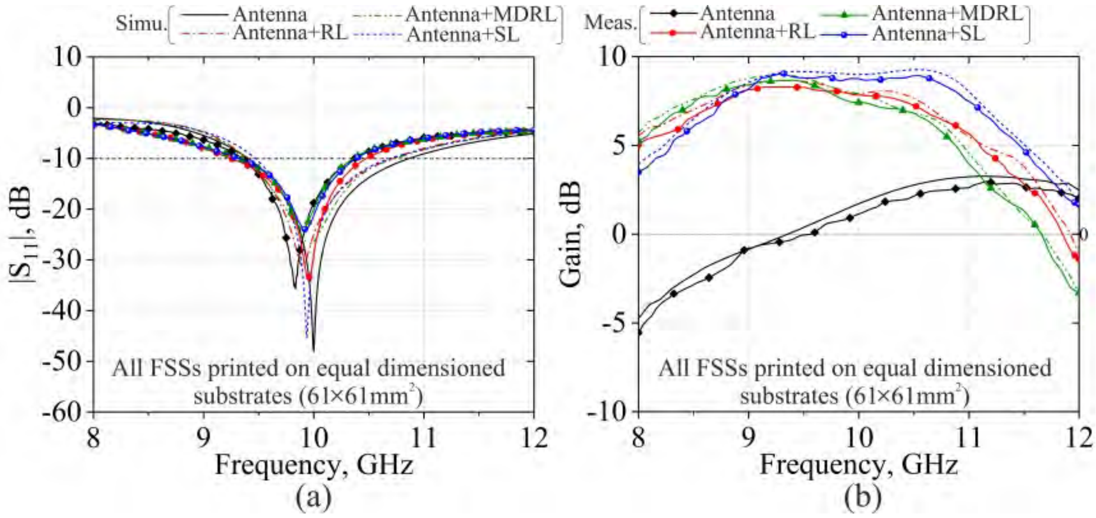

Figure 5.13: Simulated and experimentally measured (a) $|S_{11}|$ dB, and (b) Boresight gain of slot antenna alone and slot antenna integrated with RL, MDRL and SL FSS respectively

Antenna when backed by equal sized FSS reflectors, demonstrate the deviation of 0.05, 0.07, and 0.07 GHz from the simulated operating frequencies when loaded with RL, MDRL and SL FSSs respectively while, the antenna impedance bands are almost retained for all antenna configurations. Moreover, the boresight gains of all the antenna prototypes decently agree with the simulations. From the comparison, it is found that antenna operating frequency and impedance band for all three cases of loaded FSSs is still maintained. Also, a similar gain enhancement of antenna is achieved when loaded with these (61×61 mm^2) FSSs. Although, SL FSS offers superior gain enhancement especially at higher frequencies, it is not a marginally large when compared to those obtained by loading RL and MDRL FSSs with the slot antenna. Therefore, the choice of loading AS or AU FSS does not make much difference.

Other than substrate size, number of unit cells, size and geometry of of the unit structure do not matter for gain enhancement at all. Any loop type unit cell array printed on a substrate size quite larger than the planar antenna will be sufficient antenna gain enhancement. The critical parameter hat preliminarly which ensure good uniform gain within antenna operating band is the distance between antenna and the reflector array and needs optimization before integration with the antenna.

Interestingly, MDRL FSS being non-PI and AU but larger element size demonstrates as a good reflector since, it provides comparable performance with AS and PD reflectors. Simulation results and measurements are also compared in Table 5.3.

Table 5.3: Antenna Simulation and Measurement Results

	Antenna+FSS	Reflector Size	Operating Frequency (GHz)	Impedance Band, % FBW	Peak Boresight gain (dB)	Avg in-band Boresight gain (dB)	Peak Gain Enhancement(dB)	Avg Gain Enhancement(dB)
Simulated	Antenna+RL (5×5)	42.5×42	9.89	9.38-10.72, 13.33	6.37	5.93	3.10	4.23
	Antenna+SL (5×5)	40×40	9.93	9.46-10.70, 12.30	6.80	6.02	3.54	4.32
	Antenna+MDRL (5×5)	61×61	9.96	9.36-10.75, 13.82	8.96	7.69	5.70	5.99
	Antenna+RL (7×7)	61×61	9.9	9.38-10.72, 13.33	8.65	7.94	5.39	6.24
	Antenna+SL (7×7)	61×61	9.9	9.44-10.64, 11.95	9.26	9.11	6	7.41
Measured	Antenna+RL (5×5)	42.5×42	9.84	9.21-10.38, 11.94	6.36	5.56	3.39	4.87
	Antenna+SL (5×5)	40×40	9.82	9.21-10.39, 12.04	6.44	5.54	3.47	4.85
	Antenna+MDRL (5×5)	61×61	9.89	9.32-10.35, 10.47	8.67	7.86	5.70	7.17
	Antenna+RL (7×7)	61×61	9.95	9.25-10.48, 12.47	8.65	7.94	5.68	7.25
	Antenna+SL (7×7)	61×61	9.97	9.31-10.38, 10.87	9.04	8.79	6.07	8.10

From the comparison, it is clear that SL FSS being AS and PI is clearly a winner but non-PI and AU FSSs are not far behind and show comparable performance. Thus, antenna gain enhancement applications using FSRs may not require stringently to characterize FSRs for AS and PI features.

Further, the radiation patterns in both principal planes of all the antenna prototypes are obtained through measurements carried out in the same anechoic environment and normalized before presenting in Figure 5.14.

From the radiation pattern measurements of all antenna prototypes, as expected, the slot antenna radiates in both θ=0° and 180° directions. This antenna demonstrates directional radiation pattern when backed by RL, MDRL and SL FSS respectively. The back lobe (θ=180°) of the antenna is suppressed by 11 dB, 15 dB and 7 dB when antenna is loaded with 5×5 arrays of RL, MDRL and SL FSSs respectively. Additionally, the back lobe is suppressed by 14.5 dB and 16.25 dB when antenna is backed by RL and SL FSSs printed on substrates with equal dimensions to that of MDRL FSS. Therefore, SL FSS suppresses the back lobe of antenna more than RL and MDRL FSSs while RL and MDRL FSSs perform similar in case of equal substrate size. Consequently, it is found that all the reflective FSSs assist in antenna gain enhancement along boresight direction while suppressing back radiation through reflections. Also, the performance of the developed antennas fairly follows the simulations.

The relevance of AS and PI of FSSs towards antenna gain enhancement is also summarized in Table 5.4 through the comparison of previously reported antennas loaded with FSSs in the literature and the performance of present antennas loaded

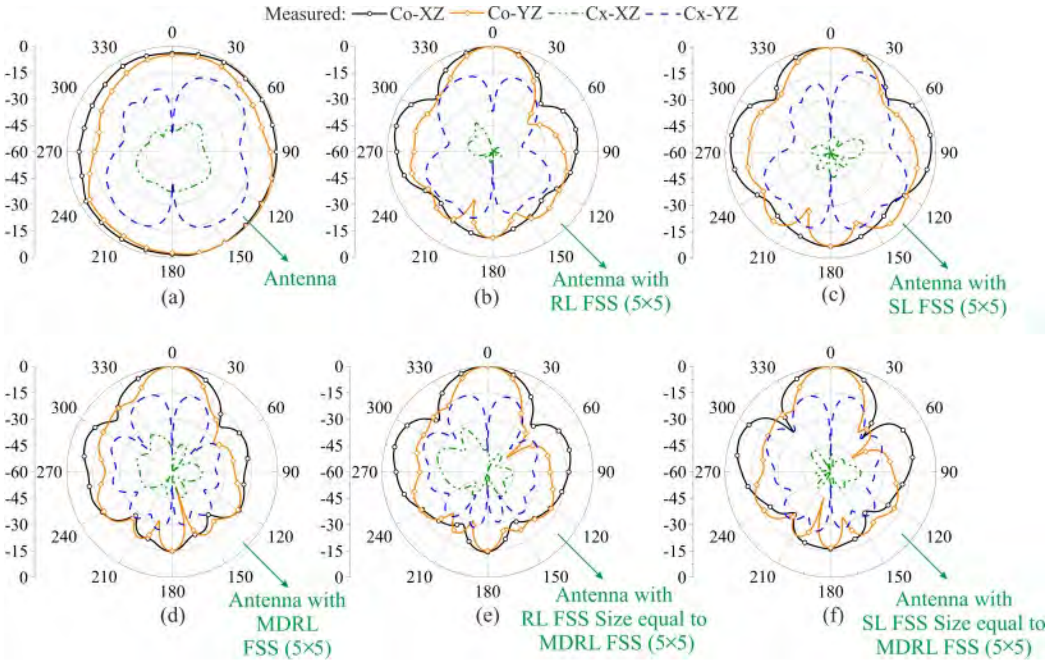

Figure 5.14: Measured radiation patterns of (a) slot antenna, slot antenna loaded with (b) RL FSS (5×5), (c) SL FSS (5×5), (d) MDRL FSS (5×5), (e) RL FSS array size equal to MDRL FSS and (f) SL FSS size equal to MDRL FSS respectively

Table 5.4: Comparison of performance of proposed FSRs performance

Ref. (Year)	Unit cell Dimensions (mm3),Unit cell description	Unit Cell Type	AS	PI	Antenna Type	Reflector (Array of unit cells:n×m)	10dB Impedance band (GHz)	Average Gain Enhancement (dB)
[118], 2018	7×7×2, Four cross shape slots connected with ring slots	Symmetric, single layered, AMC	N.A.	N.A.	Slot-Loop	(4×5)	7.5-13	3.3
[60], 2019	14×14×1.6, Four asymmetric rectangular patches with circular slots	Asymmetric, single sided, single layered	Yes	N.A.	Monopole Antenna	(6×6)	4.7-14.9	4.5
[142], 2021	14×14×1.6, Circular loop combined with two parallel metallic strips	Asymmetric, single sided, single layered	Yes	Yes	Slot Antenna	(7×7)	3.6-6.1	4
[62], 2021	7.25×7.25×2.4, Circular patch surrounded by parasitically coupled patches	Symmetric, single layered, AMC	N.A.	N.A.	Planar dipole	(5×5)	5.08-5.31	N.A.
[138], 2022	15×15×1.6, Square loop connected with inscribed hexagonal loop	Asymmetric, single sided, single layered	No	Yes, At Normal Incidence	Monopole Antenna	(2×3)	2.82-12.92	3.6
This Work(RL FSS)	8.5×14.5×1.6, RL	Asymmetric, single sided, single layered	Yes	No	Triangular slot antenna	a: (5×5), b: (7×7)	a:(9.21-10.38), b:(9.25-10.48)	a: 4.87, b: 7.25
This Work(MDRL FSS)	12.2×12.2×1.6, MDRL	Symmetric, single sided, single layered	No	Yes, At Normal Incidence	Triangular slot antenna	(5×5)	9.32-10.35	7.17
This Work(SL FSS)	6.93×6.93×1.6, SL	Symmetric, single sided, single layered	Yes	Yes	Triangular slot antenna	a:(5×5), b:(7×7)	a: (9.21-10.39), b: (9.31-10.38)	a: 4.85, b: 8.10

with RL, MDRL and SL FSSs. It is evident from present work that developed antenna prototypes integrated with either AU but PD RL FSS or AU MDRL or AS and PI SL FSSs, demonstrate a superior gain enhancement compared to previously reported antennas.

5.7 Conclusion

This study explores the influence of AS and PI FSS on applications for antenna gain improvement. Three distinct loop type FSSs such as SL, TRL and MDRL FSSs are designed and integrated with triangular slot antenna. RL and SL FSSs are formed by printing closely packed arrangements of RLs and SLs and demonstrate stopband response in the X-band frequency range with PD and PI respectively under oblique incidences. The third FSS unit cell is designed by patterning two orthogonally oriented arrays of RLs over a dielectric substrate while keeping the RLs in pairs to exhibit bandstop characteristics with PI under normal incidence. A simple microstrip line feed excited antenna with triangular slot is then produced to operate at 10 GHz. Later, the slot antenna is integrating by all the three finite FSSs composed of same number of (5×5) unit cells but with distinct substrate dimensions at an optimum separation. The significance of AS and PI is then analyzed by rotating the FSSs that are kept behind the antenna with respect to two directions that are orthogonal to one another and loading the FSSs to the two orthogonally orientations of the antenna, respectively. All the three antenna prototypes are fabricated for experimental validation. The gain enhancements of 4.87, 7.17, and 4.85 dB in the boresight direction are achieved when the antenna is loaded by 5×5 RL, MDRL, and SL FSS, respectively. The effectiveness of reflector size is further demonstrated through simulations and experiments by loading the antenna with FSSs developed on equal-sized (61×61 mm^2) substrates. It is found that AS and PI SL FSS is a clear winner by providing 8.10 dB gain enhancement but non-PI and AU RL and MDRL FSSs provide a comparable gain of 7.25 dB and 7.17 dB respectively which suggests that features like AS and PI for an FSS to be a suitable reflector do not appear to be much relevant and can be compromised for gain enhancement applications. The simulations and the measurements agree with one another to a reasonable degree.

Chapter 6

FSSs prospects for THz applications

Since, the transmission response and impact of dielectric as well as conducting materials on the conventional SL and CSL FSSs at THz and even at IR frequency range have already been explored through simulations in chapter 2, the FSSs show promise and are expected to be beneficial at THz frequency range as well. Few more conventional FSSs at THz frequency range are designed and analyzed to demonstrate bandstop and bandpass characteristics. Moreover, the features of such selective transmission may find potential solution to reduce mutual coupling and interference among adjacent functional blocks of an IC. Two such planar and non-planar FSSs are explored in this chapter.

6.1 Introduction

With increased demand of enormous data transfer rate, negligible latency, seamless, almost reliable, real-time links without interference among devices, new standards in THz regime are proposed [143]. EM waves with the frequency range from (0.1 to 10)$\times 10^{12}$ Hz are considered as THz waves and find numerous applications such as imaging and spectroscopy [144], chemical and bio-chemical sensing [145] etc. The signals at THz frequencies are required to be isolated and protected from one another to assist secure communication between devices. Therefore, a selective transmission of THz signals is necessary. FSS may provide a potential solution to such issues for THz wireless communications. At THz frequency range, metallic [146], [147], metallo-dielectric [148], [149] and all dielectric FSSs [150] have been explored for bandpass and band reject characteristics. The inherent features of selective transmission of FSSs make them feasible for few essential requirements such as mutual coupling reduction [151], EM shielding, etc. Several FSSs based on conventional unit cells such as metallic square patch [152], [153], aperture [154], loop [155], ring aperture as complementary loop [156], cross [157], [158], etc, are widely explored at microwave to optical frequency regime.

Recently, FSS are also integrated with THz antennas for gain enhancement [159], [160] and RCS reduction applications [161]. Moreover, FSSs have also been investigated in MIMO applications to minimize mutual coupling between adjacently positioned antennas [162]. Since, cross-shaped graphene-based FSS arrays [163] and inductively coupled resonators [151] are investigated as potential methods for reducing the mutual coupling between planar antennas, there is a huge scope of exploiting the inherent characteristics of FSSs at THz frequency range.

6.2 Electromagnetic isolation

To develop ICs at THz is challenging because the functional blocks of IC are susceptible to interference and power coupled by individual blocks [164]. Such ICs require a precise floorplan in order to accomplish a high level of isolation between adjacent as well as distant blocks without compromising other constraints of IC design, such as layout plan and delay budget. The stopband FSSs could be a potential solution for such challenges. In this section, metallo-dielectric FSSs based on pixeleted pattern are designed and proposed to improve isolation among functional blocks of THz ICs.

6.2.1 Unit cell design

The unit cell layouts are depicted in Figure 6.1. As displayed in Figure 6.1 (a), Square patches are arranged as a 4×4 array with gold layer of 0.1 μm thickness are patterned on a 1μm thick silicon dioxide SiO_2 substrate (ε_r=3.9). By adjusting the electrical lengths of these pixels, the transmission response of FSSs can be modified. The geometric features 'a' = 60 μm, 'p' = 90 μm, and 'g' = 30 μm are depicted in

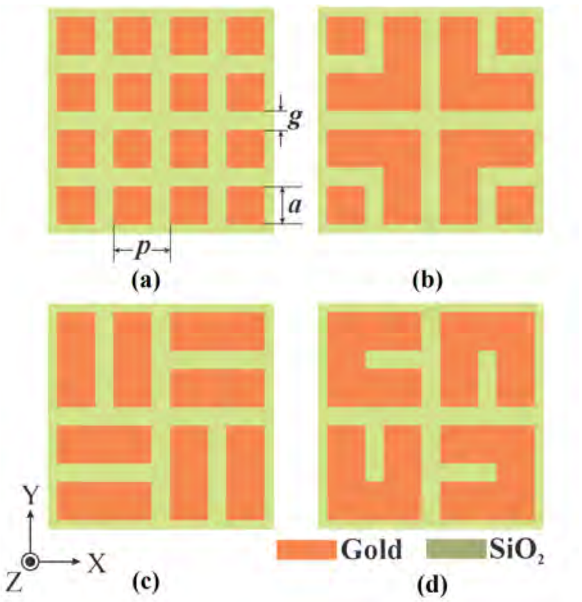

Figure 6.1: Unit cell designs (a) FSS-1, (b) FSS-2, (3) FSS-3, and (d) FSS-4

Figure 6.1. To determine the length electrically, any linear connection among any two pixels is considered to equal to $g + 2a$, whereas a bend with 90° will result in '$2g+3a$' or '$a+2p$', as shown in Figure 6.1.

6.2.2 Results and discussions

The unit structures of FSSs are evaluated using full-wave simulations, with boundary conditions employed to both vertical and horizontal orientations periodically. Figure 6.2 and Table 6.1 illustrate and compare the wave propagation properties of unit cells of all FSSs. In Table 6.1, all FSSs are assessed based on bandstop frequency (f_{stop}), passband frequency (f_{pass}), transmission, isolation 10 dB stopband (The frequency range where $|S_{21}| \leq$ -10 dB), 3 dB passband (the frequency range where $|S_{21}|$ $\geq$3dB) and at last, FBW respectively. The transmission properties of the array of unconnected and interconnected pixels resemble those of a bandstop-bandpass filter, with the bandstop frequency (f_{stop}) appearing at a lower frequency than the band-

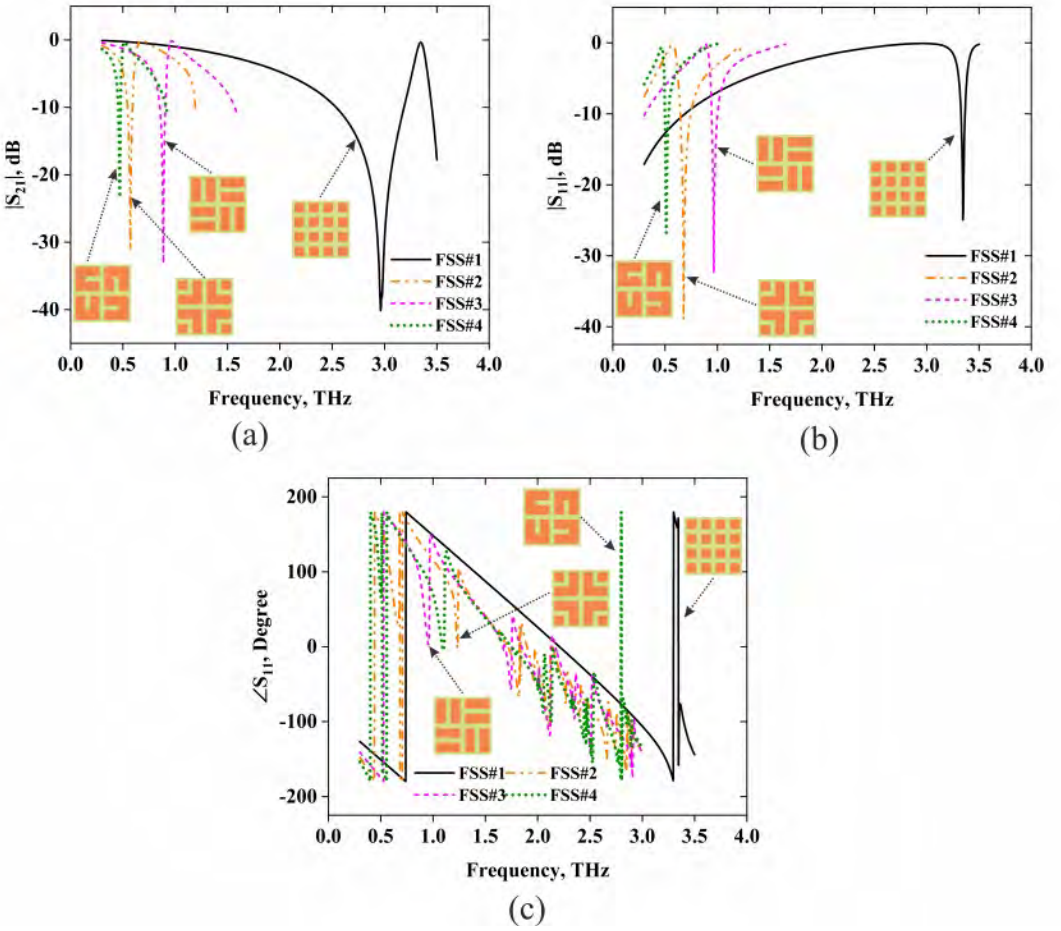

(a)

(b)

(c)

Figure 6.2: Transmission response of FSSs (THz) (a) $|S_{21}|$ (dB), (b) $|S_{11}|$ (dB), and (c) $\angle S_{11}$ (degree)

Table 6.1: Transmission properties of FSS-1 to FSS-4

FSS	StopBand			PassBand		
	f_{stop} (THz), Isolation (dB)	10dB stopband (THz)	FBW (%)	f_{pass} (THz), Transmision (dB)	3-dB Passband (THz)	FBW (%)
FSS-1	2.97 (-41.41)	2.54-3.18	22.37	3.35 (-0.45)	3.29-3.39	2.99
FSS-2	0.57 (-31.51)	0.54-0.59	8.84	0.67 (-0.10)	0.62-0.99	45.96
FSS-3	0.88 (-33.36)	0.85-0.91	6.82	0.96 (-0.16)	0.93-1.16	22
FSS-4	0.47 (-23.3)	0.45-0.47	4.34	0.51 (-0.37)	0.49-0.66	29.56

pass frequency (f_{pass}). When compared to FSS-2, FSS-3, and FSS-4, the FSS array of disconnected pixels has a broader stopband and superior signal rejection capacity. However, when interconnected over itself, the FSS array rejects bands at distinct frequencies from one another. This also indicates that interconnections tend to reduce rejection frequencies. Figure 6.2 (c) depicts that the linearity in the reflection phase of FSS-1 is maintained over a broad range of frequencies compared to the other three FSSs.

In this work, a metal over dielectric pixelated unit cell array-based FSS is presented as a method for providing electromagnetic isolation among blocks of THz IC architecture in order to combat EMI is suggested. In one FSS, square patches of metal supported by a substrate made of SiO_2 forms the structure, while in other three FSSs, the structures are formed by interconnections between individual pixels. Proposed FSSs are capable of rejecting electromagnetic THz signals between 0.3 and 3 THz. Wire bonding pads may be employed as periodically patterned arrays of decoupling FSSs to reject EMI within architecture of ICs intended for application in THz range.

6.3 Mutual coupling reduction

This section contains a three-dimensional (3D) array of dielectric micropillars of cubic form located repeatedly in a single and two dimensional grid. When the micro pillars are illuminated by EM waves from two perpendicular planes, arrays show narrow band rejection at THz frequency ranges where air is assumed to be filled in the gaps between micro pillars. Later, the gap among the micro pillars is filled with SiO_2 for purposes of comparison. Afterwards, metal is applied to dielectric pillars. The wave propagation characteristics of all THz FSSs are demonstrated and analysed using EM full-wave simulations. Observations suggest that a metal layer results in a broader band rejection than dielectric surfaces. The proposed method is an effective means to diminish interference and coupling within THz ICs.

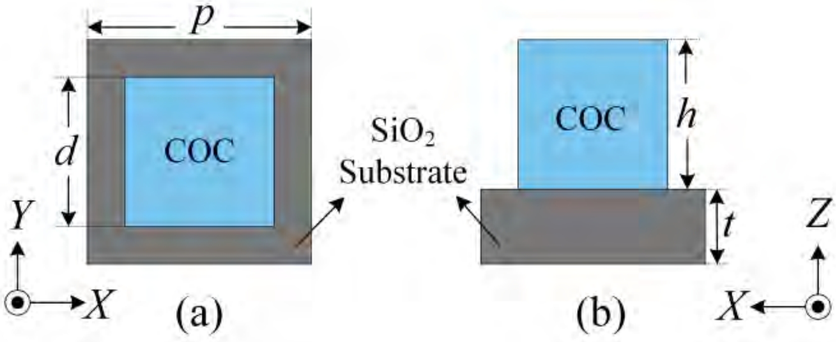

Figure 6.3: Design of micro pillar based unit cell:(a) Top View, (b) Side View

6.3.1 Design of unit cells and FSS arrays

As displayed in Figure 6.3, the proposed all-dielectric FSS (AD-FSS) is composed of up of an array of cubic pillars by depositing cyclic olefin copolymer (COC) polymer (ε_r = 2.3 and tanδ= 0.007) over a SiO_2 substrate.

The geometric parameters, where,'d' is the edge of cube, 'P' is the periodicity, and 'h' is the COC pillar height,while 't' is the SiO_2 substrate thickness, are also depicted in Figure 6.3, with values of 90, 60, 60, and 30 μm, respectively. The unit cell element is designed such that the substrate thickness and inter-pillar spacing stays constant, i.e., '$d = h$', implying that the COC pillar is actually a cubic unit cell. The periodicity,'p' is approximately 0.5 $\lambda_{eff}^{-1/2}$, where λ is the wavelength at 1 THz and ε_{eff} is the effective permittivity determined by the weighted average method. The substrate dielectric FSS (SD-FSS) is formed when the oxidation process replaces the air in inter-element spacing among COC cubic pillars with a SiO_2 layer of thickness equivalent to 'h'. In addition, a metalo-dielectric FSS (MD-FSS) can be formed by selectively metallizing only the COC cubes of an AD-FSS to produce a gold layer 0.01 μm thick.

6.3.2 Results and discussions

Figure 6.4 (a), (b), and (c) illustrate the construction of the 1×3 arrays used in AD-FSS, SD-FSS, and MD-FSS, respectively. Simulations are carried out for these finite arrays by employing wave ports in X-Y plane-shown as k_z) and Y-Z plane-shown as k_x) directions in Figure 6.4. Then, the wave ports in k_z and the k_x directions are applied to the 3×3 finite arrays of AD-FSS, SD-FSS, and MD-FSS, respectively. Since, 3×3 array look to incident waves incident from k_x or k_z directions, similar propagation characteristics are expected.

Figure 6.5 (a) compares the responses of 1×3 arrays of AD-FSS, SD-FSS, and MD-

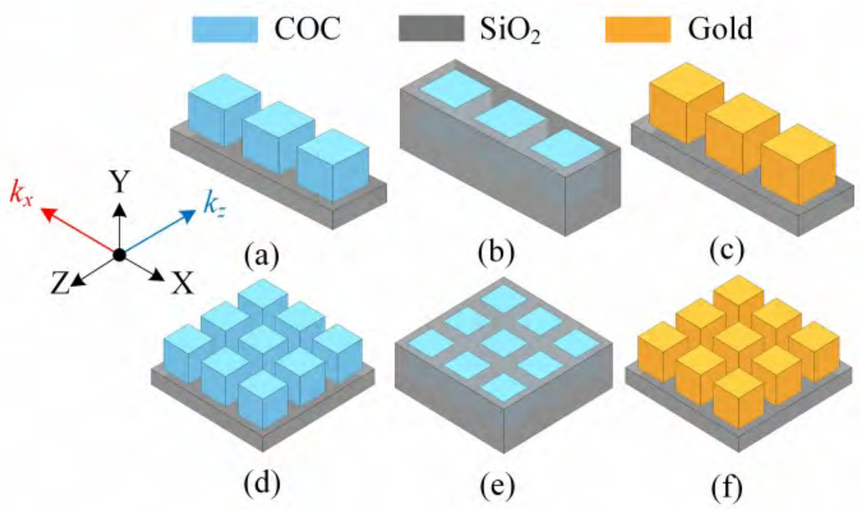

Figure 6.4: FSS (1×3) array (a) AD-FSS, (b) SD-FSS, (c) MD-FSS, FSS (3×3) (d) AD-FSS, (e) SD-FSS and (f) MD-FSS

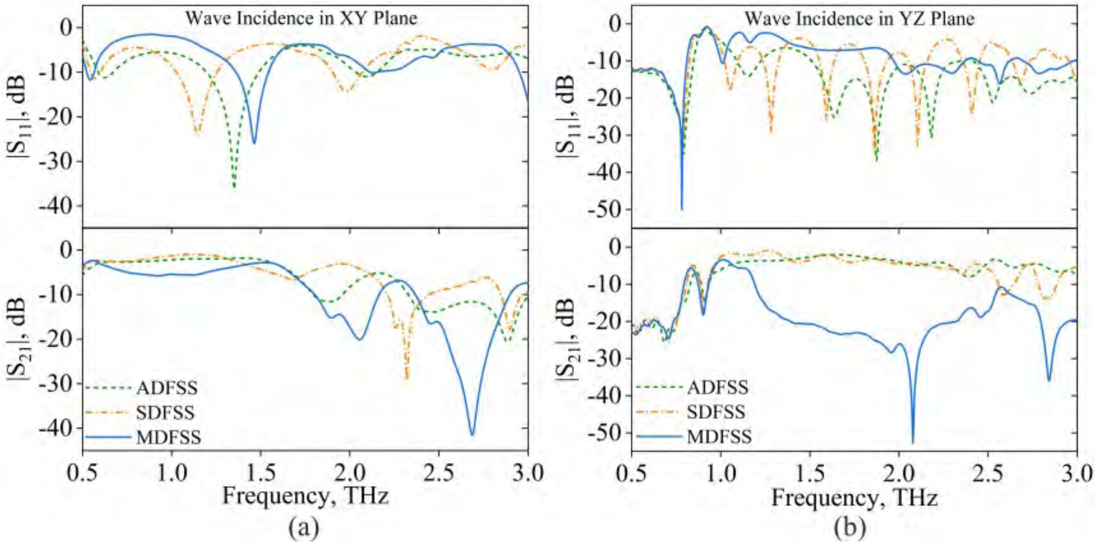

Figure 6.5: Comparison of propagation characteristics of AD-FSS, SD-FSS and MD-FSS for (a) 1×3 and for (b) 3×1 arrays

FSS when exposed to EM waves incident in the k_z direction or XY plane. AD-FSS offers wideband rejection with two center frequencies that are respectively 1.89 and 2.32 THz, whereas SD-FSS facilitates propagation at lower frequencies. SD-FSS is an excellent option for narrowband rejection applications due to the fact that it offers a stopband that is 0.24 THz broad operating at a frequency of 2.32 THz. Contrarily, MD-FSS is an excellent choice for achieving greater isolation across a broad frequency range.

Figure 6.5 (b) compares the responses of the 1×3 arrays of AD-FSS, SD-FSS, and MD-FSS when exposed to EM waves propagating in the k_x direction. AD-FSS and SD-FSS both support the partial propagation of EM as evident due to the increase in

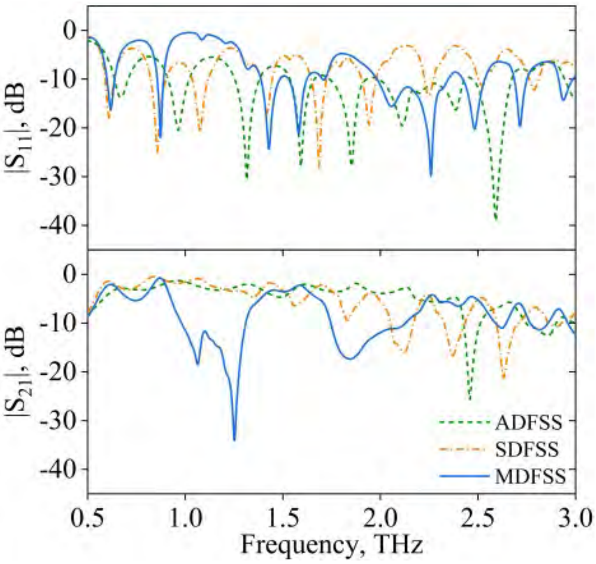

Figure 6.6: Magnitudes of transmission and reflection coefficients compared for 3×3 arrays of AD-FSS, SD-FSS and MD-FSS

Table 6.2: Comparison of COC based FSS arrays

Array	EM Wave incidence plane	Peak Isolation (dB), Frequency (THz)	Stopband	Fabrication Complexity
ADFSS	XY	-25.78, 2.88	Narrow	Low
	YZ	-25.82, 0.68		
	XY or YZ	-25.63, 2.45		
SDFSS	XY	-29.14, 2.32	Narrow	Low
	YZ	-25.59, 0.7		
	XY or YZ	-21.22, 2.63		
MDFSS	XY	-41.59, 2.68	Wide	High
	YZ	-53.04, 2.07		
	XY or YZ	-34.08, 1.24		

losses in the THz range. However, MD-FSS has an extremely broad stopband and a high level of signal isolation. Figure 6.6 compares the responses of a 3×3 array of AD-FSS, SD-FSS, and MD-FSS. MD-FSS here again exhibits a higher isolation alongwith a wider stopband near 1 THz, whereas AD-FSS exhibits a narrower bandstop at higher frequencies. SD-FSS enables transmission at lower frequencies and prohibit the transmission on EM signals partially at higher frequencies.

Table 6.2 also provides a summary of the propagation characteristics of COC based FSS arrays. MD-FSS fabrication mandates 3D metallization process, which increases the process complexity in development of ICs. If complexity is not an issue, only the interacting faces of cubic pillars may be coated with metal. However, AD-FSSs are less expensive and an effective method for preventing unwanted interferences and cross-talk at THz. In lieu of COC, more popular but lossy poly-methyl-methacrylate (PMMA) can be utilized to obtain nearly equivalent propagation characteristics. Tuning of the frequencies of stopbands is possible by further optimizing the geometrical features of COC pillars.

6.3.3 Conclusion

All dielectric and metalo-dielectric pillar based finite FSSs arrays for reduction of mutual coupling in ICs operating at THz are investigated and presented here. The cubic pillar array is organized in a single straight line and later in a square grid, while it is exposed to by EM waves from two orthogonally lateral X- and Y- directions. Both SiO_2-filled COC micro pillars based arrays and metal-coated COC micro pillars based arrays are investigated and compared. Comparing the propagation characteristics of all micro pillar based FSSs demonstrate that AD-FSS is a cost-effective and efficient in reducing mutual coupling in narrowband frequency ranges, whereas MD-FSS has a broader stopband and superior rejection magnitude. Therefore, the proposed AD-FSS and MD-FSS serve as solutions for mitigating crosstalks in THz ICs of the next generation.

Chapter 7

Conclusions and future directions

7.1 Conclusion

The thesis presents and discusses the features and characteristics of FSS reflectors and their impact on compact antennas for gain enhancement applications.

To accomplish the objectives of the thesis, the thesis begins with a comparison of CD and SL FSS. Using full-wave EM simulations, these fundamental unit cells are analysed. For an infinitely large array FSS, the characteristics of of these unit cells translated by half the periodicity in the horizontal and vertical directions remain unchanged. Comparing CD with SL-FSS suggests that SL array offers a wider bandwidth and higher signal isolation level than CD array. FSS made up of low-loss substrate show a high potential to reject incident EM waves.

With such observations, the conventional SL FSSs and its complement, CSL are further analyzed for microwave to IR frequency ranges. The transmission responses of both FSSs at 3, 15, 33 and 200 GHz are compared alongwith two frequencies in THz, i.e., 3 THz, and 300 THz. In order to develop FSSs at required operating frequency, widths of stopband and passband, signal isolation/transmission, the role of metal and dielectric layer on these FSS transmission properties are investigated. It is found that low-loss substrates increase signal isolation as expected while wave transmission degrades at THz and IR range.

Then, the rectangular loop, elliptical loop, and rhombic loop-based unit cells with asymmetric diagonals are designed and analysed to compare their transmission responses for normally incident EM waves. The responses of these FSSs are also studied when they are illuminated by obliquely incident TE/TM waves. Despite the fact that these FSSs are PD by nature, they are AS. When orthogonally oriented PD FSSs are stacked BTB on opposite sides of the FR-4 substrate, stopband with broader rejection range are observed. However, cascaded FSSs such as BTB RECT, BTB ELIP, and BTB RL FSSs exhibit similar S_{21}, whereas the reflection phases of these FSSs are nonlinear. Later, when both orthogonally oriented PD FSS arrays are printed on any one of the sides of the FR-4 substrate, these nonlinearities are compensated.

Further, DRL based wide bandstop reflectors are designed using two orthogonal layers of PD rhombic loops arranged in pair. Both layers are printed on opposite sides of the FR-4 laminate to develop a wide stopband BTB DRL FSS. By bringing both orthogonal pairs on the same side of a FR-4 substrate, the reflection phase non-linearity is compensated. The BTB DRL exhibits a wide 4.3 GHz stopband with two zero resonances at 7.9 and 10 GHz, whereas MDRL provides a 3.7 GHz wide stopband with a strong rejection magnitude capability. The effectiveness of these FSS reflectors towards compact antenna gain is then investigated. Three discinct configurations of DRL FSS reflectors such as CDRL, BTB DRL and MDRL reflectors are applied beneath a triangular slot antenna operating at 10 GHz. The antenna impedance band and radiation characteristics are then investigated through simulations. For experiments, the proposed MDRL FSS is further integrated with triangular slot antenna. The triangular slot antenna demonstrates an impedance band of 7.79 - 8.61 GHz with a boresight gain of 3.88 dB at 8.2 GHz. After the antenna is integrated with the proposed MDRL FSS, an impedance band of 640 MHz from 7.96 to 8.6 GHz with an enhancement of gain by 8.38 dB is attained in the antenna boresight at 8.31 GHz. An enhancement of 4.5 dB in antenna gain is achieved using frequency selective reflector with linear reflection phase.

Afterwards, an attempt to expand the width of the stopband to attain a wide or UWB is made. Hence, two FSS with WB and UWB rejection potential based on a RLP array are proposed and experimentally validated. On a dielectric substrate, two PD RLP unit cells orthogonally oriented to each other and arrayed in a square grid are printed BTB that exhibit PI and wide rejection band. In addition, RLP unit elements when arranged in a rectangular grid further increase the rejection BW. Similar to MDRL FSS, MRLP and MDRLP FSSs also demonstrate linearities in phase reflection. Before their fabrication and experimental verification, wave propagation and polarisation characteristics of MRLP and MDRLP FSSs are analyzed. The proposed MRLP is PI, AS and a C-band reflector possessing linear reflection phase. The MDRLP FSS is not AS but rejects UWB from 2.3 to 11.5 GHz for both TE and TM incidences.

In addition, a Norman window-shaped slot antenna is designed, and experimentally validated to exhibit a steady and bidirectional radiation pattern throughout the UWB. The effect of antenna-MDRLP reflector integration on the impedance matching and antenna radiation patterns in different arrangements is studied. The optimal configuration for experimental validations is determined, then its radiation characteristics are studied. The Norman window slot antenna exhibits a directional radiation pattern when combined with the UWB FSS as the back lobe in the antenna radiation pattern is suppressed due to the presence of UWB reflector. When FSS is applied as a reflector between the antenna, the proposed antenna exhibits an enhancement of gain by 3.6 dB in the antenna boresight. This takes the peak gain to a value of 7.86 dB in the boresight direction.

Tessellated TRL based FSS for bandstop characteristics is suggested and developed to increase the gain of a modified hexagonal slot antenna when excited by a sectoral feed for UWB frequencies. The slot antenna is integrated in different combinations with RL FSS from slot and feed sides to evaluate FSS loading on antenna performance. Slot antenna prototypes with RL FSS loaded at slot and feed sides are built and tested. The antenna has 4.31 dB peak gain in zenith and 4 dB in nadir. RL FSS loaded at feed side increases zenith gain by 2.4 dB and nadir gain by 3.8 dB.

Three loop-type FSSs- SL, RL, MDRL are also integrated with triangular slot antenna operating at 10 GHz. RL and SL FSSs are generated by printing densely packed RLs and SLs which show stopband in the X-band region with PD and PI responses under oblique incidences. MDRL also show bandstop properties with alike TE and TM responses under normal incidence. A fundamental 10 GHz microstrip line fed triangular slot antenna is then developed. Later, the three finite FSSs with the same number of (5×5) unit cells but different substrate sizes back the slot antenna at an optimal spacing. The importance of AS and PI is examined by rotating the FSSs behind the antenna in two orthogonal directions and loading them to two antenna orientations. Three separate antenna prototypes are made for experimental validation. Loading the antenna with RL, MDRL, or SL FSS increases boresight gain by 4.8, 7, or 4.8 dB. Simulations and tests show the efficacy of reflector size by loading the antenna with FSSs constructed on equal-sized (61×61 mm^2) substrates. It is found that SL FSS being AS and PI is a clear winner by providing 8.1 dB gain enhancement, but RL and MDRL FSSs, although PD and AU, provide comparable gains of 7.25 dB and 7.17 dB, respectively, recommending that features like AS and PI for an FSS to be a suitable reflector are not much relevant atleast in gain enhancement applications. FSSs at THz frequency range (300GHz-3THz) are also designed and explored for suitable application. A metalo-dielectric pixel array-based FSS is presented first as a method for providing EM isolation among adjacent and distant blocks contained within architecture of futuristic THz ICs. In one FSS, patches of square form made of gold supported by substrate made up of SiO_2 forms the structure, while in three other FSSs, the structures are formed by interconnections between individual pixels. Proposed FSSs are capable of rejecting electromagnetic THz signals between 0.3 and 3 THz. The array of pixelated form of square patches can be employed as decoupling FSSs to reject frequency bands within ICs visioned for THz communication applications if they are patterned periodically.

Finally, arrays of dielectric as well as metalo-dielectric unit structure for reduction of mutual coupling in THz ICs have also been investigated. The dielectric cubic micro pillars are organized in a single direction and in a square grid, before it is exposed to EM waves from two orthogonal directions laterally. Arrays of SiO_2-filled and metal-coated COC micro pillars are investigated. Comparing the transmission responses COC pillar based FSSs concludes that AD-FSS is a cost-effective and efficient technique for reducing mutual coupling in narrowband frequency ranges, whereas MD-FSS has a broader stopband and superior signal rejection magnitude. Therefore, the proposed AD-FSS and MD-FSS serve as solutions for mitigating EMI in THz ICs of the next generation.

The simulations and measurements exhibit reasonable agreement with each other. Overall, this thesis provides a comprehensive analysis and experimental validation of FSS reflectors for gain improvement applications in slot antennas.

7.2 Future scope and prospects

From the conclusion made from the work presented in this thesis, it is evident that there is still a wide spectrum of applications where FSSs may be designed and explored further. Apart from integrating FSSs reflectors with compact antennas, they may be employed as superstrate also to expect high directive beams with enhanced gain. These techniques may further be incorporated with multiple antennas for mutual coupling reduction and in MIMO antennas [165]. Moreover, use of active FSSs has also been introduced as key enabler approaches to attain highly directional antenna [112], reconfigurable beam generations [166],and beam steering [167] for the existing and the forthcoming wireless applications. Also, the features of reconfigurable transmission characteristics of active FSSs offer potential solutions to modern wireless communications as intelligent reflecting surfaces [168], [169], intelligent omni surfaces [170], [171] and so on.

List of Publications

Journals

- Verma, Ashish Kumar, and Rahul Singhal,“Performance analysis of frequency selective reflectors based on rectangular loop pair for wideband applications.” *AEU-International Journal of Electronics and Communications* (2023)
- Verma, Ashish Kumar, and Rahul Singhal,“Norman window slot antenna with sectoral feed backed by linear phase reflector for ultra wideband applications.” *International Journal of RF and Microwave Computer-Aided Engineering* (2022) pp(e23433); 32(12).
- Verma, Ashish Kumar, and Rahul Singhal,“Dual rhombic loop-based frequency selective surfaces for X-band applications.”*Microwave and Optical Technology Letters* 64.11 (2022): 1944-1950.

Conferences

- Verma, Ashish Kumar, and Rahul Singhal,“Planar X-Band Reflecting Surfaces Based on Rhombic Loop Pair.” *2022 IEEE Microwaves, Antennas, and Propagation Conference (MAPCON).* IEEE, 2022.
- Verma, Ashish Kumar, and Rahul Singhal,“Performance Analysis of Traditional Band Pass/Band Stop Frequency Selective Surfaces for Distinct Frequency Domains of Electromagnetic Spectrum.” *2022 IEEE Microwaves, Antennas, and Propagation Conference (MAPCON).* IEEE, 2022.
- Verma, Ashish Kumar, and Rahul Singhal,“Frequency Selective Surfaces for Electromagnetic Isolation at Terahertz Frequencies.“*2021 IEEE Indian Conference on Antennas and Propagation (InCAP).* IEEE, 2021.
- Verma, Ashish Kumar, and Rahul Singhal,“Mutual Coupling Reduction in THz Integrated Circuits using Cubic Micropillar Array.” *2021 IEEE Asia-Pacific Microwave Conference (APMC).* IEEE, 2021.
- Verma, Ashish Kumar, and Rahul Singhal,“Comparative study of translated cross dipole and square loop frequency selective surfaces for band stop characteristics in X-band.” *2020 IEEE Asia-Pacific Microwave Conference (APMC).* IEEE, 2020.

Bibliography

[1] H.-N. Dai, K.-W. Ng, M. Li, and M.-Y. Wu, "An overview of using directional antennas in wireless networks," *International journal of communication systems*, vol. 26, no. 4, pp. 413–448, 2013.

[2] A. R. Varkani, Z. H. Firouzeh, and A. Z. Nezhad, "Design of a randomised arrangement amc surfaces for rcs reduction based on equivalent circuit modelling," *IET Microwaves, Antennas & Propagation*, vol. 12, no. 10, pp. 1684–1690, 2018.

[3] J. de Dieu Ntawangaheza, L. Sun, C. Yang, Y. Pang, and G. Rushingabigwi, "Thin-profile wideband and high-gain microstrip patch antenna on a modified amc," *IEEE Antennas and Wireless Propagation Letters*, vol. 18, no. 12, pp. 2518–2522, 2019.

[4] S. Peddakrishna, T. Khan, and B. K. Kanaujia, "Resonant characteristics of aperture type fss and its application in directivity improvement of microstrip antenna," *AEU-International Journal of Electronics and Communications*, vol. 79, pp. 199–206, 2017.

[5] P. K. Panda and D. Ghosh, "Isolation and gain enhancement of patch antennas using emnz superstrate," *AEU-International Journal of Electronics and Communications*, vol. 86, pp. 164–170, 2018.

[6] V. K. Kanth and S. Raghavan, "Em design and analysis of frequency selective surface based on substrate-integrated waveguide technology for airborne radome application," *IEEE Transactions on Microwave Theory and Techniques*, vol. 67, no. 5, pp. 1727–1739, 2019.

[7] D. Sievenpiper, L. Zhang, and E. Yablonovitch, "High-impedance electromagnetic ground planes," in *1999 IEEE MTT-S International Microwave Symposium Digest (Cat. No. 99CH36282)*, vol. 4. IEEE, 1999, pp. 1529–1532.

[8] A. Monorchio, G. Manara, and L. Lanuzza, "Synthesis of artificial magnetic conductors by using multilayered frequency selective surfaces," *IEEE Antennas and Wireless Propagation Letters*, vol. 1, pp. 196–199, 2002.

[9] B. A. Munk, *Frequency selective surfaces: theory and design.* John Wiley & Sons, 2005.

[10] A. E. Farahat, K. F. A. Hussein, and N. M. El-Minyawi, “Spatial filters for linearly polarized antennas using free standing frequency selective surface,” *Progress In Electromagnetics Research M*, vol. 2, pp. 167–188, 2008.

[11] A. R. Weily, L. Horvath, K. P. Esselle, B. C. Sanders, and T. S. Bird, “A planar resonator antenna based on a woodpile ebg material,” *IEEE Transactions on Antennas and Propagation*, vol. 53, no. 1, pp. 216–223, 2005.

[12] G. I. Kiani, K. L. Ford, K. P. Esselle, A. R. Weily, and C. J. Panagamuwa, “Oblique incidence performance of a novel frequency selective surface absorber,” *IEEE Transactions on Antennas and Propagation*, vol. 55, no. 10, pp. 2931–2934, 2007.

[13] M. Nauman, R. Saleem, A. K. Rashid, and M. F. Shafique, “A miniaturized flexible frequency selective surface for x-band applications,” *IEEE Transactions on Electromagnetic Compatibility*, vol. 58, no. 2, pp. 419–428, 2016.

[14] S. Narayan, B. Sangeetha, and R. M. Jha, “Frequency selective surfaces-based high performance microstrip antenna,” in *Frequency Selective Surfaces based High Performance Microstrip Antenna.* Springer, 2016, pp. 1–40.

[15] R. S. Anwar, L. Mao, and H. Ning, “Frequency selective surfaces: a review,” *Applied Sciences*, vol. 8, no. 9, p. 1689, 2018.

[16] M. Rahman and M. Stuchly, “Transmission line–periodic circuit representation of planar microwave photonic bandgap structures,” *Microwave and optical technology letters*, vol. 30, no. 1, pp. 15–19, 2001.

[17] F. Yang and Y. Rahmat-Samii, *Electromagnetic band gap structures in antenna engineering.* Cambridge university press Cambridge, UK, 2009.

[18] Y. Zheng, J. Gao, Y. Zhou, X. Cao, H. Yang, S. Li, and T. Li, “Wideband gain enhancement and rcs reduction of fabry–perot resonator antenna with chessboard arranged metamaterial superstrate,” *IEEE Transactions on Antennas and Propagation*, vol. 66, no. 2, pp. 590–599, 2017.

[19] B. Lu, X. Gong, J. Ling, and H. W. Yuan, “Radar cross-section reduction of antenna using a stop-band frequency selective surface,” *Microwave Journal*, pp. 6–+, 2009.

[20] J. Wu and K. Sarabandi, “Reactive impedance surface tm mode slow wave for patch antenna miniaturization [amta corner],” *IEEE Antennas and Propagation Magazine*, vol. 56, no. 6, pp. 279–293, 2014.

[21] W. E. Liu, Z. N. Chen, X. Qing, J. Shi, and F. H. Lin, "Miniaturized wideband metasurface antennas," *IEEE transactions on antennas and propagation*, vol. 65, no. 12, pp. 7345–7349, 2017.

[22] G. I. Kiani, K. L. Ford, L. G. Olsson, K. P. Esselle, and C. J. Panagamuwa, "Switchable frequency selective surface for reconfigurable electromagnetic architecture of buildings," *IEEE Transactions on Antennas and Propagation*, vol. 58, no. 2, pp. 581–584, 2009.

[23] Y. Zhao, J. Fu, Z. Wang, W. Chen, B. Lv, and Q. Zhang, "Design of a broadband switchable active frequency selective surfaces based on modified diode model," *IEEE Antennas and Wireless Propagation Letters*, vol. 21, no. 7, pp. 1378–1382, 2022.

[24] W. Li, Y. Wang, S. Sun, and X. Shi, "An fss-backed reflection/transmission reconfigurable array antenna," *IEEE Access*, vol. 8, pp. 23 904–23 911, 2020.

[25] S. Ghosh and K. V. Srivastava, "Broadband polarization-insensitive tunable frequency selective surface for wideband shielding," *IEEE Transactions on Electromagnetic Compatibility*, vol. 60, no. 1, pp. 166–172, 2017.

[26] B. Sanz-Izquierdo and E. Parker, "Dual polarized reconfigurable frequency selective surfaces," *IEEE Transactions on Antennas and Propagation*, vol. 62, no. 2, pp. 764–771, 2013.

[27] P. Kong, X. Yu, Z. Liu, K. Zhou, Y. He, L. Miao, and J. Jiang, "A novel tunable frequency selective surface absorber with dual-dof for broadband applications," *Optics express*, vol. 22, no. 24, pp. 30 217–30 224, 2014.

[28] S. Zhu and R. Langley, "Dual-band wearable textile antenna on an ebg substrate," *IEEE transactions on Antennas and Propagation*, vol. 57, no. 4, pp. 926–935, 2009.

[29] A. Foroozesh and L. Shafai, "Investigation into the effects of the reflection phase characteristics of highly-reflective superstrates on resonant cavity antennas," *IEEE transactions on antennas and propagation*, vol. 58, no. 10, pp. 3392–3396, 2010.

[30] S.-C. Chiu and S.-Y. Chen, "High-gain circularly polarized resonant cavity antenna using fss superstrate," in *2011 IEEE International Symposium on Antennas and Propagation (APSURSI)*. IEEE, 2011, pp. 2242–2245.

[31] S. Ghosh and K. V. Srivastava, "Polarization-insensitive single-and broadband switchable absorber/reflector and its realization using a novel biasing technique," *IEEE Transactions on Antennas and Propagation*, vol. 64, no. 8, pp. 3665–3670, 2016.

[32] J. Lončar, A. Grbic, and S. Hrabar, "A reflective polarization converting metasurface at x-band frequencies," *IEEE Transactions on Antennas and Propagation*, vol. 66, no. 6, pp. 3213–3218, 2018.

[33] E. Arnieri, F. Greco, L. Boccia, and G. Amendola, "A siw-based polarization rotator with an application to linear-to-circular dual-band polarizers at k-/ka-band," *IEEE Transactions on Antennas and Propagation*, vol. 68, no. 5, pp. 3730–3738, 2020.

[34] J.-M. Xie, B. Li, and L. Zhu, "Dual-band circular polarizers with versatile polarization conversions based on aperture-coupled patch resonators," *IEEE Transactions on Antennas and Propagation*, vol. 70, no. 7, pp. 5584–5596, 2022.

[35] H. Wang, L. Zheng, M. Yan, J. Wang, S. Qu, and R. Luo, "Design and analysis of miniaturized low profile and second-order multi-band polarization selective surface for multipath communication application," *IEEE Access*, vol. 7, pp. 13 455–13 467, 2019.

[36] B. Anudeep, K. Krishnamoorthy, and P. Rao, "Low-profile, wideband dual-polarized 1× 2 mimo antenna with fss decoupling technique," *International Journal of Microwave and Wireless Technologies*, vol. 14, no. 5, pp. 634–640, 2022.

[37] P. Xie, G. Wang, H. Li, and J. Liang, "A dual-polarized two-dimensional beam-steering fabry–pérot cavity antenna with a reconfigurable partially reflecting surface," *IEEE Antennas and Wireless Propagation Letters*, vol. 16, pp. 2370–2374, 2017.

[38] F. Costa, A. Monorchio, and G. Manara, "An overview of equivalent circuit modeling techniques of frequency selective surfaces and metasurfaces," *The Applied Computational Electromagnetics Society Journal (ACES)*, pp. 960–976, 2014.

[39] R. Mittra, C. H. Chan, and T. Cwik, "Techniques for analyzing frequency selective surfaces-a review," *Proceedings of the IEEE*, vol. 76, no. 12, pp. 1593–1615, 1988.

[40] Y. Zouaoui, L. Talbi, and K. Hettak, "Cross dipole fss bandwidth enhancement," in *2019 IEEE International Symposium on Antennas and Propagation and USNC-URSI Radio Science Meeting.* IEEE, 2019, pp. 947–948.

[41] H. Silva, C. Silva, M. R. T. de Oliveira, E. M. F. de Oliveira, M. T. de Melo, T. R. de Sousa, and A. Gomes, "Multiband fss with fractal characteristic based on jerusalem cross geometry," *Journal of Microwaves, Optoelectronics and Electromagnetic Applications*, vol. 16, pp. 932–941, 2017.

[42] C. K. Lee and R. Langley, "Equivalent-circuit models for frequency-selective surfaces at oblique angles of incidence," in *IEE Proceedings H (Microwaves, Antennas and Propagation)*, vol. 132, no. 6. IET, 1985, pp. 395–399.

[43] M. Fallah, A. Ghayekhloo, and A. Abdolali, "Design of frequency selective band stop shield using analytical method," *Journal of Microwaves, Optoelectronics and Electromagnetic Applications*, vol. 14, pp. 217–228, 2015.

[44] M.-J. Huang, M.-Y. Lv, J. Huang, and Z. Wu, "A new type of combined element multiband frequency selective surface," *IEEE transactions on antennas and propagation*, vol. 57, no. 6, pp. 1798–1803, 2009.

[45] D. Sood and C. Tripathi, "Polarization insensitive compact wide stop-band frequency selective surface," *Journal of Microwaves, Optoelectronics and Electromagnetic Applications*, vol. 17, pp. 53–64, 2018.

[46] A. Joshi and R. Singhal, "Gain enhancement in probe-fed hexagonal ultra wideband antenna using amc reflector," *Journal of Electromagnetic Waves and Applications*, vol. 33, no. 9, pp. 1185–1196, 2019.

[47] R. S. Aziz, S. Koziel, L. Leifsson, and S. Szczepanski, "Novel versatile topologies and design optimization of wide-bandstop frequency selective surfaces for x-band, ku-band and millimeter-wave applications," *Scientific Reports*, vol. 13, no. 1, p. 1952, 2023.

[48] K. Sarabandi and N. Behdad, "A frequency selective surface with miniaturized elements," *IEEE Transactions on Antennas and propagation*, vol. 55, no. 5, pp. 1239–1245, 2007.

[49] C.-N. Chiu and K.-P. Chang, "A novel miniaturized-element frequency selective surface having a stable resonance," *IEEE Antennas and Wireless Propagation Letters*, vol. 8, pp. 1175–1177, 2009.

[50] R. Wang, Y. Yang, B. Makki, and A. Shamim, “A wideband reconfigurable intelligent surface for 5g millimeter-wave applications,” *arXiv preprint arXiv:2304.11572*, 2023.

[51] C. Mias and J. H. Yap, “A varactor-tunable high impedance surface with a resistive-lumped-element biasing grid,” *IEEE Transactions on Antennas and Propagation*, vol. 55, no. 7, pp. 1955–1962, 2007.

[52] A. P. Feresidis, G. Goussetis, S. Wang, and J. C. Vardaxoglou, “Artificial magnetic conductor surfaces and their application to low-profile high-gain planar antennas,” *IEEE Transactions on Antennas and Propagation*, vol. 53, no. 1, pp. 209–215, 2005.

[53] N. Guérin, S. Enoch, G. Tayeb, P. Sabouroux, P. Vincent, and H. Legay, “A metallic fabry-perot directive antenna,” *IEEE Transactions on Antennas and Propagation*, vol. 54, no. 1, pp. 220–224, 2006.

[54] B. P. Chacko, G. Augustin, and T. A. Denidni, “Fpc antennas: C-band point-to-point communication systems,” *IEEE Antennas and Propagation Magazine*, vol. 58, no. 1, pp. 56–64, 2016.

[55] F. Qin, S. Gao, G. Wei, Q. Luo, C. Mao, C. Gu, J. Xu, and J. Li, “Wideband circularly polarized fabry-perot antenna [antenna applications corner],” *IEEE Antennas and Propagation Magazine*, vol. 57, no. 5, pp. 127–135, 2015.

[56] L. Zhang and T. Dong, “Low rcs and high-gain cp microstrip antenna using sa-ms,” *Electronics Letters*, vol. 53, no. 6, pp. 375–376, 2017.

[57] N. Hussain, M.-J. Jeong, J. Park, and N. Kim, “A broadband circularly polarized fabry-perot resonant antenna using a single-layered prs for 5g mimo applications,” *IEEE Access*, vol. 7, pp. 42 897–42 907, 2019.

[58] H. Zhu, X. Liu, S. Cheung, and T. Yuk, “Frequency-reconfigurable antenna using metasurface,” *IEEE Transactions on Antennas and Propagation*, vol. 62, no. 1, pp. 80–85, 2013.

[59] X. Chen and Y. Zhao, “Dual-band polarization and frequency reconfigurable antenna using double layer metasurface,” *AEU-International Journal of Electronics and Communications*, vol. 95, pp. 82–87, 2018.

[60] P. Das and K. Mandal, “Modelling of ultra-wide stop-band frequency-selective surface to enhance the gain of a uwb antenna,” *IET microwaves, antennas & propagation*, vol. 13, no. 3, pp. 269–277, 2019.

[61] A. Bhattacharya, B. Dasgupta, and R. Jyoti, "Design and analysis of ultrathin x-band frequency selective surface structure for gain enhancement of hybrid antenna," *International Journal of RF and Microwave Computer-Aided Engineering*, vol. 31, no. 2, p. e22505, 2021.

[62] A. Jamali Arand and B. Abbasi Arand, "Performance enhancement of microstrip antenna using artificial magnetic conductor reflection phase characteristics," *International Journal of RF and Microwave Computer-Aided Engineering*, vol. 31, no. 8, p. e22705, 2021.

[63] R. Mark, N. Rajak, K. Mandal, and S. Das, "Metamaterial based superstrate towards the isolation and gain enhancement of mimo antenna for wlan application," *AEU-International Journal of Electronics and Communications*, vol. 100, pp. 144–152, 2019.

[64] R. Garg, P. Bhartia, I. J. Bahl, and A. Ittipiboon, *Microstrip antenna design handbook*. Artech house, 2001.

[65] S. Ghosh, T. T. Nguyen, and S. Lim, "Recent progress in angle-insensitive narrowband and broadband metamaterial absorbers," *EPJ Applied Metamaterials*, vol. 6, p. 12, 2019.

[66] S. Garg, D. Sood, K. Gopal *et al.*, "An ultrathin polarization insensitive frequency selective surface for wide stop band rf applications," *Indian Journal of Pure & Applied Physics (IJPAP)*, vol. 56, no. 3, pp. 196–202, 2018.

[67] S. Yadav, C. P. Jain, and M. M. Sharma, "Polarization independent dual-bandpass frequency selective surface for wi-max applications," *International Journal of RF and Microwave Computer-Aided Engineering*, vol. 28, no. 6, p. e21278, 2018.

[68] F. C. Segundo, A. L. P. Campos, A. Gomes, and M. d. O. Alencar, "Double layer frequency selective surface for ultra wide band applications with angular stability and polarization independence," *Journal of Microwaves, Optoelectronics and Electromagnetic Applications*, vol. 18, pp. 328–342, 2019.

[69] E. A. Parker and S. Hamdy, "Rings as elements for frequency selective surfaces," *Electronics Letters*, vol. 17, no. 17, pp. 612–614, 1981.

[70] A. K. Fahad, C. Ruan, S. A. Ali, R. Nazir, T. U. Haq, S. Ullah, and W. He, "Triband ultrathin polarization converter for x/ku/ka-band microwave trans-

mission," *IEEE Microwave and Wireless Components Letters*, vol. 30, no. 4, pp. 351–354, 2020.

[71] A. Ramezani Varkani, Z. Hossein Firouzeh, and A. Zeidaabadi Nezhad, "Equivalent circuit model for array of circular loop fss structures at oblique angles of incidence," *IET Microwaves, Antennas & Propagation*, vol. 12, no. 5, pp. 749–755, 2018.

[72] T. SureshKumar, C. Venkatesh, P. Salil, and B. Subbarao, "Transmission line approach to calculate the shielding effectiveness of an enclosure with double-layer frequency selective surface," *IEEE Transactions on Electromagnetic Compatibility*, vol. 57, no. 6, pp. 1736–1739, 2015.

[73] B. Zhang, C. Liu, J. Zhang, Z. Wu, R. Xu, and Y. Ye, "Design and measurement of an em composite material frequency selective surface in c band," *Materials Research Innovations*, vol. 19, no. sup8, pp. S8–819, 2015.

[74] F. M. Monavar and N. Komjani, "Bandwidth enhancement of microstrip patch antenna using jerusalem cross-shaped frequency selective surfaces by invasive weed optimization approach," *Progress In Electromagnetics Research*, vol. 121, pp. 103–120, 2011.

[75] D. Kanchana, S. Radha, B. Sreeja, E. Manikandan *et al.*, "Polarization dependent fss for x and ku-band frequency response," *Journal of Optoelectronics and Advanced Materials*, vol. 22, no. July-August 2020, pp. 365–370, 2020.

[76] P. Naseri, S. A. Matos, J. R. Costa, C. A. Fernandes, and N. J. Fonseca, "Dual-band dual-linear-to-circular polarization converter in transmission mode application to k/ka-band satellite communications," *IEEE Transactions on Antennas and Propagation*, vol. 66, no. 12, pp. 7128–7137, 2018.

[77] M. Saikia, S. Ghosh, and K. V. Srivastava, "Design and analysis of ultrathin polarization rotating frequency selective surface using v-shaped slots," *IEEE Antennas and Wireless Propagation Letters*, vol. 16, pp. 2022–2025, 2017.

[78] W. Tilston, T. Tralman, and S. Khanna, "A polarization selective surface for circular polarization," in *1988 IEEE AP-S. International Symposium, Antennas and Propagation.* IEEE, 1988, pp. 762–765.

[79] Z. Liu, X. Lei, J.-M. Wu, and Z.-J. Xu, "Dual-mode circular polarization selective surface cell for single-layer dual-band circularly polarized reflectarray," *International Journal of Antennas and Propagation*, vol. 2019, 2019.

[80] Y. Hao and R. Mittra, *FDTD modeling of metamaterials: Theory and applications.* Artech house, 2008.

[81] R. C. Hadarig, M. De Cos, and F. Las-Heras, "Novel miniaturized artificial magnetic conductor," *IEEE Antennas and Wireless Propagation Letters*, vol. 12, pp. 174–177, 2013.

[82] K. S. Sultan, H. H. Abdullah, E. A. Abdallah, and H. S. El-Hennawy, "Metasurface-based dual polarized mimo antenna for 5g smartphones using cma," *IEEE Access*, vol. 8, pp. 37 250–37 264, 2020.

[83] Z. Wang, Y. Dong, Y. Ning, and T. Itoh, "Miniaturized circularly polarized periodically structured surface antenna for rfid application inspired by srr," *IEEE Transactions on Antennas and Propagation*, vol. 69, no. 11, pp. 7269–7277, 2021.

[84] A. Shastri, B. Sanz-Izquierdo, E. A. Parker, S. Gao, P. Reynaert, Z. Chen, and L. Winchester, "3d printing of millimetre wave and low-terahertz frequency selective surfaces using aerosol jet technology," *Ieee Access*, vol. 8, pp. 177 341–177 350, 2020.

[85] S. Sahin, N. K. Nahar, and K. Sertel, "Dielectric properties of low-loss polymers for mmw and thz applications," *Journal of Infrared, Millimeter, and Terahertz Waves*, vol. 40, no. 5, pp. 557–573, 2019.

[86] R. T. Ako, A. Upadhyay, W. Withayachumnankul, M. Bhaskaran, and S. Sriram, "Dielectrics for terahertz metasurfaces: Material selection and fabrication techniques," *Advanced Optical Materials*, vol. 8, no. 3, p. 1900750, 2020.

[87] D. W. Peters, L. I. Basilio, A. A. Cruz-Cabrera, W. Johnson, J. Wendt, S. Kemme, and S. Samora, "Simulation, fabrication and measurement of infrared frequency selective surfaces," in *Integrated Photonics and Nanophotonics Research and Applications.* Optica Publishing Group, 2008, p. IWF5.

[88] M. Raspopoulos and S. Stavrou, "Frequency selective buildings through frequency selective surfaces," *IEEE Transactions on Antennas and Propagation*, vol. 59, no. 8, pp. 2998–3005, 2011.

[89] R. Shavit, "Frequency selective surfaces (fss) radomes," 2018.

[90] N. Liu, X. Sheng, C. Zhang, and D. Guo, "Design and synthesis of band-pass frequency selective surface with wideband rejection and fast roll-off characteris-

tics for radome applications," *IEEE Transactions on Antennas and Propagation*, vol. 68, no. 4, pp. 2975–2983, 2019.

[91] J. Kim, H.-K. Jang, J. Oh, and J. Park, "A rational design procedure for absorbers of square-loop-shaped resistive frequency selective surface placed on glass/epoxy laminate," *IEEE Transactions on Electromagnetic Compatibility*, 2022.

[92] N. Gupta *et al.*, "Low-cost electromagnetic absorbers for shield packaging," *IEEE Transactions on Components, Packaging and Manufacturing Technology*, 2023.

[93] H. Uchimura, N. Hiramatsu, and H. Yoshikawa, "Artificial magnetic conductor with electric walls and its application to small antenna functional on metal surfaces," *IEEE Transactions on Antennas and Propagation*, vol. 69, no. 9, pp. 5315–5324, 2021.

[94] A. Joshi and R. Singhal, "Probe-fed wideband amc-integrated hexagonal antenna with uniform gain characteristics for wlan applications," *Wireless Networks*, vol. 26, pp. 3569–3578, 2020.

[95] L. Kurra, M. P. Abegaonkar, A. Basu, and S. K. Koul, "Fss properties of a uniplanar ebg and its application in directivity enhancement of a microstrip antenna," *IEEE Antennas and Wireless Propagation Letters*, vol. 15, pp. 1606–1609, 2016.

[96] J. Huang, T.-K. Wu, and S.-W. Lee, "Tri-band frequency selective surface with circular ring elements," *IEEE Transactions on Antennas and Propagation*, vol. 42, no. 2, pp. 166–175, 1994.

[97] R. J. Langley and E. A. Parker, "Equivalent circuit model for arrays of square loops," *Electronics Letters*, vol. 18, no. 7, pp. 294–296, 1982.

[98] D. Ferreira, R. F. Caldeirinha, I. Cuinas, and T. R. Fernandes, "Square loop and slot frequency selective surfaces study for equivalent circuit model optimization," *IEEE Transactions on Antennas and Propagation*, vol. 63, no. 9, pp. 3947–3955, 2015.

[99] A. Pirhadi, H. Bahrami, and J. Nasri, "Wideband high directive aperture coupled microstrip antenna design by using a fss superstrate layer," *IEEE transactions on antennas and propagation*, vol. 60, no. 4, pp. 2101–2106, 2012.

[100] Z. Liu, S. Liu, J. Bornemann, X. Zhao, X. Kong, Z. Huang, B. Bian, and D. Wang, "A low-rcs, high-gbp fabry–perot antenna with embedded chessboard polarization conversion metasurface," *IEEE Access*, vol. 8, pp. 80 183–80 194, 2020.

[101] M. Feng, J. Wang, H. Ma, W. Mo, H. Ye, and S. Qu, "Broadband polarization rotator based on multi-order plasmon resonances and high impedance surfaces," *Journal of Applied Physics*, vol. 114, no. 7, p. 074508, 2013.

[102] M. Al-Joumayly and N. Behdad, "A new technique for design of low-profile, second-order, bandpass frequency selective surfaces," *IEEE transactions on antennas and propagation*, vol. 57, no. 2, pp. 452–459, 2009.

[103] D. M. Pozar, *Microwave engineering.* John wiley & sons, 2011.

[104] S. Abbasi, J. Nourinia, C. Ghobadi, M. Karamirad, and B. Mohammadi, "A subwavelength polarization sensitive band-stop fss with wide angular response for x- and ku-bands," *AEU-International Journal of Electronics and Communications*, vol. 89, pp. 85–91, 2018.

[105] A. Kocakaya and G. Çakır, "Novel angular-independent higher order band-stop frequency selective surface for x-band applications," *IET Microwaves, Antennas & Propagation*, vol. 12, no. 1, pp. 15–22, 2018.

[106] V. Shaik and K. Shambavi, "Design of dodecagon unit cell shape based three layered frequency selective surfaces for x band reflection," *Progress In Electromagnetics Research*, vol. 75, pp. 103–111, 2018.

[107] S. Roy and U. Chakraborty, "Metamaterial-embedded dual wideband microstrip antenna for 2.4 ghz wlan and 8.2 ghz itu band applications," *Waves in Random and Complex Media*, vol. 30, no. 2, pp. 193–207, 2020.

[108] R. Rajkumar and K. U. Kiran, "A compact metamaterial multiband antenna for wlan/wimax/itu band applications," *AEU-International Journal of Electronics and Communications*, vol. 70, no. 5, pp. 599–604, 2016.

[109] P. G. Metri, "Theoretical study of equilateral triangular microstrip antenna and its arrays," in *Engineering Mathematics I: Electromagnetics, Fluid Mechanics, Material Physics and Financial Engineering.* Springer International Publishing Cham, 2016, pp. 65–78.

[110] R. Kumar and Y. Kamatham, “Compact tri-band monopole antenna for 2.4/5.8 ghz wlan and 8.3 ghz itu-t applications,” in *2019 IEEE International Conference on Electrical, Computer and Communication Technologies (ICECCT)*. IEEE, 2019, pp. 1–4.

[111] N. Wang, L. Talbi, Q. Zeng, and J. Xu, “Wideband fabry-perot resonator antenna with electrically thin dielectric superstrates,” *IEEE Access*, vol. 6, pp. 14 966–14 973, 2018.

[112] M. A. Meriche, H. Attia, A. Messai, S. S. I. Mitu, and T. A. Denidni, “Directive wideband cavity antenna with single-layer meta-superstrate,” *IEEE Antennas and Wireless Propagation Letters*, vol. 18, no. 9, pp. 1771–1774, 2019.

[113] A. Lalbakhsh, M. U. Afzal, K. P. Esselle, S. L. Smith, and B. A. Zeb, “Single-dielectric wideband partially reflecting surface with variable reflection components for realization of a compact high-gain resonant cavity antenna,” *IEEE Transactions on Antennas and Propagation*, vol. 67, no. 3, pp. 1916–1921, 2019.

[114] L. Moustafa and B. Jecko, “Ebg structure with wide defect band for broadband cavity antenna applications,” *IEEE Antennas and Wireless Propagation Letters*, vol. 7, pp. 693–696, 2008.

[115] Y. Liu, Y. Hao, and S. Gong, “Low-profile high-gain slot antenna with fabry-pérot cavity and mushroom-like electromagnetic band gap structures,” *Electronics Letters*, vol. 51, no. 4, pp. 305–306, 2015.

[116] W.-Q. Li, X.-Y. Cao, J. Gao, Z. Zhang, and L.-l. Cong, “Broadband rcs reduction and gain enhancement microstrip antenna using shared aperture artificial composite material based on quasi-fractal tree,” *IET Microwaves, Antennas & Propagation*, vol. 10, no. 4, pp. 370–377, 2016.

[117] E. Moharamzadeh and A. M. Javan, “Triple-band frequency-selective surfaces to enhance gain of x-band triangle slot antenna,” *IEEE Antennas and Wireless Propagation Letters*, vol. 12, pp. 1145–1148, 2013.

[118] X. Li, Y.-C. Jiao, and L. Zhang, “Wideband low-profile cpw-fed slot-loop antenna using an artificial magnetic conductor,” *Electronics Letters*, vol. 54, no. 11, pp. 673–674, 2018.

[119] S. S. Sampath and R. Sivasamy, “A single-layer uwb frequency-selective surface with band-stop response,” *IEEE Transactions on Electromagnetic Compatibility*, vol. 62, no. 1, pp. 276–279, 2018.

[120] A. Birwal, S. Singh, and B. K. Kanaujia, “A novel design of ultra-wide stop-band single-layer frequency selective surface using square-loop and cross,” *International Journal of Microwave and Wireless Technologies*, vol. 13, no. 8, pp. 800–809, 2021.

[121] F. A. Tahir, T. Arshad, S. Ullah, and J. A. Flint, “A novel fss for gain enhancement of printed antennas in uwb frequency spectrum,” *Microwave and Optical Technology Letters*, vol. 59, no. 10, pp. 2698–2704, 2017.

[122] A. P. Raiva, *Frequency selective surfaces: Design of broadband elements and frequency stabilization techniques.* Southern Illinois University at Carbondale, 2003.

[123] F. Costa, S. Genovesi, and A. Monorchio, “On the bandwidth of high-impedance frequency selective surfaces,” *IEEE Antennas and Wireless Propagation Letters*, vol. 8, pp. 1341–1344, 2009.

[124] I. J. Bahl, *Lumped elements for RF and microwave circuits.* Artech house, 2022.

[125] G. Bharti, K. R. Jha, G. Singh, and R. Jyoti, “Design of angular and polarization stable modified circular ring frequency selective surface for satellite communication system,” *International Journal of Microwave and Wireless Technologies*, vol. 8, no. 6, pp. 899–907, 2016.

[126] Y. Ranga, L. Matekovits, K. P. Esselle, and A. R. Weily, “Multioctave frequency selective surface reflector for ultrawideband antennas,” *IEEE Antennas and Wireless Propagation Letters*, vol. 10, pp. 219–222, 2011.

[127] I. S. Syed, Y. Ranga, L. Matekovits, K. P. Esselle, and S. G. Hay, “A single-layer frequency-selective surface for ultrawideband electromagnetic shielding,” *IEEE Transactions on Electromagnetic Compatibility*, vol. 56, no. 6, pp. 1404–1411, 2014.

[128] R. A. Abdulhasan, R. Alias, K. N. Ramli, F. C. Seman, and R. A. Abd-Alhameed, “High gain cpw-fed uwb planar monopole antenna-based compact uniplanar frequency selective surface for microwave imaging,” *International Journal of RF and Microwave Computer-Aided Engineering*, vol. 29, no. 8, p. e21757, 2019.

[129] D. Kanchana, S. Radha, B. Sreeja, and E. Manikandan, “A single layer uwb frequency selective surface for shielding application,” *Journal of Electronic Materials*, vol. 49, pp. 4794–4800, 2020.

[130] R. Azim, M. T. Islam, and N. Misran, “Compact tapered-shape slot antenna for uwb applications,” *IEEE Antennas and Wireless Propagation Letters*, vol. 10, pp. 1190–1193, 2011.

[131] Liu, Lau, Xue, and Chan, “Experimental studies of printed wide-slot antenna for wide-band applications,” *IEEE Antennas and Wireless Propagation Letters*, vol. 3, pp. 273–275, 2004.

[132] G. Pan, Y. Li, Z. Zhang, and Z. Feng, “A compact wideband slot-loop hybrid antenna with a monopole feed,” *IEEE Transactions on Antennas and Propagation*, vol. 62, no. 7, pp. 3864–3868, 2014.

[133] Y.-C. Lin and K.-J. Hung, “Compact ultrawideband rectangular aperture antenna and band-notched designs,” *IEEE Transactions on antennas and Propagation*, vol. 54, no. 11, pp. 3075–3081, 2006.

[134] S. Kundu, A. Chatterjee, S. K. Jana, and S. K. Parui, “Gain enhancement of a printed leaf shaped uwb antenna using dual fss layers and experimental study for ground coupling gpr applications,” *Microwave and Optical Technology Letters*, vol. 60, no. 6, pp. 1417–1423, 2018.

[135] ——, “A compact umbrella-shaped uwb antenna with gain augmentation using frequency selective surface,” *Radioengineering*, vol. 27, no. 2, pp. 448–454, 2018.

[136] Y. Yuan, X. Xi, and Y. Zhao, “Compact uwb fss reflector for antenna gain enhancement,” *IET Microwaves, Antennas & Propagation*, vol. 13, no. 10, pp. 1749–1755, 2019.

[137] S. Kundu and A. Chatterjee, “A compact super wideband antenna with stable and improved radiation using super wideband frequency selective surface,” *AEU-International Journal of Electronics and Communications*, vol. 150, p. 154200, 2022.

[138] ——, “A new compact ultra-wideband frequency selective surface with angular stability and polarization independence for antenna radiation enhancement in microwave imaging application,” *AEU-International Journal of Electronics and Communications*, vol. 155, p. 154351, 2022.

[139] S. Sambhav, J. Ghosh, and A. K. Singh, “Ultra-wideband polarization insensitive thin absorber based on resistive concentric circular rings,” *IEEE Transactions on Electromagnetic Compatibility*, vol. 63, no. 5, pp. 1333–1340, 2021.

[140] C.-H. Lee, S.-Y. Chen, and P. Hsu, “Isosceles triangular slot antenna for broadband dual polarization applications,” *IEEE transactions on antennas and propagation*, vol. 57, no. 10, pp. 3347–3351, 2009.

[141] S. U. Rahman, H. Deng, M. Sajjad, A. Rauf, Z. Shafiq, M. Ahmad, and S. Iqbal, “Angularly stable frequency selective surface for the gain enhancement of isolated multiple input multiple output antenna,” *Microwave and Optical Technology Letters*, vol. 63, no. 11, pp. 2803–2810, 2021.

[142] A. Kumar, A. De, and R. K. Jain, “Gain enhancement using modified circular loop fss loaded with slot antenna for sub-6 ghz 5g application,” *Progress In Electromagnetics Research Letters*, vol. 98, pp. 41–48, 2021.

[143] T. Kürner, “Towards future thz communications systems,” *Terahertz science and technology*, vol. 5, no. 1, pp. 11–17, 2012.

[144] A. Mathivanan and S. Palani, “Novel polarization independent multiband thz perfect metamaterial,” *Microwave and Optical Technology Letters*, vol. 64, no. 4, pp. 694–700, 2022.

[145] C. Debus and P. H. Bolivar, “Frequency selective surfaces for high sensitivity terahertz sensing,” *Applied Physics Letters*, vol. 91, no. 18, p. 184102, 2007.

[146] J.-S. Li, Y. Li, and L. Zhang, “Terahertz bandpass filter based on frequency selective surface,” *IEEE Photonics Technology Letters*, vol. 30, no. 3, pp. 238–241, 2017.

[147] X. Chen, Y. Chen, L. Deng, F. Huang, and X. Wang, “Tailoring the band-pass properties of fss-based thz filters,” *Optik*, vol. 239, p. 166730, 2021.

[148] A. Ebrahimi, S. Nirantar, W. Withayachumnankul, M. Bhaskaran, S. Sriram, S. F. Al-Sarawi, and D. Abbott, “Second-order terahertz bandpass frequency selective surface with miniaturized elements,” *IEEE Transactions on Terahertz Science and Technology*, vol. 5, no. 5, pp. 761–769, 2015.

[149] V. Sanphuang and N. K. Nahar, “Flexible terahertz and farir polymer-supported filter,” *Microwave and Optical Technology Letters*, vol. 60, no. 11, pp. 2801–2805, 2018.

[150] D. Wang, S. Sun, Z. Feng, and W. Tan, "Complete terahertz polarization control with broadened bandwidth via dielectric metasurfaces," *Nanoscale Research Letters*, vol. 16, no. 1, pp. 1–9, 2021.

[151] J. Ghosh and D. Mitra, "Mutual coupling reduction in planar antenna by graphene metasurface for thz application," *Journal of Electromagnetic Waves and Applications*, vol. 31, no. 18, pp. 2036–2045, 2017.

[152] E. Manikandan, B. S. Sreeja, S. Radha, M. Duraiselvam, A. Gupta, and S. Prabhu, "Microfabrication of terahertz frequency-selective surface by short- and ultrashort laser ablation," *Optical Engineering*, vol. 58, no. 1, pp. 011 007–011 007, 2019.

[153] A. Ferraro, D. C. Zografopoulos, R. Caputo, and R. Beccherelli, "Guided-mode resonant narrowband terahertz filtering by periodic metallic stripe and patch arrays on cyclo-olefin substrates," *Scientific Reports*, vol. 8, no. 1, p. 17272, 2018.

[154] X. Ri-Hui and L. Jiu-Sheng, "Double-layer frequency selective surface for terahertz bandpass filter," *Journal of Infrared, Millimeter, and Terahertz Waves*, vol. 39, pp. 1039–1046, 2018.

[155] G. Bharti, K. R. Jha, and G. Singh, "A synthesis technique of single square loop frequency selective surface at terahertz frequency," *Optik*, vol. 125, no. 21, pp. 6428–6435, 2014.

[156] S. Das, K. M. Reza, and M. A. Habib, "Frequency selective surface based bandpass filter for thz communication system," *Journal of Infrared, Millimeter, and Terahertz Waves*, vol. 33, pp. 1163–1169, 2012.

[157] A. M. Melo, A. L. Gobbi, M. H. Piazzetta, and A. M. Da Silva, "Cross-shaped terahertz metal mesh filters: Historical review and results," *Advances in Optical Technologies*, vol. 2012, 2012.

[158] D. Zhai, Y. Yang, Z. Geng, B. Cui, and R. Zhao, "A high-selectivity thz filter based on a flexible polyimide film," *IEEE Transactions on Terahertz Science and Technology*, vol. 8, no. 6, pp. 719–724, 2018.

[159] P. Das and G. Varshney, "Gain enhancement of dual-band terahertz antenna using reflection-based frequency selective surfaces," *Optical and Quantum Electronics*, vol. 54, no. 3, p. 161, 2022.

[160] B. Aqlan, M. Himdi, H. Vettikalladi, and L. Le-Coq, "A 300-ghz low-cost high-gain fully metallic fabry–perot cavity antenna for 6g terahertz wireless communications," *Scientific Reports*, vol. 11, no. 1, pp. 1–9, 2021.

[161] P. Das and R. Panwar, "Broadband rcs reduction of microstrip antenna in the thz band," *Optical and Quantum Electronics*, vol. 53, no. 7, p. 410, 2021.

[162] M. Farahani, M. Akbari, M. Nedil, and T. A. Denidni, "Mutual coupling reduction in dielectric resonator mimo antenna arrays using metasurface orthogonalize wall," in *2017 11th European Conference on Antennas and Propagation (EUCAP)*. IEEE, 2017, pp. 985–987.

[163] B. Zhang, J. M. Jornet, I. F. Akyildiz, and Z. P. Wu, "Mutual coupling reduction for ultra-dense multi-band plasmonic nano-antenna arrays using graphene-based frequency selective surface," *Ieee Access*, vol. 7, pp. 33 214–33 225, 2019.

[164] T. Rider, W. B. Kuhn, and A. Wolf, "Crosstalk and emi in mixed-signal/microwave multi-layer pc boards," in *2017 IEEE International Symposium on Electromagnetic Compatibility & Signal/Power Integrity (EMCSI)*. IEEE, 2017, pp. 26–31.

[165] H. Luan, Y. Wang, C. Chen, and W. Chen, "Mutual coupling reduction of closely e/h-coupled mimo antennas through metasurfaces," in *2019 International Symposium on Antennas and Propagation (ISAP)*. IEEE, 2019, pp. 1–3.

[166] Q. Luo, S. Gao, X.-x. Yang, and J. T. S. Sumantyo, "Low-cost beam-reconfigurable directional antennas for advanced communications," *Antenna and Array Technologies for Future Wireless Ecosystems*, pp. 83–117, 2022.

[167] L.-M. Zhang, X. Ding, and B.-Z. Wang, "A low-cost beam steering antenna for indoor wireless communication," *IEEE Transactions on Antennas and Propagation*, vol. 70, no. 9, pp. 8548–8553, 2022.

[168] H. Gacanin and M. Di Renzo, "Wireless 2.0: Toward an intelligent radio environment empowered by reconfigurable meta-surfaces and artificial intelligence," *IEEE Vehicular Technology Magazine*, vol. 15, no. 4, pp. 74–82, 2020.

[169] W. Long, R. Chen, M. Moretti, W. Zhang, and J. Li, "A promising technology for 6g wireless networks: Intelligent reflecting surface," *Journal of Communications and Information Networks*, vol. 6, no. 1, pp. 1–16, 2021.

[170] S. Zhang, H. Zhang, B. Di, Y. Tan, M. Di Renzo, Z. Han, H. V. Poor, and L. Song, “Intelligent omni-surfaces: Ubiquitous wireless transmission by reflective-refractive metasurfaces,” *IEEE Transactions on Wireless Communications*, vol. 21, no. 1, pp. 219–233, 2021.

[171] S. Zhang, H. Zhang, B. Di, Y. Tan, Z. Han, and L. Song, “Beyond intelligent reflecting surfaces: Reflective-transmissive metasurface aided communications for full-dimensional coverage extension,” *IEEE Transactions on Vehicular Technology*, vol. 69, no. 11, pp. 13 905–13 909, 2020.

Brief Biography of Supervisor

Prof. Rahul Singhal is working as an Associate Professor in Department of Electrical and Electronics Engineering, BITS Pilani-Campus, Pilani. He completed his BE (Electronics Engineering) from Nagpur University in 1999 and started his teaching career in 2000. During his tenure as Lecturer, he completed his M.Tech. (Digital Communication) from Uttar Pradesh Technical University, Lucknow in 2007 and got his Ph.D. completed in 2013 at Birla Institute of Technology and Science (BITS), Pilani-Campus, Pilani. His doctoral work lies in integrated optics involving the design and technology development of optical waveguides and uniform power distribution in optical power splitters. His current research interest lies in antenna and wave propagation; optical devices and sensors; radio-over-fiber and wireless optical networks. He has authored and co-authored technical papers in various reputed international journals and conferences. He has reviewed many technical research articles published in international journals and conferences. He is senior member of the IEEE, a life-member of the Optical Society of India and the Institution of Electronics and Telecommunication Engineers (India).

Brief Biography of Candidate

Ashish Kumar Verma is a Ph.D. scholar at Birla Institute of Technology and Science (BITS), Pilani-Campus, Pilani, Rajasthan in the domain of RF & Microwave Engineering. He received B. Tech degree in Electronics and Communication Engineering from Uttar Pradesh Technical University, Lucknow and M.Tech degree in RF and Microwave Engineering from Swami Vivekanand Subharti University, Meerut. Currently, he is pursuing his Ph.D. degree from Birla Institute of Technology and Science (BITS), Pilani-Campus, Pilani, Rajasthan. His main research interests include, compact antenna design, design and analysis of periodic structures such as frequency selective surfaces, artificial magnetic conductors, electromagnetic band gap structures, etc. His skill includes design and modelling of antenna and RF circuits with CST MWS/ANSYS HFSS and measurements using vector network analyzer and anechoic chamber.